POLITECNICO
MILANO 1863
Engineering Faculty
Energy Department

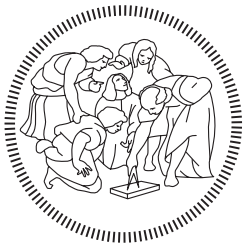

POLITECNICO
MILANO 1863

Doctoral Program in Electrical Engineering

EVOLVED FEATURES IN MVDC RAILWAYS AND HVDC NETWORKS BY ENERGY STORAGE SYSTEMS

PhD Thesis of:
Alessio CLERICI
Matr. 10186374

Tutor : Prof. Luigi PIEGARI
Supervisor: Prof. Enrico TIRONI

Chair of Doctoral Program:
Prof. Gabriele D'ANTONA

XXIX Cycle, 2013

RINGRAZIAMENTI:

I miei più sentiti ringraziamenti al Prof. Enrico Tironi, che mi ha aiutato, mi ha sopportato, mi ha (giustamente) rimproverato e mi ha ben consigliato; sono stato seguito in maniera precisa, puntuale e professionale, avendo nel contempo ampi margini di autonomia.

Ringrazio parimenti il Prof. Francesco Castelli Dezza, che mi ha aiutato nella stesura ben oltre i propri obblighi professionali, dando spunti e portando un altro punto di vista, oltre agli immancabili e sempre divertenti sghignazzi...

Al Prof. Brenna per i preziosi consigli per la parte ferroviaria, al Prof. Piegari per il tutoraggio e soprattutto per aver sopportato le mie incursioni nel suo ufficio per parlare col Prof. Castelli Dezza (credo abusivo anche lui, comunque).

Al gruppo di Dottorandi, Dottori & Co, miei compagni e piú di (dis)avventura, li scrivo in rigoroso ordine sparso, tanto loro conoscono benissimo i miei preferiti: Christian Laurano (Wiki-trash, autoritá in campo musicale e di costume, dicono s'intenda anche di misure, ma sicuramente Zanoni ha qualcosa da ridire in proposito), Michele Zaononi (& Francesca, che lo frequenta nonostante lui sia un bassista e pure un misurista, massima combinazione mondiale scaccia-donne) Simone Barcellona (cinque Euro non esistono, ma li scoccio lo stesso), Matteo Corti (& Andrea, che nonostante le apparenze nomastiche é donna), Giacomo Leone (non chiedo di sua sorella per eleganza), Ludovico Badini (& Chiara), Nicola Toscani (mio idolo, meglio anche di Renato Pozzetto e Jerry Calá messi assieme, lui sa perché), Simone Negri (il Moralizzatore, sguardo glaciale e orecchie di velluto), Luca Giussani (il Matriciologo, puó invertire qualsiasi cosa abbia un determinante diverso da zero, mai dopo le 21:00 perché altrimenti perde l'ultimo Besanino), Davide De Simone (Telespalla Bob), Alberto Carboni (l'uomo delle multinazionali, prematuramente scomparso, dalle stanze del Politecnico) Satish Kumar (Brown Sugar).

Al gruppo di ex colleghi, eccitatori e non eccitatori (ovvero impiegati nei sistemi di eccitazione statica, la malizia sta sempre nell'occhio di chi legge!): Gianfranco Meregalli (Gggianfrrrr), Alessandro Rocchi (The Rock), Alessandro Corda (Cordiño) Marco Barera, Paolo Casiraghi, Fabio Veschi (Athos, Portos e Aramis, rispettivamente!), Domenico Mangiola (D'Artagnan), Roberto Bernacchi (Colonnello Bernacca), Roberto Speciale (Aarobbé), Igor Tacconi (Aigor), Federico Bosi (BosiCAD), Fabio Papa (UPSman), Stefano Pellegrini, Luciano Rusignuolo (Rus), Marco (Philadelfia) Leicht, Rosella Cellesi, Sara Saltalamacchia, Manrico Campinoti, Marika Mozzato, Simonetta Sommariva e scusatemi se ho dimenticato qualcuno....

Al gruppo di colleghi attuali, che mi hanno accolto benissimo (li ho intortati bene, la prima impressione é quella che conta!), cui spetta l'onore e l'onere di sopportarmi per gli anni a venire: Chiara Gandolfi, Riccardo Chiumeo, Alberto Villa, Roberto Zuelli, Mattia Cabiati, Massimiliano Volta, Houriyeh Shadmehr, Liliana Tenti e Marilena Martinelli. Colleghi (ma non troppo!), saluto anche Anna Realini e Valerio Angelucci, per il supporto psicologico e per le divertenti discussioni alla macchinetta del caffé.

Parentame, li ringrazio tutti per la pazienza di questi anni, in primis Mami e Papi, con l'augurio che possano godersi serenamente gli anni a venire; i nonni Adriana e Mario, che hanno passato qualche momento di difficoltá ma che se la cavano sempre molto bene a prescindere dalla carta d'identitá; la zia Cristina, che mi scarrozzava con la Y10 all'asilo nel 1989 e mi ha sempre fatto sentire a casa; Giuseppe, Chiara, Sofia e Lorenzino (il mio *Popotto*), a cui auguro di non trovare tanto presto un cassetto della sua altezza, crescere é piú seccante di quanto si pensi, meglio restare piccoli per un po'...

A Federica (ballerina, nel senso che balla), Federica (Ballerini, nel senso di cognome, da non confondere con la precedente), Enrica, Eleonora, Esther, Silvietta, Noemi, Valentina, Francesca, Cristina, Debora e Marta: tutte, a modo vostro ed in tempi diversi, avete contribuito a rendere questi ultimi 10-15 anni un po' piú... (precisazione necessaria, alcune sono solo amiche e hanno pesanti responsabilitá su alcune delle mie scelte di vita, sappiatelo!)

A Marco, Omar e Andrea (Max), amici maschi pochi, ma buoni: ci si vede magari meno di prima, ma fa sempre piacere ritrovarsi!

A Marchino ed Allison, soprattutto amici ma anche raddrizza-schiena di fiducia, anche loro hanno responsabilitá, ma col senno di poi, beh avevano ragione!

E ultima, ma importante molto e assai, a Barbara (la mia *Bresaolina*), che ha sempre creduto in me e che mi vuole tanto bene (e allora lo vedi che la cosa é reciproca?)

Questo lavoro é stato parzialmente finanziato dal Fondo di Ricerca per il Sistema Elettrico nell´ambito dell´Accordo di Programma tra RSE S.p.A. ed il Ministero dello Sviluppo Economico - D.G. Nucleare, Energie rinnovabili ed efficienza energetica - in ottemperanza del DM, 8 marzo 2006.

INDEX

FIGURES

TABLES

ABSTRACT

For decades, Alternating Current (AC) has been the standard for most of electric power systems worldwide; Direct Current (DC) was confined in few fields of interest, usually in networks or grids designed for specific purposes (e.g. rail traction or very long distances transmission lines).

Such paradigm is changing since the beginning of the 21^{th} Century, when technological progress in power electronics made DC able to compete against AC in many fields: presently, a huge number of DC power devices is used at every level of our society, in private, business, industry and services.

This huge revolution only touched marginally the mentioned pre-existing DC networks; many remarkable improvements have been got in such areas, but the general shape or function of those systems are still the same: in railway field, as example, the most of DC distribution is still based on old-style diode rectifies; majority of High Voltage Direct Current (HVDC) transmission lines are still based on classic Line Commutated Converters (LCC) technology.

In recent years, both in AC and DC networks, a new set of critical issues is emerging: higher load peaks are creating problems of voltage stability and power quality; grid inertia is lowering by huge penetration of renewable-not-programmable energy sources.

This work analyzes railway grids and HVDC links, two of the most relevant DC power systems of today; in both of them, evolved features are introduced by Energy Storage Systems (ESS) and innovative Power Electronics Converters (PEC): energy recovery and voltage stabilization about traction; synthetic inertia about HVDC. Due to fast dynamic performances and high level of controllability, power converters and ESS can mitigate above mentioned issues.

Investment costs are lowering but still relevant, thus technical-economical evaluation is needed; because such analysis is extremely complex, some simplifications have been introduced, using precautionary hypothesis.

Approach is top-down, considering equipment as part of a plant, mainly focusing on functionalities; several configurations are tested and validated by simulations. Later on, design solutions are analyzed, control algorithms are explained and compared, presenting advantages and disadvantages.

INTRODUCTION

Since 1890, after the conclusion of the so-called "War Of Currents", Alternating Current (AC) became the standard for most of electric system worldwide; the main reason for such choice was definitely practical: the transformer at first, the induction motor later on, made AC power the way to be transferred and used with low electrical losses and high mechanical efficiency, driving the Second Industrial Revolution in the last years of the 18^{th} Century.

Main disadvantages of Direct Current (DC) respect to AC were the impossibility of efficient voltage scaling by transformers, the difficulty in generating high voltages into the dynamos and frequent maintenance required by DC motors (both due to collectors wearing).

Such paradigm changed since the last decades of the 20^{th} Century, for two main reasons:

- Power electronics progresses: new solid-state based converters have been developed, by-passing both the problems of voltage scaling and defects of DC motors;

- Spread of information technology and microelectronics (Third-Fourth Industrial Revolution): all Personal Computers (PCs), portable devices, modern electronic gadgets, smart-phones and so on are DC based.

Due to previous reasons, nowadays great and growing interest is emerging about DC power all over the world.

This huge revolution only touched marginally some pre-existing DC networks: DC power, initially prominent respect to AC (see Appendix C), has been confined in few fields of interest, usually in networks or grids specifically designed for specific purposes; main examples are rail traction catenary supply (so-called DC-wayside distribution) and very long distances transmission lines (so-called HVDC links).

In those fields, technological aspects as conversion efficiency and devices reliability have been improved a lot, but the general layout of systems has remained almost the same.

In 3 kV DC railways, as example, DC-wayside distribution is still mainly based on old-style diode rectifies; they are very robust, reliable and quite efficient, but they are not versatile, nor designed to adapt themselves to different energetic scenarios.

HVDC links have been developed because of necessity, in some cases, to overpass specific technical limits of AC: high inductive and capacitive effects, need of intermediate substations, infrastructure costs (pylons, cables) etc.; through years, systems have been empowered a lot and technology became much more efficient, but most of power converters worldwide (also brand new ones, in many cases) are still classic Line

Commutated Converters (LCC), thyristor-based; they are robust and powerful, but they cannot be operated as VSC (Voltage Source Converters), nor control reactive power flow at AC side. Actually, HVDC are mainly intended as point-to-point links between different AC areas, they are not fully integrated in a meshed network (even multi-terminal HVDC links are very rare).

In recent years, both in AC and DC, a new set of critical issues about power transmission and distribution is growing:

- higher and higher power loads are creating problems of voltage stability and power quality, especially where network is weak; about traction, as example, modern trains on 3 kV DC railway are high power demanding, they cause deep voltage drops in acceleration and power waste during braking;

- low-carbon economic models generated the huge penetration of renewable-not-programmable energy sources; the result was a progressive dismiss of the traditional AC rotating generators, or their different way of utilization (cold stand-by); as a result, grid inertia is lowering and distributed power production makes network control and stability much more complex than in the past.

Energy Storage Systems (ESS) technology is actually mature to provide a significant contribution in supporting DC and AC grids; innovative power electronic converters, due to their fast dynamic performances and high level of controllability, can modulate power flows from and to ESS.

This work aims to introduce ESS in two of the most relevant power DC networks of today, to get evolved features and mitigate above mentioned issues:

- energy recovery and catenary voltage stabilization in DC-wayside distribution system of a 3 kV DC railway;

- synthetic inertia control in HVDC-VSC power stations.

Apart technological issues, railway field is traditionally quite conservative: insiders definitely prefer proved and reliable equipment, even if less advanced; aware of that, main focus of the project regards integration of new equipment with existing infrastructure; due to this, first part of the activity has been mostly organized as a feasibility study, in which some solutions (hardware and controls) have been implemented, sized and simulated in order to be included in actual or future installations; the main goal is a smooth transition to new and evolved features, giving tangible gains in terms of performance and/or functionalities.

Railway field id also extremely cost-effective: ESS prices are lowering but they are still relevant, especially for innovative (non-standard) equipment. A technical-economical evaluation is needed; because such analysis is extremely complex, target is not a precise business plan, rather an expenses check; when simplifications have been introduced, hypothesis were precautionary.

On the other way, HVDC field is presently changing a lot, new IGBT-based VSC converters can compete against small-medium LCC in terms of rated power, providing extra features; in this case, main project issues are implementing an effective control algorithm for a given mission (eg. synthetic inertia action) and finding how to access needed energy; due to this, second part of the work is not related to a specific case

study; several solutions have been implemented and compared each other on the same benchmark grid, highlighting positive and negative aspects. The learning process led to achieve good results in terms of final performances.

In detail, activity is structured as follows.

Chapter 1 analyzes a 3 kV DC local railway with high penetration of modern (power demanding) trains; main technological challenges are: save energy and boost catenary voltage without oversizing the existing traction substations. After a preliminary analysis about recoverable energy, the problem is tackled by introducing DC-wayside ESS to improve regenerative braking and catenary voltage stabilization; layouts and sizing results then are validated by simulations. Brief economical scenarios are presented, showing a reasonable technical-economical comparison of the solutions.

Chapter 2 studies a model of an IGBT-based HVDC grid, in order to stabilize AC frequency with synthetic inertia algorithms; main technological challenges are: implement an efficient inertial algorithm into the VSC converter control and avoid frequency fluctuations through different synchronous areas. After several studies and simulations, target is achieved by means of innovative synthetic inertia algorithms and with an oversizing of VSC converters DC filters.

In both chapters, approach is top-down, considering equipment as part of a plant, mainly focusing on functionalities; later on (also in appendixes), system structures are deepen considering in detail some aspects: design solutions are analyzed, control algorithms are explained and compared.

A brief historical background about DC development through years is in appendix.

Nomenclature is summarized at the end of document.

CHAPTER 1

3 kV DC RAILWAY

Despite high-speed rails have been developed in AC, most of conventional and local trains in Europe (Italy, Spain, Poland, Belgium, parts of Czech Republic, Slovakia, Slovenia, Ukraine and Russia, see Fig. 1.1) and worldwide (Canada, Brazil, South Africa, some parts of U.S.A.) still adopt 3 kV DC.

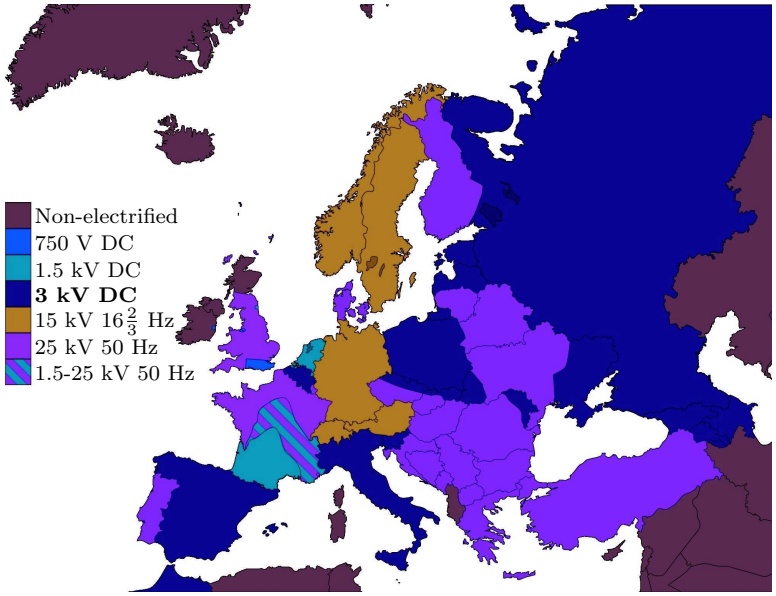

Figure 1.1: Map of rail electrification systems in Europe. (Source: Wikimedia Commons).

Those grids are most certainly the widest and powerful DC distribution networks in those areas, even if totally dedicated to traction purpose.

Continuing research is actually developed to increase performances at every level of the system: infrastructure, rolling stock, communication, safety etc.

Internationally, one of main targets is the integration of several countries railways in a common system to achieve higher level of interoperability; European Community is a clear example of such trend, as described in following section.

1.1 International scenario: European railway projects

As a member of European Community, Italy is involved in international projects whose target is the integration and harmonization of different countries systems.

Merlin project of the EU 7th Framework Programme has the main aim and purpose to *"investigate and demonstrate the viability of an integrated management system to achieve a more sustainable and optimised energy usage in European electric mainline railway systems."* [5]

The project produced a total of 33 deliverables in 36 months of activity, 13 of them are public; after a general description and characterization of a generic mainline railway system [6], several technical and economical challenges have been tackled by using real scenarios as case studies.

In particular, scenario 3 investigated about reduction of power peaks consumption and cost in a suburban 3 kV network in Malaga (Spain).

Project provided two different tools, SDMT (Strategic Decision Making Tool) and REM-S (Railway Energy Management System) [7]; a wide number of simulations have been performed, taking into account many constraints and variables, to define ESS best configuration (sizing, displacement, cost etc.) to minimize power and energy peaks along the line. After further optimization and CBA (Cost-Benefit Analysis), a pilot case was then implemented on site, validating theoretical results.

Merlin project also highlighted some issues related to practical implementation; the most relevant are:

- Energy meters calibration and interoperability among international railways is still an open point, due to many different situations in all Member States;

- Energy savings algorithms and strategies are strictly dependent on permanent communication links between trains, substations, railway operators etc.; the heaviest effort in term of expenses is therefore in communication technology.

Due to previous points, optimization tools and simulations must be compliance with the specific track under test; in case of limited amount of data and/or lack of communication, sophisticated analysis like SMDT/REM-S is not possible.

Another remarkable European railway project is the Horizon 2020 In2Rail, ended in 2018 after 36 months of activity; its mission is summarized below:

"European railways have to deliver increased productivity to fulfil the growth demand across all modes in freight and passenger services by 80% and 50% respectively by 2050. In2Rail will pave the way for the optimisation of the design of core infrastructure elements as well as improve the management of the railway system by adopting a holistic approach."

Those projects involved many main players in the international railway market, including universities, research centers, manufacturers, operators and authorities; main goal is making the future European railway network much more reliable, resilient, cost-efficient and powerful: as example, the latest Shift2Rail initiative, as an ideal prosecution of In2Rail [8], *"aims to double the capacity of the European rail system and increase its reliability and service quality by 50 %, all while halving life-cycle costs."*

A PhD thesis can approach only a little part of above mentioned project targets. As example, Merlin Project scenario 3 in Malaga is quite similar to the one studied in the followings: 3 kV DC supply, about 30 km of length, train average frequency about

20-25 minutes, some sections with single track; main issue: lack of catenary receptivity opposing wide train power peaks.

This work goes in the same direction, but analysis cannot be performed at the same level of accuracy and with the same optimization tools. In comparison, results could be intended as pilot (or exploratory) investigations prior to a punctual and detailed analysis like Malaga case study.

1.2 Local scenario: 3kV DC railway in Italy

Previous section presented an overview of actual an future European Projects related to railways development and optimization.

Italy has a strong historical background on 3kV DC traction, with a total electrification of about 12000 km all over the country (Fig. 1.2). Most of national gird is today owned by RFI (Rete Ferroviaria Italiana, Italian Railway Network), while some local and regional lines are owned by private or mixed societies (e.g., in Northern Italy, Ferrovienord).

Figure 1.2: Map of railway system in Italy in 2017. More than 70% is electrified at 3kV DC. (Source: rfi.it).

By the technical point of view, prior to international standards and norms, RFI

specifications (former Ferrovie dello Stato group) have been for decades the benchmark for infrastructure design and operation, including power supplies characteristics, converter topology, sizing and performances. Most detailed documentation is available in [1, 2, 9, 10, 11, 12], in Italian language only.

This work considers only a small part of such big scenario. It was decided to focus on DC-wayside infrastructure of Italian regional and local 3 kV railways, because they represent about 50% of the total railway traffic in Italy, with an average of almost 3 Million commuters per day (see Fig. 1.3).

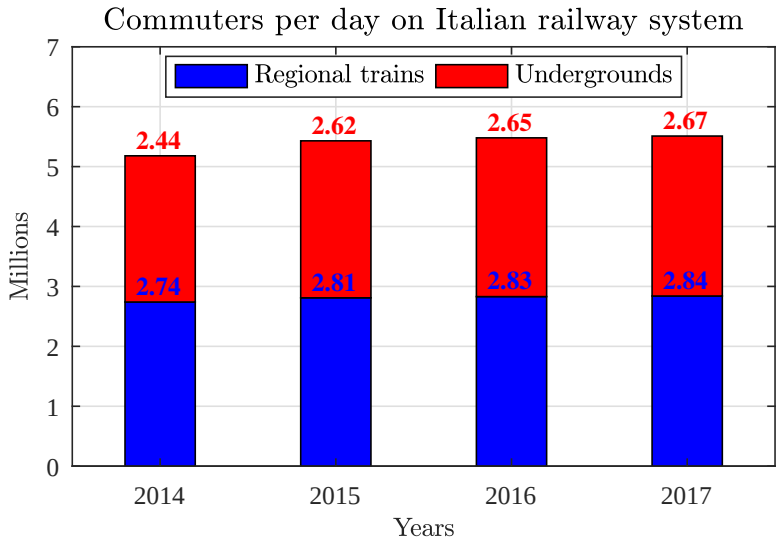

Figure 1.3: Train commuters (blue) and metro passengers (red) per day in Italy from 2014 to 2017. (Source: Pendolaria 2017, Legambiente).

In ten years, apart minor downturn, the number of regional train passengers (commuters, for the most part) has increased (see Fig. 1.4).

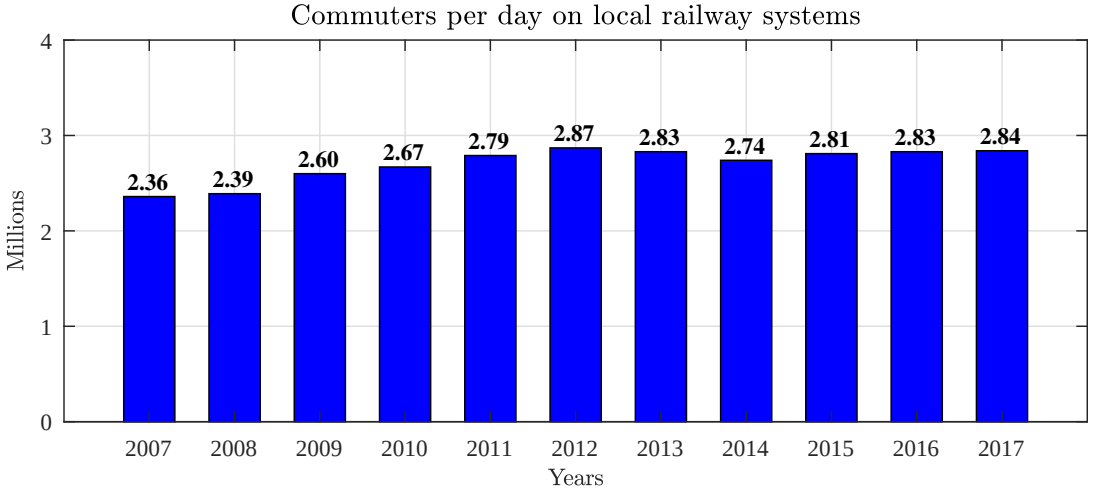

Figure 1.4: Commuters on regional and local trains per day in Italy from 2007 to 2017. (Source: Pendolaria 2017, Legambiente).

Situation is not uniform in all the country; in Lombardy for instance (Northern Italy), where railway system is well developed and electrification is capillary, increase has been about +31.5% since 2009 [13]. Data demonstrate that, when investment occurs and service is adequate, commuters choose railway respect to others way of private transportation, more expensive and polluting (see Fig. 1.5).

Figure 1.5: Production of CO_2 (grams per passenger-kilometer) of the most common transportation systems. (Source: EEA, European Environmental Agency, 2016).

More investments mean modern and comfortable trains but also improvements on infrastructure; at first, make existing lines able to handle growing traffic.

Next section will shortly present state of the art about electrification in the Italian 3 kV DC railway network.

The aim is to better understand actual technology issues, in order to define improvement solutions.

1.3 State of the art: DC railway layout in Italy

Fig. 1.6 shows the typical schematic diagram of actual 3 kV DC railway traction substation (TSS) according to above mentioned Italian specifications (RFI).

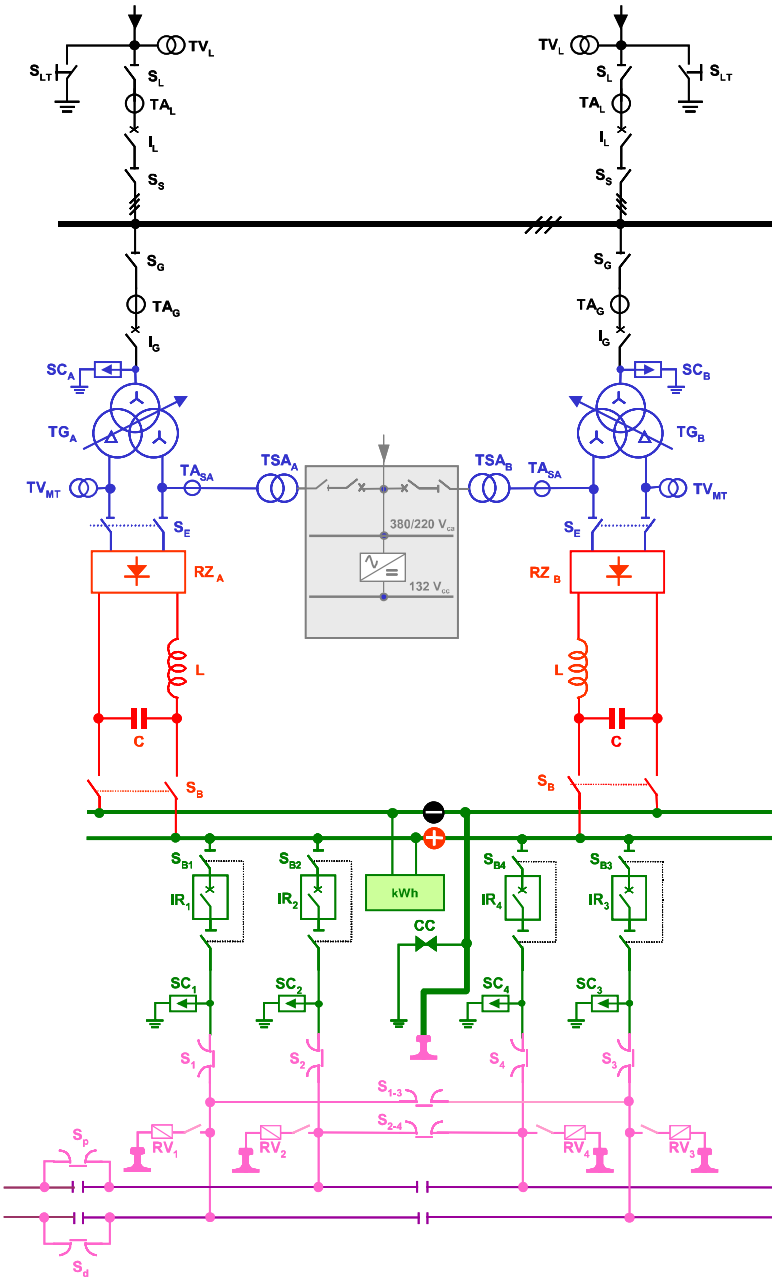

Figure 1.6: Schematic diagram of actual 3 kV DC railway traction substation (TSS) according to RFI standard. (Source: rfi.it).

In the most general layout, a TSS is equipped with two diode rectifiers and feeds a double railway line. More complex solutions (more rectifiers/tracks) are possible.

Fundamental components are drawn in different colors:

- black: AC feeder and main AC busbars;

- blue: HV/MV rectifier transformer (TG) and auxiliary power transformer (TSA);
- gray: AC and DC auxiliary power supply;
- red: diode rectification group (RZ), DC filter (L-C) and disconnectors (S);
- green: DC busbars, disconnectors and fast DC switches (IR);
- pink: DC feeders, disconnectors and rails;
- purple: DC catenary lines;

Each assembly contains other devices, like surge arresters (SC), earthing switches (CC), measurement voltage transformers (TV), measurement current transformers (TA) and power meter (kWh).

In general, each rectification group is designed to be fed independently through AC, and it can energize every portion of catenary (right or left side, even and odd rail) by means of proper disconnectors setup. All groups are put in parallel on DC busbars, DC feeders are protected against fault by fast DC switches.

Actually, most of substations are fed by HV primary lines, rated voltage 132-150 kV AC. Due to insulation and safety requirements, all AC equipment is installed outdoor and overhead, as shown in Fig. 1.7.

Figure 1.7: Outdoor AC side of modern 3 kV DC traction substation. (Source: Wikimedia Commons).

Needed space is relevant, and investment too (about 3 Million € for a "standard" double-group substation); this is a serious obstacle in realizing new substations, therefore sizing must be set carefully.

Next section shows substation power ratings and displacement along railways according to RFI standard [10].

1.3.1 Power ratings

As said, HV lines feed TSS power transformers. Each group is sized to fulfill power ratings according to line traffic.

Standard sizes are used by RFI [1, 2, 12], which essential data are listed in Tab. 1.1.

Table 1.1: TSS transformers data according to size.

Parameter	unit	Size 66	Size 132	Size 150
Rated primary voltage	(kV)	63 ± 5.6%	125 ± 8%	150 ± 8%
Type	-	Yyd11	Yyd11	Yyd11
Transformation ratios				
- Parallel rectifiers	-	63000/2710	125000/2710	150000/2710
- Series rectifiers	-	63000/1355	125000/1355	150000/1355
Rated power	(kVA)	3880	5750	5750
Rated active power	(kW)	3600	5400	5400
Total weight				
- Oil type	(kg)	18760	28000	28000
(Oil weight)	(kg)	5500	8550	8500
- Dry type	(kg)	17500	-	-
Short circuit voltage	(%)	<13.5	<13.5	<13.5

Low power groups (3.6 MW) were used in early installations, presently high power groups (5.4 MW) are preferred.

Besides rated power, overload prescriptions are demanding; RFI considers two cases:

a) +100% overload for 2 hours;

b) +133% overload for 5 minutes;

according to time diagram in Fig. 1.8.

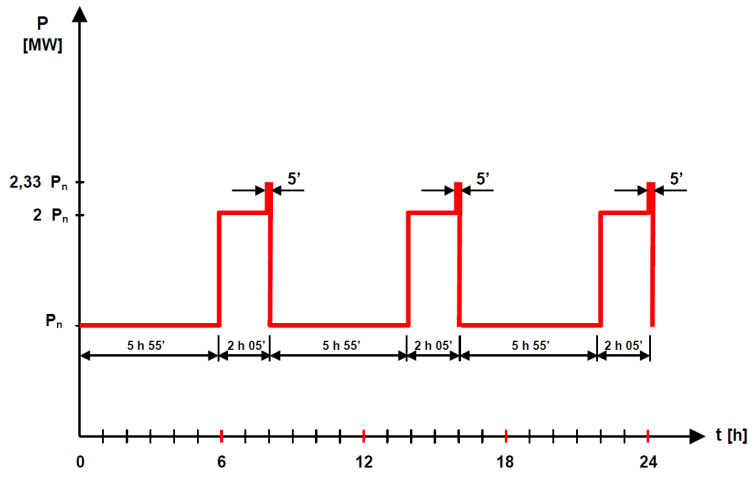

Figure 1.8: Overload time diagram for TSS power transformers. (Source: RFI [1, 2]).

Each rectification group is composed of two 6-pulse diode rectifiers, each one supplied by a secondary winding of power transformer. On DC side, rectifiers can be connected in series or parallel, to obtain a 12-pulse reaction (Fig. 1.9);

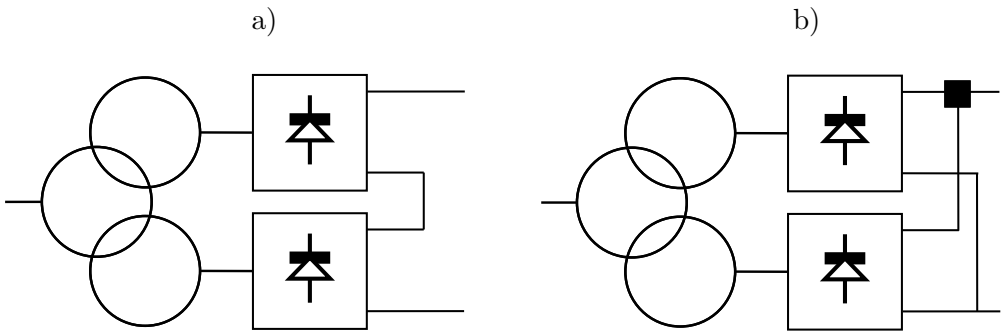

Figure 1.9: Rectification group topology. a) Series. b) Parallel.

For parallel connection, inter-phase DC-inductor (black square in Fig. 1.9b) is needed if leakage inductance between secondary windings is not enough to limit circulating currents due to instantaneous voltage gap between rectifiers (DC output is the same in mean value only).

About power electronics, considering limited overload margin of silicon devices respect to transformers (especially oil type, that have huge thermal capacitance), rectifier sizing is a little larger:

a) +100% overload for 2 hours;

b) +150% overload for 5 minutes;

with the same time digram of Fig. 1.8.

It means that each rectifier module must work at 200% of rated load for two hours, then at 250% of rated load for fifteen more minutes; because five minutes is enough for power electronics to reach steady state, in practice rectifiers are fully sized 2.5 times rated power.

RFI specifies rectifiers capability cases with rms current limits, as shown in Tab. 1.2.

Table 1.2: Standard rms currents for every single TSS rectifier in overload cases.

P_n (kW)	Rectifier group configuration	I_n (A)	case a) (A)	case b) (A)
3600	Series	750	1500	2100
3600	Parallel	375	750	1050
5400	Series	1500	3000	3500
5400	Parallel	750	1500	1750

Regarding DC voltage, prescriptions refer to "average available voltage" and "minimum absolute voltage", whose limits are listed in Tab. 1.3.

Abnormal conditions mean as example a line with a fail substation, or a line restart after a catenary fail with many trains in queue; normal conditions mean a line in the most crowded period of the day (rush hours).

Table 1.3: Standard pantograph voltage limits.

Conditions		normal	abnormal
Average available voltage	(V)	≥3000	≥2700
Minimum absolute voltage	(V)	2500	2300

Transformers are equipped with tap-changers on secondary side, in oder to boost DC voltage in case of rectifier heavy load.

1.3.2 Displacement and catenary

Before 1965, typical distance between 3 kV DC TSS was 40 km, with 4 MW of total power (two mercury-arc rectifiers of 2 MW each); after 1965, new and more powerful locomotives made necessary TSS empowering with silicon-based 3.6 MW groups, and also reduction of average substation displacement at 20 km. In 1970s, general layout of railway grid included 20 km displaced TSS, equipped with two silicon-based groups of 3.6 MW each.

Engineering of "Direttissima" Florence-Rome (very first project of high speed track in Europe) led to increase further TSS power, with a third group of 3.6 MW or by introducing new 5.4 MW rectification units. Up today, general RFI guidelines consider a TSS every 20 km for standard lines and every 15 km on high speed lines (3 kV DC).

"Standard" TSS is equipped with two 5.4 MW groups as described above; in some cases, a third back-up group is installed. Also catenary cross-section grew respect to early installations.

Up to 1960, standard catenary had been composed by a copper supporting rope of 120 mm^2 and two copper contact wires of 100 mm^2; total cross-section 320 mm^2. Due to traffic and speed growing (up to 150 km/h), section was increased to 440 mm^2 by installing an additional supporting rope of 120 mm^2. After 1976, speed on "Direttissima" Florence-Rome reached 250 km/h; to improve power collection from catenary, section was raised to 540 mm^2 (2x120 mm^2 supporting ropes plus 2x150 mm^2 contact wires). In particular cases (high slope of high traffic) cross-section can reach 610 mm^2 (2x155 mm^2 supporting ropes plus 2x150 mm^2 contact wires).

According to explained evolution, actual RFI standard is summarized in Tab. 1.4, where cross-section is function of line maximum speed and traffic.

Table 1.4: Standard catenary cross-sections for 3 kV DC lines.

Line type		Catenary	Supporting ropes		Contact wires	
Max. speed (km/h)	Traffic intensity	Section (mm^2)	Number	Section (mm^2)	Number	Section (mm^2)
200	Low	320	1	120	2	100
200	Medium	440	2	120	2	100
200	High	610	2	155	2	150
250	Medium	540	2	120	2	150
250	High	610	2	155	2	150

Actually, DC-wayside infrastructure is stressed by two main trends of railway market:

- growing power demanding of modern trains;

- line congestion due to increase of commuters traffic.

Such issues are much more relvant in local and regional lines, as described in detail in next section.

1.4 Local and regional 3 kV DC railways issues

Typically, about 60% of the total propulsion energy of a train goes into kinetic energy; for local and regional trains, due to continuous starts and stops, this leads strong power peaks along the catenary line. As result, growing traffic makes DC load really unstable, so big voltage drops occur during train accelerations.

Early solution to smooth such effect with conventional diode rectifiers was a generous equipment oversizing, both in terms of rated power and no-load voltage; since the beginning of DC traction, substation had been designed with wide overload margins (see Par. 1.3.1).

Due to traffic rising and trains empowering, rates of substation converters increased constantly in the past decades; displacement, on the other side, became closer. Anyway, in some lines, there are still issues: high voltage drops result in the need of much more current, especially in acceleration phase, when it is more necessary. Facing the increase of line power losses, this also led to upgrade catenary cross-sections. The result is a strong impact on the infrastructure.

Besides economical considerations, increasing diode rectifier no-load voltage to face short time power peaks has technical defects too: it reduces catenary receptivity.

Modern trains are regenerative, during braking phases energy can be re-injected into catenary, to be used by other ones; train converters are sized for a maximum rated voltage (typically 4 kV DC), the most catenary no-load voltage is high, the most train voltage is easily pushed above threshold during braking.

Local and regional trains are not so frequent (typically a train every 10'-25') to guarantee a significant self-redistribution of power; nevertheless, the amount of stops in regional and sub-urban railway lines, thus the theoretical available braking energy, is not negligible. Braking rheostats are then engaged more frequently and huge power peaks are wasted: loss of efficiency becomes relevant.

In synthesis, because regional traffic is generally growing (and it is going to increase further), and modern trains power is demanding, conventional strategies for DC grid empowering are not sufficient anymore.

Railway is characterized by impulsive power flows, very concentrated in time and space: it means that, for above reasons, a global network empowering is poorly effective, because it faces a periodic or impulsive problem using a constant solution.

Another way to match modern railway needs with efficient power consumption is wanted.

1.5 Why improving 3 kV DC railway: targets

Previous sections described state of the art in actual regional and local 3 kV DC railway system in Italy, highlighting issues related to lack of voltage controllability along the catenary, braking losses and in general a global increase of power peaks on the DC-wayside distribution system; as mentioned, such aspects are well known internationally, and several solutions have been proposed by European projects.

In a futuristic scenario, most of European railway distribution system could be converted into intelligent AC power supplies [14] or even in 9 kV DC [15]: anyway, such solution is not applicable in a short time, for evident economic and logistic reasons.

In the meantime, another approach for DC railway could be the replacement of actual diode rectifier substations with fully controlled AC/DC VSC converters, in order to control catenary voltage and recover braking energy through AC grid; a "smart substation" based on this concept is under development in Italy, near Forlí, as RFI pilot project with JRC (Joint Research Committee).

Anyway, boosting voltage on substations is only a little part of the solution (as shown in Par. 1.3.1, diode rectifiers have already tap-changers on power supply transformer), because most of local trains start and stop far away from substations; furthermore, re-injecting energy into the AC grid could be difficult or even impossible, both for technical and regulatory issues; as example, high power peaks can create harmonic distortion and recovered energy must be measured and economically compensated.

Another approach could be increasing the number of substations; this way, power supply would be much more "distributed", and hopefully closer to trains any time. In this last case, the main problem is economical and practical: actual railway substations are definitely expensive, they require erection permissions, accessibility, space and so on. Strong MV or HV AC supply is needed nearby too.

For all above reasons, railway grid empowering should be performed also by using Energy Storage Systems (ESS).

This chapter has the main purpose of evaluating benefits about integration of ESS into a 3 kV DC regional line, in order to reduce issues highlighted in previous section; activity has been developed independently by JRC works as a feasibility study about local DC railway improvements means of innovative equipment. Concept is the following: a better redistribution of the power flows along the catenary by small-medium bidirectional converter and ESS placed along the line (DC-wayside installation) in stand-alone configuration.

ESS energy and power results are still based on the specific line, so they are influenced by high level of customization in terms of converter/storage sizing and equipment siting along the catenary; especially for technical/economical scenarios, results are therefore not unique or self-conclusive; anyway, besides punctual results, some general conclusions have been achieved.

To reduce as much as possible costs and impact on existing infrastructure, such devices can be installed into a shelter or into stations spare-areas; actually, most of local stations have been automated, ticket offices have been closed and replaced by ticket-machines, those areas are free and segregated by passengers. This last solution is very interesting because stations imply necessarily train starts and stops (therefore local power flows). Those "stand-alone substations" will also support conventional rectifiers doing a series of evolved features, which are described in the followings.

Next section presents the project road map.

1.6 Railway research: road map and contributions

As mentioned, respect to other similar activities in literature, this study is not financed nor actively supported by any railway company or operator; available data have been collected from previous projects, GPS measurements, site surveys, papers, technical specifications and best practice.

Activity wants to figure out if stand-alone DC-wayside ESS implementation on a chosen railway is technically reasonable and economically sustainable; therefore, road map is structured essentially like a feasibility study: performing a sophisticated analysis is not a goal; assumptions and simplifications, when made, are pejorative; this way, results are precautionary by technical and economical point of view; as said, this can be considered the first step for a wider research study or a real engineering project in which many players are involved.

Methodology is step-by-step listed below:

- a rail track to be tested is chosen; after data collection, train recoverable energy is briefly estimated by means of simple case studies: despite many pejorative hypothesis, estimation is consistent, then further analysis are justified;
- using available data of infrastructure and trains, mathematical models are implemented and used in simulations to refine early estimations; simulations validate some data and reject other ones; analysis proceeds on validated data;
- ESS whose performances match simulations is sized and its contribution is investigated in performing braking energy recovery and then catenary voltage support;
- due to good technical response of ESS contribution, brief economical scenarios are implemented.

Apart data collection, most of efforts have been concentrated on system modeling and simulations, control implementation and fine tuning (see Appendix B); chosen algorithms (PID and droop) are well known, for some reasons:

- given performances are satisfactory, no further complexity is then required;
- a mature and proved technology is definitely preferred in case of critical controls, because behavior is much more predictable;
- the simpler controls are, the higher level of reliability is expected;
- results are easily intelligible.

In addition, railway world is historically quite conservative, insiders are much more worried about practical aspects like reliability, safety and maintenance prior to achieve advanced functionalities.

Catenary supply is the best example of such mentality: high power controlled inverters are available in the market since many years, but most of DC-wayside distribution is nowadays still done with the same, old, diode rectifiers; apart evident cost gap with a full converter, rectifiers are reliable, simple, easy to maintain and quite standard.

ESS and power converters can give more than rectifiers, but a full replacement of old equipment is actually premature (also economically). That is why this chapter tries to match in the smoothest way old and new technologies.

Technical analysis is shown in the followings.

1.7 Recovery

Due to high convoy frequencies and relevant numbers of start-stops, braking energy recovery has been extensively treated regarding urban light rail or subway applications [16, 17, 18, 19, 20]; in such cases, a statistical approach becomes essential in order to assess the effective amount of recovery, due to energy self-redistribution.

Regarding local or regional trains, approach is quite different: at first, it is important understand if significant energy savings can be achieved; lack of frequency (typically only a train every 15'-30') can be potentially balanced by other advantages:

a) specific energy and power are considerably higher than a light train;

b) grid receptivity is definitely lower.

In addition, the amount of stops in a regional and sub-urban railway line, thus the theoretical available energy, is not negligible.

As stated in Par. 1.3, diode rectifiers TSS are power unidirectional, so braking energy, kinetic or potential, must be drawn in another way. Before coming into deep about recovery technology, equipment displacement and so on, some basic calculations about the effective amount of such energy must be done: in the followings, two case studies will be described.

First one regards potential energy W_{t_p} given by a retain braking along a downhill.

Second one estimates the kinetic energy W_{t_k} given by a full-stop braking along a flat track.

Calculations are strongly dependent on train mass, whose final value is given by model and composition. In this work, TSR (Treno Servizio Regionale - Regional Service Train) are considered; they are the most part of Trenord (local railway operator in Lombardy) fleet on Milan-Como and Milan-Varese lines; they have high performances in terms of acceleration, and they all equipped with regenerative braking systems.

Main data for maximum and minimum compositions are listed in Tab. 1.5.

Table 1.5: TSR composition data.

Model	Data	Value
TSR	Maximum mass	550t (8 railcars)
TSR	Minimum mass	210t (3 railcars)

About rail track, Saronno-Como Lago line was chosen (Fig. 1.10). Saronno is the most important Ferrovienord hub and main crossroads for northern Lombardy lines (Varese, Como Lago). It is also a TSS; other smaller TSS are located in Portichetto-Luisago and Como Camerlata. Due to historical reasons, TSS group sizing is different from RFI standards (see Tab. 1.6).

Table 1.6: TSS location and data.

1) Saronno	P_{s_1}	6.99 MW	3 groups 2.33 MW each
2) Portichetto-Luisago	P_{s_2}	4.46 MW	2 groups 2.23 MW each
3) Como Camerlata	P_{s_3}	3.90 MW	1 group

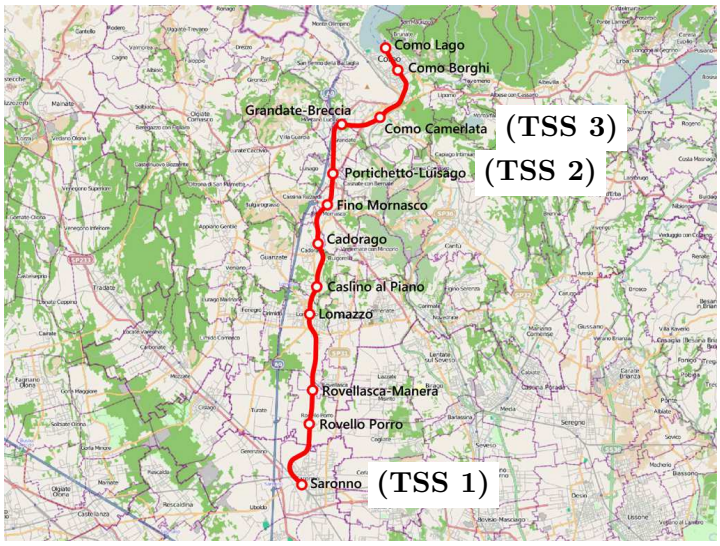

Figure 1.10: Saronno-Como Lago line map. (Source: Wikimedia commons).

Como Lago is close to Swiss border, final part of the line is single track with a steep descent between Como Camerlata and Como Borghi stations (52 m high drop).

For frequency times, official timetable for a standard (not express) ride has been used. Data are summarized in Tab. 1.7.

Table 1.7: Saronno-Como Lago track distances and official timetable.

Distance ⟶ (m)	Gap (m)	Time ⟶ (s)	Gap (s)	Altitude ⟶ (m)	Gap (m)	Station
0	0	0	0	212	0	Saronno
3581	3581	240	240	237	25	Rovello Porro
5182	1601	420	180	249	12	Rovellasca-Manera
8960	3778	660	240	296	46	Lomazzo
10390	1430	840	180	301	5	Caslino al Piano
12491	2101	960	120	296	-5	Cadorago
14726	2235	1200	240	315	19	Fino Mornasco
16168	1442	1380	180	303	-12	Portichetto-Luisago
18841	2673	1620	240	307	4	Grandate-Breccia
20807	1966	1860	240	272	-35	Como Camerlata
23778	2971	2160	300	220	-52	Como Borghi
24931	1153	2400	240	205	-15	Como Lago

Such cases are very ideal, real train cruise is a mix of both situations and splitting energy in two components is quite complex.

Regarding initial calculations, results provide ideal recoverable energies and they will be later used as benchmark for ESS sizing during numerical simulations.

An issue is how to split between recovered energy by electric braking and the wasted energy by mechanical brakes; such aspect is quite difficult to handle, because mechanical brakes are always available for safety reasons, and train driver can decide to use them

instead of electrical ones.

Anyway, braking procedure is quite automatic in most of modern rolling stock, to maximize the opportunity of regeneration: typically, electric brakes are engaged at high and medium speed, mechanical ones are used at low speed and in parking only.

In the followings, therefore, some assumptions about speed thresholds have been done, and also it was supposed the train driver is expert and well trained about electrical braking, avoiding unnecessary mechanical brakes usage.

1.7.1 Case study 1: potential energy recovery

A convoy that rides a descent at constant speed uses brakes to retain; apart equipment losses, total potential energy is wasted into braking energy.

A relevant amount of energy cannot be recovered because of mechanical friction, electrical conversion losses and (eventual) usage of mechanical brakes. Being as much as possible precautionary, a global system efficiency $\eta_t = 0.8$ is set, globally considering all above conditions; potential energy W_{t_p} is given by:

$$W_{t_p} = \eta_t m_t g(h_{t_1} - h_{t_2}) \tag{1.1}$$

being m_t as the total convoy mass, g the gravity acceleration and $(h_{t1} - h_{t2})$ the height drop.

Potential active power P_{t_p} results from travel time T_p:

$$P_{t_p} = \frac{W_{t_p}}{T_p} \tag{1.2}$$

As mentioned, chosen downhill is the 52 m drop between Como Nord Camerlata and Como Nord Borghi. Because stations are close to descent borders, Tab. 1.7 provides a travel time T_p of about 5' (300s) and a braking space $s_{t_p} = 2791$ m. About speed, it is supposed for simplicity constant and equal to:

$$V_{t_p} = \frac{s_{t_p}}{T_p} = \frac{2791}{300} = 9.3 \text{ m/s} \tag{1.3}$$

Such speed is definitely enough for electric braking usage, therefore the full amount of potential energy was assumed recoverable.

In Tab. 1.8 results of (1.1) and (1.2) are given, for maximum and minimum TSR compositions.

Table 1.8: Potential energy and power calculations.

Model	Composition	W_{t_p} (MJ)	P_{t_p} (MW)
TSR	8 railcars	224	0.75
TSR	3 railcars	86	0.29

A simplified representation of potential energy recovery is shown in Fig. 1.11.

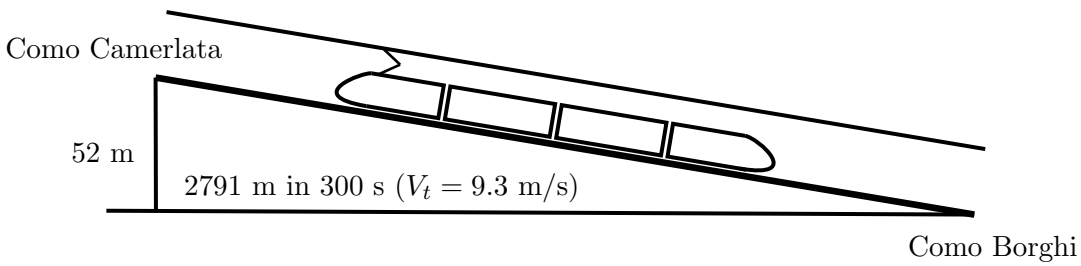

Figure 1.11: Potential energy case.

In a dual way, in next section a kinetic energy recovery case is investigated.

1.7.2 Case study 2: kinetic energy recovery

A convoy rides a flat track and brakes to decelerate from crusade speed to zero; apart equipment losses, total kinetic energy is wasted into braking energy.

Same considerations of Par. 1.7.1 about train global efficiency η_t are valid: same value is used, in order to better compare two cases each other; kinetic energy W_{t_k} is given by:

$$W_{t_k} = \frac{1}{2}\eta_t m_t (v_{t_1}^2 - v_{t_2}^2) \tag{1.4}$$

being $(v_{t_1} - v_{t_2})$ the speed drop.

As stated before, regenerative brake is not working at low speed, v_{t2} is the chosen threshold. Kinetic active power P_k results from braking time T_k:

$$P_{t_k} = \frac{W_{t_k}}{T_k} \tag{1.5}$$

About initial speed, taking into account track limits [21], $v_{t_1} = 25$ m/s.

According to TSR datasheet [22], $v_{t_2} = 1.5$ m/s; acceleration a_t is supposed constant and equal to -0.55 m/s^2; this is a simplification as considering retain speed V_t constant.

Due to previuos considerations, T_k is given:

$$T_k = \frac{v_{t_2} - v_{t_1}}{a_t} = \frac{1.5 - 25}{-0.55} = 43 \text{ s} \tag{1.6}$$

and also braking space s_{t_k}:

$$s_{t_k} = v_{t_1} T_k + \frac{1}{2} a_t {T_k}^2 = 25 \cdot 43 - \frac{1}{2} \cdot 0.55 \cdot 43^2 = 566 \text{ m} \tag{1.7}$$

In table 1.9 results of (1.4) and (1.5) are given, for maximum and minimum TSR compositions; in this case, basically all stops from Saronno to Grandate-Breccia and vice versa can be considered for calculations.

Table 1.9: Kinetic energy and power calculations.

Model	Composition	W_{t_k} (MJ)	P_{t_k} (MW)
TSR	8 railcars	137	3.21
TSR	3 railcars	52	1.22

A simplified representation of kinetic energy recovery is shown in Fig. 1.12.

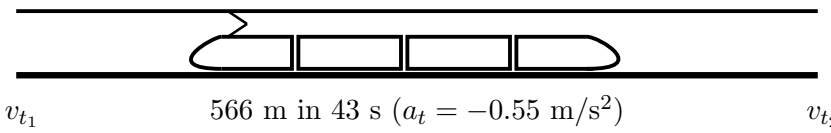

Figure 1.12: Kinetic energy case.

1.7.3 Case studies analysis

Previous analysis was based on simple calculations with high level of simplification:

- constant speed during retain (V_{t_p});
- constant acceleration during stop (a_t).

Obtained data are summarized in Fig. 1.13.

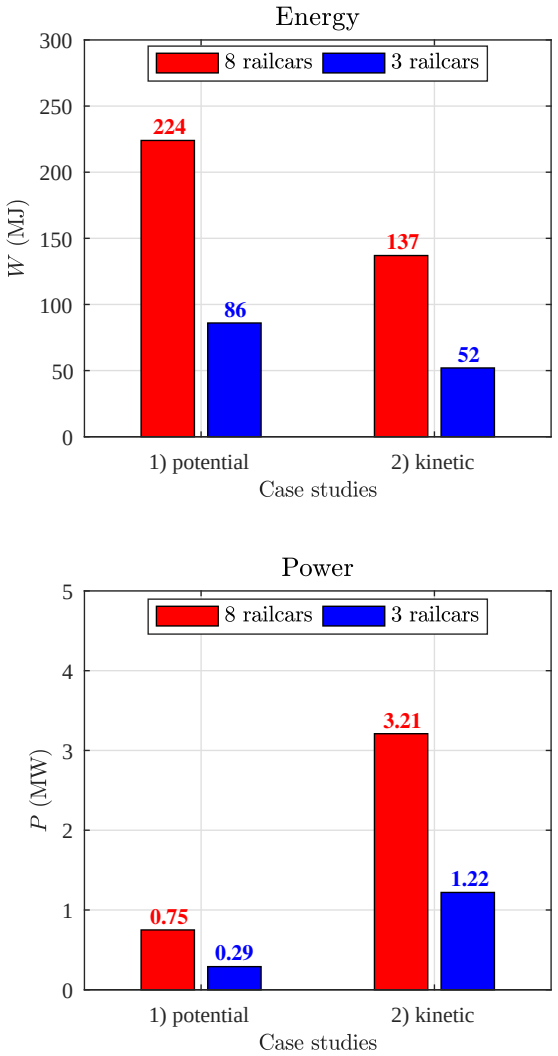

Figure 1.13: Case studies results: a) energy; b) power.

They are far to be accurate, but they led to a couple of significant results:

a) theoretical energy a local train can generate during braking is definitely relevant;

b) in two cases, energy and power could be quite different.

In particular, a) justifies the necessity to investigate much more deeper about the effective amount of energy can be withdrawn, while b) suggests different strategies to handle a possible wide capability span.

Comparing Tab. 1.8 with Tab. 1.9, it seems case 1 (potential energy recovery) is going to produce big amount of energy in a long time (300 s), with low power peaks (0.75 MW); on the other way, kinetic energy recovery (case 2) results in high power peaks (3.21 MW) in a shorter time (43 s) with less available energy (133 MJ, compared to 224 of case 1).

Trying to classify such aspects, it is said that case 1 is much more "energy oriented", while case 2 is definitely "power oriented"; such nomenclature is quite common in literature talking about automotive, networking and so on [23].

About electrical energy storage systems, previous classification is related to two main factors:

I) power electronic converters sizing;

II) storage specific technology.

Considerations about points I) and II) are presently premature, because a validation of preliminary calculations in needed.

Due to this, in next sections further simulations and modeling have been performed on the same track (Saronno-Como Lago), by implementing a more detailed rail grid model and by using real train speed profiles coming from GPS measurements.

Main target is obtaining a train current profile $I_t(t)$ and later on all power flows on the catenary line, including braking losses.

Simulations will consider 8 railcars TSR case, as the most significant and challenging in terms of recovery and equipment sizing (and also costs). This led to cover all train compositions and recover energy as much as possible any time.

At first, network model and simulation strategy are presented.

1.7.4 Railway DC network model

Consider a generic power DC network shown in Fig. 1.14; it's composed by:

- DC voltage generators, with their own series resistors;
- Active/passive loads on the nodes, modeled as ideal current generators;
- Resistors between each node, to model line losses and voltage drops;

Line parameters are represented as pure resistors, because inductive and capacitive components are supposed to be not relevant in a DC quasi-static power flow; at first, it's also assumed that parasitic elements have time constants much more faster than the power flow dynamics, so they are neglected.

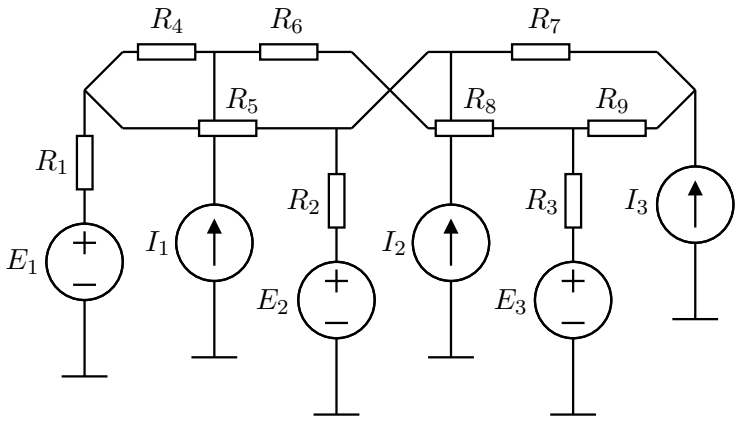

Figure 1.14: Structure of a power DC network portion.

This representation is a generalization of other typical structures; as example, in a ring network or in a cantilevered line, only one DC generator exists.

Nodes voltages are function of DC sources, line loads and loads displacement on the network; active loads can increase locally the nodal voltages. Nodal voltage method is the most appropriate way to define power flows; assuming that network is composed by:

- N nodes;
- real DC voltage generators;
- ideal DC current generators.

General matrix equation can be written:

$$\mathbf{G} \cdot V = I \tag{1.8}$$

with:

$$\mathbf{G}_{(N-1),(N-1)} = \begin{bmatrix} g_{1,1} & g_{1,2} & \cdots & g_{1,(N-1)} \\ g_{2,1} & g_{2,2} & \cdots & a_{2,(N-1)} \\ \vdots & \vdots & \ddots & \vdots \\ g_{(N-1),1} & g_{(N-1),2} & \cdots & g_{(N-1),(N-1)} \end{bmatrix} \tag{1.9}$$

$$V_{(N-1),1} = \begin{bmatrix} v_1 \\ v_2 \\ \vdots \\ v_{(N-1)} \end{bmatrix} \tag{1.10}$$

$$I_{(N-1),1} = \begin{bmatrix} i_1 \\ i_2 \\ \vdots \\ i_{(N-1)} \end{bmatrix} \tag{1.11}$$

and:

$$g_{n,n} = \sum g \text{ converging at node } n \text{ from other nodes } (n \in N) \tag{1.12}$$

$$g_{n,m}|_{n \neq m} = -\sum g \text{ between node } n \text{ and node } m \ (m, n \in N) \tag{1.13}$$

$$v_n = \text{nodal voltage between node } n \text{ and the reference node } (n \in N) \tag{1.14}$$

$$i_n = -\sum \text{currents converging at node } n \ (n \in N). \tag{1.15}$$

DC voltage generators are turned into DC current generators in Fig. 1.15.

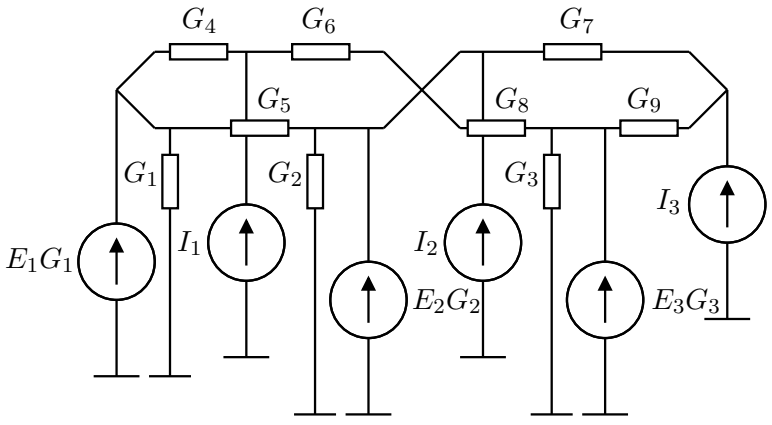

Figure 1.15: Current equivalent DC network portion.

Node voltages are given by:

$$V = \mathbf{G}^{-1} \cdot I \tag{1.16}$$

Such method can be applied also for traction network, with a series of constraints:

- TSS have diode rectifiers, so current flow can be unidirectional only;
- train is moving along the line, so **G** matrix elements (and also dimensions of the matrix itself) are time-variant;
- modeling train as a current generator, braking current injection needs parasitic elements (capacitors) to limit voltage rising at realistic levels;
- effects of braking rheostats and also ESS behavior have to be considered;

All equipment models are described in the followings.
TSS rectifier model is shown in Fig. 1.16.

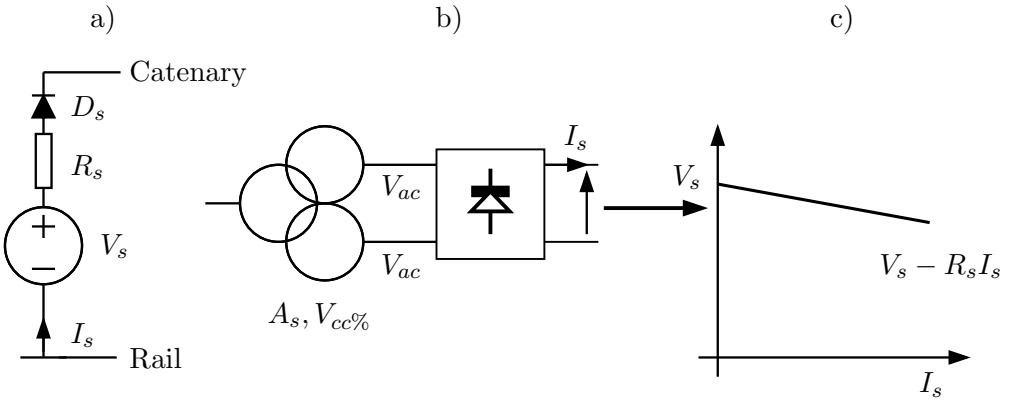

Figure 1.16: TSS rectifier model. a) circuit used in simulations; b) AC/DC converter main data; c) loading characteristics.

It is an ideal DC voltage generator, whose value (V_s) is the three-phase 12-pulses diode rectifier no-load voltage; converters are parallel type (Fig. 1.9 b), phase-to-phase AC input voltage is V_{ac}:

$$V_s = \frac{3\sqrt{2}}{\pi} V_{ac} \tag{1.17}$$

R_s is a series resistor that emulates rectifier voltage drop due transformer short circuit reactance $V_{cc\%}$ (in percentage); loading characteristic in Fig. 1.16 c) is given.

A_s is TSS transformer rated power, n is total number of groups in parallel in the same TSS, all supposed equal for simplicity:

$$R_s \equiv \frac{V_{cc\%}}{100} \frac{V_{ac}^2}{n \cdot A_s} \tag{1.18}$$

D_s is the series diode that avoids reverse current flow; according to measurement conventions, TSS current I_s can be positive only.

For this model, diode voltage drop is not considered.

As stated before, train is modeled by a controlled current generator (I_t), as shown in Fig. 1.17.

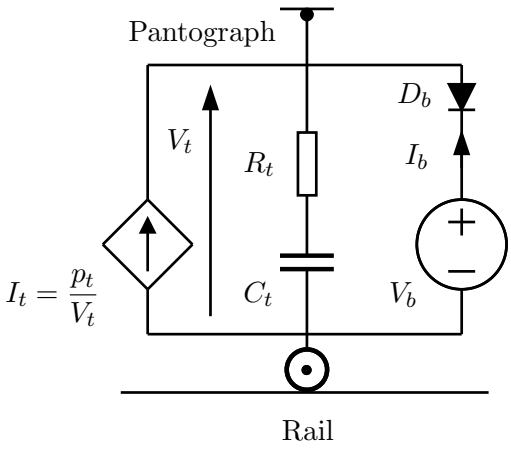

Figure 1.17: Functional train model, including equivalent circuit of braking rheostats and filter.

I_t setpoint time by time is given by instantaneous traction power (p_t) and voltage at pantograph (V_t); calculations are detailed in the followings. During traction phases, according to measurement conventions, I_t is negative.

Regenerative braking means injecting current into catenary, so I_t becomes positive; due to parasitic capacitance, voltage start rising with a certain slope; a R-C branch (R_t and C_t) models such effect, including also train converter filter, that is a relevant part of the total capacitance.

Train filter data are listed in Tab. 1.10:

Table 1.10: Train filter data.

$R_t = 0.1\ \Omega$	$C_t = 3.6$ mF

When V_t goes above a threshold (in Italy usually 4 kV), a control engages a DC/DC chopper and some rheostats (so-called braking rheostats) are connected between pantograph and rail; the chopper drives current (braking current) and rheostats waste energy, reducing the voltage; the control modulates the current to limit the voltage up the threshold.

In the model, this effect is obtained as follows: if train voltage V_t is above threshold V_b, braking diode D_b starts conducting and an ideal DC voltage generator V_b is connected in parallel to train; braking current I_b is thus the current of V_b. According to measurement conventions and diode polarity, I_b is negative only (braking rheostats cannot give energy to catenary).

All previous models are combined into DC railway in Fig. 1.18. All devices (TSS,

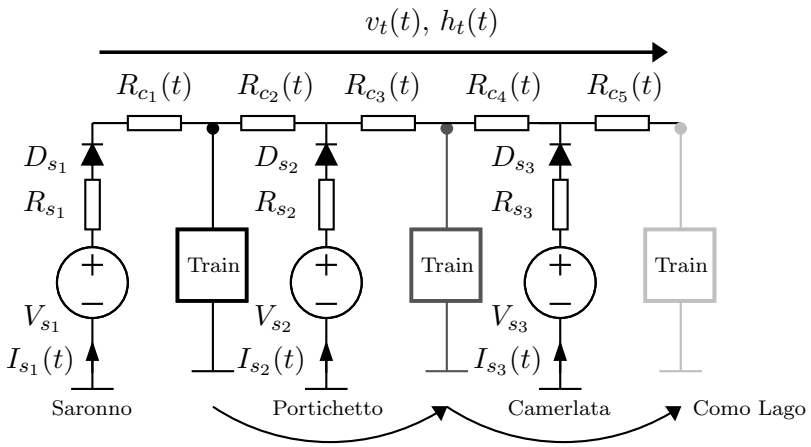

Figure 1.18: DC railway model used for first simulation. Train model is shown in Fig. 1.17.

train, ESS etc.) are connected to catenary grid through an electric port; every port is defined by proper voltage and current (Fig. 1.19).

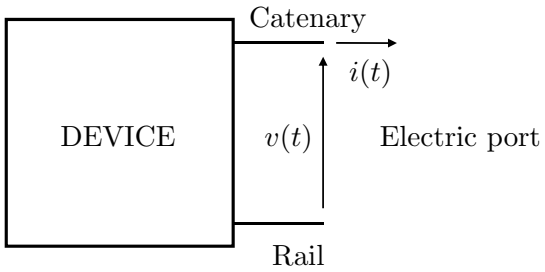

Figure 1.19: Electric port and measurement conventions.

According to measurement conventions, positive active power comes out from the device and feeds the catenary, while negative active power comes from catenary to the generic device; losses leave the catenary or anyway they don't reach the catenary, so they are measured to be always negative.

In such a way, it is quite simple to determine power and energy flows from and to catenary during the simulations by the sign of results; as example, TSS power is generated and then it is always positive, train power is negative when energy is consumed for traction and positive during regenerative braking; rheostatic breaking, on the other way, is always negative. Using the same approach, case studies data

(Tab. 1.8 and Tab. 1.9) are considered positive; data represent power and energy the train can theoretically provide the catenary in ideal conditions.

In the very first simulation, ESS is not included, for two reasons:

- available energy can be computed by train braking energy only;

- ESS displacement along the line must be defined.

Catenary is modeled as a series of time varying resistors $R_c(t)$, whose values change according to train position.

Train starts from Saronno station and arrives at Como Lago, passing trough Portichetto and Camerlata TSS; this causes heavy network reconfiguration, G matrix elements and even matrix dimensions change continuously as a function of time.

Due to this, mathematical approach in (1.8-1.16) is still valid, but anytime a change in G matrix occurs, the solution must be recalculated, taking into account system constraints.

GPS measurements let to calculate train current profile time by time, are shown in next section.

1.7.5 GPS data

Fig. 1.20 reports GPS train speed profile vs. time, with corresponding acceleration:

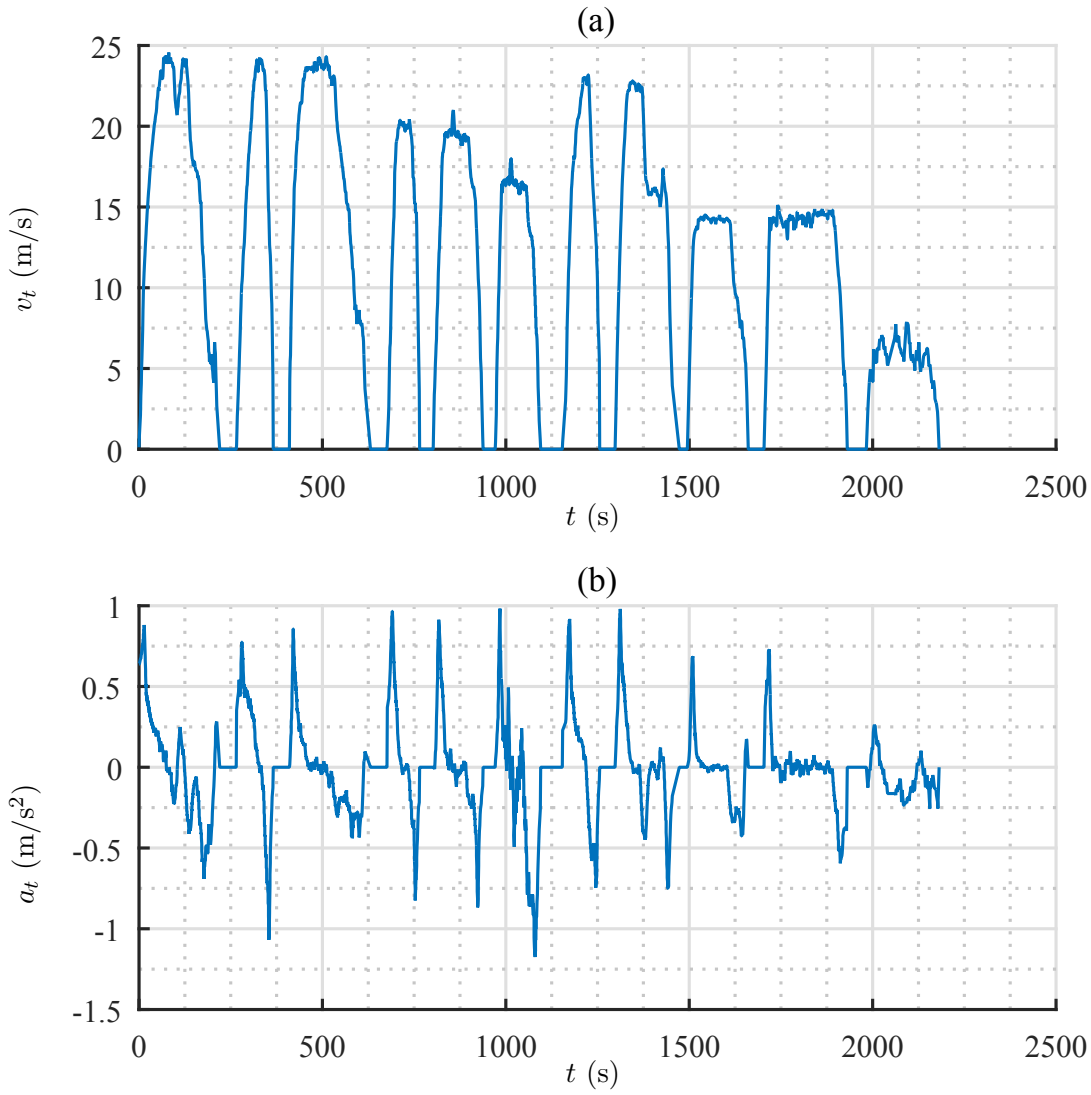

Figure 1.20: Rail track from Saronno to Como Lago. (a) GPS measured train speed v_t vs. time t. (b) Calculated train acceleration a_t vs. time t.

Data refer to a 8-railcars TRS traveling alone from Saronno to Como Lago (weekend timetable, one train per hour). Choosing appropriate train setup to record GPS data is an issue; during rush hours little shifts in the timetable can generate appreciable delays, slowdowns and so on. Also failure rates are higher. It is possible that energy profile is going to be changed by such conditions and maybe by drivers overcompensations (deeper braking and stronger accelerations).

On the other way, more trains could improve the available energy (by braking at the same time) or they could recover each other out (one train accelerates when another

one brakes). Such conditions are very random, so the decision was to consider one train only, to have a precise idea of the effective braking energy by every convoy. This also allows a more reasonable comparison with previous preliminary calculations.

It must be noted that, for this line, even during the week trains frequency is about 30 minutes on total travel time of 40 minutes: the mutual interaction between convoys is therefore hopefully quite little. The same approach was used in [24]. Acceleration peaks are very visible and they represent the kinetic energy recovery cases.

Fig. 1.21 shows, for the same train, GPS altitude profile vs. time, and the corresponding track percentage slope.

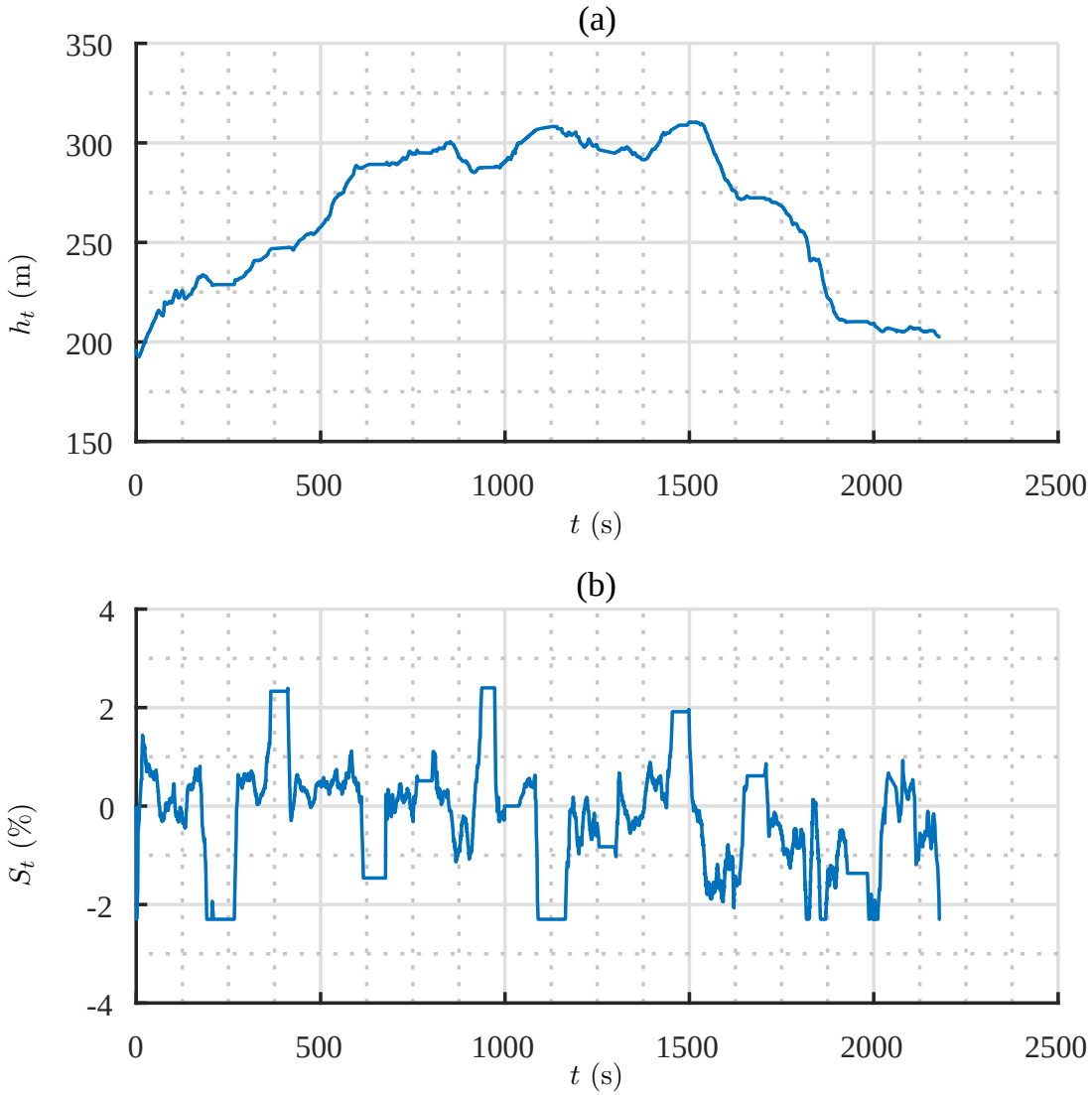

Figure 1.21: Rail track from Saronno to Como Lago. (a) GPS measured altitude h_t vs. time t. (b) Track percentage slope S_t vs. time t.

It is quite visible the descent from Como Camerlata to Como Borghi, in which speed in Fig. 1.20 a) is almost constant (1750 s $< t <$ 2000 s).

Speed, acceleration and slope are input data for calculations in the followings.

1.7.6 Train current profile

Model in Fig. 1.17 uses train instantaneous traction power p_t to obtain train current profile I_t: p_t is given by formulas shown in [25, 26], and here below summarized.

Train traction force F_t is defined:

$$F_t(t) = (1 + k_m)m_t\Big\{a_t(t) + g\Big[A + Bv_t(t)^2 + \frac{S_t(t)}{100}\Big]\Big\} \tag{1.19}$$

Train traction power p_t is depending on many quantities that can be either positive, negative or zero; according to F_t sign, p_t becomes:

$$\begin{cases} p_t(t) = -\dfrac{1}{\eta_t}F_t(t)v_t(t) - p_{aux} \\ F_t(t) \geq 0 \end{cases} \tag{1.20}$$

$$\begin{cases} p_t(t) = -\eta_t F_t(t)v_t(t) - p_{aux} \\ F_t(t) < 0 \end{cases} \tag{1.21}$$

Input is detailed as follows:

- v_t and a_t are train GPS speed and acceleration profiles;
- η_t is the train global electrical and mechanical efficiency (0.8);
- m_t is the train mass ($550 \cdot 10^3$ kg);
- k_m is the equivalent train rotating mass coefficient (0.1);
- g is the gravity acceleration (9.81 m/s^2);
- $A+Bv_t(t)^2$ is a binomial practical formula to globally evaluate specific friction and aerodynamic losses for a passengers rail convoy ($A = 2.5 \cdot 10^{-3}$, $B = 3.24 \cdot 10^{-6}$);
- S_t is the track percentage slope;
- p_{aux} is a base load due to train auxiliary systems (about 40 kW per railcar, according to TSR datasheet).

Data have been found using experimental GPS profiles of Par. 1.7.5 and typical values cited in bibliography for TSR train.

Train current profile is given by:

$$I_t(t) = \frac{p_t(t)}{V_t(t)} \tag{1.22}$$

V_t will be dynamically calculated time by time at every simulation step, so resulting current will be updated continuously.

As expected, if current is positive, according to conventions in Fig. 1.17, energy is provided from train to catenary, while negative current means energy absorbed by train from catenary.

Calculated train current profile vs. time is shown in Fig. 1.22.

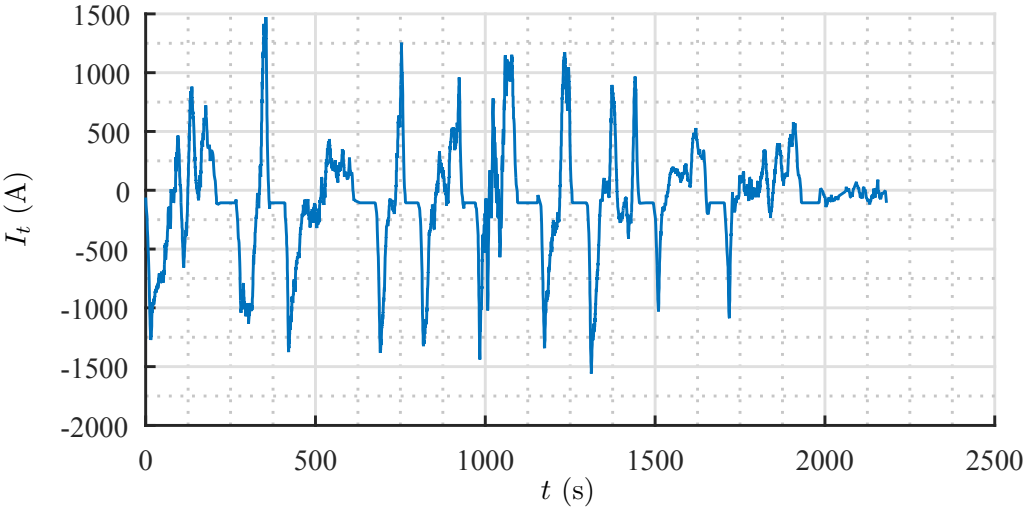

Figure 1.22: Calculated train current profile I_t vs. time t.

Once I_t profile is given, model is fully tuned using data shown below.
TSS parameters in Tab. 1.11 are computed according to (1.17) and (1.18).

Table 1.11: TSS model parameters.

TSS	V_{ac} (V)	A_s (MVA)	n	$V_{cc\%}$ %	R_s (Ω)	V_s (V)
1) Saronno	2750	2.33	3	7	0.0724	3713
2) Portichetto-Luisago	2750	2.23	2	10	0.1620	3713
3) Como Camerlata	2750	3.9	1	8	0.1482	3713

About catenary, section of cords along the line is not fully constant, and also TSS disconnectors setup (as shown in Fig. 1.6) can create several points in which conductors are put in parallel, depending on necessity.

For simplicity, according to all cords available data, average per-length resistance r_c of 0.04 Ω/km is considered; probably, resulting catenary voltage in acceleration could be a little bit overestimated, but this let to compute a simpler grid matrix and reducing simulations time.

Finally, simulation is run in order to find a more precise value of braking energy.

1.7.7 Simulation 1: braking energy

Using data by Par. 1.7.5 and 1.7.6 in model of Fig. 1.17, simulation of 8-railcars TSR travel from Saronno to Como Lago is performed.

Pantograph voltage profile in shown in Fig. 1.23(a). Corresponding braking current profile is in Fig. 1.23(b).

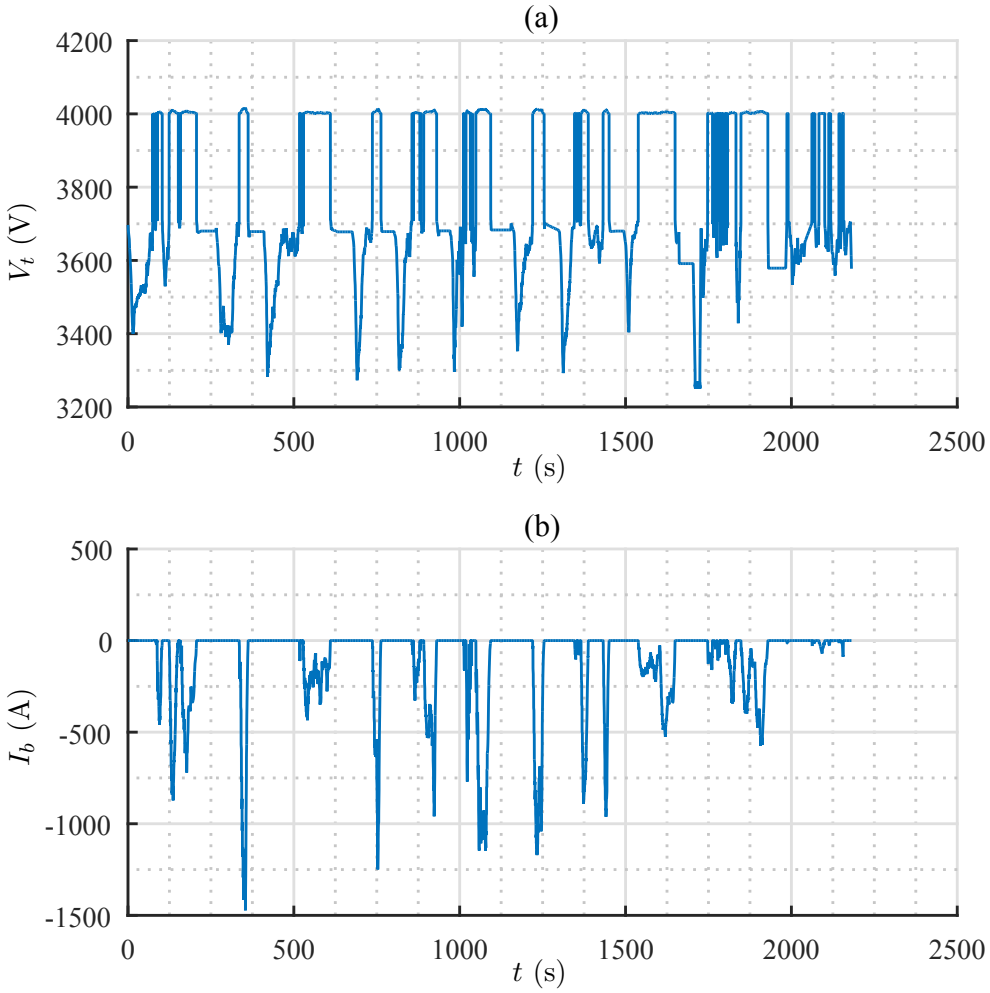

Figure 1.23: Simulation 1 results. (a) Pantograph voltage profile V_t vs. time t. (b) Braking current profile I_b vs. time t.

Being DC network not receptive, during braking phases the pantograph voltage goes immediately above the substation voltage V_s, to be controlled at V_b by the braking rheostats.

Rheostatic braking power p_b along the line is shown in Fig. 1.24.

As mentioned, two distinct cases have to be found and compared with initial calculations.

Crossing altitude and accelerations profiles in Fig. 1.21 with power in Fig. 1.24, the energy intensive case (1) is the above mentioned descent from Como Camerlata to

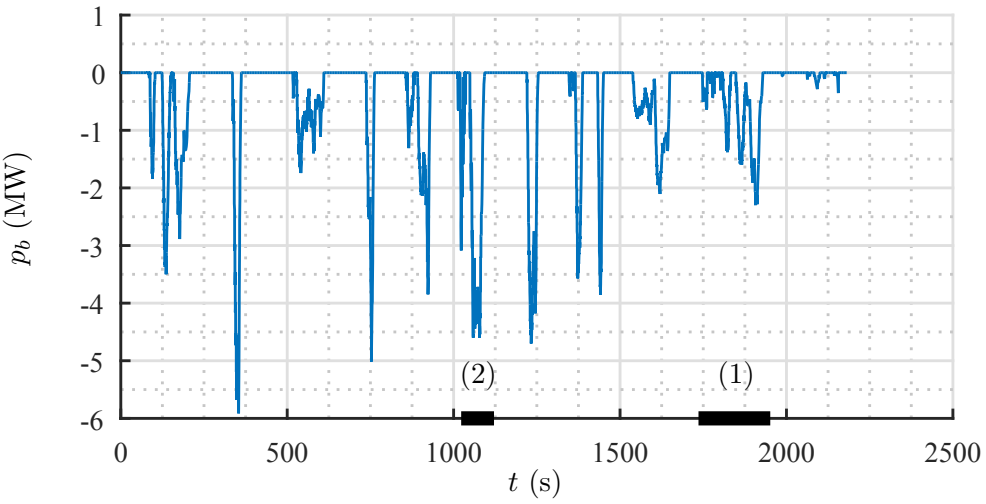

Figure 1.24: Simulation 1 results. Rheostatic braking power profile p_b vs. time t. (1) refers to energy intensive case, train rides a downhill braking; (2) refers to power intensive case, train brakes on the flat till stop. Data are used in (1.23) and (1.24) to fill Tab. 1.12.

Como Borghi.

The power intensive case (2) is a full stop braking to arrive in Fino Mornasco from Cadorago.

Being T_b the braking time, rheostatic power P_b and energy W_b result:

$$P_b = \frac{1}{T_b}\int_0^{T_b} p_b(t)dt = \frac{1}{T_b}\int_0^{T_b} V_b I_b(t)dt \tag{1.23}$$

$$W_b = \int_0^{T_b} V_t(t) I_b(t)dt = \int_0^{T_b} V_b I_b(t)dt \tag{1.24}$$

Results are provided in Tab. 1.12; they are compared with 8 railcars cases of Tab. 1.11 and 1.12:

Table 1.12: Simulation 1 results and comparison with initial calculations (W_t and P_t). Case numbers refer to Fig. 1.24. 8-railcars TSR. $\eta_t = 0.8$.

Case	W_b (MJ)	P_b (MW)	T_b (s)	$\hat{p_b}$ (MW)	W_t (MJ)	P_t (MW)	T_p (s)	T_k (s)
(1) Energy intensive	-110	-0.65	173	-2.41	224	0.75	300	-
(2) Power intensive	-135	-2.34	56	-4.55	137	3.21	-	43

Matching preliminary calculations with simulations, power intensive data are quite aligned; regarding energy intensive, initial calculations were highly overestimated.

A one-by-one comparison is almost impossible, but some considerations to explain such differences arise.

About power intensive:

- acceleration during braking is not so as constant as expected; anyway, theoretic data set well fits real GSP data by the energy point of view, being W_b and W_{t_k} well aligned;

- nevertheless energies are almost equal, simulation braking time (56 s) is a little bit longer than supposed T_k (43 s); that depends on many uncontrollable factors (like the driver guide style), so real power peak is lower than theoretic one.
  According to (1.5), by a linear proportion it can be verified that:

$$\frac{|P_b|}{T_b} = \frac{2.34}{56} = 0.042 \simeq \frac{|P_{t_k}|}{T_k} = \frac{2.21}{43} = 0.051 \tag{1.25}$$

  so power data differential between calculations and simulation is reasonable.

About energy intensive:

- despite the train travels at almost constant speed, slope changes continuously; anyway, theoretic data set well fits real GSP data by the power point of view, being P_b and P_{t_c} well aligned;

- nevertheless powers are almost equal, simulation braking time (173 s) is slightly different from assumed T_p (300 s), because preliminary calculations could not take into account train start from zero to crusade speed, in which all potential energy is used to accelerate the convoy.
  According to (1.2), by a linear proportion it can be verified that:

$$\frac{|W_b|}{T_b} = \frac{110}{173} = 0.64 \simeq \frac{|W_{t_p}|}{T_p} = \frac{224}{300} = 0.74 \tag{1.26}$$

  so energy data differential between calculations and simulation is reasonable.

Nevertheless, available braking energy, so theoretical recoverable energy, is still relevant; ESS will be then implemented and tested in another simulation.

1.7.8 ESS model

Before implementing ESS model and control, some considerations about equipment displacement are necessary; according to previous results, energy and power are quite high, so finding an appropriate installation site is not banal.

Displace ESS along railway track (DC-wayside ESS) or on-board is presently matter of discussion [27]; studies show that on-board solutions maximizes the local energy recovery, but at the end they are not convenient by the mechanic and economic point of view:

- ESS extra weight reduces significantly global train efficiency;

- ESS size takes out precious space for paying passengers.

In this work, DC-wayside solution is preferred and analyzed; ESS is sometimes far from the train braking point, so the recovery is not maximized.

A smart displacement along the line could compensate such effect; many studies have been done to implement algorithms or strategies to optimize such aspect, also known as ESS siting [28, 29, 30, 31].

Apart energy optimization, one of main targets in railway management is reducing as much as possible infrastructure costs, especially in existing lines, where lack of space along the track and urbanistic constraints are usually an issue.

Due to this, to handle high power peaks in a safe and efficient way, existing TSS seem to be the most appropriate place to install extra equipment: ESS siting is far to be optimal, but impact on existing infrastructure is minimum; it is the very first attempt to introduce such technology into regional and local railway system, so a compromise is needed.

About ESS functioning, it must drain current from catenary when needed, so an appropriate model is a controlled current generator.

All above considerations lead to model shown in Fig. 1.25.

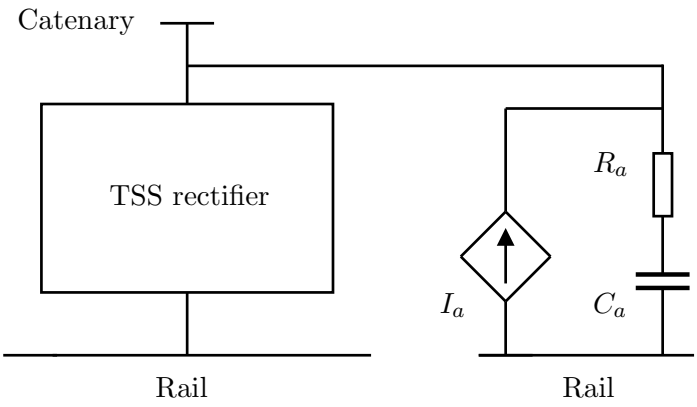

Figure 1.25: Functional model of ESS with TSS rectifier.

Current generator control is described in the followings, ESS is placed in parallel to TSS rectifier, a storage failure does not affect train operation, being TSS rectifier still operational.

According to measurement conventions, I_a is negative when the storage is in charge.

A R-C branch models a high pass filter for catenary voltage smoothing, in the same way as the train filter.

ESS filter data are listed in Tab. 1.13.

Table 1.13: ESS filter data.

$R_a = 0.1\ \Omega$	$C_a = 0.03$ mF

If catenary voltage goes above charge threshold V_{a_c}, ESS must start charging in order to recover train energy and avoid as much as possible braking rheostats utilization. Looking for an appropriate control technique, PID solution is chosen.

PID control is the state of the art in many kind of automatic machinery and controllorers [32, 33, 34], so system response can be shaped by "classical" techniques.

Respect to other simpler controls (eg. a basic droop action), small steady state errors and good dynamic response are expected, even if tuning is a little more complex.

Fig. 1.26 shows ESS PID-based control diagram; because grid is mostly resistive, no derivative action is needed, so it is modeled as PI only:

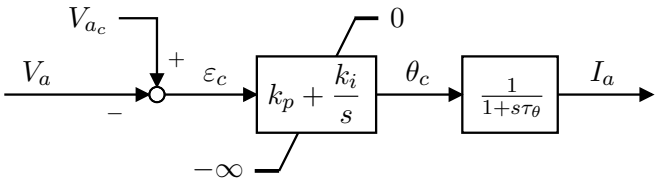

Figure 1.26: Block diagram of ESS PI control.

This model controls current generator I_a of Fig. 1.25; error signal ε_c is given by:

$$\varepsilon_c = V_{a_c} - V_a \tag{1.27}$$

The signal is conditioned by a PI controller with anti-windup configuration; the upper response is saturated at zero, while there is no limit for the charge current.

Discharge control is not included because it is supposed that the total energy stored during charge is completely re-injected into catenary line in the following loading phase; with only one train on the line, this is reasonable.

Output is filtered by a first time constant τ_θ (2 ms), to smooth oscillations in the control variable and simulate the ESS converter delay of response.

When V_a is above V_{a_c}, negative I_a is drained by the catenary. As soon as V_a moves below V_{a_c}, ε_c changes sign but control action θ_c is saturated at zero; ESS control is stopped and no more power is absorbed.

Tuning parameters are listed in Tab. 1.14, controller synthesis is described in detail in Appendix A.

Table 1.14: ESS tuning parameters.

V_{a_c} (V)	k_p (-)	k_i (-)	τ_θ (s)
3880	1	10	0.002

Such model will be used in next simulation; despite its relative simplicity, it well represents ESS behavior; same solution has been already successfully used in other works [35, 36].

1.7.9 Simulation 2: ESS recovery

Second simulation considers energy savings by DC-wayside ESS placed inside existing TSS.

Main goal is comparing braking energy respect to simulation 1 and then computing saved energy, taking into account ESS efficiency. Calculations will be performed using the same two cases as previously, energy intensive (1) and power intensive (2).

Fig. 1.27(a) shows catenary voltage profile with ESS action; corresponding braking current profile is reported in Fig. 1.27(b).

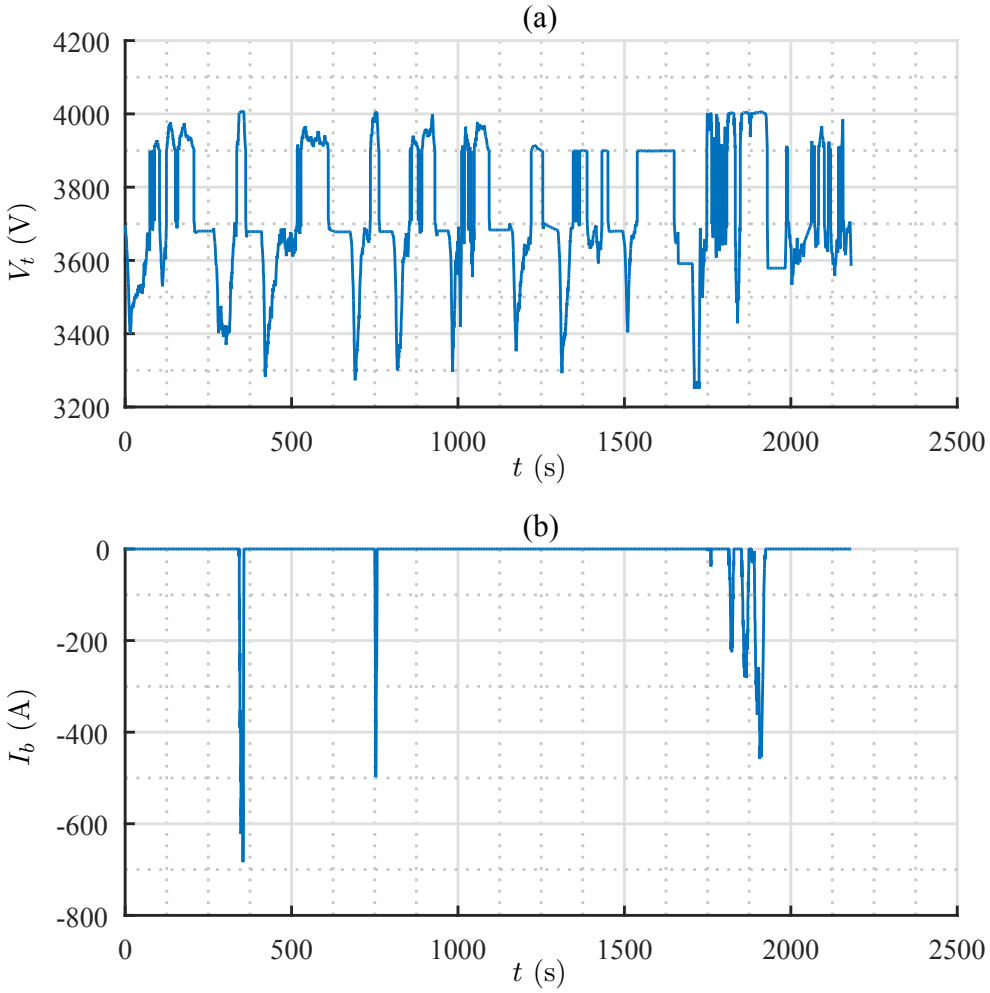

Figure 1.27: Simulation 2 results. ESS inside TSS. (a) Pantograph voltage profile V_t vs. time t. (b) Braking current profile I_b vs. time t.

With this second setup, pantograph voltage reaches the braking threshold few times only; braking current is greatly reduced and the most of current is captured by ESS (I_a); instantaneous power profiles in ESS substations $p_a(t)$ are shown in Fig. 1.28.

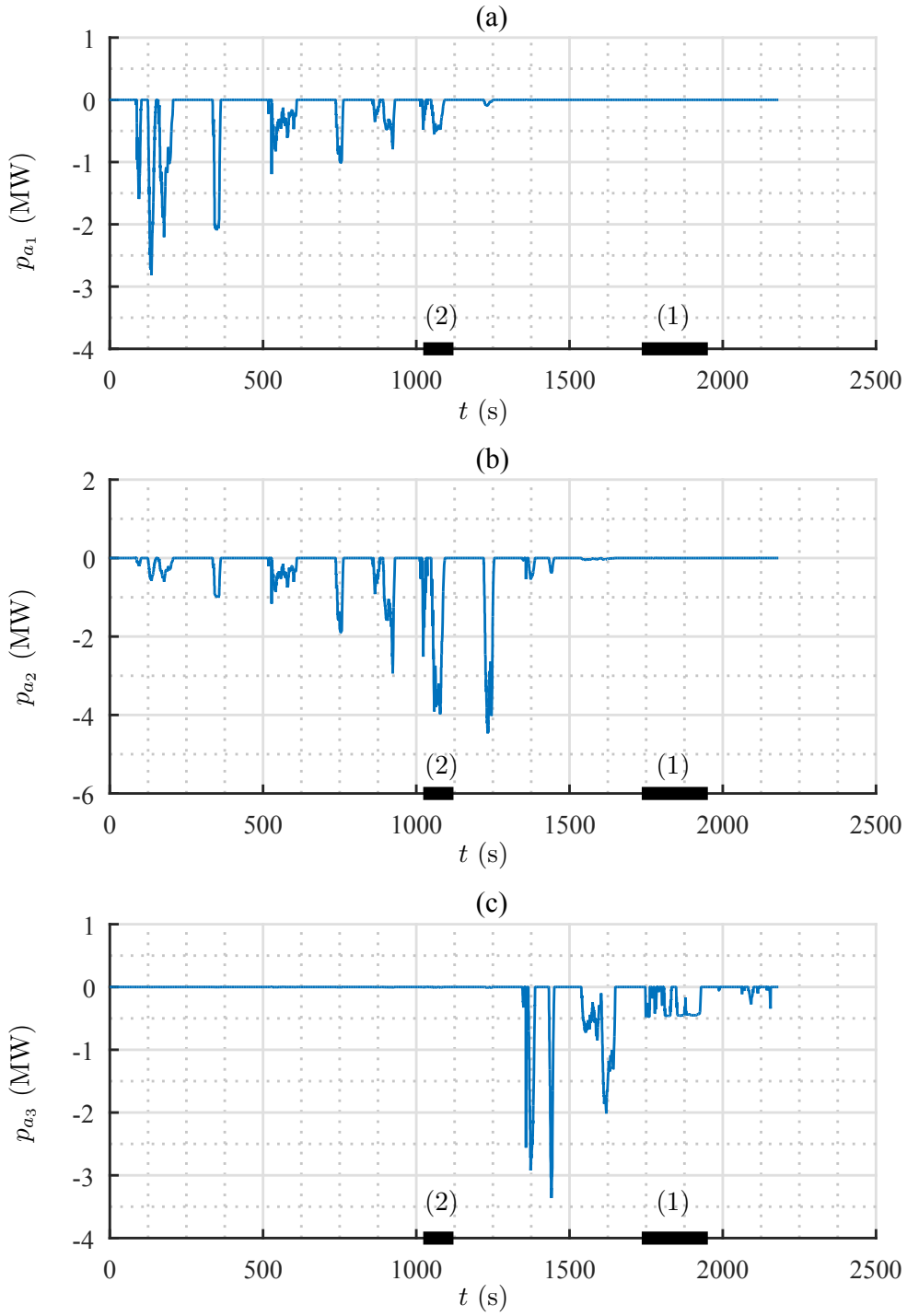

Figure 1.28: Simulation 2 results. ESS inside TSS. (a) ESS power profile in Saronno p_{a_1} vs. time t; (b) ESS power profile in Portichetto p_{a_2} vs. time t. (c) ESS power profile in Como Camerlata p_{a_3} vs. time t; cases (1) and (2) are the same as Fig. 1.24; data used in (1.28) and (1.29) to fill Tab. 1.15.

Considering global ESS efficiency in charge η_{a_c} of 0.8, results of energy savings are

provided in Tab. 1.15; data are split by TSS and, as said, they are the same as Tab. 1.12, for direct comparison between braking and storage energy.

Table 1.15: Simulation 2 results. Energy and power of ESS. Data split by substation and total. Cases refer to Fig. 1.28 and have to be compared to Fig. 1.24 and Tab. 1.12. 8-railcars TSR. $\eta_{a_c} = 0.8$.

Case	TSS	W_{a_c} (MJ)	P_a (MW)	T_a (s)	$\hat{p_a}$ (MW)
(1)	Saronno	0	0	173	0
(1)	Portichetto	0	0	173	0
(1)	Como Camerlata	-38	-0.27	173	-0.46
(1)	Total energy intensive	-38	-	-	-0.46
(2)	Saronno	-12	-0.27	56	-0.57
(2)	Portichetto	-89	-2.01	56	-3.96
(2)	Como Camerlata	0	0	56	0
(2)	Total power intensive	-101	-	-	-3.96

Being T_a the ESS working time, ESS power P_a and charged energy W_{a_c} result:

$$P_a = \frac{1}{T_a}\int_0^{T_a} p_a(t)dt = \frac{1}{T_a}\int_0^{T_a} V_{a_c} I_a(t)dt \tag{1.28}$$

$$W_{a_c} = \eta_{a_c}\int_0^{T_a} V_{a_c} I_a(t)dt \tag{1.29}$$

In next section, all data and simulations results will be critically compared and analyzed.

1.7.10 Data analysis

Initial calculations in Tab. 1.8 and 1.9, also shown in Fig. 1.13 have been already compared with simulation results of Tab. 1.12 in Par. 1.7.7; as said, simulations and analysis consider only 8-railcars TSR, as the most relevant case for energy recovery.

Following comments arise:

- energy intensive (potential) results were highly overestimated.
- power intensive (kinetic) data were quite aligned;

About energy intensive (case 1), unfortunately ESS displacement is not optimal to perform a satisfactory recovery: TSS is placed at the end of the downhill, so recovery is not an issue.

Comparing Tab. 1.12 with Tab. 1.15, it is evident how, apart ESS converter efficiency, the whole kinetic energy (power intensive, case 2) is properly captured.

In detail:

- Portichetto ESS only captures the most of kinetic energy (89 MJ), with an active power of about 2 MW; Saronno and Como Camerlata contribution is basically inconsistent (12 and 0 MJ, respectively);
- Como Camerlata effect in potential recovery is probably not sufficient (38 MJ) to justify equipment installation.

In addition, track from Grandate-Breccia to Como Lago is single, while from Saronno to Grandate-Breccia is dual: consequently, only one train at a time will ever run Como Camerlata downhill.

Due to above considerations, and according to simulation and calculation results, energy intensive case will no longer considered in this work.
It seems therefore the most promising technique for energy recovery is based on kinetic energy (power intensive).

The total amount of TSS energy during the whole simulation time T_s (2220 s) is given by:

$$\begin{aligned} W_s = \int_0^{T_s} \Big\{ & [V_{s_1} - R_{s_1} I_{s_1}(t)] I_{s_1}(t) + \\ & + [V_{s_2} - R_{s_2} I_{s_2}(t)] I_{s_2}(t) + \\ & + [V_{s_3} - R_{s_3} I_{s_3}(t)] I_{s_3}(t) \Big\} dt = \\ & = 1450 \text{ MJ} \end{aligned} \tag{1.30}$$

According to Tab. 1.15, the most of braking energy is available nearby Portichetto: every single train gives about 89 MJ. ESS placed in Portichetto is therefore definitely effective.

Supposing a further ESS storage device efficiency in discharge η_{a_d} of 0.85, the total stored energy the equipment can re-inject into the catenary at every train passage is:

$$W_{a_c} \eta_{a_d} \tag{1.31}$$

Net energy is therefore 85 % of 89 MJ, so 76 MJ: about 5 % of total. Anyway, minimum storage sizing has to consider the charge efficiency only, so 89 MJ.

This case shows that the amount of kinetic savable energy is a relevant percentage of the total. Unfortunately, captured energy cannot be used to stabilize catenary during train accelerations, being ESS placed inside the TSS, where voltage is kept very high by diode rectifiers.

Observing V_t profile in Fig. 1.27(a), it can be noted that catenary voltage far from TSS sometimes goes below 3300 V, generating higher current peaks due to train power demand. Such aspect reduces systems global efficiency, because power losses strongly depend on currents.

A different displacement of Portichetto ESS could partially compensate voltage drops by proper power injections, performing a satisfactory energy recovery at the same time.

This double effect can be reached by a stand-alone ESS only, in order to be placed far away from diode TSS diode rectifiers.

Effective saved energy depends on the storage technology, that is expected to be optimized in order to manage different power profiles; no storage system models have been considered in previous simulations, because they do not affect significantly energy calculations; given results show the necessity to use a power oriented storage technology; for instance, as suggested in [37] and [38], batteries are probably much more energy intensive oriented, while supercapacitors are definitely much more power intensive oriented [19, 27, 16].

In next section, power intensive ESS will be also used to stabilize catenary voltage, placing a stand-alone system between Saronno and Portichetto stations; being voltage support a local effect, a smaller part of the railway will be analyzed and simulated again, introducing new control schemes to get expected functionalities.

1.8 Catenary voltage support

Recovery by ESS inside regional and local TSS has been presented in previous section and also treated in literature [36].

Despite saving energy produces a certain voltage stabilization along the track, voltage is still very variable, especially far from TSS: big drops and high peaks occur during train acceleration and braking.

In some "weak points", temporary local injection of current (active power) can prevent and compensate the falling of voltage below minimum admissible values; modern trains power is demanding, high voltage drops result in the need of much more current, with increase of line power losses. Voltage support makes a reduction of traction currents (so line losses) at a given train power.

Traditionally, solution against deep voltage drops is oversizing TSS diode rectifiers, increasing no-load voltage to face short time power peaks.

Unfortunately, higher catenary voltage also causes:

- more frequent peaks in braking, with energy waste due to utilization of train rheostats;

- rectification groups price increase, being converters sizing for railway market (insulation and overload prescriptions) definitely challenging.

The result is a strong economical impact on the infrastructure; such aspects are well-known in literature about urban rail [20] and tramways [39].

Looking for a solution to obtain both energy recovery and voltage stabilization, that is possible only by placing recovery systems far from electrical substations.

A stand-alone ESS could be a choice; ESS sizing is less challenging than a full scale rectification group, and no AC power network is required on site (electrification costs are by-passed).

As previously, costs reduction is desired; in these last years, many local and regional railways passengers stations have been re-organized, by replacing ticket offices with automatic machines.

Fig. 1.29 shows an example of such condition: Caslino al Piano passenger station; ticket window is now closed and the ticked machine is in the waiting room, on the left. Fig. 1.30, shows station outside, marking the former ticket office space respect to waiting room; two rooms are equal in surface (about 30 m^2), because each one occupies exactly half of station ground floor.

Those modifications made available areas inside passengers buildings, already segregated and near to rails and to catenary lines.

ESS could be placed inside existing passengers buildings; such implementation is innovative and reduces significantly infrastructure costs.

Stand-alone ESS will therefore monitor the catenary voltage, and inject locally the needed power to compensate the voltage drops, as schematically shown in Fig. 1.31. Equipment can operate between two TSS or on a terminal line; diode rectifiers have the loading characteristic already shown in Fig. 1.16 c); in the followings, a stand-alone ESS placed between two TSS along the Saronno-Como Lago regional 3 kV DC line will be simulated. Two control solution will be compared, in order to stabilize the catenary voltage. System efficiency increase is given by reducing catenary losses and by braking energy recovery.

Figure 1.29: Caslino al Piano passengers station inside: ticket window (closed) and automatic ticket machine (green cubicle on the left); room measures $6 \cdot 5$ m^2, for a total surface of 30 m^2.

Figure 1.30: Caslino al Piano station outside: former ticket office space and passengers waiting room.

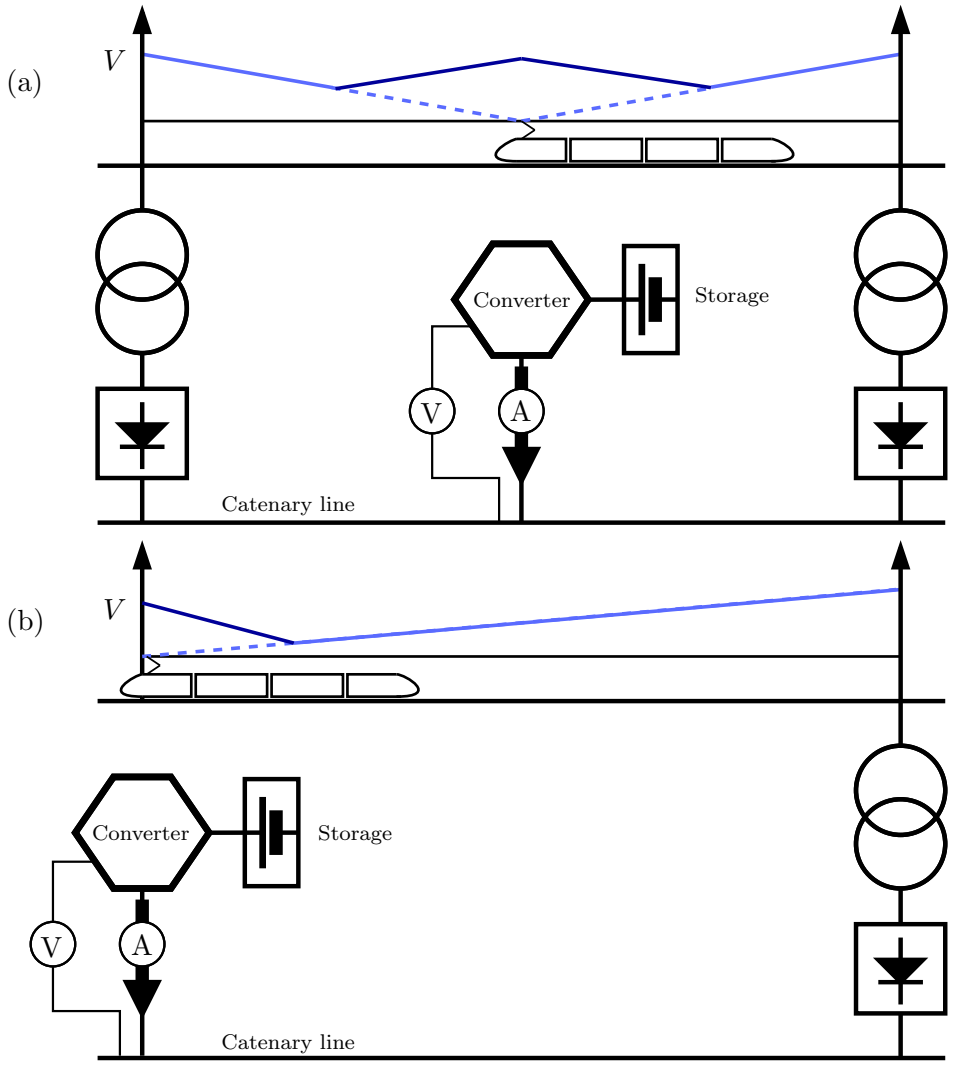

Figure 1.31: Catenary voltage support concept.
(a) Between two TSS.
(b) On a terminal line.

Before control algorithms, next section presents in detail an ideal stand-alone ESS concept and simulations as benchmark to obtain expected features.

1.8.1 Stand-alone ESS concept and ideal control

Fig. 1.32 shows a stand-alone ESS placed along a DC catenary, far from other TSS.

Bidirectional power flow is confined in the DC section through the ESS, being TSS diode rectifiers unidirectional. Being a stand-alone device, system must generate by itself high quality auxiliary supplies, fully independent by external power. Train

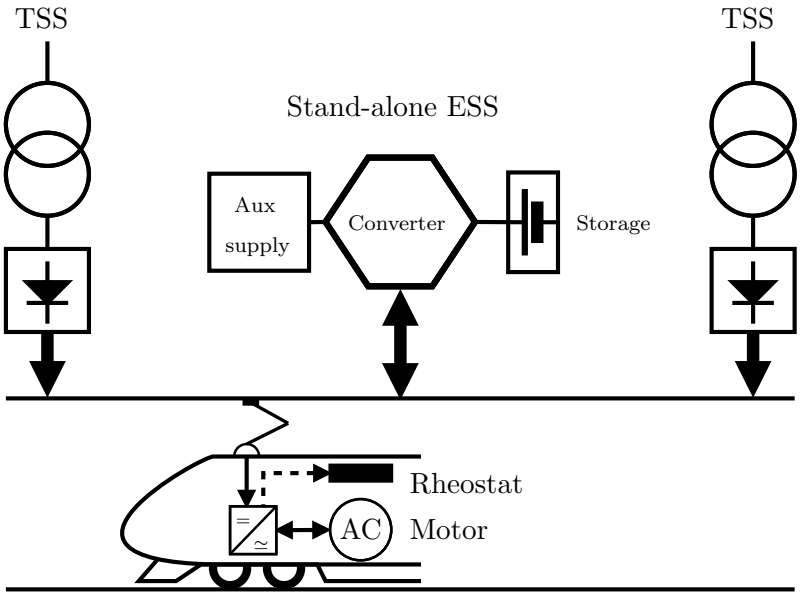

Figure 1.32: ESS stand-alone concept for voltage stabilization and energy recovery. Equipment is far from diode rectifiers traction substations (TSS). As stand-alone device, it can generate its own auxiliary supply by catenary voltage.

traction system is supplied through catenary line: a DC/AC converter provides power to AC motors, while a DC/DC chopper is engaged in case pantograph voltage reaches upper threshold; in such case, a power rheostat dissipates energy and keeps voltage within operative limits. A functional train model has been presented in Par. 1.7.4 and shown in detail in Fig. 1.17.

ESS target is avoiding train rheostats engage by absorbing power from catenary and limiting voltage drops by injecting power into catenary.

An ideal ESS control system is therefore designed to keep the catenary voltage at ESS terminals V_a within a certain band, between a charge (V_{a_c}) and a discharge (V_{a_d}) threshold;

$$V_{a_d} \leq V_a(t) \leq V_{a_c} \tag{1.32}$$

As previous simulations in last section, equipment capability is not considered at first stage, in order to obtain the very maximum current rates and properly quantify total energy savings; according to obtained data, capability limitations will be included in ESS control algorithms presented in the followings.

Ideal controlled ESS has been modeled as shown in Fig. 1.33, to provide initial simulation results.

Equipment operates like a perfect surge arrester when $V_a \geq V_{a_c}$ and like a perfect voltage booster when $V_a \leq V_{a_d}$.

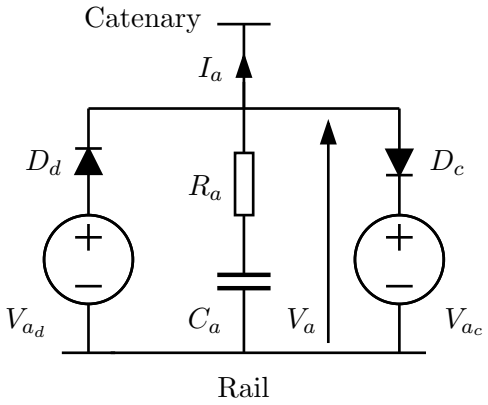

Figure 1.33: Functional model of ideal ESS control. A couple of ideal voltage generators is set at V_{a_d} and V_{a_c}, with discharge and charge diodes D_d and D_c. A parallel R-C branch models ESS converter filter.

If catenary voltage is above threshold V_{a_c}, diode D_c starts conducting and voltage is clamped at V_{a_c}; according to measurement conventions, ESS current I_a is negative (system in charge). If catenary voltage is below threshold V_{a_d}, diode D_c starts conducting and voltage is boosted at V_{a_d}; according to measurement conventions, ESS current I_a is positive (system in discharge).

Ideal controlled ESS has infinite capability, it can exchange energy with no limits and with no power thresholds. It has an efficiency in charge (η_{a_c}), and in discharge (η_{a_d}), defined in the followings (see Par. 1.8.5).

As in train recovery simulations, a R-C branch models a high pass filter for catenary voltage smoothing.

ESS filter data are listed in Tab. 1.16 (equal to Tab. 1.13).

Table 1.16: ESS filter data.

$R_a = 0.1\ \Omega$	$C_a = 0.03$ mF

1.8.2 Railway and train models

Same considerations of Par. 1.7.4 are still valid, but for this specific case a little portion of previous DC railway line (Saronno-Como Lago) has been simulated.

Also in this model, diode voltage drops (some volts) are not considered. The railway line model is shown in Fig. 1.34.

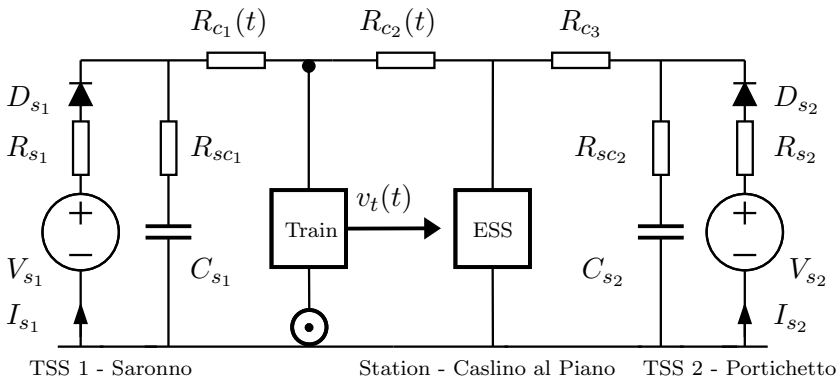

Figure 1.34: Model used for cateanry voltage support simulations. R-C branches model TSS smoothing filters.

Diode TSS are placed at both sides of the track.

Being catenary voltage the main focus of such simulation, smoothing filters have been placed also inside TSS, like in real installations; TSS have different equipment, as shown in Tab. 1.11: three groups of 2.3 MW each for Saronno, two groups of of 2.3 MW each for Portichetto-Luisago; also transformers short-circuit ratio is not the same (7% for Saronno and 10% for Portichetto-Luisago).

TSS equivalent data are listed in Tab. 1.17.

Table 1.17: TSS equivalent data.

Saronno	$V_{s1} = 3713$ V	$R_{s_1} = 0.07\ \Omega$	$R_{sc_1} = 0.1\ \Omega$	$C_{s_1} = 1.08$ mF
Porticheto-Luisago	$V_{s2} = 3713$ V	$R_{s_2} = 0.16\ \Omega$	$R_{sc_2} = 0.1\ \Omega$	$C_{s_2} = 0.72$ mF

Capacitance modeling is essential during the braking phase, otherwise train voltage V_t will immediately reach the voltage braking threshold (V_b = 4 kV), engaging the rheostats. Catenary voltage drops are given by line resistances; according to available data, per-length resistance r_c of 0.075 Ω/km is considered. Series inductances have been neglected, focusing on active losses.

Reminding to [28] for an optimal ESS siting, equipment was supposed to placed in Caslino al Piano station (Tab. 1.7), inside former ticket office room (Fig. 1.29, 1.30).

As prevuoisly, train is modeled by a controlled current generator (I_t), here repeated in Fig. 1.35 for clarity.

I_t setpoint time by time is given by instantaneous traction power (p_t) and voltage at pantograph (V_t); calculations are detailed in the followings. During traction phases, according to measurement conventions, I_t is negative.

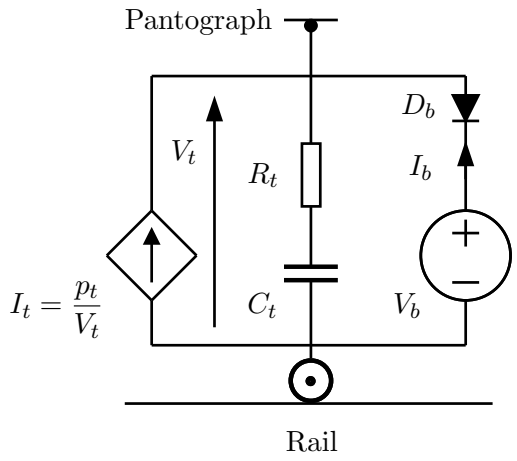

Figure 1.35: Functional train model, including equivalent circuit of braking rheostats and filter.

Regenerative braking means injecting current into catenary, so I_t becomes positive; due to parasitic capacitance, voltage start rising with a certain slope; a R-C branch (R_t and C_t) models such effect, including also train converter filter, that is a relevant part of the total capacitance.

Train filter data are listed in Tab. 1.18 (equal to Tab. 1.10).

Table 1.18: Train filter data.

$R_t = 0.1\ \Omega$	$C_t = 3.6$ mF

Train starts from Lomazzo station and arrives at Caslino al Piano.
As previously, mathematical approach in (1.8-1.16) is still valid, the algorithm must be cycled time by time, taking into account system constraints.

GPS data and train current profile for this simulation are shown next.

1.8.3 GPS data

GPS measurements between Lomazzo and Caslino al Piano stations have been performed, providing position, speed and altitude profiles.

Respect to previous GPS data, these ones have been performed on a 6-railcars TSR (Treno Servizio Regionale - Regional Service Train), considering a more realistic average composition: trains during the day can vary from 3-4 up to 7-8 railcars, according to traffic and rail stock availability.

GPS train position d_t vs. time is shown in Fig. 1.36.

Fig. 1.37(a) reports GPS train speed profile v_t vs. time; acceleration profile a_t is shown in Fig. 1.37(b).

This part of the track has a maximum drop of around 5-6 m only. Calculation of the punctual slope is not reliable due to commercial GPS resolution; the average slope S_t on the section has been used to calculate the train power contribution by potential energy.

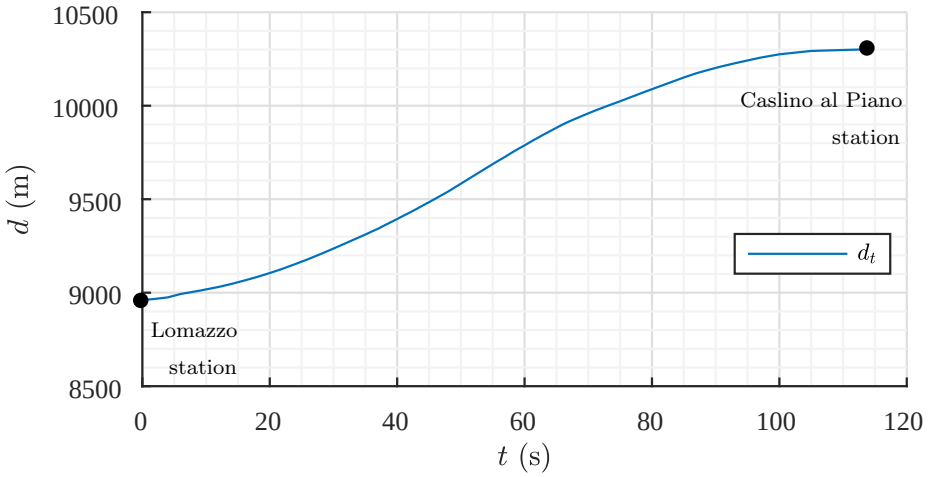

Figure 1.36: Rail section from Lomazzo to Caslino al Piano stations. GPS train position d_t vs. time t.

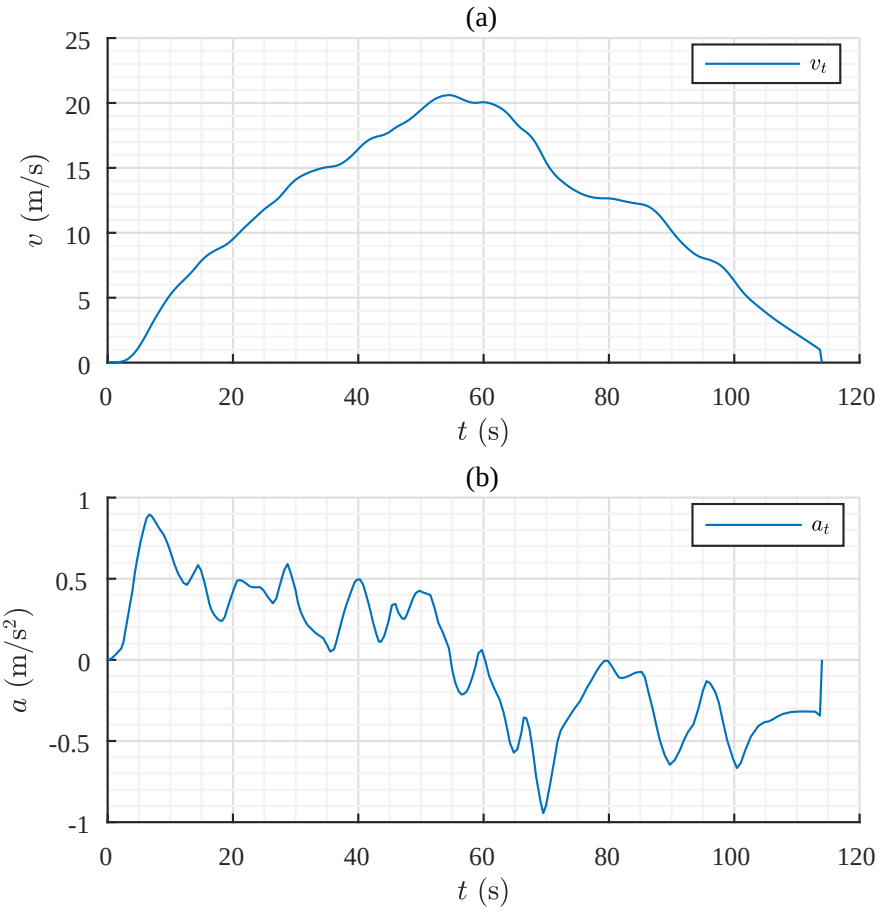

Figure 1.37: Rail section from Lomazzo to Caslino al Piano. GPS train speed v_t vs. time t (a) and acceleration a_t vs. time t (b).

1.8.4 Train power profile

As previously, real data concern GPS train measurements (d_t, v_t and a_t) have been used to implement train power profile into simulations; as for model presented in Par. 1.7.4, formulas shown in [25, 26] are used.

Train traction force F_t formula is here repeated, a complete descriptions of single quantities is in Par. 1.7.6.

$$F_t(t) = (1 + k_m)m_t\Big\{a_t(t) + g\Big[A + Bv_t(t)^2 + S\Big]\Big\} \tag{1.33}$$

According to F_t sign, train power p_t is:

$$\begin{cases} p_t(t) = -\dfrac{1}{\eta_t}F_t(t)v_t(t) - p_{aux} \\ F_t(t) \geq 0 \end{cases} \tag{1.34}$$

$$\begin{cases} p_t(t) = -\eta_t F_t(t)v_t(t) - p_{aux} \\ F_t(t) < 0 \end{cases} \tag{1.35}$$

Train power profile p_t vs. time is shown in Fig. 1.38.

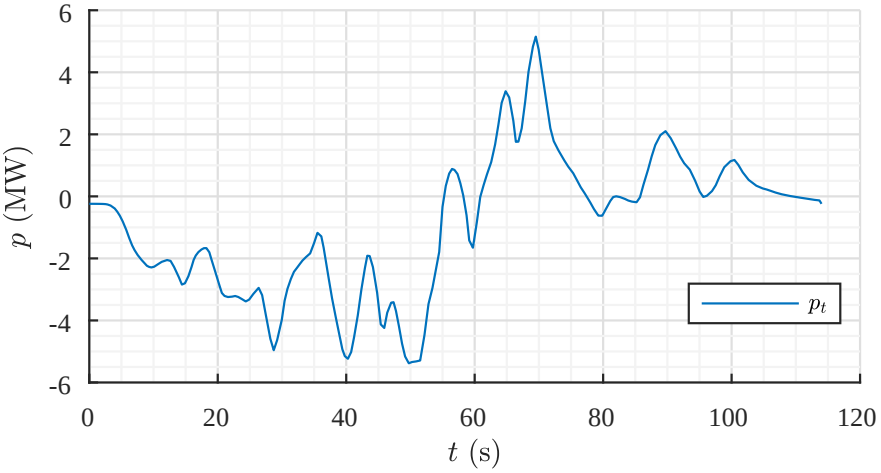

Figure 1.38: Train power profile p_t vs. time t. If value is positive, according to conventions in Fig. 1.35, power is provided from train to catenary, while negative value means power absorbed by the train from catenary.

Train current profile is given by (1.22).

Next section presents simulations performed on system model with ideal controlled ESS.

1.8.5 Simulation 3: ideal controlled ESS

Using data and model of Fig. 1.35 without ESS, train voltage profile V_t is given in Fig. 1.39(a).

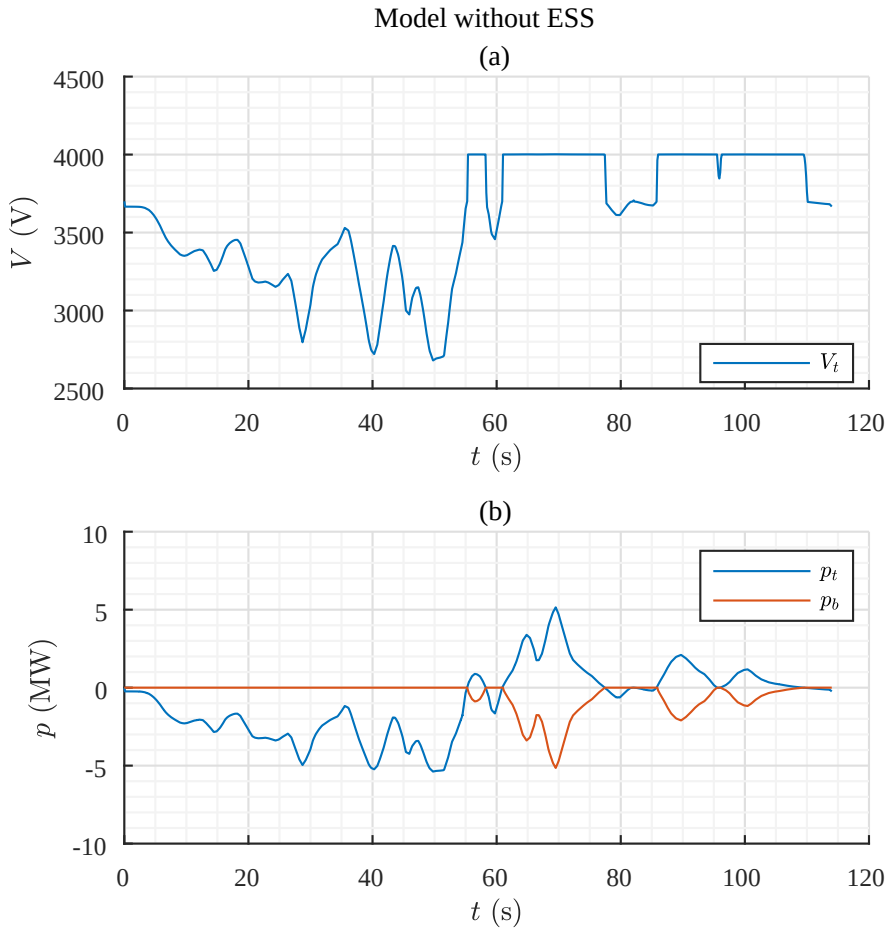

Figure 1.39: Simulation results without ESS. (a) Train voltage profile V_t vs. time t. (b) Train power profile p_t and rheostatic braking power profile p_b vs. time t according to model in Fig. 1.35.

During braking phases, train voltage goes immediately above the substation voltage V_s, to be controlled at V_b by the braking rheostats.

In acceleration, voltage drops below 3 kV several times.

According to International Standards [40], absolute minimum train voltage V_{tmin} is 2000 V; assuming ESS receptivity distance d_a of about 8 km, $r_c = 0.075$ Ω/km and train power peak $|\hat{p}_t|$ of 5 MW:

$$V_{a_d} = V_{tmin} + \frac{|\hat{p}_t|}{V_{tmin}} r_c d_a = 3500 \text{ V} \tag{1.36}$$

V_{a_c} has been set at 3900 V to get a symmetric span respect to TSS no-load voltage (3700 V).

Simulation is then repeated with ideal controlled ESS model of Fig 1.33(a); train voltage and catenary voltage at ESS terminals profiles are shown in Fig. 1.40(a).

ESS power p_a is reported in Fig. 1.40(b), with train power p_t and rheostatic braking power p_b.

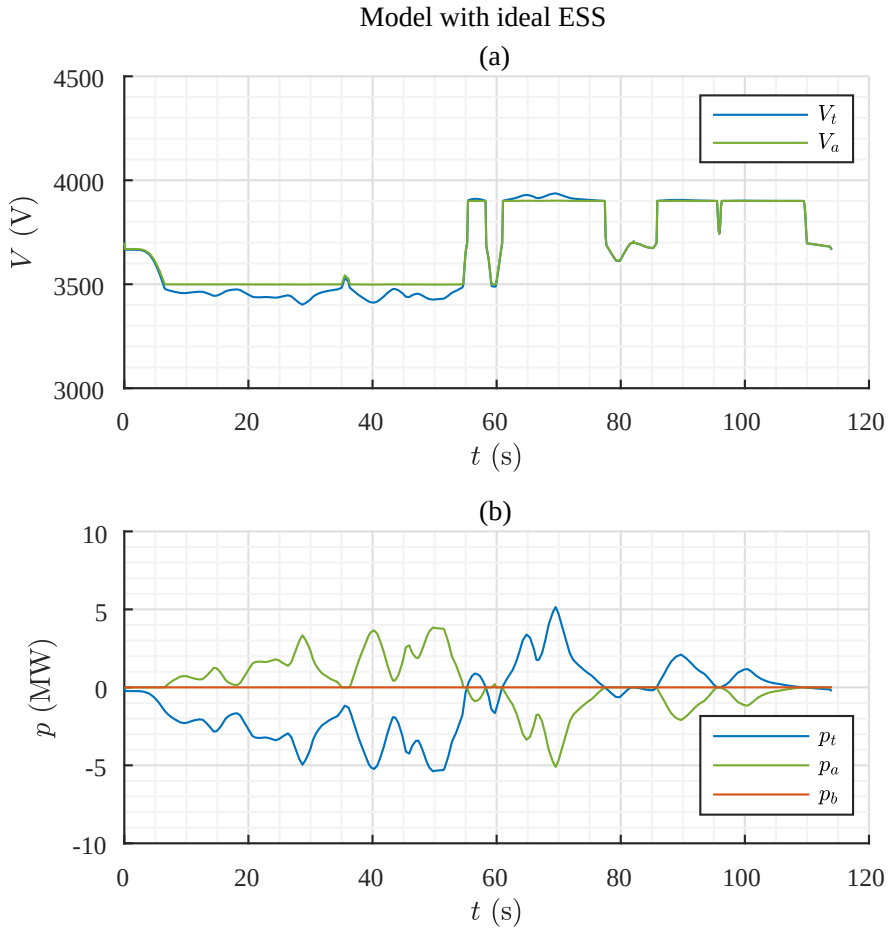

Figure 1.40: Simulation results with ideal controlled ESS. (a) Train voltage profile V_t and catenary voltage at ESS terminals V_a vs. time t. (b) Train power profile p_t, rheostatic braking power profile p_b and ESS power profile p_a vs. time t.

Catenary losses p_{j_c} are given by:

$$p_{s_1}(t) + p_{s_2}(t) + p_t(t) + p_b(t) + p_a(t) + p_{jc}(t) = 0 \tag{1.37}$$

with TSS instantaneous power:

$$p_{s_1} = (V_{s_1} - R_{s_1} I_{s_1}) I_{s_1} \tag{1.38}$$

$$p_{s_2} = (V_{s_2} - R_{s_2} I_{s_2}) I_{s_2} \tag{1.39}$$

ESS losses are computed differently in charge (p_{ja_c}) and discharge (p_{ja_d}) as a portion of the ESS power exchanged with the catenary (p_a). ESS average efficiency in charge (η_{a_c}) and discharge (η_{a_d}) are given.

In discharge, $p_t < 0$, $p_a > 0$, $p_{j_c} < 0$, $p_{j_{a_d}} < 0$, so:

$$p_{j_{a_d}}(t) = \left(1 - \frac{1}{\eta_{a_d}}\right) p_a(t) \tag{1.40}$$

In charge, $p_t > 0$, $p_a < 0$, $p_{j_c} < 0$, $p_{j_{a_c}} < 0$, so:

$$p_{ja_c}(t) = (1 - \eta_{a_c})p_a(t). \tag{1.41}$$

According to previous definitions, p_a quantity has a different physical meaning in charge and in discharge:

- in charge, it is the GROSS power the ESS receives from catenary; accordingly, W_{a_c} is the gross energy, including $W_{j_{ac}}$; besides losses, net energy $\eta_{a_c}W_{a_c}$ does charge the ESS;

- in discharge, it is the NET power the ESS provides the catenary; accordingly, W_{a_d} is the net energy (not including $W_{j_{ad}}$); gross energy is given by W_{a_d}/η_{a_d}.

It must be noted, also, that in this case total discharged energy W_{a_d} is greater than the total charged energy W_{a_c} (in module); this happens because simulation starts with a train acceleration and then it is concluded with a braking; it only considers train travel time, focusing on total energy exchanged between ESS and catenary.
Train cannot generate more braking power than absorbed traction power, and no ESS discharge limits are imposed; as a consequence, there is not a complete thermodynamic cycle, in sense that initial ESS charge is not fully restored.

In order to compute system efficiency, energy cycle must be closed considering also:

- ESS initial pre-charge, at a level sufficient to provide all needed energy in discharge;

- ESS post-charge, to restore initial charge and set equipment ready for another cycle.

Theoretically, pre-charge is necessary once only, or anyway is very rare (eg. once per day), while post-charge is mandatory at every cycle.

A basic representation of ESS cycle is given in Fig. 1.41.

During the whole cycle, energy must be within ESS operative limits ($W_{a_{max}}$ and $W_{a_{min}}$); W_{a_1} and W_{a_2} represent maximum and minimum ESS energies during the cycle, respectively.

As shown, ESS starts working already pre-charged (W_{a_1}); train acceleration causes a discharge up to W_{a_2} during t_d:

$$W_{a_1} - \int_{t_0}^{t_0+t_d} \Big[p_a(t) - p_{ja_d}(t)\Big]dt = W_{a_2} \tag{1.42}$$

$$W_{a_1} - \int_{t_0}^{t_0+t_d} \Big[p_a(t) - \Big(1 - \frac{1}{\eta_{a_d}}\Big)p_a(t)\Big]dt = W_{a_2} \tag{1.43}$$

$$W_{a_1} - W_{a_d} + W_{j_{a_d}} = W_{a_2} \tag{1.44}$$

$$W_{a_1} - W_{a_d} + \Big(1 - \frac{1}{\eta_{a_d}}\Big)W_{a_d} = W_{a_2} \tag{1.45}$$

As expected, because of losses, initial charge W_{a_1} must be greater than W_{a_d}.

During braking, energy is recovered in t_c; initial energy W_{a_1} is reset to original value in t_{pc} (post-charge time), by absorbing power $p_{a_{pc}}$; as said, in such phase measured

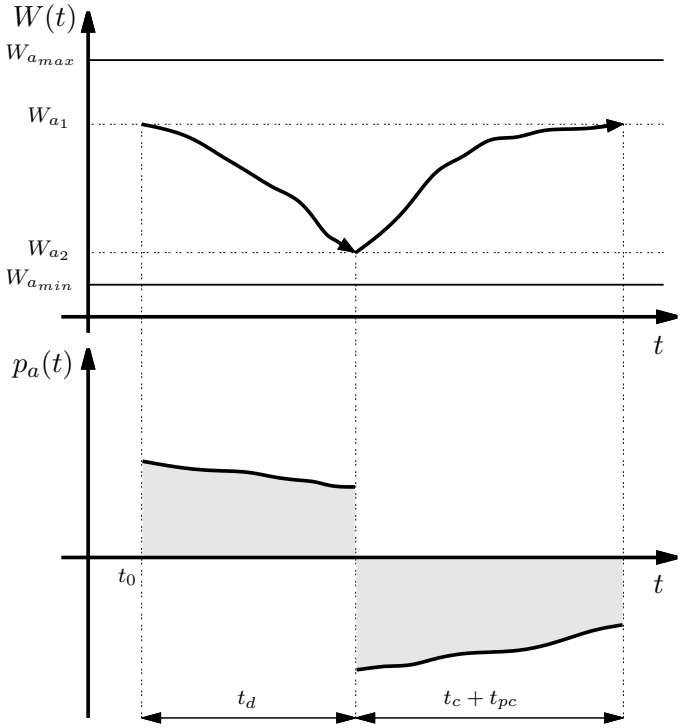

Figure 1.41: ESS cycle representation. a) Energy. b) Power.
Profiles are general and indicative.

energy is gross, so net quantities must be computed:

$$W_{a_2} - \int_{t_d}^{t_d+t_c+t_{pc}} \Big[\eta_{a_c} p_a(t) + \eta_{a_c} p_{a_{pc}}(t)\Big] dt = W_{a_1} \tag{1.46}$$

$$W_{a_2} - \eta_{a_c} W_{a_c} - \eta_{a_c} W_{a_{pc}} = W_{a_1} \tag{1.47}$$

Imposing for simplicity $W_{a_2} = 0$ in (1.45) and (1.47), post-charge energy the ESS must absorb can be achieved:

$$W_{a_1} = \frac{W_{a_d}}{\eta_{a_d}} \tag{1.48}$$

$$W_{a_{pc}} = -\left(W_{a_c} + \frac{W_{a_d}}{\eta_{a_d}\eta_{a_c}}\right) \tag{1.49}$$

Supposing post-charge process not different by another charge by the efficiency point of view, condition of (1.41) is still valid; then post-charge losses are:

$$W_{j_{a_{pc}}} = (1-\eta_{a_c}) W_{a_{pc}} = -(1-\eta_{a_c})\left(W_{a_c} + \frac{W_{a_d}}{\eta_{a_d}\eta_{a_c}}\right) \tag{1.50}$$

In order to compute ESS cycle efficiency, catenary losses during post-charge are still missing.

During ESS duty, power is "imposed" by train needs, and catenary losses have been computed accordingly; during post-charge, instead, there's a further degree of freedom,

that is the ESS current profile; it is supposed the post-charge is performed at constant current $I_{a_{pc}}$.

Because of train frequencies, post-charge can be performed when track is empty, so circuit in Fig. 1.34 becomes time invariant and equivalent to Fig. 1.42, as shown below.

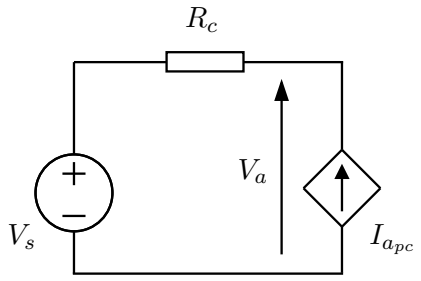

Figure 1.42: Post-charge circuit representation. ESS is a current generator ($I_{a_{pc}}$); catenary is modeled by total equivalent resistance R_c and TSS are replaced by a unique Thevenin voltage generator V_s. TSS diodes and filters are not relevant so they are neglected.

In this way, with the same equivalent recharge, catenary losses are strongly dependent by I_a intensity.

As example:

1) post-charge at $I_{a_{pc}}$ in t_{pc};

$$W_{j_{c_1}} = -R_c I_{a_{pc}}^2 t_{pc} \tag{1.51}$$

2) post-charge at $10 \cdot I_{a_{pc}}$ in $t_{pc}/10$:

$$W_{j_{c_2}} = -R_c (10 I_{a_{pc}})^2 \frac{t_{pc}}{10} = 10 W_{j_{c_1}} \tag{1.52}$$

In practice, system energy losses are linear respect to current, so post-charge phase should be performed at low current and slowly (so-called refill charge), both to increase efficiency, both to preserve integrity and durability of the storage equipment.

About simulation case, due to long time between two consecutive trains (15-20 minutes), post-charge can be tuned in order to make catenary losses almost negligible if compared to ESS stabilization phase ($W_{j_{c_{pc}}} << W_{j_c}$).

Example in ideal controlled ESS: reduce post-charge catenary losses at one hundred of catenary losses during ESS stabilization phase (filter circuits are neglected).

According to Fig. 1.34 and 1.42:

$$R_c = \left(\frac{1}{R_{s_1} + R_{c_1} + R_{c_2}} + \frac{1}{R_{s_2} + R_{c_3}} \right)^{-1} = 0.134\ \Omega \quad , \quad V_s = V_{s_1} = 3713\ \text{V} \tag{1.53}$$

As first approximation, being low current expected, voltage at ESS terminals (V_a)

can be set at V_s (it will be verified later);

$$W_{a_{pc}} = I_{a_{pc}} V_s t_{pc} \quad , \quad t_{pc} = \frac{W_{a_{pc}}}{V_s I_{a_{pc}}} \tag{1.54}$$

$$W_{j_{c_{pc}}} = -R_c \; {I_{a_{pc}}}^2 t_{pc} = \frac{1}{100} W_{j_c} \quad , \quad -R_c \frac{I_{a_{pc}} W_{a_{pc}}}{V_s} = \frac{1}{100} W_{j_c} \tag{1.55}$$

$$I_{a_{pc}} = -\frac{V_s W_{j_c}}{100 R_c W_{a_{pc}}} = -33.8 \text{ A} \tag{1.56}$$

$$t_{pc} = 430 \text{ s} \tag{1.57}$$

$$(t_{pc} \ll 15' \text{ verified})$$

$$R_c I_{a_{pc}} = -4.5 \text{ V} \tag{1.58}$$

$$(V_a \simeq V_s \text{ verified})$$

Coefficient of reduction could be also a parameter and set arbitrarily.

About ESS, efficiency has been supposed not dependent by current but by energy, so it is invariant by the charge profile: this is reasonable considering power electronics components losses, cooling systems consumptions etc.

ESS post-charge energy is provided by TSS, so:

$$W_{s_{pc}} = -W_{a_{pc}} \tag{1.59}$$

System global efficiency η is:

$$\eta = 1 - \frac{\left| W_{j_{a_c}} + W_{j_{a_d}} + W_b + W_{j_c} + W_{j_{a_{pc}}} \right|}{\left(W_{s_1} + W_{s_2} + W_{s_{pc}} \right)} \tag{1.60}$$

Simulation results and calculations are listed in Tab. 1.19.

Table 1.19: Simulation results. Cases refer to Fig. 1.39 and 1.40. 6-railcars TSR. $\eta_{a_d} = 0.85$, $\eta_{a_c} = 0.8$.

Case	W_b (MJ)	W_{a_d} (MJ)	W_{a_c} (MJ)	$W_{j_{a_d}}$ (MJ)	$W_{j_{a_c}}$ (MJ)	W_{j_c} (MJ)	$W_{j_{a_{pc}}}$ (MJ)
NO ESS	-54.0	0	0	0	0	-25.6	0
Ideal contrtolled ESS	0	73.3	-53.8	-12.9	-10.8	-6.6	-10.8

Case	W_{s_1} (MJ)	W_{s_2} (MJ)	$W_{s_{pc}}$ (MJ)	$\lvert\hat{p_b}\rvert$ (MW)	$\lvert\hat{p_a}\rvert$ (MW)	η (-)	$\Delta\eta\%$ (%)
NO ESS	86.9	94.6	0	5.2	0	0.56	-
Ideal controlled ESS	45.1	43.8	54.0	0	5.1	0.71	+27 %

Ideal controlled ESS effects are remarkable: according to (1.60), percentage efficiency gap $\Delta\eta_{\%}$ is increased of 27 %; braking rheostatic energy W_b is set to zero, catenary losses are lower; Despite extra ESS post-charge and losses, total TSS energy is reduced and this increases global efficiency.

Fully cover the ideal ESS capability appears anyway technically and economically unreasonable, ESS power should be close to a standard TSS (about 6 MW); also storage sizing must be chosen too.

In following simulations with controlled ESS model, power will be limited, in order to define a more realistic equipment hardware (both converter and storage device).

1.8.6 Controlled ESS model

Further simulations have been later performed modeling ESS as in Fig. 1.43: I_a is a current generator whose setpoint comes from different ESS control solutions presented in the followings: droop action (Par. 1.8.7) and PID control (Par. 1.8.8).

Train and ESS filter data are still the same listed in Tab. 1.16 and 1.18.

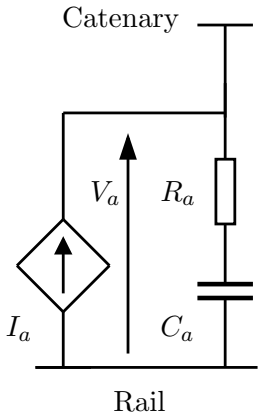

Figure 1.43: ESS modeled by a controlled current generator. I_a comes from controls described in sections 1.8.7 and 1.8.8 A parallel R-C branch models ESS converter filter.

ESS performances depends on control topology and setting; detailed description of tuning process is reported in Appendix A.

According to previous simulations results, controlled variable I_a will be also limited within charge and discharge thresholds (I_{a_c},I_{a_d}):

$$I_{a_c} \leq I_a \leq I_{a_d} \tag{1.61}$$

ESS instantaneous power is limited at p_{amax}, in order to provide a more realistic system sizing; p_{amax} threshold has been chosen by recovery simulation results (Tab. 1.15): active power of Portichetto ESS was about 2 MW; because also Lomazzo station is on a flat track, a similar behavior is expected.

I_{a_c} and I_{a_d} limits are then dynamically adjusted as shown in Fig. 1.44, taking into account also ESS maximum current (I_{amax}), resulting from power converter physical limits.

Catenary voltage is filtered by a first time constant τ_c (50 ms), to avoid sudden current peaks due to division block.

According to RFI (Rete Ferroviaria Italina, *Italian Railway Network*) [10], minimum average catenary voltage in normal conditions (V_{amin}) is 3000 V; limiting ESS power up to p_{amax} with V_{amin}, means:

$$I_{amax} = \frac{p_{amax}}{V_{amin}} = \frac{2 \cdot 10^6 \ W}{3 \cdot 10^3 \ V} = 667 \ A \tag{1.62}$$

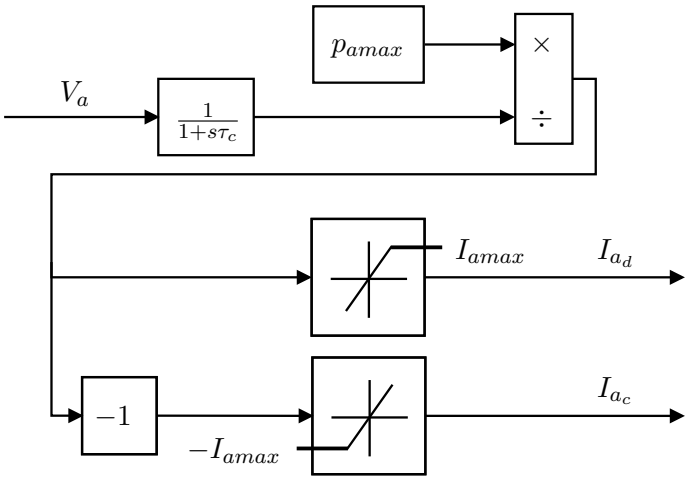

Figure 1.44: I_{a_c} and I_{a_d} dynamic adjustment to limit ESS maximum instantaneous power (p_{amax}) and ESS maximum current I_{amax}.

ESS action is limited in case of excessive catenary voltage drop, so power electronics converter sizing is set accordingly.

For these simulations, no overload capability is foreseen, equipment maximum power is also rated power; this contributes in lowering component costs.

In the followings, two control solutions above mentioned will be compared looking at respective advantages and disadvantages; at first, control schemes are explained.

1.8.7 ESS droop action

In Fig. 1.45 a block diagram of the droop action is shown.

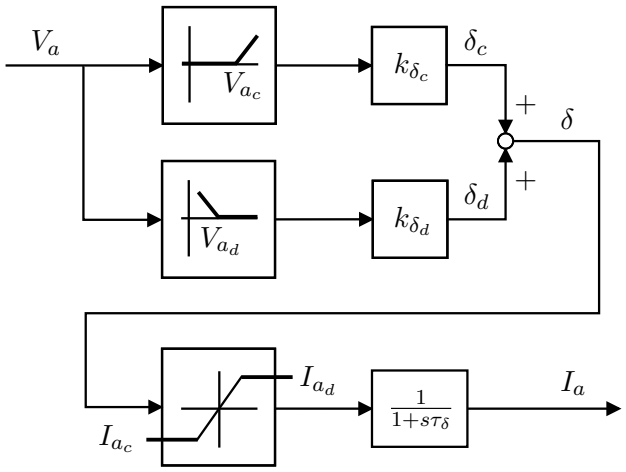

Figure 1.45: Block diagram of droop action.

Droop actions δ_c and δ_d are given by voltage V_a conditioned by dead zone blocks and then multiplied by droop coefficients k_{δ_c} or k_{δ_d}; those coefficients impose the strength of the droop action. Output is filtered by a first time constant τ_δ (2 ms), to smooth oscillations in the control variable and simulate the ESS converter delay of response.

When V_a is above V_{a_c}, negative I_a is drained by the catenary up to I_{a_c}, positive I_a is injected up to I_{a_d} as soon as V_a is below V_{a_d}.

Droop action static characteristic is shown in Fig. 1.46.

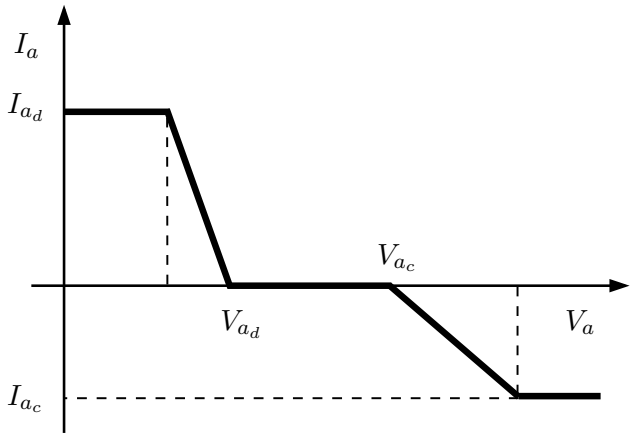

Figure 1.46: Droop action static characteristic. Profile is indicative.

Global action δ is limited within the system capability by a saturation block, whose limits are dynamically adjusted by control in Fig. 1.44.

Such action is fast and simple to implement: only a couple parameters tuning is required; droop is widely used in AC microgrids [41], synchronous machines [42] and static conversion systems [43, 44]. It contrasts voltage variations without a precise setpoint to follow, so it's supposed to be less accurate than a PID control.

1.8.8 ESS PID control

In Fig. 1.47 a block diagram of the PID control is shown.

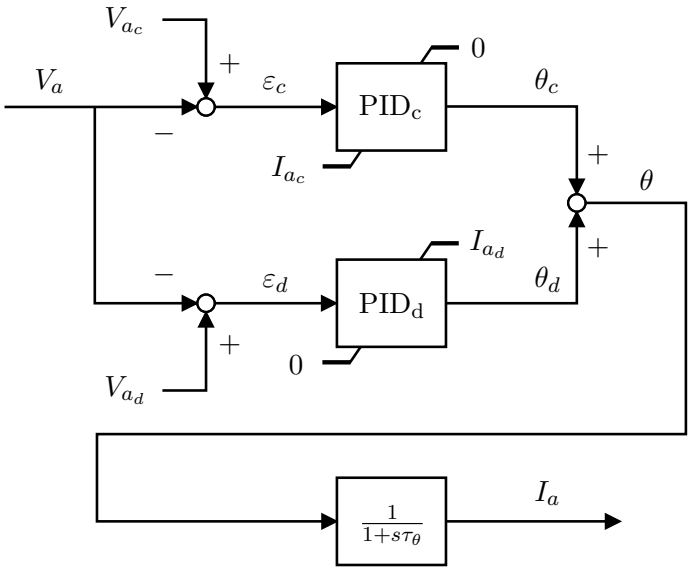

Figure 1.47: Block diagram of PID control.

As in the droop action, the control is split in two parts, charge and discharge; error signals ε_c and ε_d are given by:

$$\varepsilon_c = V_{a_c} - V_a \tag{1.63}$$

$$\varepsilon_d = V_{a_d} - V_a \tag{1.64}$$

Error signals are conditioned by two independent PID controllers PID$_c$ and PID$_d$, with anti-windup configuration.

Saturation limits are given by splitting condition (1.61):

$$\text{PID}_c : I_{a_c} \leq I_a \leq 0 \tag{1.65}$$

$$\text{PID}_d : \quad 0 \leq I_a \leq I_{a_d} \tag{1.66}$$

Limits are dynamically adjusted by control in Fig. 1.44.

Output is filtered by a first time constant τ_θ (2 ms), to smooth oscillations in the control variable and simulate the ESS converter delay of response.

When V_a is above V_{a_c}, negative I_a is drained by the catenary to keep V_a exactly equal to V_{a_c} (if I_{a_c} is enough). As soon as V_a moves below V_{a_c}, ε_c changes sign but control action θ_c is saturated at zero. When V_a is below V_{a_d}, positive I_a is injected into catenary to keep the voltage at V_{a_d} (if I_{a_d} is enough).

Such configuration has the possibility to shape the system response by "classical" control techniques based on Bode criterion (Appendix A); this solution is the state of the art in many kind of automatic machinery [32, 33, 34].

Respect to a droop, small steady state errors and good dynamic response are expected, thus tuning is usually a little more complex. Control strategies comparison is given by simulations in the followings.

1.8.9 Simulation 4: droop action and PID control

PID and droop tuning parameters are listed in Tab. 1.20: k_{δ_c}, k_{δ_d} and k_p are set to have a droop action in charge and discharge that is equal to PID static gain action (see Appendix A).

Table 1.20: ESS tuning parameters.

	V_{a_c} (V)	V_{a_d} (V)	k_{δ_c} (A/V)	k_{δ_d} (A/V)	k_p (-)	k_i (-)	k_{δ_d} (-)
Droop	3900	3500	-10	10	-	-	
PID	3900	3500	-	-	1	10	0

In Fig. 1.48 and 1.49 simulations of droop action ESS and PID control ESS are shown.

Numerical results according to (1.37−1.60) are provided in Tab. 1.21.

Table 1.21: Simulation results. Cases refer to Fig. 1.39, 1.48 and 1.49. 6-railcars TSR. $\eta_{a_d} = 0.85$, $\eta_{a_c} = 0.8$.

Case	W_b (MJ)	W_{a_d} (MJ)	W_{a_c} (MJ)	$W_{j_{a_d}}$ (MJ)	$W_{j_{a_c}}$ (MJ)	W_{j_c} (MJ)	$W_{j_{apc}}$ (MJ)
NO ESS	-54.0	0	0	0	0	-25.6	0
Droop ESS	-10.6	54.5	-43.4	-8.7	-10.8	-9.7	-7.3
PID ESS	-10.3	60.6	-43.7	-8.7	-10.8	-9.0	-9.1

Case	W_{s_1} (MJ)	W_{s_2} (MJ)	$W_{s_{pc}}$ (MJ)	$\lvert\hat{p_b}\rvert$ (MW)	$\lvert\hat{p_a}\rvert$ (MW)	η (-)	$\Delta\eta$% (%)
NO ESS	86.9	94.6	0	5.2	0	0.56	-
Droop ESS	55.0	55.9	36.7	3.1	2.0	0.69	+23 %
PID ESS	52.0	52.1	45.4	3.1	2.0	0.68	+21 %

Comparing Tab. 1.19 with 1.21, ESS effects are still consistent: +23 % and +21 % of efficiency gap with droop and PID, respectively; furthermore, this result is achieved with a limited converter power.

Also a reasonable sizing of the storage unit (about 60 MJ, according to W_{a_d} =60.6 MJ) is achieved.

Regarding differences between the two controls, PID has, as expected, a more precise control of the catenary voltage limits, therefore less catenary losses; in charge, ESS energies are the same for both controls, but PID is better because catenary voltage fluctuations could engage the train braking rheostats and reduce drastically the global system efficiency; therefore, a well-precise control strategy is needed. On the other way, in discharge there's no need of precise voltage control, and the PID control, to achieve a perfect stabilization, uses more energy than droop; as a consequence, ESS losses are bigger and the catenary losses reduction doesn't compensate such gap. That's why in the last simulations the global system efficiency is less in PID than in droop.

Both droop and PID techniques are then combined into a "mixed control", looking for an algorithm optimization.

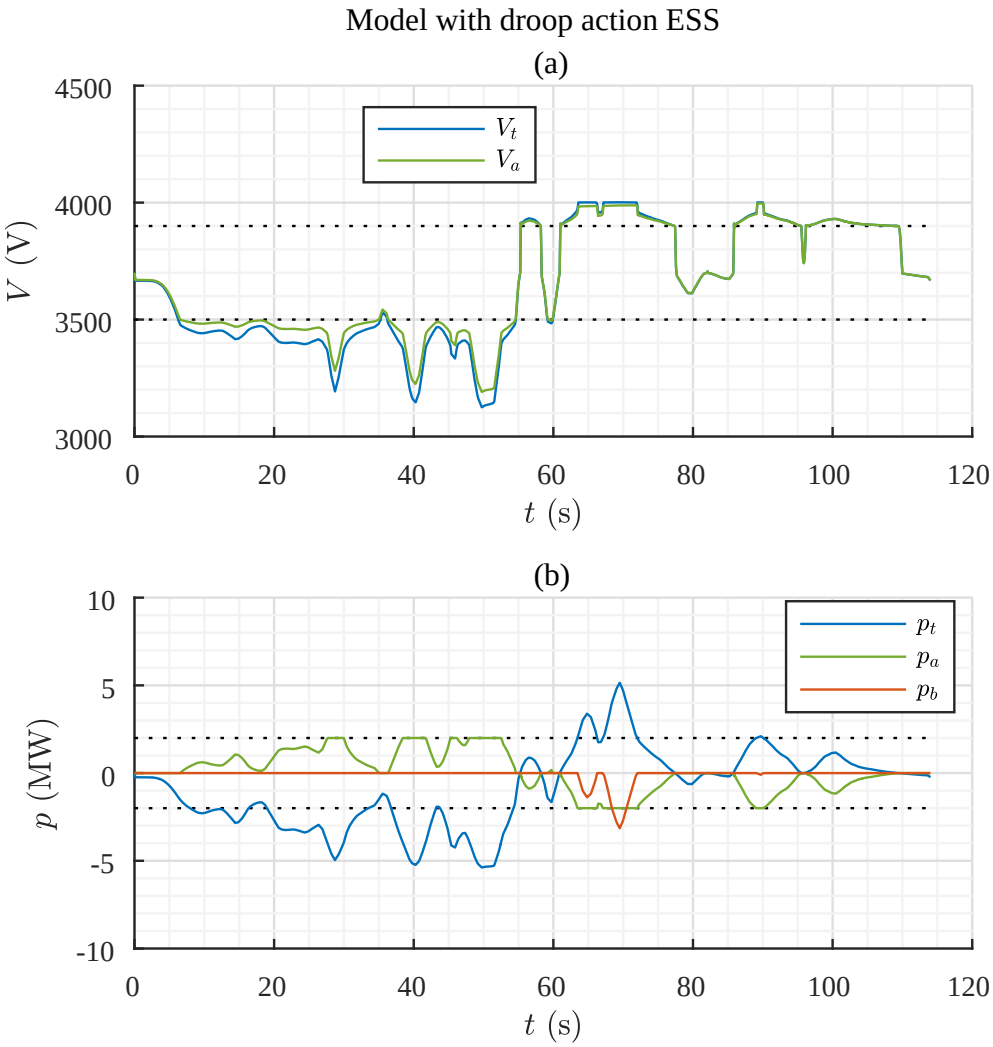

Figure 1.48: Simulation results with droop action ESS. (a) Train voltage profile V_t and catenary voltage at ESS terminals V_a vs. time t. (b) Train power profile p_t, rheostatic braking power profile p_b and ESS power profile p_a vs. time t according to model in Fig. 1.46.

1.8.10 Simulation 5: control optimization

After droop and PID simulations, ESS control algorithm has been upgraded, integrating features coming from previous models; new simulations are expected to provide further benefits by the energy point of view.

Previous section highlighted relevant features about droop and PID:

- droop showed a better efficiency in discharge phase, boosting up catenary voltage;

- PID was better in charge, limiting overvoltages.

According to such conclusions, both features have been combined into a "mixed control" diagram, looking for respective advantages: as shown in Fig. 1.50, PID is implemented in charge and droop in discharge, resulting in global control action γ; as usual, output is filtered by a first time constant τ_γ (2 ms), to smooth oscillations in the control variable and simulate the ESS converter delay of response.

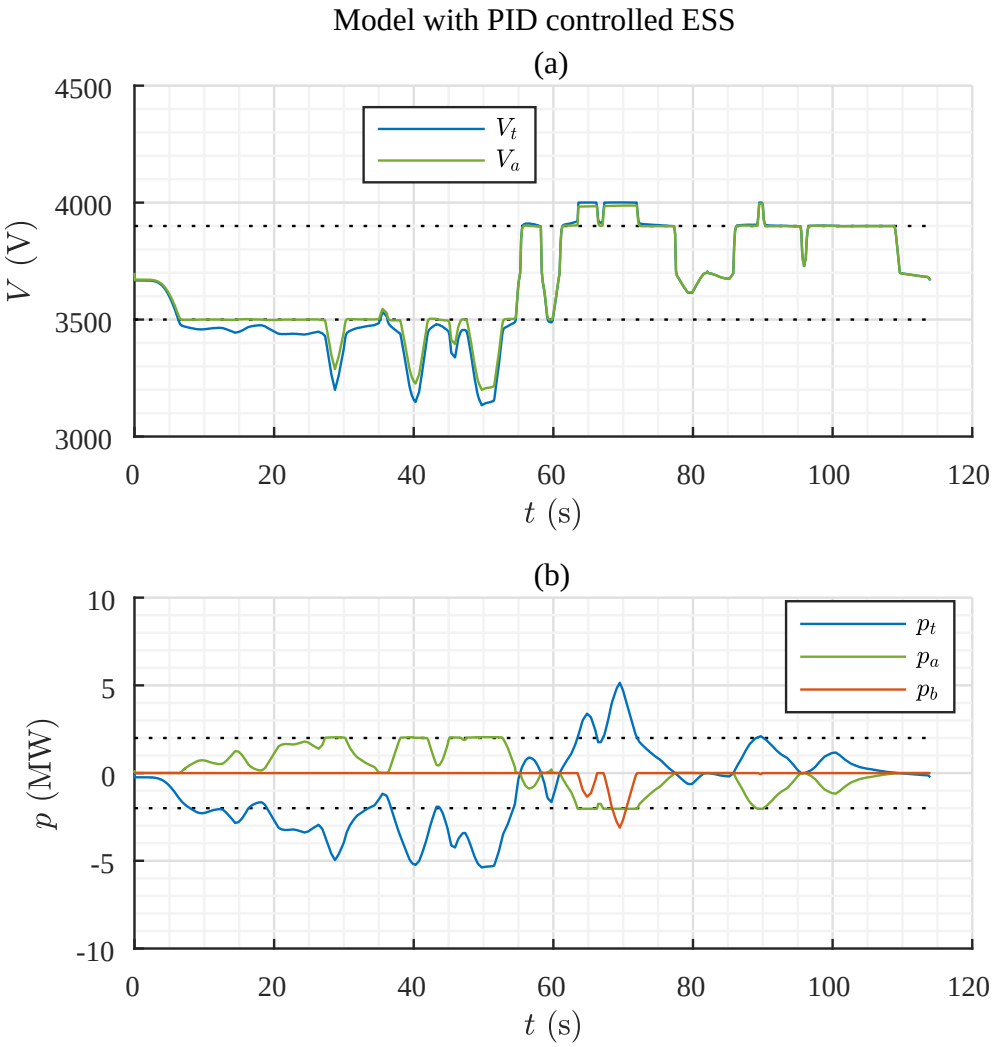

Figure 1.49: Simulation results with PID controlled ESS. (a) Train voltage profile V_t and catenary voltage at ESS terminals V_a vs. time t. (b) Train power profile p_t, rheostatic braking power profile p_b and ESS power profile p_a vs. time t according to model in Fig. 1.47.

Such solution is quite innovative, a different kind of control in two distinct areas of the catenary voltage profile is achieved; upper voltage is strongly limited by PID, avoiding as much as possible train rheostats activation, while droop just modulates the control action around lower voltage threshold, so ESS power flow is smoother.

Differences in two approaches depend mainly on regulators topologies, in particular the so-called "static project": it defines regulator capability in erasing the steady-state error or reducing it withing a given tolerance.

In the particular case, PID is tuned to give zero steady-state error at any time, while droop is basically a simple proportional gain control; steady-state error amplitude is depending on module of droop coefficient k_{δ_d} itself.

A deeper description of regulators design and tuning is given in Appendix A.

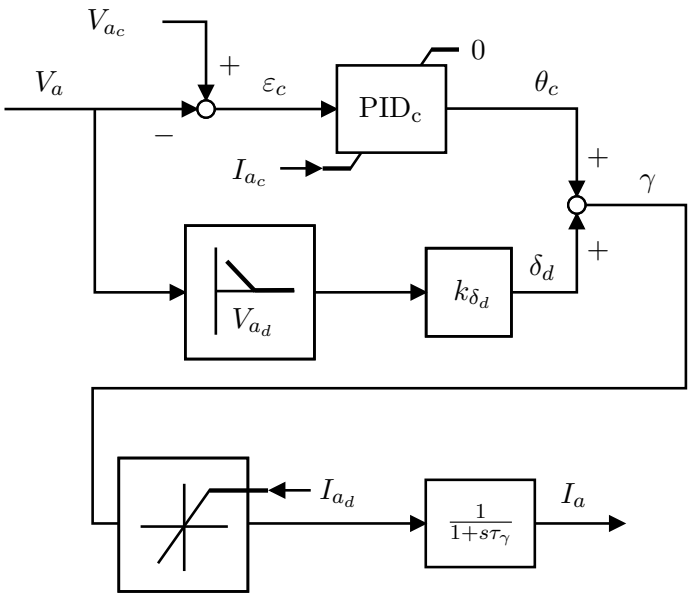

Figure 1.50: Block diagram of mixed control: PID in charge, droop in discharge. Current limits are coming from control in Fig. 1.44.

Fig. 1.51 shows mixed-control simulations profiles.

Both actions are active as soon as enough ESS power and current are available; ESS current I_a, as previously, is dynamically adjusted and limited at I_{amax} and by p_{amax} according to Fig. 1.44 diagram.

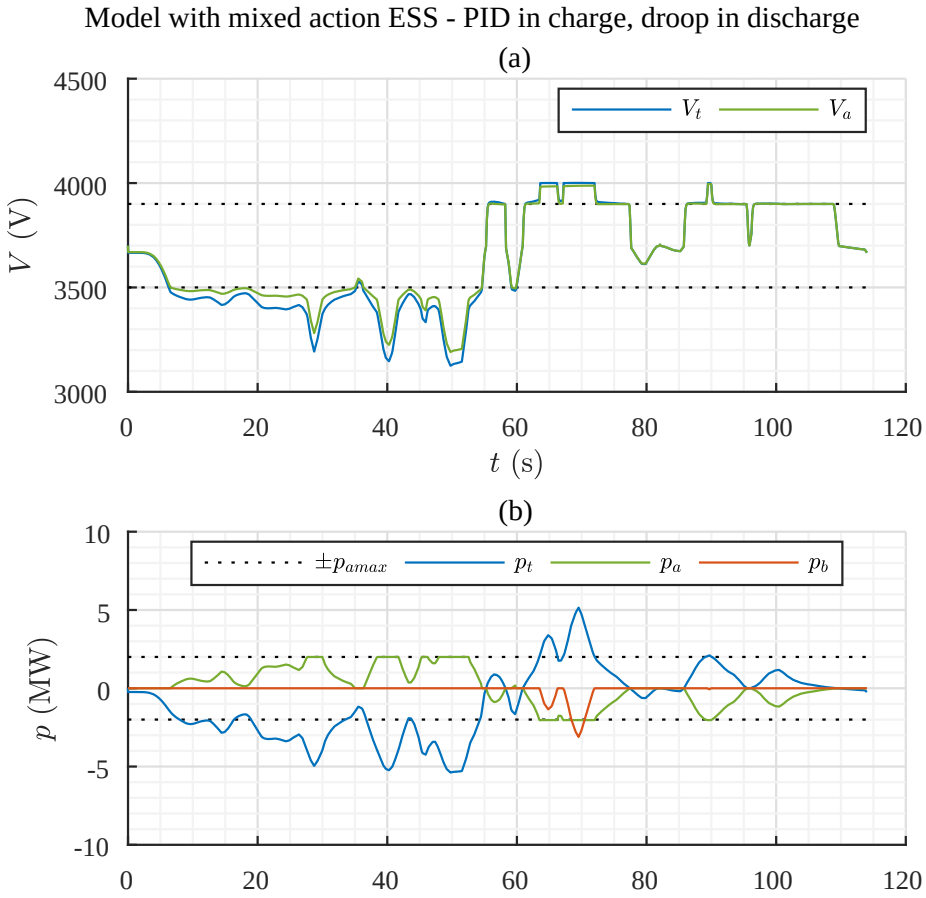

Figure 1.51: Simulation results with mixed action ESS - PID in charge, droop in discharge (Fig. 1.50) . (a) Train voltage profile V_t and catenary voltage at ESS terminals V_a vs. time t. (b) Train power profile p_t, rheostatic braking power profile p_b and ESS power profile p_a vs. time t.

Fig. 1.52 shows current profiles and limitation action on ESS.

Numerical results are listed in Tab. 1.22.

In the next section, all data and simulations results will be critically compared and analyzed.

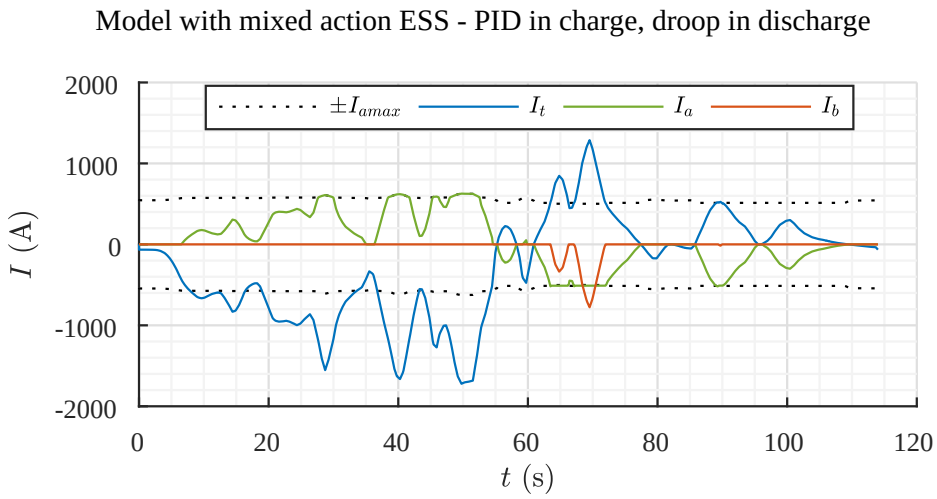

Figure 1.52: Simulation results with mixed action ESS - PID in charge, droop in discharge. Train current profile I_t, braking current profile I_b and ESS current profile I_a vs. time t according to model in Fig. 1.47. ESS current limits are dynamically adjusted by control in Fig. 1.44 because of catenary voltage variations.

Table 1.22: Control optimization results. Cases refer to Fig. 1.39, 1.40 and 1.51. 6-railcars TSR. $\eta_{a_d} = 0.85$, $\eta_{a_c} = 0.8$.

Case	W_b (MJ)	W_{a_d} (MJ)	W_{a_c} (MJ)	$W_{j_{a_d}}$ (MJ)	$W_{j_{a_c}}$ (MJ)	W_{j_c} (MJ)	$W_{j_{a_{pc}}}$ (MJ)
NO ESS	-54.0	0	0	0	0	-25.6	0
Ideal contrtolled ESS	0	73.3	-53.8	-12.9	-10.8	-6.6	-10.8
"Mixed contrtol" ESS	-10.3	54.5	-43.7	-9.6	-8.7	-9.6	-7.3

Case	W_{s_1} (MJ)	W_{s_2} (MJ)	$W_{s_{pc}}$ (MJ)	$\lvert\hat{p_b}\rvert$ (MW)	$\lvert\hat{p_a}\rvert$ (MW)	η (-)	$\Delta\eta\%$ (%)
NO ESS	86.9	94.6	0	5.2	0	0.56	-
Ideal controlled ESS	45.1	43.8	54.0	0	5.1	0.71	+27 %
"Mixed contrtol" ESS	55.0	55.9	36.4	3.1	2.0	0.69	+23 %

1.8.11 Data analysis

Comparing Fig. 1.51 with Fig. 1.48 and Fig 1.49, differences are minimal but substantial:

- droop action let the voltage going a little bit below V_{a_d} during ESS discharge;
- PID control blocks voltage raise precisely at V_{a_c} during ESS charge.

Such effects are much more evident by comparing numerical results of Tab. 1.22 with Tab. 1.19 and 1.21:

- Mixed control efficiency is close to ideal controlled ESS, despite ESS peak power in two cases is slightly different (2 MW for mixed control, up to p_{amax}, 5.1 MW for ideal ESS);
- ESS losses in charge and discharge correspond to minimum values of PID and droop, respectively.

Above results demonstrate the mixed control is actually optimized for catenary voltage stabilization function, due to necessity to execute ESS discharge and charge in different ways:

- voltage boosting does not require an absolute precise control, that is in fact self-defeating; it may use more energy than necessary with no appreciable gains by the efficiency point of view;
- voltage peak limitation, on the other way, must be fully precise, otherwise braking rheostat engaging produces high power losses.

Mixed control approach well demonstrates the necessity in choosing the right control technique depending of the desired effect: in general, the most sophisticated, precise, or robust controller could not be the best ever solutions in terms of equipment efficiency.

Implementing this control is also quite simple, only "classical" PID tuning technique are needed: a further advantage during the project and the commissioning phases.

All above statements compliance initial expectations of Par. 1.6: system developed gives good performance at a reasonable level of complexity, using in a smart way a combination of well known, proved control strategies.

According to (1.60), total losses in mixed control case are bigger than ideal control case, but also energies coming from traditional TSS have grown accordingly (mainly due to braking losses, absent in ideal control case): final ratio is almost the same.

That is mainly caused by restrictions on maximum available ESS power and current: in acceleration, the difference has to be fulfilled by traditional TSS, and such current gives extra losses by passing through the catenary cables; in braking, lack of ESS receptivity causes train rheostats engaging. Anyway, because final efficiency is the same, 2 MW ESS setup appears to be a good compromise between energy recovered and costs; smaller ESS means less investment on equipment, but also more energy wasted in braking and more energy coming from TSS. In practice, a well-tuned mixed control ESS with power limitation at 2 MW has almost the same effect of an ideal controlled ESS with unlimited power capability.

About storage sizing, according to (1.48), $W_{a_{max}}$ is chosen by using ideal controlled ESS results:

$$W_{a_1} = \frac{W_{a_d}}{\eta_{a_d}} = \frac{73.3}{0.85} = 86 \text{ MJ} \longrightarrow W_{a_{max}} = 90 \text{ MJ} \tag{1.67}$$

Respect to mixed control ESS data, using ideal ESS data gives an oversizing ratio of about +33%; that is a reasonable margin to overcome components aging and avoid deep discharge.

In the followings, sizing and economical aspects will be analyzed in detail with some scenarios.

1.9 ESS sizing and payback

This chapter showed functions of braking energy recovery and catenary voltage stabilization on a 3 kV DC regional railway track; the work presented studies about such functionalities, and also proposed controllers approach in order to optimize the needed effect.

Mathematical results and calculations demonstrated consistent gains in terms of energy savings and a general improvement on system global efficiency; besides environmental considerations, better energy utilization goes to a general rationalization of the existing and future electrical substations.

It is now reasonable to quantify how much such equipment can be profitable by the economic point of view; as mentioned in Par. 1.6, this study is not directly supported by infrastructure manager (Ferrovie Nord) nor by rolling stock operator (Trenord); respect to other European projects, in which many players provided detailed financial and economic data, the analysis cannot be obviously so accurate; anyway, as a feasibility study, main target is not a precise budget, rather an expenses check; in other terms, ESS on a 3 kV railway must at least cover costs with reasonable payback time.

Infrastructure cost reduction was a general guideline during the whole study: first step is therefore a quotation of the recovered energy at market price: the simplest but also the most precautionary approach is using a flat tariff, neglecting aspects related to peak shaving or hourly rates; this is a huge simplification but it is also a very useful benchmark: if business cases with flat rates are profitable, any other kind of compensation will generate further gains.

Relevant savings also come from rational utilization of infrastructure: ESS equipment was then placed inside existing TSS, where free spaces are still available, or inside dismissed rooms in passengers stations, yet segregated and close to catenary lines; limit erection costs means a more profitable business plan or a shorter payback time.

No train operator is included in case studies, due to following reasons.

Since several years, after a process of privatization of the national and local railways, infrastructure manager and train operator(s) have been split in different entities. As a result, train operators involvement in infrastructure projects has become difficult: in general, they have a wait-and-see attitude, for some reasons:

- as mentioned before, lack of certified and uniquely calibrated meters makes difficult quantify the effective recovered energy on train side, thus the implementation of any kind of economic compensation;

- agreements to handle practical and economic aspects are needed, bureaucracy issues between different companies have to be discussed and solved;

- some of the heaviest expenses about the mentioned communication links (see Par. 1.6) should be taken by train operators;

- train operators are mainly focused on issues related to index of punctuality, trains failure rate, predictive maintenance etc.

On the other side, infrastructure managers are generally not involved in solving above mentioned train operators issues.

Besides mentioned reasons, it is also quite difficult to quantify train operators benefits coming from an improved catenary power system: as example, savings due to

lower utilization of mechanical brakes, but such target could be tackled with a smarter utilization of electric brakes, thus with no necessity of ESS implementation; a smoother catenary voltage profile could result in less stress for on board converters, but how this aspect is impacting on equipment lifetime is very hard to predict.

Above considerations lead to implement two studies in which infrastructure manager only is considered:

- A brief economic scenario about braking energy savings, based on budgetary quotations and ESS installations inside TSS;
- A study of converter and storage investment balancing about catenary voltage stabilization equipment placed inside existing passengers stations.

First study is necessary to prove the economic convenience of energy savings (at least); then, a more detailed analysis has been done about benefits related to catenary voltage stabilization.

Hopefully, in the near future railway system will be more and more integrated, many players will collaborate actively to achieve a high level of efficiency and performance both in energy management and quality of service.

1.9.1 Brief economic scenario

Consider energy recovery function described in Par. 1.7; after simulations and data analysis, some preliminary economic calculations are presented, in order to investigate about the effective installation of storage equipment on the railway line.

According to Tab. 1.15, net energy recovered by Portichetto ESS from a single train is considered (89 MJ); with an average frequency of about 36 trains per day (official timetable [45]), in a year 13140 trains run the line.

Energy rates for non-domestic utilities depends on contracts with the distributors and also on consumptions; in our case, according to (1.30), every train passage consumes 1450 MJ; in a year, the total expected energy is therefore $1450\ \text{MJ} \cdot 13140 = 19.05 \cdot 10^6$ MJ, corresponding at 5292 MWh.

With such yearly consumptions, Italian Energy Authority indicates an energy cost of 15.92 c€/kWh (Euro-cent per kWh), corresponding at 4.42 c€/MJ [46]. As explained previously, equipment consists of a 2 MW converter and a 90 MJ storage device.

Quotations for both converter and storage are given, considering prices coming from budgetary offers by private companies (with no executive project, a punctual quotation cannot be given).

Converter is valued 225000 €: such cost includes installation and commissioning, but not yearly maintenance, that is valued about 10000 €/year (manpower and spare parts only, extra costs are supposed to be covered by infrastructure budget).

For storage device two alternative solutions have been quoted:

A) Lithium batteries, at a cost of 150000 €;

B) Supercapacitor banks, at a cost of 400000 €.

Lithium batteries have been included as comparison and because of installation inside TSS, where authorized personnel only is admitted and where restrictive fire prescriptions are still adopted.

All prices are about 15% overestimated, including costs for installation, commissioning and some spare parts supplying.

Yearly gainings (YG) are based on energy savings (1.31), energy cost (C_W), and number of trains per year (K):

$$YG = W_{a_c} \eta_{a_d} C_W K \tag{1.68}$$

Generally, in railway field, only long term investments are suitable, because infrastructure has to be efficient for years and no speculative initiatives are allowed: typical target time is about 30 years.

Lithium batteries, considering reasonable charge/discharge rates, can be guaranteed for a lifetime of about 5 years (LT_A=5 years); supercapacitors have an expected lifetime much more longer, around 15 years (LT_B=15 years) with no appreciable degrade.

According to previous considerations, investment time span involves storage equipment replacement, while converter lifetime is guaranteed up to end, with only ordinary maintenance needed.

Being Y=30 years the investment span, batteries and supercapacitors replacements can be calculated:

$$\frac{Y}{LT_A} = 6 \text{ batteries replacements} \tag{1.69}$$

$$\frac{Y}{LT_B} = 2 \text{ supercapacitors replacements.} \tag{1.70}$$

Investment costs IC include converter initial price, converter maintenance for (Y-1) years, and storage device price for number of replacements; all prices are computed and actualized year by year by the CAGR (Compound Annual Growth Rate) formula; considering $t = 0$ investment start and $t = y$ the generic year between zero and Y:

$$IC_y = IC_0 \cdot (CAGR + 1)^y \tag{1.71}$$

About maintenance, a positive CAGR of 0.025 (2.5% per year) is considered; for storage equipment, supposing price reduction through years of batteries and supercapacitors, CAGR is negative: -0.015 (-1.5% per year); such value also includes growing general inflation.

Investment gainings IG include essentially yearly gainings YG, also actualized by CAGR of 0.025:

$$IG = \sum_{y=1}^{Y} YG_1 \cdot (CAGR + 1)^y \tag{1.72}$$

Results are summarized in Tab. 1.23.

Table 1.23: Investment results in Y=30 years for cases . Cases split by storage technology.

Year	Case A) Conv. (k€)	Stor. (k€)	Maint. (k€)	YG (k€)	Case B) Conv. (k€)	Stor. (k€)	Maint. (k€)	YG (k€)
0	225.0	125.0	0.0	0.0	225.0	400.0	0.0	0.0
1			10.3	45.4			10.3	45.4
2			10.5	46.5			10.5	46.5
3			10.8	47.7			10.8	47.7
4			11.0	48.8			11.0	48.8
5		115.9	11.3	50.1			11.3	50.1
6			11.6	51.3			11.6	51.3
7			11.9	52.6			11.9	52.6
8			12.2	53.9			12.2	53.9
9			12.5	55.3			12.5	55.3
10		107.5	12.8	56.7			12.8	56.7
11			13.1	58.1			13.1	58.1
12			13.4	59.5			13.4	59.5
13			13.8	61.0			13.8	61.0
14			14.1	62.5			14.1	62.5
15		99.6	14.5	64.1		318.9	14.5	64.1
16			14.8	65.7			14.8	65.7
17			15.2	67.3			15.2	67.3
18			15.6	69.0			15.6	69.0
19			16.0	70.7			16.0	70.7
20		92.4	16.4	72.5			16.4	72.5
21			16.8	74.3			16.8	74.3
22			17.2	76.2			17.2	76.2
23			17.6	78.1			17.6	78.1
24			18.1	80.0			18.1	80.0
25		85.7	18.5	82.0			18.5	82.0
26			19.0	84.1			19.0	84.1
27			19.5	86.2			19.5	86.2
28			20.0	88.4			20.0	88.4
29			20.5	90.6			20.5	90.6
30			0.0	92.8			0.0	92.8
Total	225.0	626.1	429.0	1991.5	225.0	718.9	429.0	1991.5
IB				711.4				618.6

Investment balances IB are:

$$\mathrm{IB_A} = \mathrm{IG} - \mathrm{IC_A} = 711400 \text{ €} \tag{1.73}$$

$$\mathrm{IB_B} = \mathrm{IG} - \mathrm{IC_B} = 618600 \text{ €} \tag{1.74}$$

ESS installation on a railway line seems feasible and convenient by the energetic and economic point of view: calculations show a concrete investment return for both solutions. Solution (A) seems to be more convenient than (B), but some considerations are necessary:

- investment calculations do not consider equipment de-commissioning costs and storage system disposal; because lithium batteries replacements are triple respect to supercapacitors, such costs could be relevant;

- lithium batteries chemicals are more polluting than supercapacitors and more difficult to recycle; in the actual green economy scenario, supercapacitors are generally most sustainable than batteries;

- investment calculations do not consider loss of gainings due to equipment out of service for de-commissioning; once again, the least replacements take place, the most on duty equipment is profitable;

- as previously stated, batteries (and lithium in particular) are subjected to concrete fire risks; safety costs and risk evaluations are supposed to be higher respect to supercapacitors.

Summarizing, investment (A) is more convenient but it is also less "green" and implies a wider number of interventions for equipment replacement, disposal, recycling etc.; solution (B) is expected to be less invasive and more sustainable, and only a little less profitable (-11%).

Due to all considerations and analysis above, supercapacitors have been chosen; preponderant reason is anyway related to fire risks: batteries have been widely used in ESS railway applications since several years [47, 48], but always into TSS, segregated and far from passengers.

In the study, ESS in stand alone configuration are supposed to be installed into existing passengers stations, and travelers safety must be anytime guaranteed; moreover, even if less profitable, also supercapacitor solution as an investment return, so implementation can be justified by the economic point of view.

Better ESS solution is the one than can match a good recovery, reasonable costs (present and future) and both adequate levels of sustainability and safety.

About equipment sizing, converter rated power and storage device capacity, some evaluations are performed in next session: ideally, a huge ESS can increase as maximum energy savings and maximize system efficiency due to best recovery, but such benefits cannot compensate excessive equipment costs, so investment will not be profitable.

Also in such case, a trade off between performances and costs is necessary.

1.9.2 Converter and storage investment balancing

Previous section focused on payback about braking energy only, as a part of a wider work about 3 kV DC railways recovery system [36]. In this section, model will be upgraded considering effects of catenary voltage stabilization.

To evaluate such aspects, mixed control ESS simulations have been repeated as previously, varying ESS instantaneous maximum power (p_{amax}) from 1 MW to 6 MW. Four cases have been created, whose benchmark is number 2: sizing is the same used

to analyze energy recovery payback. Hopefully, case 2 will be the most convenient also by the investment point of view.

According to simulations, storage has been sized as previously, using (1.48): the same oversizing ratio (about +33 %) has been considered; sizing cases are:

$$1)\ W_{a_1} = \frac{W_{a_d}}{\eta_{a_d}} = \frac{36.6}{0.85} = 43 \text{ MJ} \xrightarrow{+33\ \%} W_{a_{max}} = 60 \text{ MJ} \tag{1.75}$$

$$2)\ W_{a_1} = \frac{W_{a_d}}{\eta_{a_d}} = \frac{54.5}{0.85} = 64 \text{ MJ} \xrightarrow{+33\ \%} W_{a_{max}} = 90 \text{ MJ} \tag{1.76}$$

$$3)\ W_{a_1} = \frac{W_{a_d}}{\eta_{a_d}} = \frac{62.0}{0.85} = 73 \text{ MJ} \xrightarrow{+33\ \%} W_{a_{max}} = 100 \text{ MJ} \tag{1.77}$$

$$4)\ W_{a_1} = \frac{W_{a_d}}{\eta_{a_d}} = \frac{62.0}{0.85} = 73 \text{ MJ} \xrightarrow{+33\ \%} W_{a_{max}} = 100 \text{ MJ} \tag{1.78}$$

Simulations results according to sizing listed above are presented in Tab. 1.24. Case 3) and 4) have same sizing due to equal energy discharged W_{a_d}.

Table 1.24: Power and energy results for equipment sizing investment. Cases refer to mixed control with ESS split by maximum power p_{amax}. 6-railcars TSR. $\eta_{a_d} = 0.85$, $\eta_{a_c} = 0.8$.

Case	W_b (MJ)	W_{a_d} (MJ)	W_{a_c} (MJ)	$W_{j_{a_d}}$ (MJ)	$W_{j_{a_c}}$ (MJ)	W_{j_c} (MJ)	$W_{j_{a_{pc}}}$ (MJ)
1)	-23.6	36.6	-30.4	-6.5	-6.1	-14.3	-4.7
2)	-10.3	54.5	-43.7	-9.6	-8.7	-9.6	-7.3
3)	-0.1	62.0	-52.6	-10.9	-10.5	-8.0	-7.7
4)	0	62.0	-53.8	-10.9	-10.8	-8.1	-7.5

Case	W_{s_1} (MJ)	W_{s_2} (MJ)	$W_{s_{pc}}$ (MJ)	$\lvert\hat{p_b}\rvert$ (MW)	$\lvert\hat{p_a}\rvert$ (MW)	η (-)	$\Delta\eta\%$ (%)
1)	65.2	68.3	23.5	4.1	1.0	0.65	-6 %
2)	55.0	55.9	36.4	3.1	2.0	0.69	-
3)	50.9	50.9	38.5	1.1	4.0	0.73	+6 %
4)	50.9	50.9	37.3	1.4	5.1	0.73	+6 %

The same yearly scenario used in Par. 1.9.1 has been used, in order to compare results from two different analysis.

Also the non-domestic utilities energy cost (C_W) by Italian Energy Authority [49] is the same (gross price of 15.92 c€/kWh, equal to 4.42 c€/MJ).

Budgetary quotations for ESS converters (split by power) and storages (split by capacity) are reported in Tab. 1.25.

As mentioned, private companies provided budgetary quotations only because an executive project is not purpose of this work.

A 2 MW converter is still valued 225000 € (as previously), while for bigger ones price per Megawatt is reduced a little because of lower impact of fixed costs (project, engineering, testing and so on); on the other side, a 1 MW unit has a cost per Megawatt a little higher, for the opposite reason. Yearly maintenance costs are the same as previously (10000 €/year). The same actualization ratings and the same computation formula (CAGR) have been used.

Table 1.25: ESS converters and storage devices budgetary prices according to cases in Tab. 1.24.

Converter size (MW)	Converter price (€)	Storage size (MJ)	Storage price (€)
1) $p_{amax} = 1$	150000	$W_{a_{max}} = 60$	305000
2) $p_{amax} = 2$	225000	$W_{a_{max}} = 90$	400000
3) $p_{amax} = 4$	375000	$W_{a_{max}} = 100$	425000
4) $p_{amax} = 6$	450000	$W_{a_{max}} = 100$	425000

About storage device, according to analysis in Par. 1.9.1, lithium batteries have been excluded: installation constraints has to be considered: ESS is supposed to be placed into passenger stations, and not anymore into TSS.

Equipment will be fully segregated but passengers will be close to it, in the same building. To avoid as much as possible fire risk [50], supercapacitors have been preferred.

Apart safety considerations, in these years, nano-technology has been improved [51], supercapacitors are competitive against lithium batteries for railway duties.

In addition, the state of charge (SOC) can be easier estimated by measuring voltage (V_b in the specific case) and knowing the structure of the cell [52, 53]. Besides above mentioned considerations, supercapacitor technology has been preferred also for longer expected system durability (15 years, the same as Par. 1.9.1), so less replacements during investment span.

Yearly gainings for this second analysis are calculated as difference between TSS energy with and without ESS; this includes post-charge energy.

Case 2 ($p_{amax} = 2$ MW) is used as example:

$$\mathrm{YG} = \Big[\overbrace{(W_{s1} + W_{s2})}^{\text{NO ESS}} - \overbrace{(W_{s1} + W_{s2} + W_{s_{pc}})}^{\text{case 2}}\Big]\mathrm{C_W K} \tag{1.79}$$

Revenues are given by ESS savings and by lower TSS energy respect to NO ESS case (Tab. 1.19). As mentioned in Par. 1.7, multiple trains effect is not detailed in this feasibility study, as it would require a wider statistical basis and mathematical approach [54]. Same calculations of (1.70), (1.71), (1.72) and (1.73) are performed for the four cases: results are shown in Tab. 1.26 and Tab. 1.27. Comparing Tab. 1.26 and 1.27 with Tab. 1.23, results are slightly different: with catenary voltage stabilization action, investment balance is never profitable; the result is anyway expected, if considering the global ESS cycle:

- with energy recovery approach, basically only braking energy is re-injected into catenary, so ESS does not need to be post-charged at every cycle; the result is that the most energy is recovered, the most gainings are high, no matter catenary voltage profile during train accelerations;

- with catenary voltage support, as seen by simulations, power is injected to avoid excessive voltage drop; it happens ESS discharged energy is more than braking recovery; post-charge is necessary at every cycle and such quantity goes to reduce the amount of total saved energy, and gainings are modest.

Table 1.26: Investment results in Y=30 years with catenary voltage stabilization. Cases 1) and 2) of Tab. 1.24.

Year	Case 1) Conv. (k€)	Stor. (k€)	Maint. (k€)	YG (k€)	Case 2) Conv. (k€)	Stor. (k€)	Maint. (k€)	YG (k€)
0	150.0	305.0	0.0	0.0	225.0	400.0	0.0	0.0
1			10.3	14.6			10.3	20.4
2			10.5	15.0			10.5	20.9
3			10.8	15.3			10.8	21.4
4			11.0	15.7			11.0	21.9
5			11.3	16.1			11.3	22.5
6			11.6	16.5			11.6	23.0
7			11.9	16.9			11.9	23.6
8			12.2	17.3			12.2	24.2
9			12.5	17.8			12.5	24.8
10			12.8	18.2			12.8	25.4
11			13.1	18.7			13.1	26.1
12			13.4	19.1			13.4	26.7
13			13.8	19.6			13.8	27.4
14			14.1	20.1			14.1	28.1
15		243.1	14.5	20.6		318.9	14.5	28.8
16			14.8	21.1			14.8	29.5
17			15.2	21.7			15.2	30.2
18			15.6	22.2			15.6	31.0
19			16.0	22.8			16.0	31.8
20			16.4	23.3			16.4	32.6
21			16.8	23.9			16.8	33.4
22			17.2	24.5			17.2	34.2
23			17.6	25.1			17.6	35.1
24			18.1	25.7			18.1	35.9
25			18.5	26.4			18.5	36.8
26			19.0	27.1			19.0	37.8
27			19.5	27.7			19.5	38.7
28			20.0	28.4			20.0	39.7
29			20.5	29.1			20.5	40.7
30			0.0	29.9			0.0	41.7
Total	150.0	548.1	429.0	640.6	225.0	718.9	429.0	894.3
IB				-486.5				-478.6

Above considerations goes to an important result: ESS functions must be foreseen according to expected targets: a monetary payback can result from braking energy recovery only.

The effective gain, by placing a stand-alone ESS on 3 kV railway with the purpose of catenary voltage stabilization, is the possibility to locally empower the grid without

Table 1.27: Investment results in Y=30 years with catenary voltage stabilization. Cases 3) and 4) of Tab. 1.24.

Year	Case 3) Conv. (k€)	Stor. (k€)	Maint. (k€)	YG_2 (k€)	Case 4) Conv. (k€)	Stor. (k€)	Maint. (k€)	YG_2 (k€)
0	375.0	425.0	0.0	0.0	450.0	425.0	0.0	0.0
1			10.3	24.5			10.3	25.3
2			10.5	25.2			10.5	25.9
3			10.8	25.8			10.8	26.5
4			11.0	26.4			11.0	27.2
5			11.3	27.1			11.3	27.9
6			11.6	27.8			11.6	28.6
7			11.9	28.5			11.9	29.3
8			12.2	29.2			12.2	30.0
9			12.5	29.9			12.5	30.8
10			12.8	30.6			12.8	31.5
11			13.1	31.4			13.1	32.3
12			13.4	32.2			13.4	33.1
13			13.8	33.0			13.8	34.0
14			14.1	33.8			14.1	34.8
15		338.8	14.5	34.7		338.8	14.5	35.7
16			14.8	35.5			14.8	36.6
17			15.2	36.4			15.2	37.5
18			15.6	37.3			15.6	38.4
19			16.0	38.3			16.0	39.4
20			16.4	39.2			16.4	40.4
21			16.8	40.2			16.8	41.4
22			17.2	41.2			17.2	42.4
23			17.6	42.2			17.6	43.5
24			18.1	43.3			18.1	44.6
25			18.5	44.4			18.5	45.7
26			19.0	45.5			19.0	46.8
27			19.5	46.6			19.5	48.0
28			20.0	47.8			20.0	49.2
29			20.5	49.0			20.5	50.4
30			0.0	50.2			0.0	51.7
Total	375.0	763.8	429.0	1077.3	450.0	763.8	429.0	1108.7
IB				-490.5				-534.1

installing a full-scale TSS. In practice, a well sited and properly tuned ESS can keep energy at low losses when line is empty and inject it to shave train power peaks; braking energy recovery lets to further increase system global efficiency.

The effect is like a "virtual TSS".

Considering traditional TSS costs (about 3 Mil€ turnkey), investing on ESS be-

comes interesting, especially in areas where no AC power is easily available or erection is difficult due to high urbanization around the line. Finding a general trade-off between equipment sizing and investment is complex and it is not part of this study; about the specific case, looking at Tab. 1.26, case 1) seems to be the one that minimizes financial losses at the end of the target period: in other words, being TSS cost almost constant because of railway standardization, the optimal ESS is the one that has a reasonable cost and guarantees the minimum results in terms of performances. Fig. 1.53 shows simulation results of case 1): catenary voltage reaches many times 3000 V (very minimum lower threshold in normal conditions) while train rheostats are engaged almost continuously during braking.

Effect of such a small equipment on catenary voltage are negligible, practical gains does not justify equipment installation.

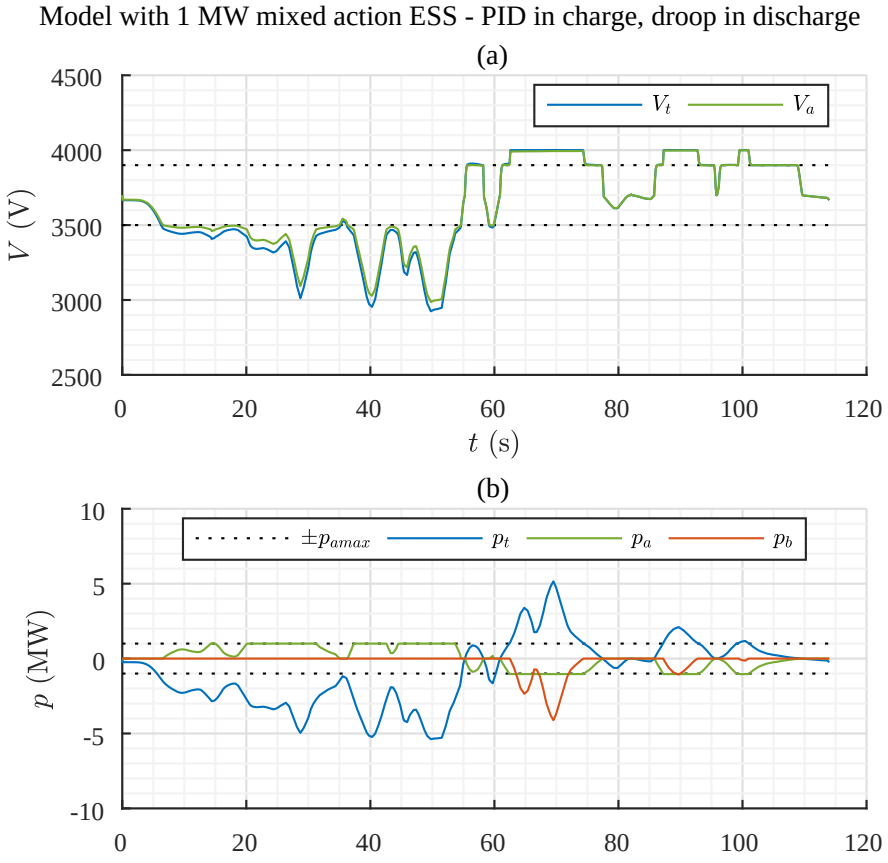

Figure 1.53: Simulation results of case 1) (1 MW/60 MJ equipment) with mixed action ESS - PID in charge, droop in discharge (Fig. 1.50) . (a) Train voltage profile V_t and catenary voltage at ESS terminals V_a vs. time t. (b) Train power profile p_t, rheostatic braking power profile p_b and ESS power profile p_a vs. time t.

Nevertheless case 1) is the least "lossy" by the investment point of view, it is far to be optimal in terms of performances.

Case 2) has been treated as benchmark in the study, it is the second in terms of investment losses, and simulations results are definitely better than case 1): comparing Fig. 1.39 with Fig. 1.51, the 2 MW/90 MJ ESS keeps all the time catenary voltage above 3100 V; it well works like a TSS, at about one fifth of the initial TSS investment

(625000 €).

Looking for performance improvements, in Fig. 1.54, simulations results of case 4) are shown.

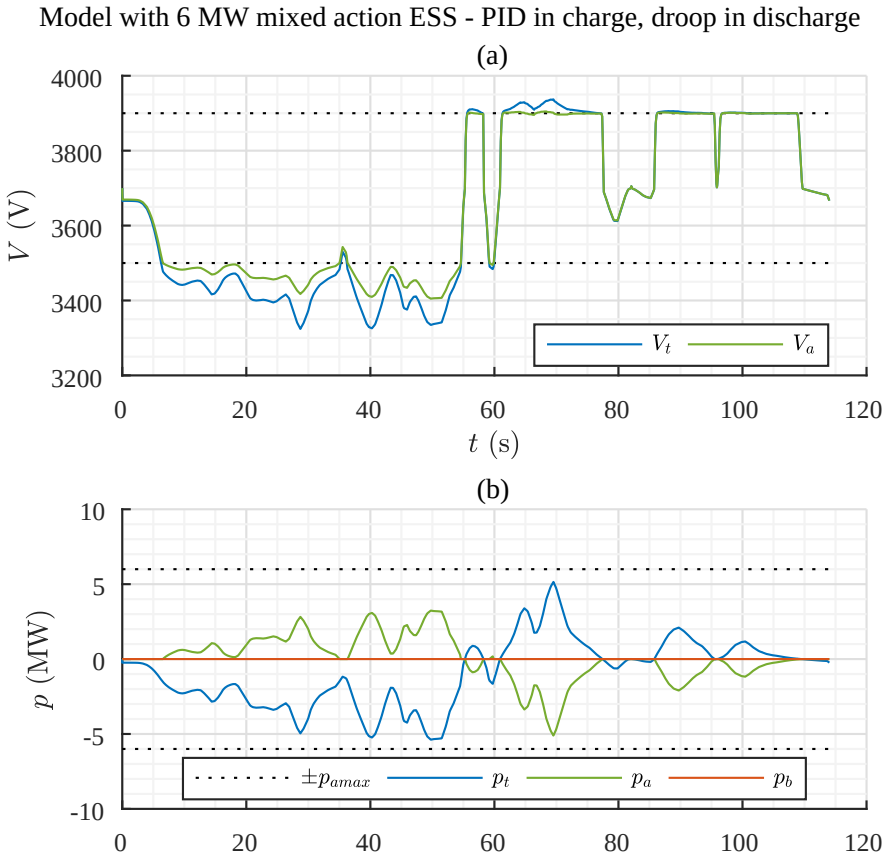

Figure 1.54: Simulation results of case 4) (6 MW/100 MJ equipment) with mixed action ESS - PID in charge, droop in discharge (Fig. 1.50) . (a) Train voltage profile V_t and catenary voltage at ESS terminals V_a vs. time t. (b) Train power profile p_t, rheostatic braking power profile p_b and ESS power profile p_a vs. time t.

Comparing Fig. 1.51 with Fig. 1.54, results in terms of catenary voltage profile are pretty similar: lower values are still around 3200-3400 V, definitely above minimum threshold in normal conditions; braking rheostats are never engaged; in case 2) rheostats are engaged only a few seconds and energy loss is minimum.

Small difference of performance does not compensate the gap of equipment cost.

Same effects on catenary voltage can be observed in Fig. 1.55, in which simulation of case 3) is shown.

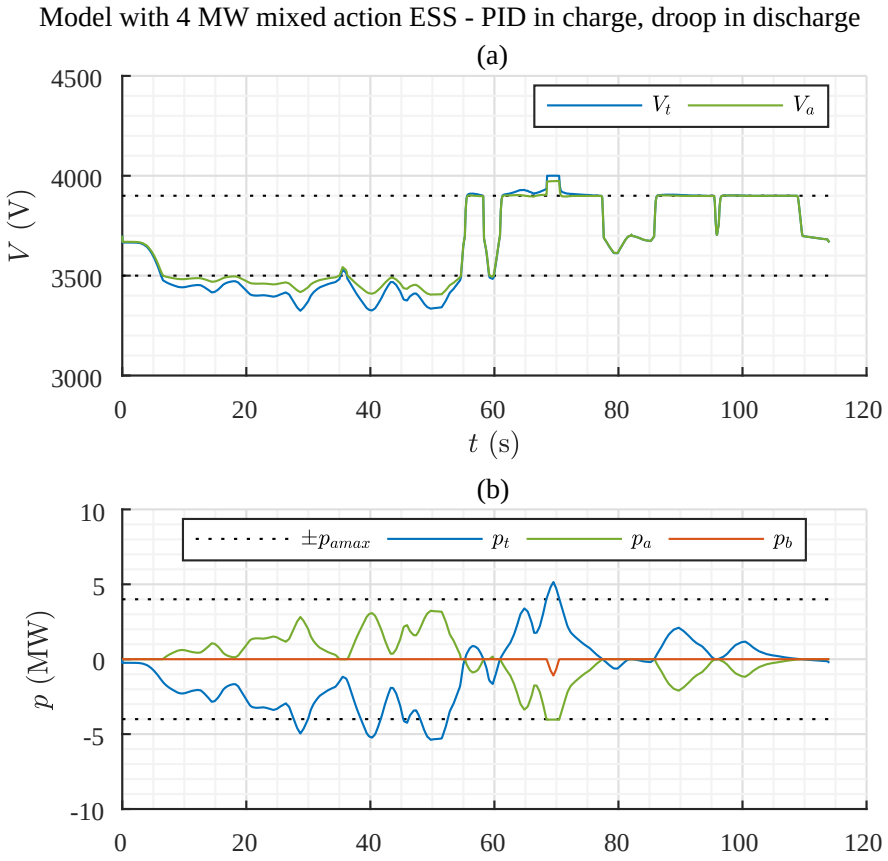

Figure 1.55: Simulation results of case 3) (4 MW/100 MJ equipment) with mixed action ESS - PID in charge, droop in discharge (Fig. 1.50) . (a) Train voltage profile V_t and catenary voltage at ESS terminals V_a vs. time t. (b) Train power profile p_t, rheostatic braking power profile p_b and ESS power profile p_a vs. time t.

Also in this case, extra costs respect to case 2) are not justified.

Investment scenarios and simulations demonstrate that sizing of case 2) is actually the optimal one for the study in object: it has the better cost/benefits ratio in terms of performance and cost.

In general, it has been seen that, besides energy recovery, the better way to invest on ESS systems in railway is comparing equipment effect on catenary voltage respect to a traditional TSS, balancing technical performances and costs.

In addition, stand-alone ESS can provide extra functionalities and services diode rectifiers cannot perform; energy recovery and catenary voltage support occupy only a small rate of the total daily duty.

Extra functionalities can be achieved by engineering equipment like a multiport device; in this way, a stand alone ESS can be used as described in following section.

1.10 ESS extra functionalities

Fig. 1.56(a) and (b) summarize DC-wayside ESS studied in previous sections for a 3 kV DC railway; system can absorb energy during the breaking, and inject it later to support convoy acceleration and stabilize catenary voltage. The power flow becomes bidirectional but confined in the DC section of the network, with no necessity of reversible AC/DC converters at substations.

Train rheostats are still operational, but for backup only; no rheostats waste and reduction on catenary losses goes to a global increase of efficiency.

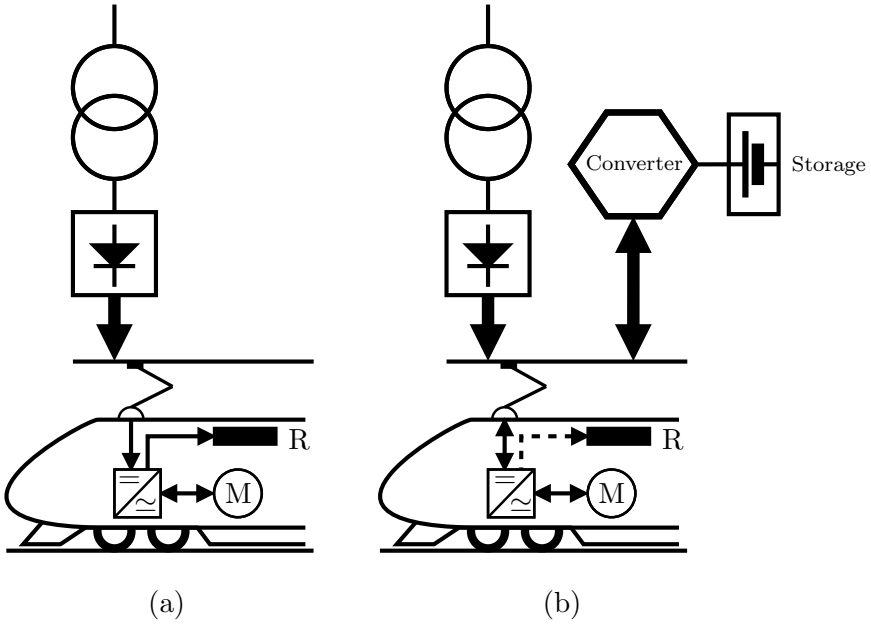

Figure 1.56: ESS utilization in 3 kV DC railway for energy savings.
(a) Conventional system with no recovery.
(b) System with converter and ESS.

Due to wide storage capacity, DC-wayside ESS can be also used for different utilizations, especially when recovery is not taking place. Further ESS missions are not directly based energy efficiency, they focus on global optimization of the rail service. Previous section described two main innovative functions with ESS systems in 3 kV DC railway: braking energy recovery and catenary voltage support; in particular, second function has been performed by using stand-alone equipment, with no necessity of external power supply.

Such condition is an advantage by the point of view of electrification costs and versatility, but it has some drawbacks:

- equipment must generate by catenary its own supply, using the storage when track is out of service (eg. at night during maintenance sessions);

- catenary voltage is slightly different by conventional auxiliary supply levels, and also very disturbed and variable.

In addition, as previous simulations showed, ESS equipment worked e few times per hour only, being in stand-by for most of the day; it could be used to perform extra tasks or useful functionalities, being also much more convenient by the economical point of view.

Above considerations can be easily addressed by implementing the power converter as a multiport.

In the followings, a general concept about multiport converters and ESS will be presented; its application will be seen in particular for the specific case of DC railway field, with some examples and simulations on specific tasks.

Power electronic converter structure will be described briefly in Appendix B, looking for a suitable configuration to guarantee a good level of performance, safety and system scalability.

1.10.1 Multiport concept

Considering a "conventional" ESS (Fig. 1.57), it is composed of two many parts:

- a storage device, of any nature or technology (eg. electrochemical, electrostatic or electromagnetic);
- a power electronics converter, of any kind of structure or control, connected to a single grid (AC or DC);

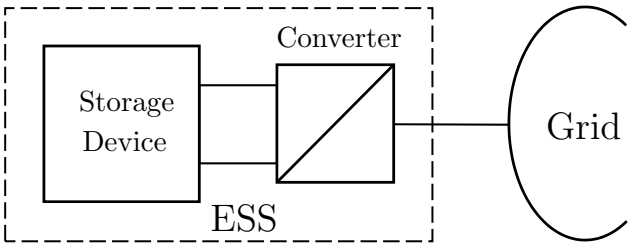

Figure 1.57: Generic "conventional" ESS base structure and network connection.

This structure is usually connected to a single grid by means of an electric port (Fig. 1.19), and it can manage bidirectional power flows. A multiport is a device with several electric ports; in the specific case, each port is basically a front-end converter: this condition lets the system to handle multiple power flows at the same time, at different voltage and frequency (AC and even DC).

Because power flows must be balanced any time, one of more ports are usually connected to storage devices; in this way, further flexibility is provided.

Due to such features, the possibility to distribute energy through different networks/loads at the same time becomes relevant; increasing of energy price and growing attention about efficiency and environment make the multiport ESS an ideal device to save energy normally wasted during a system duty.

Stored energy could be used for different tasks and applications, resulting in a global optimization of the storage usage (and also in a better economic payback).

Following this approach, a multiport based ESS can be shown as in Fig. 1.58: many electric ports (here represented by single lines, for simplicity) can connect several storage modules, different kind of grids (in some cases both DC and AC) and several (active/passive) loads; arrows represent power flows (in most cases bidirectional).

Converter structure can be modular also, to ensure higher scalability and reliability.

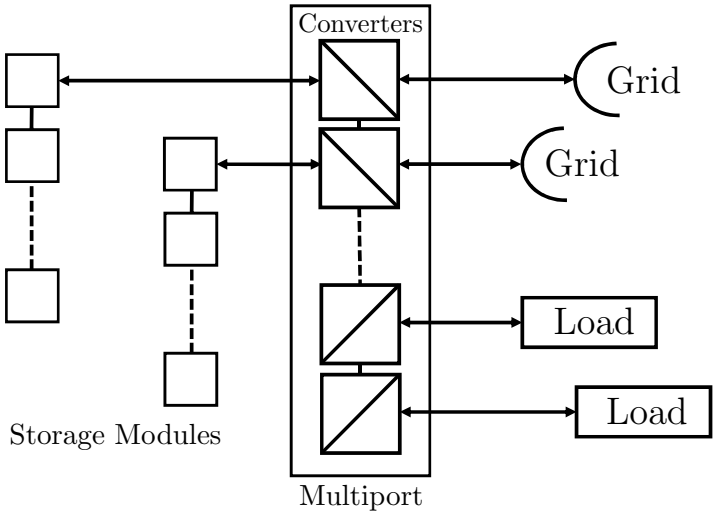

Figure 1.58: Multiport based ESS structure (modular).
Double side arrows on loads means active loads.

Multiport converters are presently in great consideration in many fields of applications, eg. for renewable energy handling [55], hybrid power sources and vehicles [56, 57]. Some interesting applications of modular multiport and ESS are:

- high quality islands supply;
- backup and emergency catenary supply;
- de-icing;

Being such systems at different power and voltage levels, a multiport configuration is a good choice to manage ESS. A brief explanation of missions is given in the followings.

1.10.2 High quality islands supply

Catenary voltage is very disturbed and definitely too high to feed electronics. The multiport converter can be used to lower and stabilize it, in order to generate stable and uninterrupted supplies. As shown in Fig. 1.59, the system generates AC or DC low voltage supplies; it monitors and stabilizes them despite catenary oscillations, using storage elements. Such high quality power feeds auxiliaries circuits into a TSS (Fig. 1.59(a)) and powers the multiport controller itself, especially in case of stand-alone installations along the catenary line (Fig. 1.59(b)).

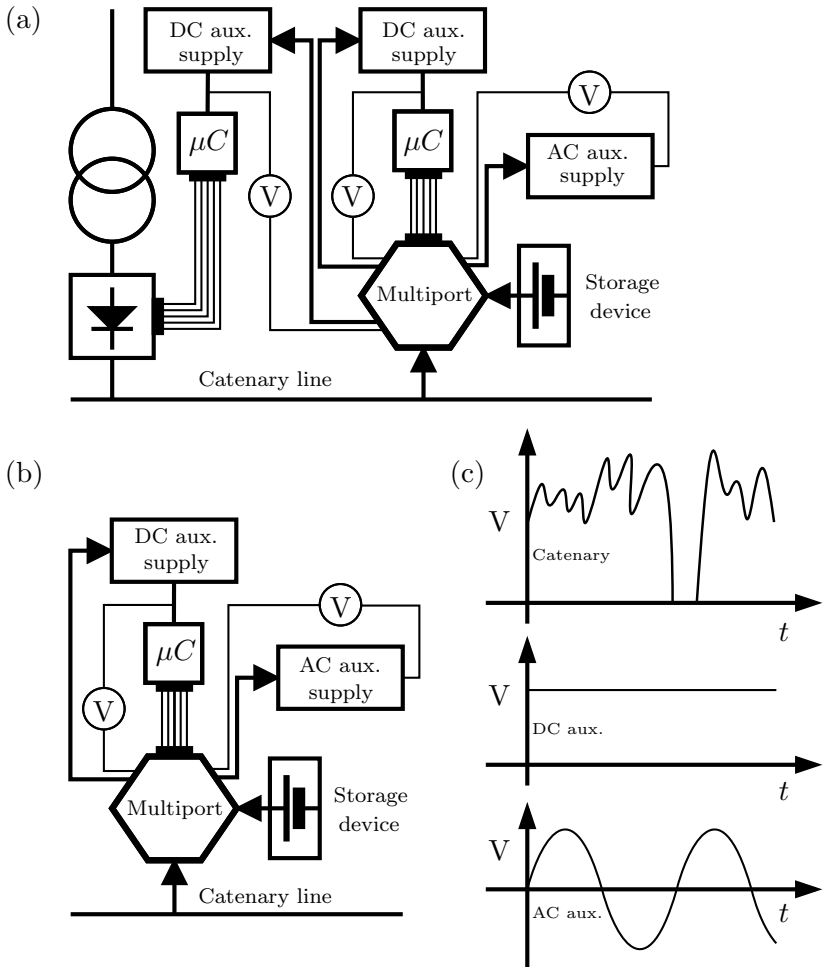

Figure 1.59: High quality DC island supply concept.
(a) Multiport inside a substation.
(b) Stand alone multiport.
(c) Catenary and auxiliary voltages profile (indicative).

Storage also guarantees the so-called black start: system keeps electronics alive and operational as much as possible, even in case of catenary voltage loss (eg. for periodic maintenance on the railway, typically at nights for local and regional lines); in this way, equipment in stand-by mode can be on duty as soon as convoys circulation restarts.

Considering low power required by control electronics compared to the great storage capacity, expected stadn-by autonomy will be very long.

1.10.3 Backup and emergency catenary supply

Due to faults or breakdowns on the railway, trains can lose main power for a long time; on board batteries can't provide full services operations; energy from a wayside storage can give energy for auxiliaries (air conditioning or heating) till the catenary voltage recovery.

As shown in Fig. 1.60, if the section with convoy and multiport is not faulty, it can be segregated from the rest of the grid; the system can monitor DC catenary sections and, in case of voltage loss, can operate as "temporary substation"; maximum load current is limited by the actual state of charge. When voltage in the grid is recovered, catenary sections can be reconnected.

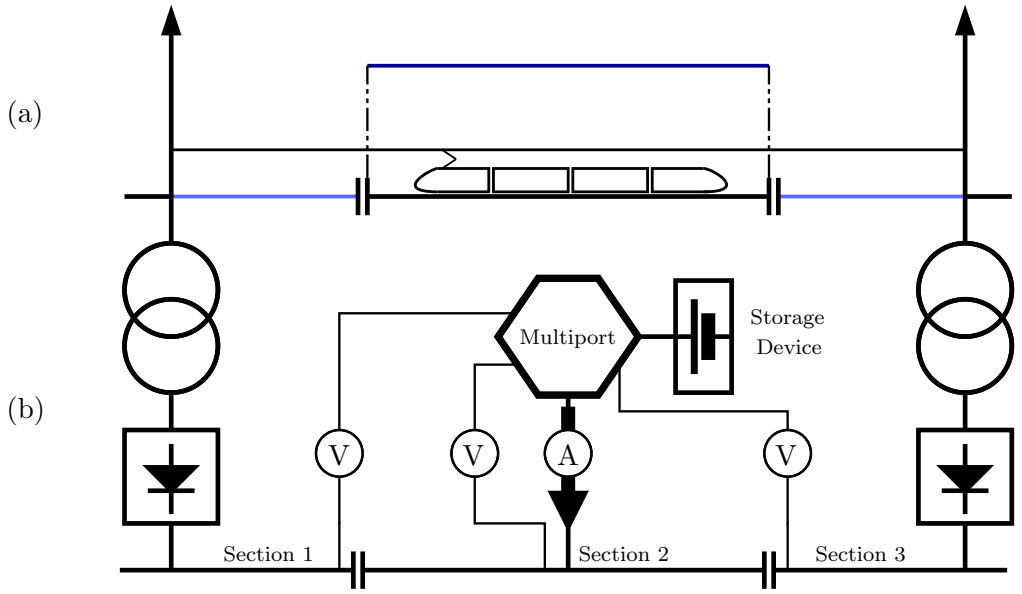

Figure 1.60: Backup and emergency catenary supply concept.
(a) Catenary section on voltage.
(b) Mltiport along catenary sections.

The procedure requires anyway a high level of automation, to disconnect the faulty branch in a short time and activate the ESS; in addition, several measurements, coming from other catenary sections, must be transferred to ESS.

Such action could be interesting into long tunnels, placing a DC-wayside stand-alone ESS inside and automatic disconnectors at both edges; if power is enough, ESS energy could be also used to move the train outside the tunnel (especially if black-out occurs when train is still running and traction power is needed to keep speed only and not to accelerate from standstill).

1.10.4 De-icing

Ice is a serious problem for railway, it can create failures and compromise traffic. Damages can occur in both catenary and rails:

- ice sleeves formed on catenary by cold weather and wind can destroy pantograph shoes by mechanical action (friction or strain) or by electrical sparkling;
- ice can block rail switches, especially during snowfalls.

Only solution against ice is heating: about ice sleeves, apart losses given by trains passage, some rheostats can be connected between catenary and rail to force current circulation; apart safety, such solution is not practical because many losses are given by rheostats themselves and not by the catenary wire, where they are useful for de-icing.

A couple of stand-alone multiport converters can exchange power each other to force current flow through the catenary wire, as shown in Fig. 1.61:

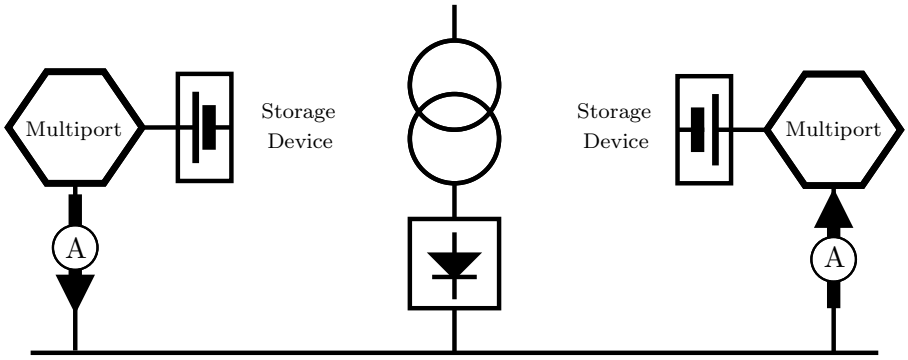

Figure 1.61: Catenary de-icing concept.
Left ESS discharges at high current and right ESS charges to force power flow. TSS provides extra power to compensate catenary losses, so the process can be reversed at the end of the cycle.

Apart from equipment losses, heat is concentrated on catenary, because energy goes from an ESS to another and vice versa; process is basically the same as post-charge described in Par. 1.8.4; in this case, goal is using as much current as possible, and cycling the operation many times, in order to maximize catenary losses.

About switches, in case of ice they can be equipped with heaters: they are rude rheostats supplied in LV for safety reasons; each one consumes about 3 kW, and in some cases power them up is not easy:

- on a remote track (eg. a mountain pass) electrification costs are prohibitive;
- in big stations power access is theoretically easy, but there are hundreds of switches (eg. in Roma Termini, Rome, about 300) and supply all of them at the same time in LV is not banal.

A multiport DC-wayside ESS can spill power from catenary and supply heaters in both cases, because equipment can be sized according to systems needs.

Next subsection provides a brief example of some applications described above by means of a stand-alone multiport simulation.

1.10.5 Multiport simulation

This last subsection shows simulation results on a stand-alone multiport converter, designed to fulfill requirements and perform functions described previously.

Fig. 1.62 shows the hardware concept:

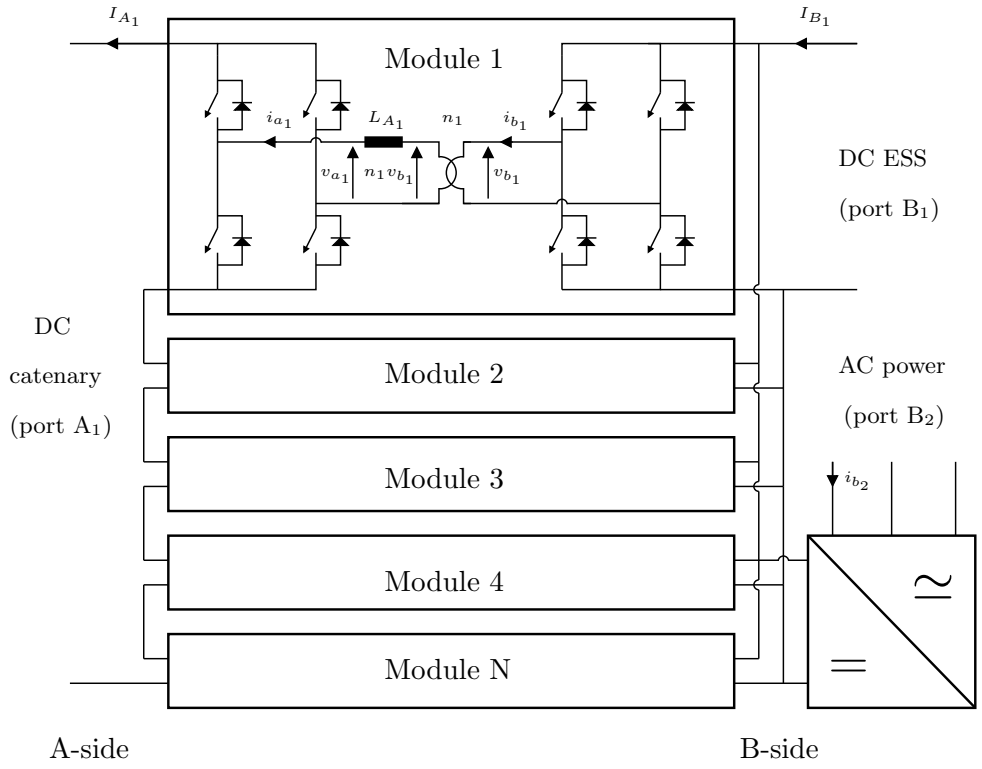

Figure 1.62: Hardware concept of a stand-alone Dual Active Bridge (DAB) modular multiport converter on 3 kV DC railway. Modules are put in series on DC catenary (port A_1), to withstand the voltage level; embedded PETs provide galvanic insulation and voltage scaling; module outputs are all connected in parallel, creating a common link to feed DC storage units (port B_1); AC grid (port B_2) can be connected through an interface converter.

Equipment has the following features, in order to match requirements empathized in previous sections:

- modular structure has been chosen to provide system scalability and achieve a certain level of redundancy;
- basic module layout is composed of a Dual Active Bridge converter (DAB); it includes a Power Electronics Transformer (PET), providing both galvanic insulation for safety and proper voltage scaling to match ESS operative limits; respect to other configurations like NPC (Neutral Point Clamped) or FC (Flying Capacitance), DAB uses less power components;
- A-side ports are connected in series on catenary side, so they can handle high voltages, peaks and sparks; control is designed to share equally total voltage on single modules;

- module outputs are all connected in parallel, creating a common link to feed DC loads (ESS on port B_1); AC power (port B_2) is generated by the same link through an interface converter. This way, power flows on B-side are fully independent.

Theoretical current and voltage waveforms of a single DAB (Module 1 in Fig. B.9) are shown in Fig. 1.63.

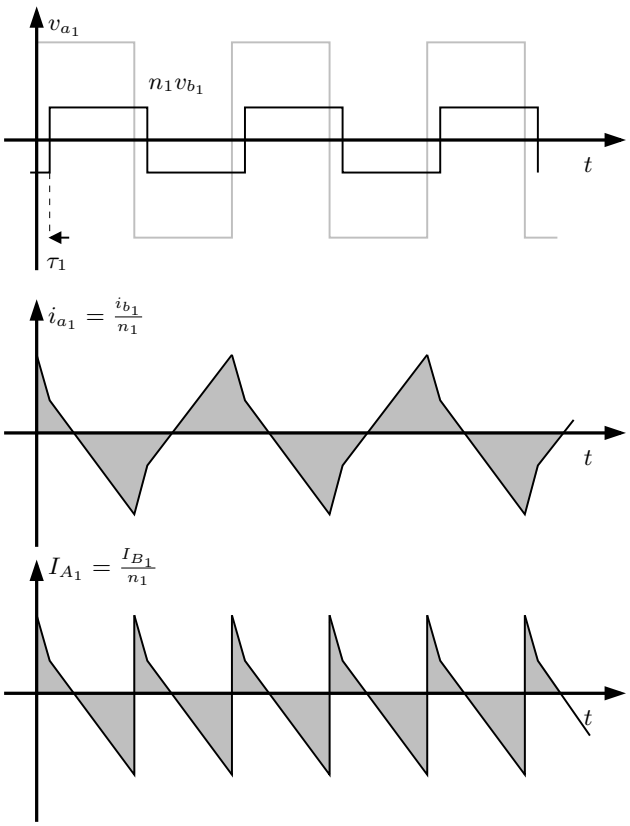

Figure 1.63: Single module DAB converter ideal current and voltage waveforms.

Shift τ_1 between v_{a_1} and $n_1 v_{b_1}$ generates a voltage drop across inductor L_{A_1} that makes alternating currents i_{a_1} i_{b_1} flow in both sides of the transformer. Currents are then rectified (I_{A_1} and I_{B_1}), so they have a strong direct component; the result is an active power transfer through A-side and B-side (more details about DAB converter are given in Appendix B).

Regarding railway field, a similar device has been presented as traction PET in [58]; a 50 kW prototype PET is presently placed as DC-wayside pilot installation on a regional railway in Italy [59]. The multiport shown in Fig. 1.62 and the control in Fig. 1.50 have been modeled together in Matlab/Simulink to be tested. System is connected to catenary line at port A_1; port B_1 exchanges power through a supercapacitor module with an initial voltage of 750 V DC; a DC/AC inverter feeds a three-phase 400 V AC line (port B_2) with a load of about 100 kW (eg. substation auxiliaries and a set of switches heaters).

In the test, a power peak p_t of about 1.30 MW is injected into catenary by a braking train for 3.5 s. System is designed to limit the pantograph voltage V_t at V_{a_c}. Converter

rated power is 2 MW; ESS capacity is limited at a tenth of the optimal size found in Par. 1.9.2 (9 MJ instead of 90) to empathize the variation of V_{B_1}.

Simulation results are shown in Fig. 1.64.

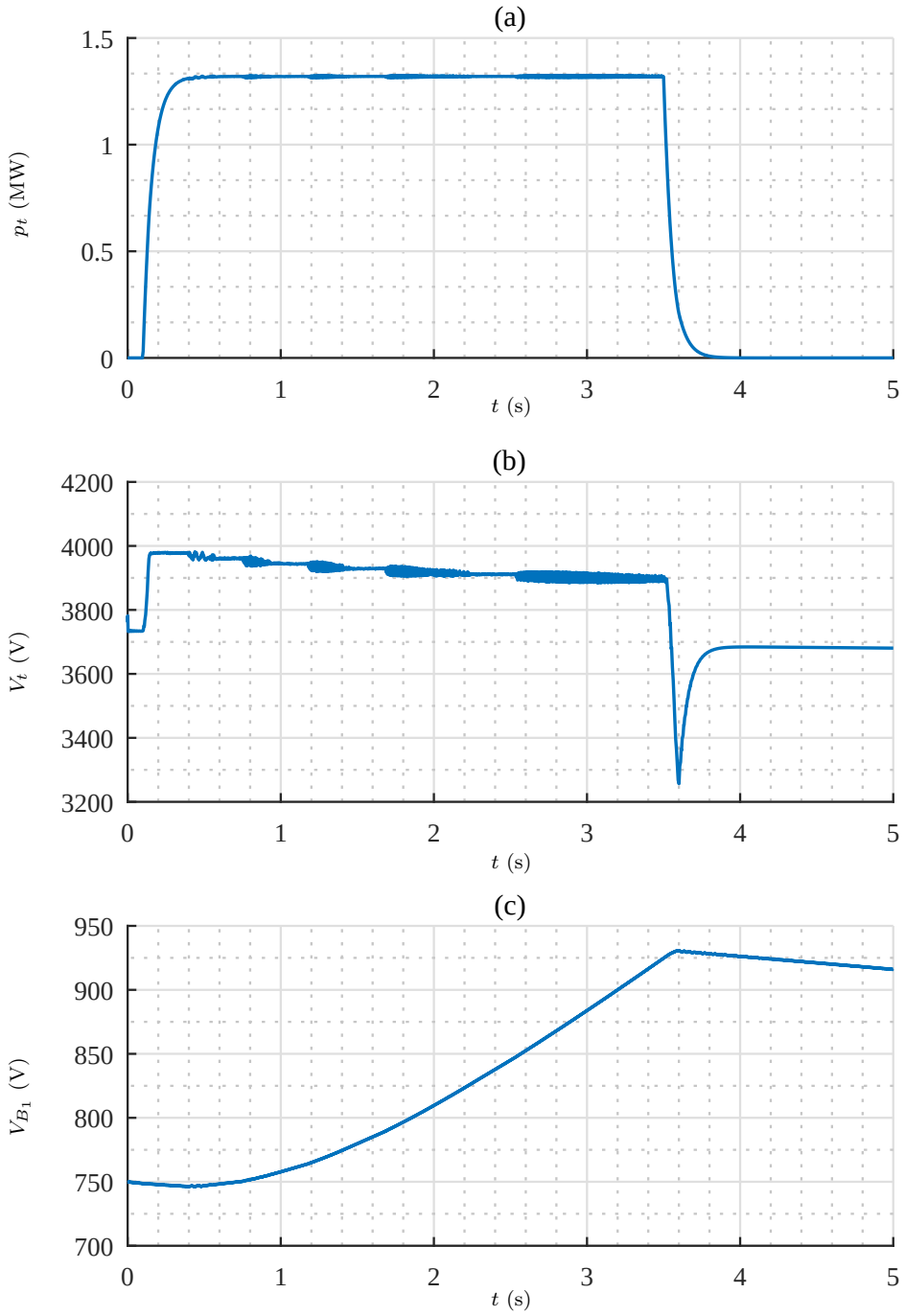

Figure 1.64: Multiport system test results. (a) Train power peak p_t vs. time t. (b) Pantograph voltage profile V_t vs. time t. (c) DC ESS storage module voltage V_{B_1} vs. time t.

As soon as the catenary voltage increases, the converter starts regulating by charging the supercapacitor bank; the voltage at its terminals starts increasing fast: from

750 V DC it reaches almost 930 V DC at the end of the power peak.

Despite the wide variation at its terminals, the DC/AC inverter keeps the voltage at the AC load at rated value. As soon as train power peak ends, the catenary voltage goes under threshold V_{ac} and the charge is stopped; AC power supply is still active. ESS is then discharged slowly by the modest AC load consumption. In Fig. 1.65 multiport currents and voltages are shown.

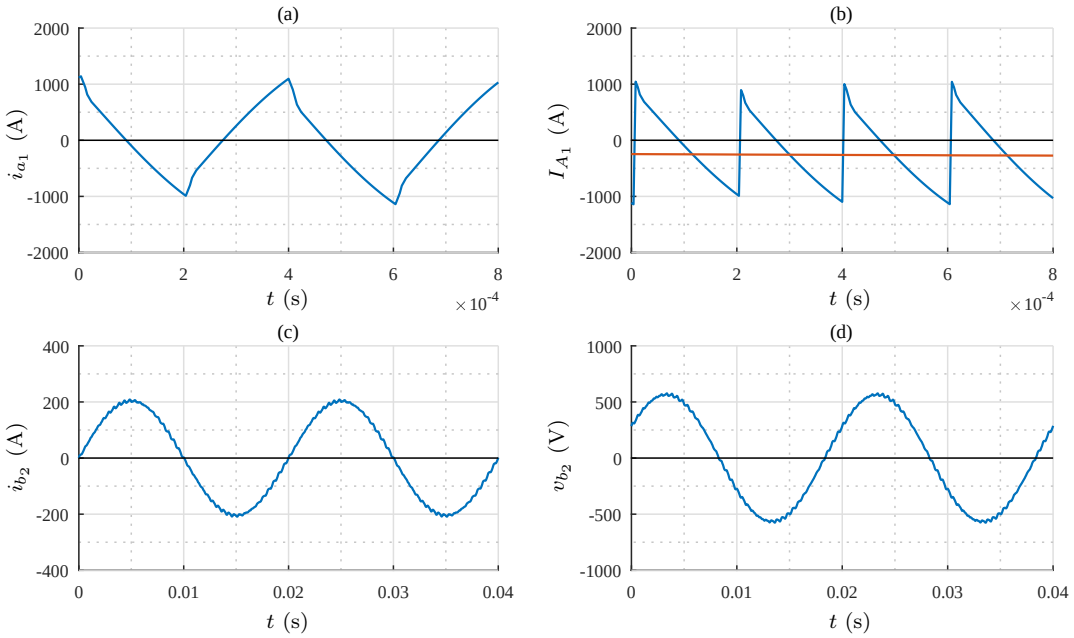

Figure 1.65: Multiport converter test results.
(a) Port A_1 alternating current i_{a_1} vs. time t.
(b) Port A_1 rectified current I_{A_1} (blue) and its direct component (red) vs. time t.
(c) Port B_2 alternating current i_{b_2} vs. time t.
(d) Port B_2 alternating voltage (phase-to-phase) v_{b_2} vs. time t.

AC voltage and current at Port B_2 are stable and well shaped.

High frequency currents of Port A match ideal ones in Fig. 1.63; slopes are a little different due to different phase shift and port voltages amplitude, but shapes are almost the same.

Such test shows a good system response and validates previous considerations about stand-alone ESS and multiport utilization. Results also validate the goodness of ESS equipment modeling in various situations; for long-time simulations (eg. more than 10 seconds) and to evaluate global system response on catenary, model of Fig. 1.43 is definitely satisfactory; for a complete and exhaustive overview of all multiport currents and voltages in a short time (eg. 5 s) a power electronics model like the one in Fig. 1.62 is a better choice.

All studies results are then summarized in following conclusive section.

1.11 Chapter conclusions

This chapter studied innovative solutions for improving performances of regional 3 kV DC railway lines through ESS. Activity has been developed as feasibility analysis for a future executive projects or deeper research activities.

Preliminary calculations gave promising results about savings by recoverable braking energy. A railway grid model was then implemented and several simulations have been performed to confirm initial calculations results.

GPS measurements on the real track increased model characterization; a mechanical train model and a well-tuned ESS control were used to make the system as much as possible accurate.

Modeling focused on methodological approach, in order to perform fast and reliable simulations; respect to more sophisticated projects or industrial solutions [60, 61, 62], easy implementation and fast tuning were preferred.

Simulations about braking recovery with ESS placed into existing TSS provided a good feedback about available energy: it was the first step to introduce such technology on existing lines with minimum impact on infrastructure.

Kinetic energy recovery was aligned to expectations, so it was also used for payback evaluations.

Potential energy case was not satisfactory due to bad substations displacement; then simulations focused on kinetic case as benchmark for further studies.

The study provided indications for converters and storage sizing, to better fit technical and economical feasibility with network optimization. By proper control algorithms, relevant part of the total traction energy given by the substations can be recovered.

Being placed inside TSS, storage systems had limited capability of controlling catenary voltage fluctuations; the second part of the work studied stand-alone ESS effect in stabilizing catenary, increasing both efficiency and energy savings. Stand-alone equipment has been placed into free spaces of a passenger station, keeping infrastructure costs low.

Two kinds of equipment controls were tested: Droop action was more efficient and useful in ESS discharge, PID control was instead the better choice in ESS charge; A mix of two strategies has been then implemented and tested.

Early simulations considered an ideal ESS with unlimited capability; efficiency gain was evident but equipment sizing was economically unacceptable.

Due to several simulation scenarios, ESS converter capability of 2 MW resulted an optimal trafe-off between components sizing, energy savings and efficiency gain.

About storage device, same simulations resulted in an optimal energy sizing of 90 MJ; like other works [59, 63, 64, 65], supercapacitors have been preferred respect to batteries, because of intrinsic safety and expected durability.

About braking energy recovery, a brief economic scenario gave encouraging results in terms of payback time, due to the relevant amount of saved energy.

Regarding catenary voltage support, power injection during train accelerations increased consistently payback time: ESS worked as "stand-alone substation", so economical gainings have been quantified in terms of erection costs of a traditional AC/DC TSS. Also in such case, results were encouraging.

In addition, several ESS extra functionalities have been presented, in order to make ESS installation much more versatile, desirable and convenient for railway manager; in these cases, equipment has to be realized as a (modular) multiport ESS, to handle

several power sources at the same time.

Converter topology choice or practical implementation has not been threated in deep, focusing on control strategies and equivalent effect on the network; anyway, brief implementations of a DAB multiport converter and a storage device have been simulated; results showed the feasibility of described functionalities in terms of hardware.

Despite its relative simplicity, economic scenarios confirmed that optimal trade-off between costs and savings is the key factor to obtain reasonable gainings and justify the investment; when properly sized and placed, stand-alone DC-wayside ESS can be a relevant asset in a regional or local railway, with many trains per day and limited grid receptivity.

As highlighted by other projects, effective energy recovery will be anyway always related to specific project implementation, to be optimized case by case.

Activity resulted in several publications for conferences and magazines as selected parts of available material [35, 36, 66].

Next chapter will study innovative solutions for HVDC transmission systems.

CHAPTER 2

HVDC TRANSMISSION

As mentioned in Introduction, most of HVDC converters worldwide are LCC (Line Commutated Converters) type, based on "old" thyristors; VSC (Voltage Source Converters) type, based on "new" IGBTs are today the most advanced technology available for HVDC systems, due to regulation possibilities (AC voltage and reactive power) and relatively low harmonic impact on the existing network.

HVDC links have been for decades the only way to overpass limits of AC technology in very particular conditions, like sea connections, different frequency standards (eg. 50 Hz to 60 Hz between Paraguay and Brazil) or very long distance transmission lines (see Fig. 2.1).

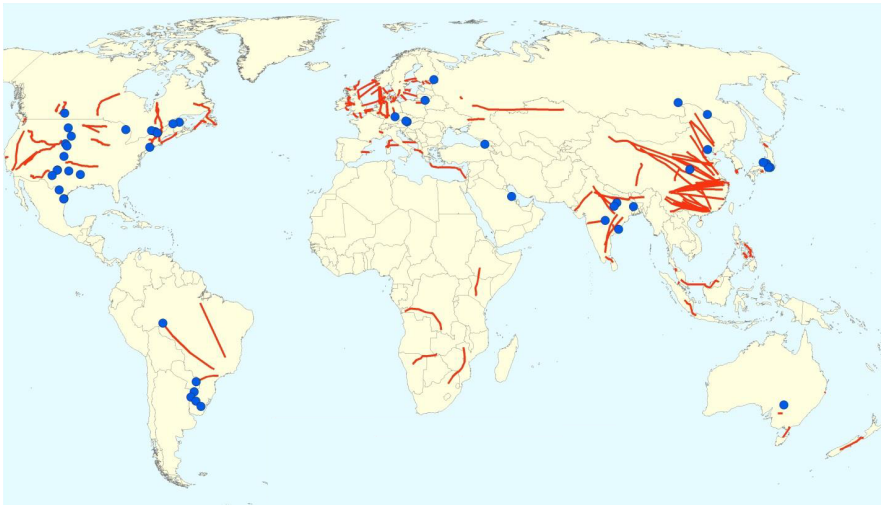

Figure 2.1: Map of HVDC connections worldwide, existing or planned: RED: transmission lines, BLUE: back-to-back stations. (2018. Source: [3]).

In the near future, such systems will also empower and stabilize AC networks of wide geographic areas; European Union is presently carrying on projects in this direction, in collaboration with other countries, as described in following section.

2.1 International scenario: HVDC projects

As one of the leaders in World energy economy, China is proposing since 2016 a HVDC connection with European Union, to transfer Renewable Energy Sources (RES) power between the two continents; presently, three main routes have been identified, preliminary cost-benefit analysis are promising; system will be designed *"in a way to maximize the generation yielding, the trade benefits and the efficiency in operation"*. [3]

Unfortunately, several local conflicts and territorial disputes are still in progress along the planned routes (see Fig. 2.2).

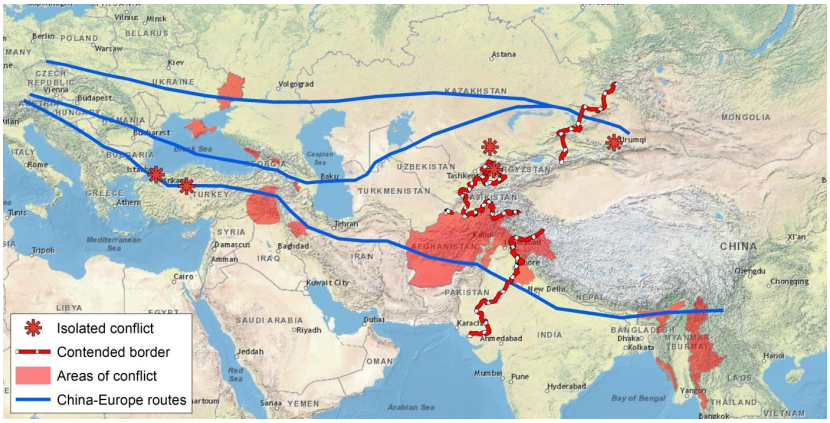

Figure 2.2: Map of China-Europe HVDC routes and conflicts; (2018. Source: [3]).

Prior to tackle technological challenges, political, religious and civil struggles must be resolved.

Besides Europe and China, global trend is increasing interconnections among different AC synchronous areas; due to above mentioned performances, HVDC is the adequate technology for such purposes.

The most ambitious project in such sense is the creation of a worldwide HVDC meshed grid through every AC synchronous areas, to transfer power and realize all ancillary functions a modern grid is going to need (see Fig. 2.3).

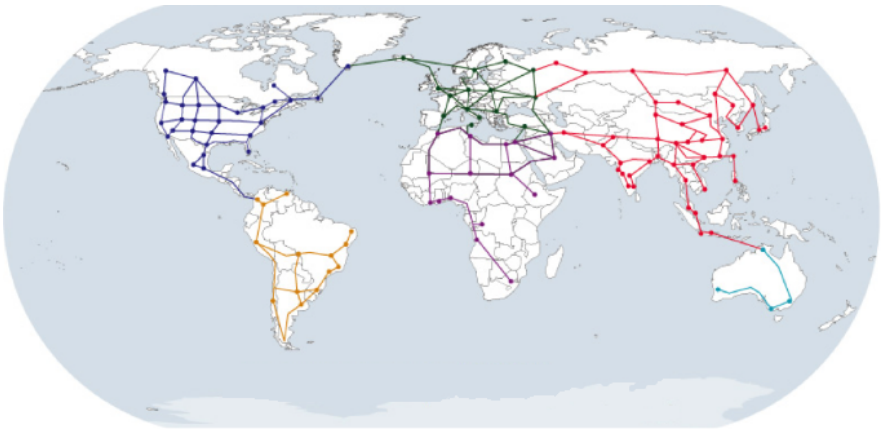

Figure 2.3: Map of expected future worldwide HVDC grid. 2018. Source: Renewable Energy World.

2.2 Local scenario: HVDC in Italy

In Fig. 2.4, a map of actual and future HVDC connections in Europe is shown.

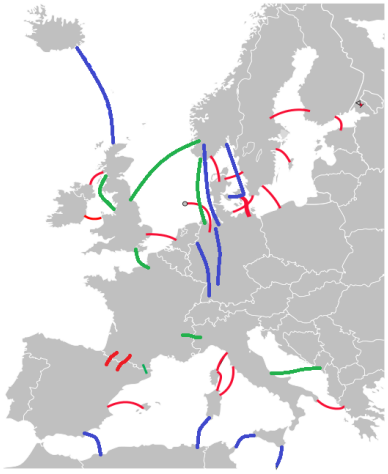

Figure 2.4: Map of HVDC connections in Europe: RED: existing, GREEN: under construction, BLUE: in project. (2018. Source: Wikimedia Commons).

In the European scenario, Italy has a strong tradition and technological background in HVDC technology, due to necessity of connecting Sardinia island to mainland: SACOI (Sardinia-Corsica-Italy) link is operational since 1966 (see Appendix C) and it is going to be completely refurbished and empowered in next years.

In such conditions, HVDC systems are presently one of the most useful solutions to manage RES dispatch, reduce carbon-based power sources and guarantee at the same time an adequate level of energy supply:

"The existing Sardinia-Corsica-Italy link is approaching the end of its lifetime (2023) and, according to the Corsican Energy Plan (PPE), the supply of Corsican load under security conditions could not be possible without the SACOI link. Refurbishment of the link and upgrade of the terminal point in Lucciana will make possible to avoid the urgent installation (by 2023) of about 60 MW of diesel engines and an open cycle power station, mainly necessary for security reasons. Regarding the Sardinian system, taking into account that all the existing power plants are very aged (three main generation poles commissioned between 1986 and 2000), SACOI is essential for guaranteeing Security of Supply and Resilience. Without the SACOI link it will be necessary to refurbish the oldest power plants present in Sardinia, in order to have satisfying performance and availability indexes. At present, any unavailability of the existing SACOI leads to higher needs of resources able to provide the necessary ancillary services in Sardinia". [67]

Other project under development is a HVDC line between Italy and France: the link will empower transmission capacity of about 40%, contributing to the development of European electricity grid [68].

According to Terna spa (Italian TSO) and ENTSO-e (European Network of Transmission System Operators), HVDC are strategically relevant for European network empowering and stabilization [69, 70].

To better understand research activity about HVDC features improvement, some brief informations about state of the art and technology are presented.

2.3 State of the art: HVDC configurations layout

Apart specific converter technology, another important classification about HVDC systems is the type of connection between terminals; fully detailed classification is given in [71], taking into account also environmental and regulatory issues; for this work, two main configuration families are presented:

I) Monopolar;

II) Bipolar.

A simplified schematics of monopolar link is shown in Fig. 2.5.

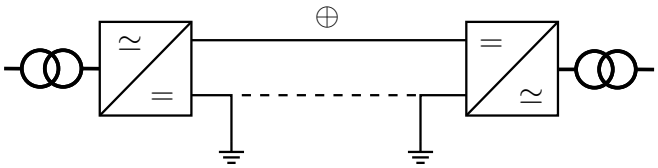

Figure 2.5: Simplified schematics of a monopolar HVDC system.

Main advantage of such solution is that one cable only is strictly necessary to close the circuit: this was the standard for sea connections, in which water is used as returning conductor through electrodes; for land links, ground is sometimes used too [72], but in some cases a second cable (dotted line) must be added.

Monopolar converters are the simplest to implement but, because of unique DC level, reliability is poor due to lack of redundancy.

Limitations in monopolar links are overcame by bipolar converters, whose schematics is shown in Fig. 2.6.

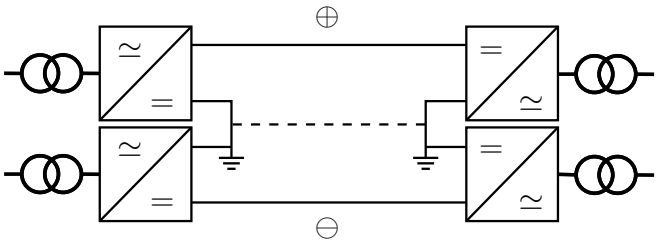

Figure 2.6: Simplified schematics of a bipolar HVDC system.

Two DC voltage levels are generated, usually opposite and symmetric; to be fully independent, each pole has its own power supply and converter. DC voltages are therefore referred to a "neutral" point. Neutral point does not need a cable (dotted line) to close the circuit; when not strictly necessary, it is usually grounded at both sides (in sea links, by means of electrodes).

Nevertheless a higher level of complexity and a greater number of components, main advantage of bipolar solution is the possibility to use half polarity at a time, guaranteeing a higher level of reliability due to intrinsic redundancy.

It is important to note that pole numbers is formally independent by converter structure; as example, a unipolar system could be realized with two converters in cascade (like bipolar) without accessing the neutral point; on the other way, a bipolar system can be realized also with a NPC (Neutral Point Clamped) converter, or with any kind of configuration in which a neutral point is available (see Fig. 2.7).

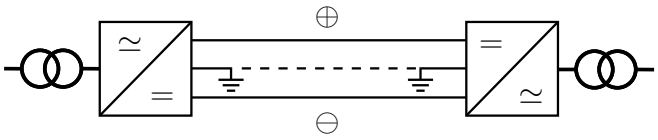

Figure 2.7: Simplified schematics of a NPC bipolar HVDC system.

Such solution is a compromise; system preserves a certain level of control simplicity and multilevel structure limits harmonic content; anyway, no redundancy concept can be investigated.

More complex solutions include a bigger number of modules (and also multiple AC power supplies), as shown in Fig. 2.8. Such configurations are common for very high

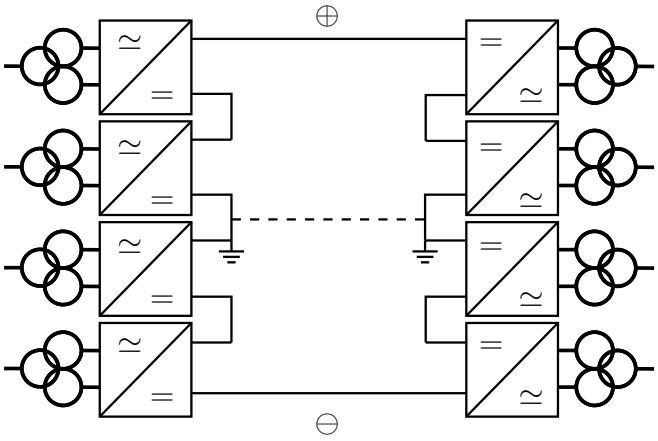

Figure 2.8: Modular HVDC. Converters with multiple AC power supplies and three-windings transformers to increase harmonic cancellation phenomena. Final DC stage is necessarily unipolar or bipolar only.

power HVDC Classic systems (some GW), in which power needs do require a high number of converters and thyristor switching makes necessary harmonic cancellation by using different transformer groups; about HVDC-VSC Light systems (power up to 1 GW), bipolar structure has also become a benchmark for most recent installations (eg. SACOI refurbishment).

Nevertheless converters technology, arrangement and complexity, HVDC power stations are quite similar in terms of global layout, with a series of common assemblies and components.

In this work, NPC-three-level bipolar structure has been chosen to model HVDC-VSC converters used in synthetic inertia simulations; the choice is due to the relative

simplicity of implementation respect to much more sophisticated layouts (like modular HVDC), and also to reduce as much as possible computational burden; however, simulation model resulted satisfactory by the performance point of view, because NPC anyway guarantees a good harmonic behavior and the bipolar configuration.

2.3.1 Power stations layout

In Fig. 2.9, a HVDC monopolar power station layout is shown.

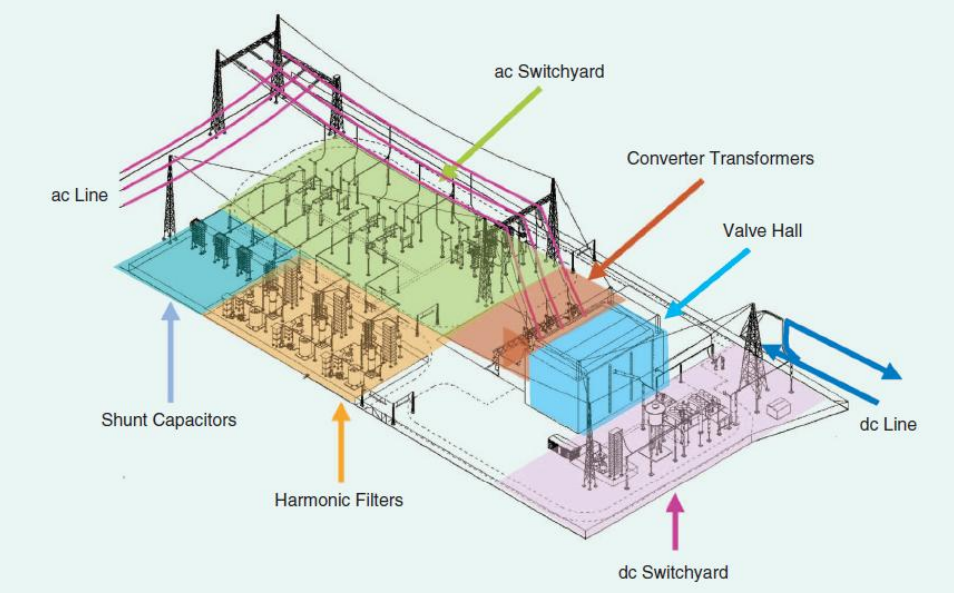

Figure 2.9: Example layout of a monopolar HVDC conversion station. Source: Electrical Power Systems Technology.

In Fig. 2.10, instead, a HVDC bipolar power station layout is shown.

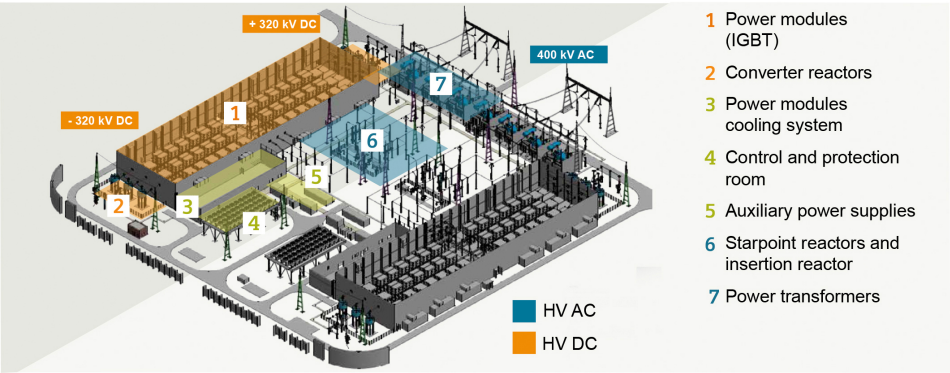

Figure 2.10: Example layout of a bipolar HVDC conversion station (VSC-based). Source: Siemens www.siemens.com/press.

Technology, components, displacement and also power ratings are quite different in two cases, but following assemblies are essential:

a) AC feeder and main AC lines;

b) HV converter transformers;

c) AC-side converter filters and inductors;

d) power electronics valves and modules;

e) DC-side filters and smoothing reactors;

f) main DC line.

In this work, a IGBT-based HVDC-VSC network is considered: every power station is modeled as shown in Fig. 2.11; about components sizing and structure, detailed informations are available in literature [73, 74, 75, 76, 77].

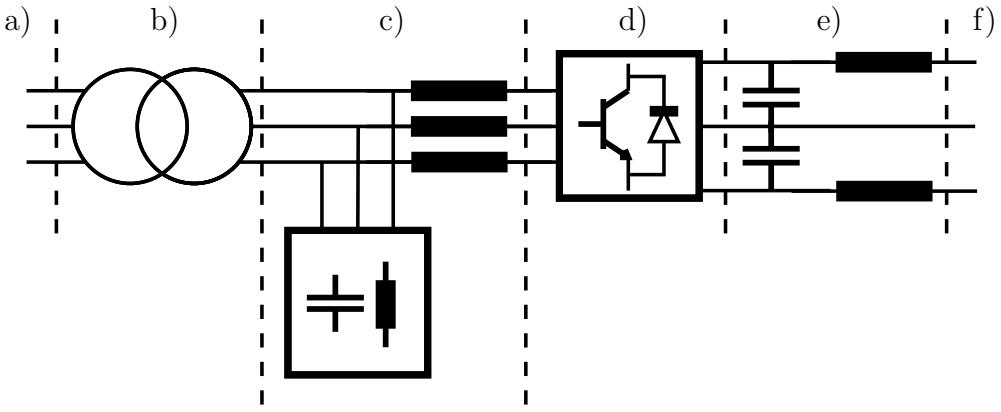

Figure 2.11: Power station model used in simulations: main essential assemblies are listed above.

2.3.2 HVDC station control

There are two main kinds for controlling modern VSC-based power stations:

i) PQ: station controls active and reactive power exchanged with AC grid it is connected to; such kind of control is sometimes called *Slave*, because station has no control of DC-side voltage, thus it cannot operate as slack node of a DC grid;

ii) VQ: station controls DC voltage and reactive power exchanged with AC grid it is connected to; such kind of control is sometimes called *Master*, because station operates as slack node of DC grid it is connected to.

According to previous list, usually a HVDC system has one *Master* station (or node) and one or more *Slaves*; more than one *Master* is still possible but in that case power flow on DC side is not directly controlled, being dependent by voltage drops and line equivalent resistance.

Also lack of a *Master* is possible, but in that case power flow through stations (including losses) must be tuned accordingly, otherwise DC link voltage will raise er lower depending on positive or negative global balance.

Power control is the key factor to obtain evolved features from HVDC converters; as shown in the followings, AC grids issues are today mainly related to manage fast and non-programmable power flows coming from RES.

2.4 Power grids issues

The problem of climate change has been addressed in recent years in Europe by subsidizing the development of alternative energy sources that are not-greenhouse gases. European policies introduced in last 15 years realized an increase in production and sharing of renewable energy (mainly solar and wind).

Nonetheless, further increase in RES is expected over the next 20 years: European Commission expressed ambitious targets about renewables diffusion up to 2030. Main issue about such heavy penetration of new and different power sources is their intrinsic unpredictable nature; production is independent and decoupled by final users demand.

Into existing AC based network, this is a well known problem in terms of power balancing, peak shaving and regulation: many traditional power plants are more and more frequently used as "backup" for renewable sources, to guarantee the network a sufficient amount of cold reserve. Thermoelectric plants have a standard degree of load reserve, positive and negative, which make them suitable for the compensation of network unbalances: nowadays, procedures to ensure that rotating generators production is reduced (or increased) very quickly to compensate lack of renewable is very stressful for electromechanical equipment. Furthermore, RES have generally limited ability to support AC system management compared to conventional synchronous machines directly connected to the network; main reasons of such behavior are:

- technological: renewable generators are linked to AC network through power electronics converters, that have very fast dynamic response respect to conventional rotating machines; this is generally considered an advantage in terms of control and regulation, but it means also very fast power transients and increasing of network stiffness.

- topological: big renewable power plants are usually located in remote areas due to environmental and urbanistic reasons (eg. noise for wind turbines, wide surface requirements for photovoltaic panels) and they are spread all over the country to reduce their unpredictability (statistically, loss of wind/sun in one area could be compensated by an increase somewhere else); this way, interconnection between such plants and network could be weak, because grid is poorly meshed.

According to previous points, increasing penetration of renewable sources can lead to a deterioration of AC grid frequency.

AC grid frequency is a global indicator of balance between electricity production and load demand. Any imbalance induces variations in frequency; recovery takes place by several level of regulation controls (typically three: primary, secondary and tertiary) but transient behavior (ratio, amplitude and period of oscillations), is mainly depending on grid equivalent inertia [78].

Into a traditional AC grid, both energy production and big inertia are given by rotating machines: during imbalances, relatively slow primary regulators (average response time 15-35 seconds) can stop frequency drift with modest final offset (primary regulation does not compensate frequency mismatch, it just stops it); rated valued is then reset in a longer time (minutes or more).

Renewable-based sources have usually poor equivalent inertia, and installed power has became consisting: coexistence with standard alternators is difficult, primary regulators can compensate imbalances but frequency transient could be sometimes very close to network operative limits, with serious possibility of extreme countermeasures (forced load rejection or plants disconnection).

A better way to face dangerous grid imbalances is then needed.

2.5 Why improving HVDC grids: targets

HVDC-VSC links can be a valid solution to face all issues explained above; a proper usage of such connections can generate multiple positive effects on AC grid:

1) HVDC conversion stations decouple dynamics of AC networks they are connected to; a frequency drift can be blocked or spread to several synchronous or asynchronous areas depending on available cold reserve [79];

2) HVDC can transfer active power efficiently over long distances: power plants can be located even far from AC loads (eg. offshore wind turbines [80]), with no appreciable impact on grid robustness;

3) HVDC links can increase AC grid equivalent meshing, with possibility to control power flows between several networks: imbalances can be quickly resolved, due to fast converter response [81, 82].

Some of above features are "native" by HVDC-VSC technology, but their action must be properly handled by means of control algorithms and system design [83, 84].

Presently, HVDC research for frequency regulation is mainly focused on two targets:

I. definition of control strategies for VSC converters of HVDC systems for increasing the virtual inertia of the system ("emulation" of traditional synchronous generators) [85];

II. creation of multi-terminal connections with HVDC systems between different synchronous areas to control power exchanges in order to balance the required load [86].

Such research topics are not mutually exclusive, they can coexist creating a new efficient transmission system, that is able to incorporate a high percentage of RES and handle frequency issues in a distribute way [87].

Among all ancillary functions, synthetic inertia is one of the most prominent and appreciated by national and international TSOs.

Main target of this chapter is therefore the study of synthetic inertia algorithms, and their implementation into HVDC stations. The approach is innovative because inertial energy is not provided by AC grids but it is stored into the HVDC section itself; in this way, frequency drift is not propagated among different synchronous areas.

2.6 HVDC research: road map and contributions

As mentioned, respect to previous chapter activity, this study is not related to a specific project or a real case study; modeled grids must be considered as much as possible general: power rates, lines, topology and so on have been chosen to empathize some aspects of the research and to highlight peculiarities of the various solutions implemented.

Looking for effective HVDC synthetic inertia algorithms, at first a benchmark case is needed: first simulation is a "simple" HVDC link (2 nodes between two AC networks) with primary frequency control and an AC load step; during simulation, a wide frequency disturbance occurs.

In the followings, project proceeds on the same grid with subsequent improvements, using a trial-error approach:

- an ideal synthetic inertia algorithm is tested, trying to define maximum improvements benchmark about frequency control;
- with energetic calculations, the power needed to perform an ideal synthetic inertia algorithm is found; power converter DC filter capacitors are sized accordingly to access such energy; this leads the control not to propagate frequency disturbance in second AC grid;
- with same test setup, several kinds of real (based on HVDC power converter dynamics) algorithms have been implemented, tested and compared; comparison is between algorithm themselves but also with benchmark case; positive and negative peculiarities are highlighted;
- algorithms with bad results are abandoned or modified to improve performances;
- best algorithm is then used on a multi-terminal HVDC grid, testing system response with other grid controls (droop action).

As a theoretical approach, a sensitivity analysis tries to assess the correlation about DC capacitors sizing and synthetic inertia effect; methodology is different respect to previous chapter, in which engineering and economical issues were predominant; the reason is that this part of the project is included in a wider research activity financed by the Research Fund for the Italian Electrical System under the Contract Agreement between RSE S.p.A. and the Ministry of Economic Development.

In following sections, synthetic inertia control of a HVDC link will be deeply analyzed and tested.

At first, the model used to implement power grid inertia is presented.

2.7 Power grid inertia

Consider a basic "conventional" generation system composed as shown in Fig. 2.12. P_M is motor mechanical power, P_G is generator electrical power and P_L is load electrical power.

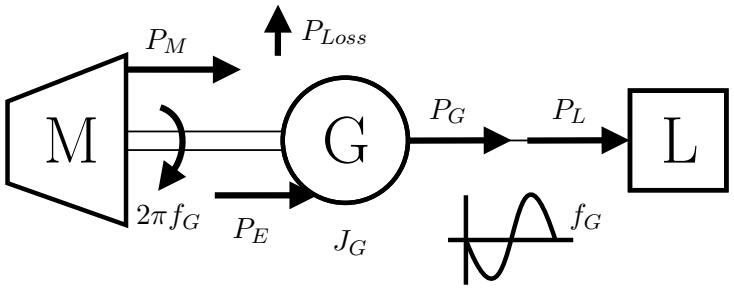

Figure 2.12: Conventional generation system model.

Efficient power P_E is the electrical power the generator can produce from P_M apart mechanical and electrical losses:

$$P_E(t) = P_M(t) - P_{Loss}(t) \tag{2.1}$$

At rated frequency (f_{Gn}) power is fully balanced between load and generator and also between generator and motor (eg. a turbine).

For simplicity, mechanical motor frequency equals generator electrical frequency. In steady state, efficient power is equal to generator electrical power ($P_E = P_G$).

When a load change occurs, motor mechanical frequency (thus generator electrical frequency) f_G deviates because of power mismatch: considering whole system inertia momentum J_G, following differential equation is given:

$$P_E(t) - P_L(t) = (2\pi)^2 f_G(t) J_G \frac{df_G(t)}{dt} \tag{2.2}$$

A generalization of inertia momentum in a complex grid with N rotating machines and K loads is given by:

$$J_g = \sum_{i=1}^{N} J_{Gi} \quad , \quad P_e = \sum_{i=1}^{N} P_{Ei} \quad , \quad P_l = \sum_{i=1}^{K} P_{Li} \tag{2.3}$$

So (2.2) becomes:

$$P_e(t) - P_l(t) = (2\pi)^2 f_g(t) J_g \frac{df_g(t)}{dt} \tag{2.4}$$

In per unit (p.u.), using grid rated apparent power A_{gn} (active powers are computed pretending unitary power factor) and grid rated frequency f_{gn} as base values:

$$P_{epu}(t) - P_{lpu}(t) = \Delta P_{pu}(t) = \frac{(2\pi f_{gn})^2}{A_{gn}} f_{gpu}(t) J_g \frac{df_{gpu}(t)}{dt} \tag{2.5}$$

$$P_{epu} = \frac{P_e}{A_{gn}} \quad , \quad P_{lpu} = \frac{P_l}{A_{gn}} \quad , \quad f_{gpu} = \frac{f_g}{f_{gn}} \tag{2.6}$$

Equation (2.5) is not linear, it cannot be implemented into a simulation by means of a rational transfer function. Moreover, its solution could be not unique and depends on system initial state and input.

To obtain a more usable model, (2.5) is linearized around steady state frequency value $f_{gpu}(0)$.

$$\Delta f_{gpu}(t) = f_{gpu}(t) - f_{gpu}(0) \tag{2.7}$$

$$\Delta P_{pu}(t) \approx \frac{(2\pi f_{gn})^2}{A_{gn}} f_{gpu}(0) J_g \frac{d\Delta f_{gpu}(t)}{dt} = \frac{(2\pi f_{gn})^2}{A_{gn}} f_{gpu}(0) J_g \frac{df_{gpu}(t)}{dt} \tag{2.8}$$

Machine inertial momentum is usually expressed through its equivalent starting time T_{avvG}, defined as follows: it represents time needed to accelerate the machine from zero to rated frequency f_{Gn}, by means of a constant torque equal to:

$$C_{Gn} = \frac{P_{Gn}}{2\pi f_{Gn}}. \tag{2.9}$$

Considering torques instead of powers, (2.2) becomes linear, as follows:

$$C_G(t) - C_L(t) = 2\pi J_G \frac{df_G(t)}{dt}. \tag{2.10}$$

Substituting (2.9) into (2.10) and integrating from zero to T_{avvG}:

$$\int_0^{T_{avvG}} \frac{P_{Gn}}{2\pi f_{Gn}} dt = \int_0^{T_{avvG}} 2\pi J_G \frac{df_G(t)}{dt} dt \tag{2.11}$$

$$\frac{P_{Gn}}{2\pi f_{Gn}} T_{avvG} = \int_0^{f_{Gn}} 2\pi J_G df_G \tag{2.12}$$

$$\frac{P_{Gn}}{2\pi f_{Gn}} T_{avvG} = 2\pi J_G f_{Gn} \tag{2.13}$$

$$T_{avvG} = J_G \frac{(2\pi f_{Gn})^2}{P_{Gn}} \tag{2.14}$$

For a complex grid, equivalent starting time T_{avvg} is found accordingly:

$$T_{avvg} = J_g \frac{(2\pi f_{gn})^2}{A_{gn}} \quad , \quad A_{gn} = P_{gn} \tag{2.15}$$

Linear model of (2.8) becomes:

$$\Delta P_{pu}(t) \approx T_{avvg} f_{gpu}(0) \frac{d\Delta f_{gpu}(t)}{dt} \tag{2.16}$$

Typical grid loading or unloading profiles are power steps (2.17) or power ramps (2.18).

$$\Delta P_{pu} = 0 \ , \ t < 0 \ , \ \Delta P_{pu} = c_1 \ , \ t \geq 0 \tag{2.17}$$

$$\Delta P_{pu} = 0 \ , \ t < 0 \ , \ \Delta P_{pu} = c_1 t \ , \ t \geq 0 \tag{2.18}$$

As a consequence, linear torque-based model of (2.10) properly fits power-based model of (2.2) only if $f_G(0)$ is far from zero and quite stable. In other words, power profiles are a scaling of torque profiles when speed is high and acceleration is low.

Such concept is extended from a single machine to a grid; because rated grid frequency is effectively far from zero, linear model of (2.8) becomes:

$$\Delta P_{pu}(t) \approx T_{avvg} f_{gpu}(0) \frac{d\Delta f_{gpu}(t)}{dt} = T_{avvg} f_{gpu}(0) \frac{df_{gpu}(t)}{dt} \tag{2.19}$$

Linear model is then used to compute system response with power inputs shown before (power step and power ramp):

$$\begin{cases} \Delta P_{pu} = 0 \ , \ t < 0 \ \ ; \ \ \Delta P_{pu} = c_1 \ , \ t \geq 0 \\ \\ f_{gpu}(t) = f_{gpu}(0) \ , \ t \leq 0 \ \ ; \ \ f_{gpu}(t) = \dfrac{c_1}{T_{avv} f_{gpu}(0)} t + f_{gpu}(0) \ , \ t > 0 \end{cases} \tag{2.20}$$

$$\begin{cases} \Delta P_{pu} = 0 \ , \ t < 0 \ \ ; \ \ \Delta P_{pu} = c_1 t \ , \ t \geq 0 \\ \\ f_{gpu}(t) = f_{gpu}(0) \ , \ t \leq 0 \ \ ; \ \ f_{gpu}(t) = \dfrac{c_1}{2T_{avv} f_{gpu}(0)} t^2 + f_{gpu}(0) \ , \ t > 0 \end{cases} \tag{2.21}$$

Fig. 2.13 compares closed form solutions of (2.20) and (2.21) to non-linear ones, computed numerically; system is tuned with following data:

$$f_{gpu}(0) = 1 \quad , \quad c_1 = 1 \quad , \quad T_{avvg} = 1 \text{ s} \quad , \quad \Delta P_{pu} = 1 \tag{2.22}$$

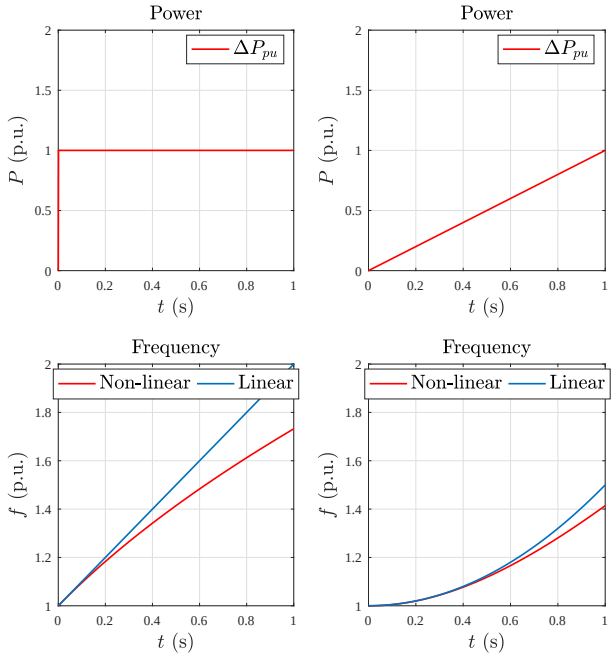

Figure 2.13: Comparison between linear and non-linear model response at rated frequency.

According to previous considerations, for small frequency deviations around rated value, linear model well represents system response. In real grids, acceptable frequency deviations must be within a narrow tolerance band (−0.05 p.u. ; +0.03 p.u. in most severe transients [4]). This way, linear model can be implemented into simulations.

For comparison, same calculations are repeated with:

$$f_{gpu}(0) = 0.01 \quad , \quad c_1 = 1 \quad , \quad T_{avvg} = 1 \text{ s} \quad , \quad \Delta P_{pu} = 1 \tag{2.23}$$

and results are shown in Fig. 2.14.

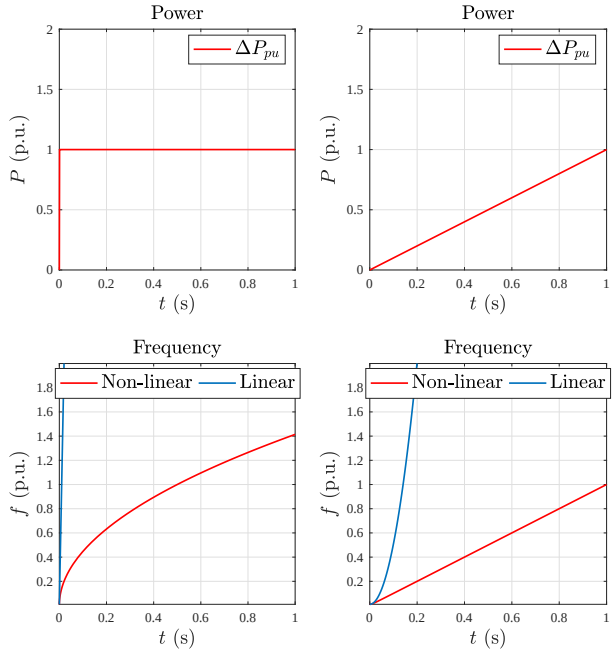

Figure 2.14: Comparison between linear and non-linear model response at low frequency.

Despite system is properly linearized, because of low initial frequency, difference between numerical and linear solutions is huge.

Summarizing, linear power-based model of (2.15) can be used when:

1) $f_{gpu}(0) \gg 0$: model initial frequency is far from zero (eg. rated value);

2) $f_{gMAXpu} - f_{gpu}(0) \ll 1 \quad , \quad f_{gminpu} - f_{gpu}(0) \gg -1$: maximum (minimum) frequency deviation is small compared to initial value;

In Laplace domain, (2.15) can be converted considering as state variable $\Delta f_{gpu}(t)$ or $f_{gpu}(t)$; in first case:

$$\Delta P_{pu}(s) = T_{avvg} f_{gpu}(0)[s\Delta F_{gpu}(s) - \Delta f_{gpu}(0)] \tag{2.24}$$

By definition of steady state, $\Delta f_{gpu}(0) = 0$, so:

$$\frac{\Delta F_{gpu}(s)}{\Delta P_{pu}(s)} = \frac{1}{sT_{avvg} f_{gpu}(0)} = G(s) \tag{2.25}$$

$G(s)$ in (2.25) is the transfer function of the linear model:

$$\Delta F_{gpu}(s) = \frac{1}{sT_{avvg}f_{gpu}(0)}\Delta P_{pu}(s) = G(s)\Delta P_{pu}(s) \tag{2.26}$$

In second case:

$$\Delta P_{pu}(s) = T_{avvg}f_{gpu}(0)[sF_{gpu}(s) - f_{gpu}(0)] \tag{2.27}$$

$f_{gpu}(0)$ can be anything, so:

$$\frac{\Delta P_{pu}(s)}{sT_{avvg}f_{gpu}(0)} = F_{gpu}(s) - \frac{f_{gpu}(0)}{s} \tag{2.28}$$

$$F_{gpu}(s) = G(s)\Delta P_{pu}(s) + \frac{f_{gpu}(0)}{s} \tag{2.29}$$

Equation (2.29) shows full frequency profile is given by transfer function of (2.25) plus a constant contribution equal to frequency initial condition.

System model is shown in block diagram of of Fig. 2.15.

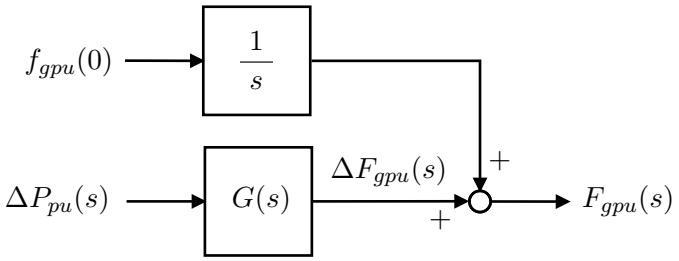

Figure 2.15: Grid linear model block diagram in Laplace domain.

2.7.1 Primary frequency control

With no further control, grid frequency in model (2.15) would diverge to infinite in case of load rejection ($P_{epu}(t) - P_{lpu}(t) > 0$) or it would collapse to zero in case of load increase ($P_{epu}(t) - P_{lpu}(t) < 0$).

Primary control is designed to stop frequency deviations due to power unbalance, by changing $P_{epu}(t)$ accordingly.

Regulating generators modify their own power setpoint P^0_{Epu} according to a characteristic ($P_{Epu} = f(f_{Gpu})$): it is called *droop* (σ_{Gpu}), and it is shown in Fig. 2.16.

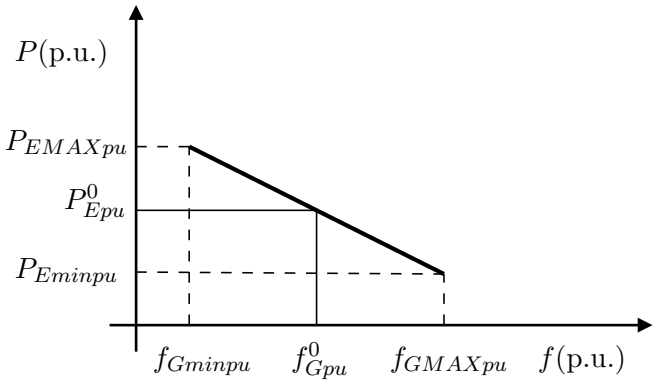

Figure 2.16: Droop characteristic.

$$\sigma_{Gpu} = \frac{f_{GMAXpu} - f_{Gminpu}}{P_{EMAXpu} - P_{Eminpu}} \tag{2.30}$$

P_{EMAXpu} and P_{Eminpu} are maximum and minimum generator efficient power limits, respectively. In normal conditions, each regulating machine must operate within a thicker band in order to guarantee a minimum amount of power reserve in loading or unloading. For Italy, according to TSO grid code [4], such limits are shown in p.u. in Fig. 2.17 (base value is rated machine electrical power P_{Gn}).

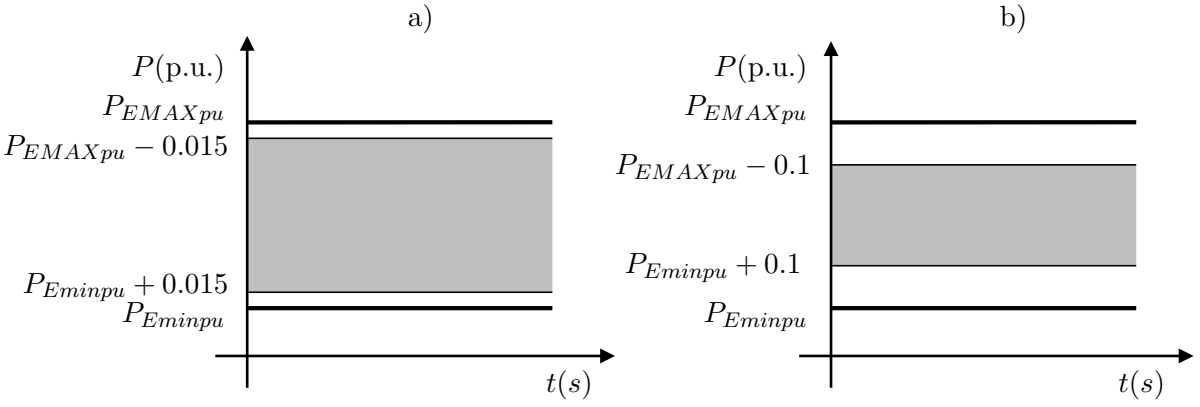

Figure 2.17: Regulating generators power reserve. a) Landside; b) Islands.
Grey area is the normal conditions working area; source: Terna [4].

Also f_{GMAXpu} and f_{Gminpu}, maximum and minimum limits of machine frequency, are imposed [4, 88]:

$$f_{GMAXpu} = \frac{51.5 \text{ Hz}}{50 \text{ Hz}} = 1.03 \quad ; \quad f_{Gminpu} = \frac{47.5 \text{ Hz}}{50 \text{ Hz}} = 0.95 \tag{2.31}$$

A complex grid is composed by many regulating generators, with different power limits and droop settings; for simplicity, generalizing previous concept, machine frequency becomes grid frequency and a global droop coefficient σ_{gpu} is defined:

$$\sigma_{gpu} = \frac{f_{gMAXpu} - f_{gminpu}}{P_{eMAXpu} - P_{eminpu}} \tag{2.32}$$

P_{eMAXpu} and P_{eminpu} are maximum and minimum equivalent efficient power the grid can dispatch through the node where frequency change is measured; in such case, as shown in Fig. 2.18, new grid working point $P_{epu}^{(1)}$ is given.

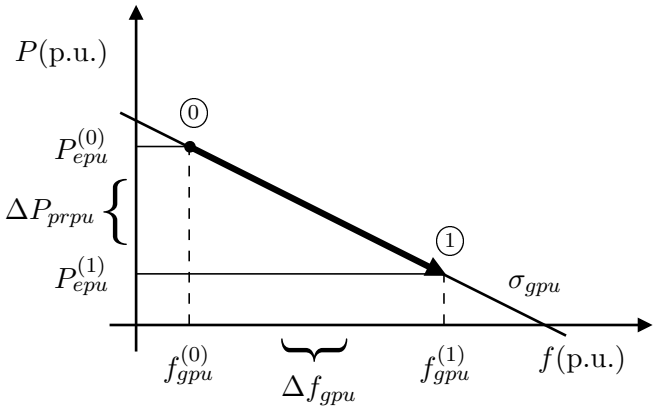

Figure 2.18: Grid working point changing in case of frequency deviation (static characteristics).

Using same nomenclature as (2.15), assuming $f_{gpu}^{(0)} = f_{gpu}(0)$ and $P_{epu}^{(0)} = P_{epu}(0)$:

$$\Delta f_{gpu} = f_{gpu} - f_{gpu}(0) \tag{2.33}$$

$$\Delta P_{prpu}(t) = P_{epu}(t) - P_{epu}(0) = -\frac{1}{\sigma_{gpu}} \Delta f_{gpu}(t) \tag{2.34}$$

Equation (2.34) expresses a static characteristics between frequency and power: final result is reached in steady-state only; in real systems, relationship is a function of time, that depends on many physical factors: frequency regulators dynamics, delays, dead bands, measurements and so on.

For this study purposes, all above conditions can be simply and efficiently emulated by a lead-lag network, as seen in literature [89].

In Laplace domain, dynamic response of (2.34) becomes:

$$\Delta P_{prpu}(s) = -\frac{1}{\sigma_{gpu}} \frac{1 + sT_1}{1 + sT_2} \Delta F_{gpu}(s) = -R_{pr}(s) \Delta F_{gpu}(s) \tag{2.35}$$

with T_1 and T_2 as lead and lag time constants, respectively. In p.u., inverse of *droop* is equal as system *regulating energy*.

2.7.2 Rate of Change of Frequency (ROCOF)

Consider again Fig. 2.15 and transfer functions (2.26-2.29), assuming $f_{gpu}(0) = 1$: as shown in Fig. 2.13, in the very first time of a load step (ΔP_{pu}), frequency variation is a ramp with a certain slope; such slope can be calculated from p.u. values and it is called ROCOF (Rate Of Change Of Frequency); it results:

$$\text{ROCOF} = \frac{\Delta P_{pu}}{T_{avvg}} \tag{2.36}$$

ROCOF is then a useful index to define grid inertial behavior: the lower the values is, the greater inertia is.

Purpose of synthetic inertia algorithm on a grid is reducing ROCOF by means of proper power flows; such action must be very fast, in order to smooth frequency deviations at the beginning of load transients, before effect of primary regulation.

As said in Par. 2.5, HVDC links generate multiple positive effects in connecting AC grids each other. In addition, modern VSC converters have quicker dynamics than traditional rotating equipment used for frequency regulation; they are then ideal candidates to fulfill inertial tasks.

In the followings, simulations will be performed, comparing ROCOF values achieved.

Simulation model is presented in next section.

2.7.3 Simulation model

System model of Fig. 2.15 is updated with primary regulator transfer function $R_{pr}(s)$, as shown in Fig. 2.19; complete power grid frequency system is called $P(s)$.

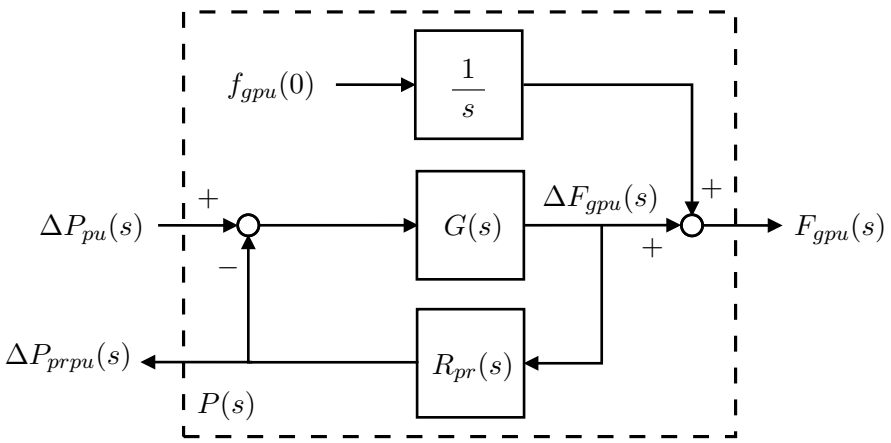

Figure 2.19: Grid linear model and primary frequency regulator block diagram in Laplace domain.

$P(s)$ is included into a Matlab/Simulink grid model setup (Fig. 2.20), to control a variable frequency generator that represents AC grid 1.

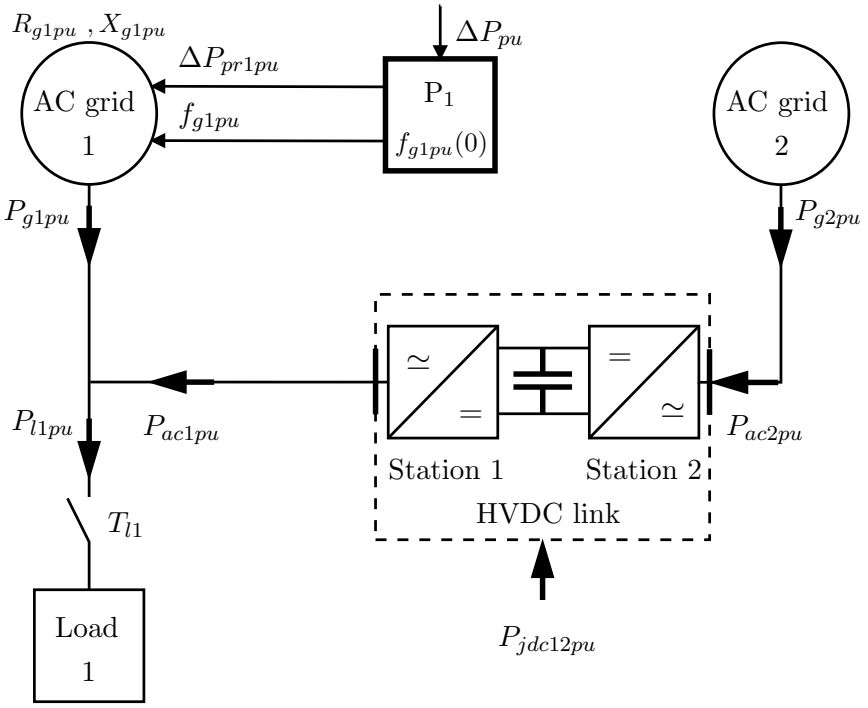

Figure 2.20: Network used in simulations. AC grid 1 frequency system (bold square) is shown in Fig. 2.19.

Positive power flow measurements are given by arrows; P_{ac1pu} and P_{ac2pu} have the same direction, so HVDC link can be seen as a natural prosecution of AC grid 2. Due to measurement convention, HVDC link losses ($P_{jdc12pu}$) are negative by definition.

Network settings are summarized in Tab. 2.2.

Table 2.2: HVDC stations and AC grids data.

Quantity	Symbol	Value	Unit
Station 1 rated power	A_{ac1n}	200	MVA
Station 1 rated DC voltage	V_{dc1n}	200	kV
Station 2 rated power	A_{ac2n}	200	MVA
Station 2 rated DC voltage	V_{dc2n}	200	kV
AC grid 1 rated power	A_{g1n}	2000	MVA
AC grid 1 rated voltage	V_{g1n}	230	kV
AC grid 1 rated frequency	f_{g1n}	50	Hz
AC grid 1 per unit resistance	R_{g1pu}		-
AC grid 1 per unit reactance	X_{g1pu}		-
AC grid 2 rated power	A_{g2n}	2000	MVA
AC grid 2 rated voltage	V_{g2n}	230	kV
AC grid 2 rated frequency	f_{g2n}	50	Hz
AC grid 2 per unit resistance	R_{g2pu}		-
AC grid 2 per unit reactance	X_{g2pu}		-
Load 1 rated power	P_{l1}	160	MW

About model in Fig. 2.20:

- AC grid 2 is also modeled as AC grid 1; according to simulations targets, f_{g2pu} should remain constant during load transients (no power unbalances are going to affect AC grid 2);

- load steps (ΔP_{pu}) are modeled as constant impedances: power profiles should be therefore dependent from frequency and voltage deviations. To model as much as possible "pure" power steps, grid short circuit impedance in p.u. (R_{gpu} , X_{gpu}) is chosen accordingly low; such approximation is reasonable because rated grid power is chosen considerably higher than load rated power; detailed model sizing is presented in the followings;

- as said at previous point, because of low values of R_{gpu} , X_{gpu}, line voltage drops during loadings are negligible; as a result, no AC grids voltage control have been implemented;

- every AC grid is connected to a HVDC-VSC AC/DC station; at simulations beginning ($t = 0$), power flows (bold arrows) are fully balanced and system is in steady state.

In the followings, several synthetic inertia algorithms are implemented into HVDC-VSC power converters; at first, ideal concept of synthetic inertia action is presented.

2.8 Ideal synthetic inertia algorithm

An intuitive way to realize a synthetic inertia action has been already treated in literature [90], by using a signal that is proportional to grid frequency derivative[1] through a gain k_{si}; in Laplace domain:

$$P_{sipu}(s) = -\frac{sk_{si}}{1+s\tau}\Delta F_{gpu}(s) = -R_{si}(s)\Delta F_{gpu}(s) \tag{2.37}$$

In per unit, the contribution is summed to primary control, as shown in Fig. 2.21.

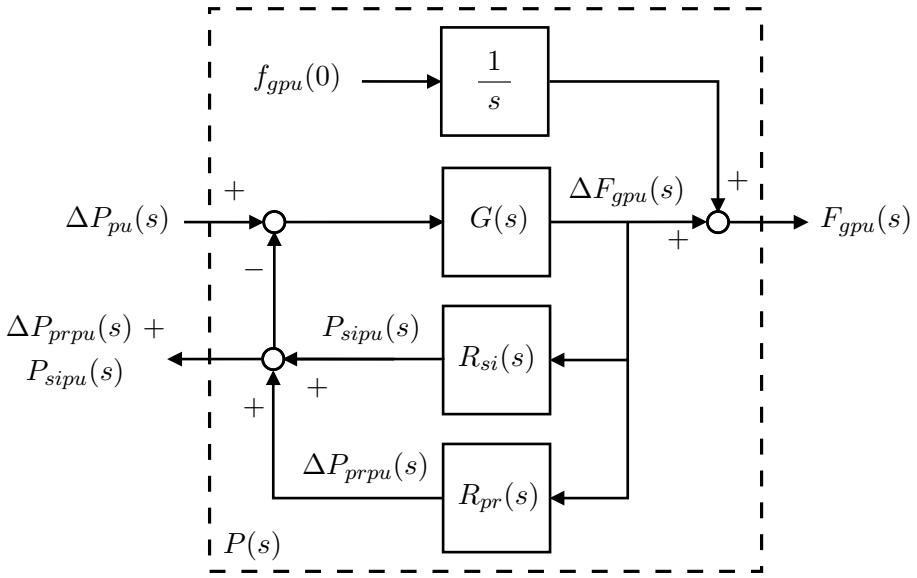

Figure 2.21: Ideal synthetic inertia regulator $R_{si}(s)$ and primary frequency regulator $R_{pr}(s)$ in Laplace domain applied to grid linear model in per unit.

According to Fig. 2.21 and ROCOF definition (Par. 2.7.2), k_{si} is a time and (2.36) becomes:

$$\text{ROCOF} = \frac{\Delta P_{pu}}{T_{avvg} + k_{si}} \tag{2.38}$$

The effect is equal as connecting to AC grid a synchronous machine whose starting time is k_{si}.

Nevertheless $R_{is}(s)$ has a simple concept, it is probably the most effective solution in terms of performances, but physical implementation is not easy due to numeric derivative: to avoid untimely activation and disturbances, frequency signal must be filtered, reducing the speed of response. In the followings, this kind of algorithm will be called ideal synthetic inertia, and it will be used to tune inertial solutions based on HVDC-VSC converters by the energy point of view.

A simulation with no synthetic inertia algorithm is performed, as benchmark for system intrinsic performances.

[1] Numerical simulations have been performed; usage of pure derivative could be critical, so a washout filter (high-pass) was preferred:

$$\frac{s}{1+s\tau}$$

τ has been set equal to a simulation step size, to avoid computational issues.

2.8.1 Simulation 1: no synthetic inertia algorithm

A load flow on grid in Fig. 2.20 has been performed, in order to set network at steady state with HVDC link at rated power. AC grid 1 and AC grid 2 frequencies are set to 50 Hz [$f_{g1pu}(0)$=$f_{g2pu}(0)$=1].

Results in p.u. are listed in Tab. 2.3 (base power A_{g1n}=2000 MVA).

Table 2.3: Initial load flow results in p.u. for load step tests (base power A_{g1n}=2000 MVA).

Input	Symbol	Value	Comment
Station 1 active power	P_{ac1pu}	-0.080	
Station 1 DC voltage	V_{dc1pu}	1	Base voltage V_{dc1n}=200 kV
Output	**Symbol**	**Value**	**Comment**
Station 2 active power	P_{ac2pu}	-0.074	
Station 2 DC voltage	V_{dc2pu}	0.99	Base voltage V_{dc2n}=200 kV

Primary frequency regulator on AC grid 1 has been tuned as shown in Tab. 2.4:

Table 2.4: AC grid 1 primary frequency controller tuning.

T_{avvg1} (s)	T_{11} (s)	T_{21} (s)	σ_{g1pu} (p.u.)
8	3.3	10	0.05

Equivalent AC grid 1 start time T_{avvg1} is set at 8 s, typical value for the chosen rated power.

According to (2.35), droop coefficient σ_{g1pu} is set to achieve, in case of load step $P_{l1pu} = 0.08$, a maximum frequency deviation in steady state (Δf_{g1pu}) of:

$$-0.004 \leq \Delta f_{g1pu} \leq 0.004 \tag{2.39}$$

$$\sigma_{g1pu} \leq \frac{|\Delta f_{g1pu}|}{P_{l1pu}} = 0.05 \tag{2.40}$$

Station 1 is set as *Slave*, while station 2 is set as *Master*; DC voltage, active and reactive power setpoints are the ones given by load flow results in Tab. 2.3.

At T_{l1}=1 s, a load step on AC grid 1 is given. As said, $P_{l1pu} = 0.08$ (160 MW, base power 2000 MVA).

Simulation 1 power profiles are shown in Fig. 2.22.

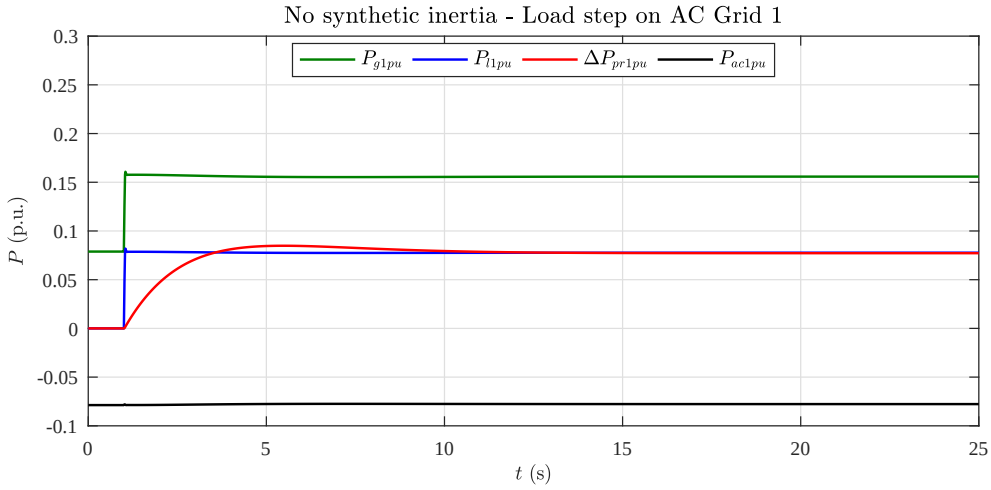

Figure 2.22: Simulation 1 results: power profiles on AC grid 1 with no synthetic inertia. Base power: 2000 MVA.

As shown in Fig. 2.22, primary frequency control balances power in about 15 s after loading; primary power is provided by AC grid 1 itself, P_{ac1pu} is constant and steady at -0.08 p.u., as set in station 1 controller.

Frequency profile (in Hz) and MFD (Maximum Frequency Deviation) are shown in Fig. 2.23.

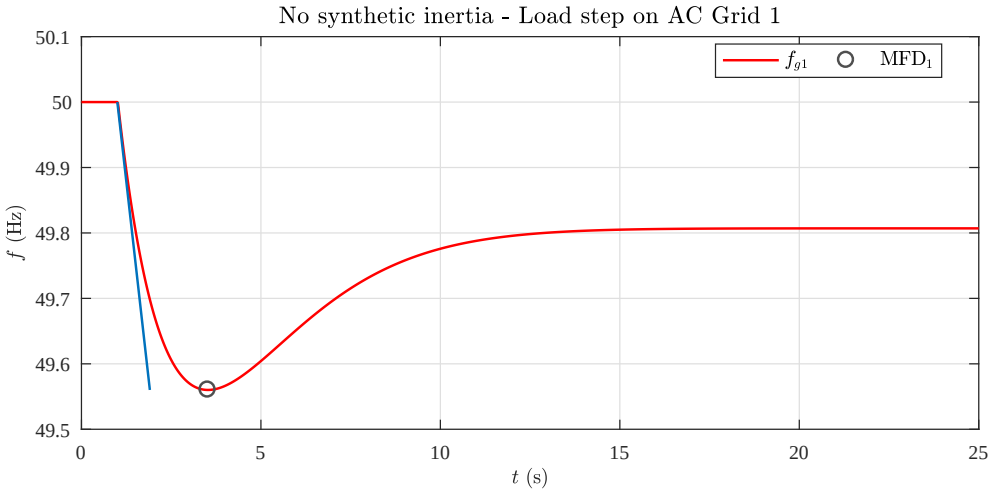

Figure 2.23: Simulation 1 results: frequency profile and MFD (Maximum Frequency Deviation) on AC grid 1 with no synthetic inertia. The slope of blue straight line shows graphically ROCOF$_1$ trend at the beginning of transient.

AC grid 1 frequency profile as a lowering right after the loading, to be stopped by primary frequency control at 49.8 Hz after 15-20 s. According to (2.39) and (2.40), steady state value Δf_{g1pu} is achieved:

$$\Delta f_{g1pu} = \frac{49.8 \text{ Hz} - 50 \text{ Hz}}{50 \text{ Hz}} = -0.004 \tag{2.41}$$

Maximum Frequency Deviation (MFD) is 440 mHz.

Simulation 1 numerical results are summarized in Tab. 2.5:

Table 2.5: Simulation 1 results: no synthetic inertia.

Simulation	T_{avvg1} (s)	ROCOF$_1$ (Hz/s)	MFD$_1$ (mHz)
1) No synthetic inertia	8	-0.5	-440

First simulation showed state of the art about AC grid 1 primary regulation intervention; next simulation implements synthetic inertia presented in Par. 2.8, to improve grid frequency response.

2.8.2 Simulation 2: ideal synthetic inertia

Simulation 1 is repeated using controller shown in Fig. 2.21 in replacement of the one in Fig. 2.19. Synthetic inertia power (P_{si1pu}) is supposed to come from an ideal source inside AC grid 1 itself.

Simulation grid setup is shown in Fig. 2.24.

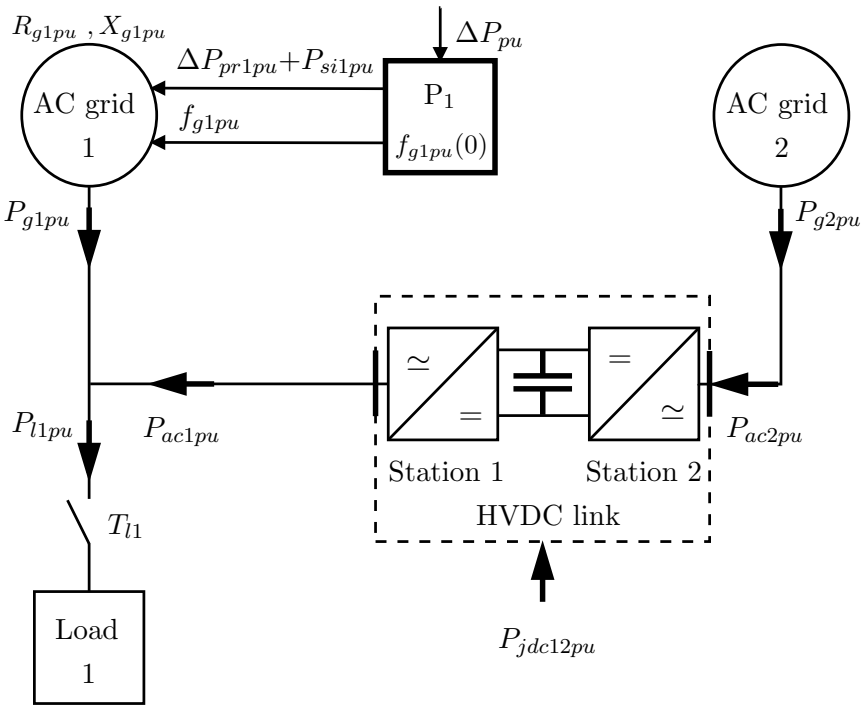

Figure 2.24: Network used for ideal synthetic inertia simulations. AC grid 1 frequency system (bold square) is shown in Fig. 2.21.

Steady state conditions before load step are the same, as shown in Tab. 2.3; in such configuration, HVDC stations are both controlled as *Slaves*, to guarantee a constant power flow through DC link.

Synthetic inertia coefficient is set as one half of AC grid 1 starting time:

$$k_{si1} = \frac{T_{avvg1}}{2} = 4 \text{ s} \tag{2.42}$$

Targets of simulation 2 are:

- testing ideal synthetic inertia algorithm quantifying frequency response improvement on AC grid 1;
- measure the amount of power (and energy) the HVDC link has to provide when inertial control will be delegated to station 1 converter.

Simulation 2 power profiles are shown in Fig. 2.25.

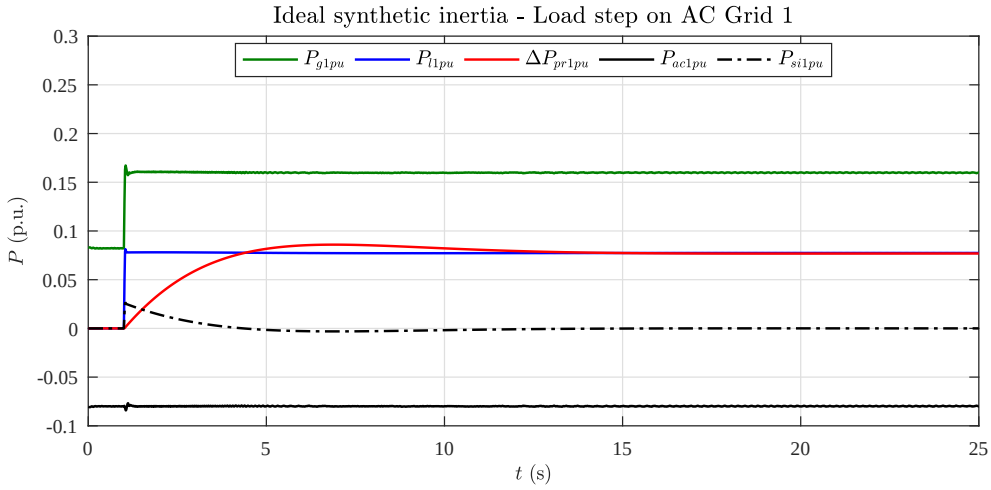

Figure 2.25: Simulation 2 results: power profiles on AC grid 1 with ideal synthetic inertia. Base power: 2000 MVA.

As shown in Fig. 2.25, primary frequency control still balances power in about 15 s after loading, with a lower slope; such effect is positive because of less stress in mechanical equipment. Primary power P_{pr1pu} is provided by AC grid 1 itself, P_{ac1pu} is constant and steady at -0.08 p.u., as set in station 1 controller.

Inertial power P_{si1pu} has a peak in the very beginning of transient (T_{l1}), then it goes to zero with same trend of primary power; when primary regulator is in steady state, frequency deviation is stopped, then frequency derivative is null. At t=25 s, system is in a new steady state.

Fig. 2.26 shows station power profiles (AC side) and their setpoint, respectively.

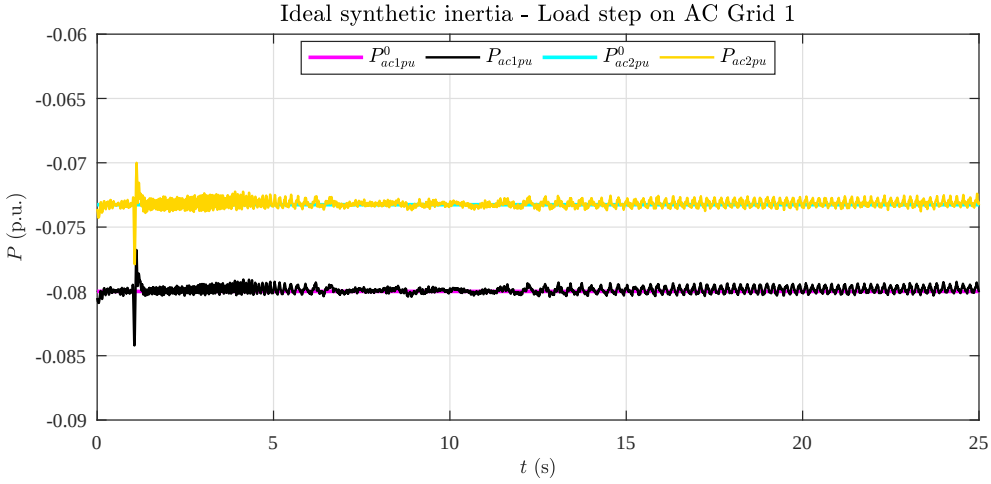

Figure 2.26: Simulation 2 results: HVDC stations power profiles (and setpoint) with ideal synthetic inertia.

Base power: 2000 MVA.

Apart minor oscillations around T_{l1} (1 s), stations regulators perfectly follow setpoint given by power flow computed in steady state condition; the result is that load step effect is not propagated to AC grid 2 neither to DC link.

Fig. 2.27 shows voltage profiles of HVDC stations (DC link voltage at both sides): like Fig. 2.26, besides a spike at T_{l1}, voltages stay set at their respective values in steady state.

Summarizing, HVDC section is completely "transparent" to AC grid 1 load step.

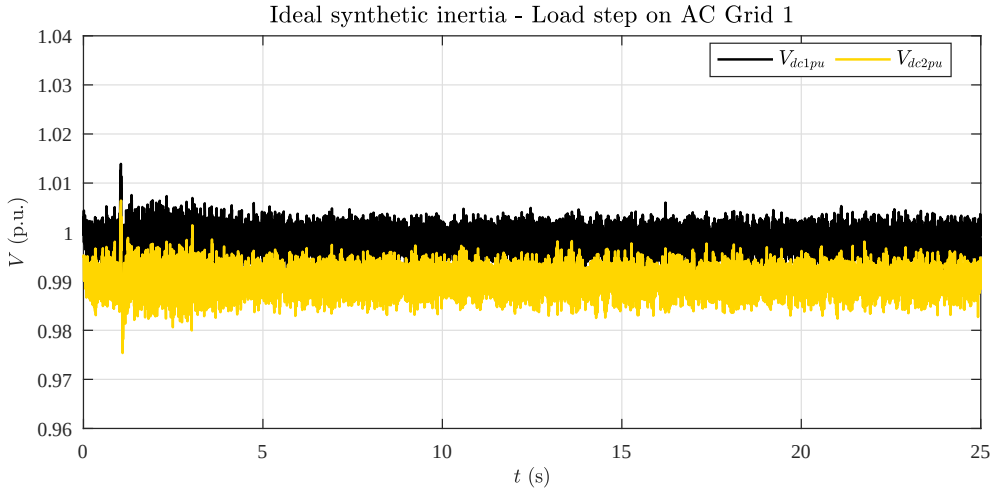

Figure 2.27: Simulation 2 results: HVDC stations voltage profiles with ideal synthetic inertia.
Base voltage: 200 kV.

About AC grid 1, frequency profile (in Hz) and MFD are shown in Fig. 2.28. Results of simulation 1 (no synthetic inertia) are plot in black for direct comparison.

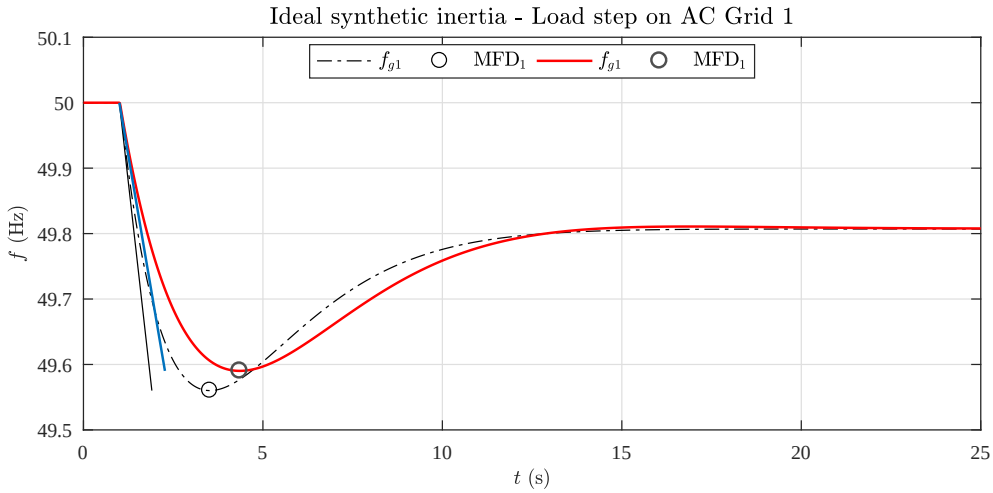

Figure 2.28: Simulation 2 results: frequency profile and MFD (Maximum Frequency Deviation) on AC grid 1 with ideal synthetic inertia. The slope of blue straight line shows graphically ROCOF$_1$ trend at the beginning of transient.
Results of simulation 1 (no synthetic inertia) in black for direct comparison.

Simulation 2 numerical results are summarized in Tab. 2.6 and compared to simulation 1 (no synthetic inertia): improvements in terms of ROCOF are relevant (-33%); there are also minor benefits about MFD (-7%).

Table 2.6: Simulation 2 results: ideal synthetic inertia.

Simulation	T_{avvg1} (s)	k_{si1} (s)	ROCOF$_1$ (Hz/s)	MFD$_1$ (Hz)
1) No synthetic inertia	8	0	-0.50	-440
2) Ideal synthetic inertia	8	4	-0.33 (-34%)	-410 (-7%)

Such results show two important aspects:

- synthetic inertia contribution must be as fast as possible when a load step occurs;
- synthetic inertia effect cannot change frequency profile but only ROCOF in the very first time of transients.

Energy provided by P_{si1pu} on AC grid 1 is given by:

$$W_{sinet1}(t) = \int P_{si1pu}(t)dt. \tag{2.43}$$

Energy profile is shown in Fig. 2.29. At about t=4 s, inertial energy has a peak.

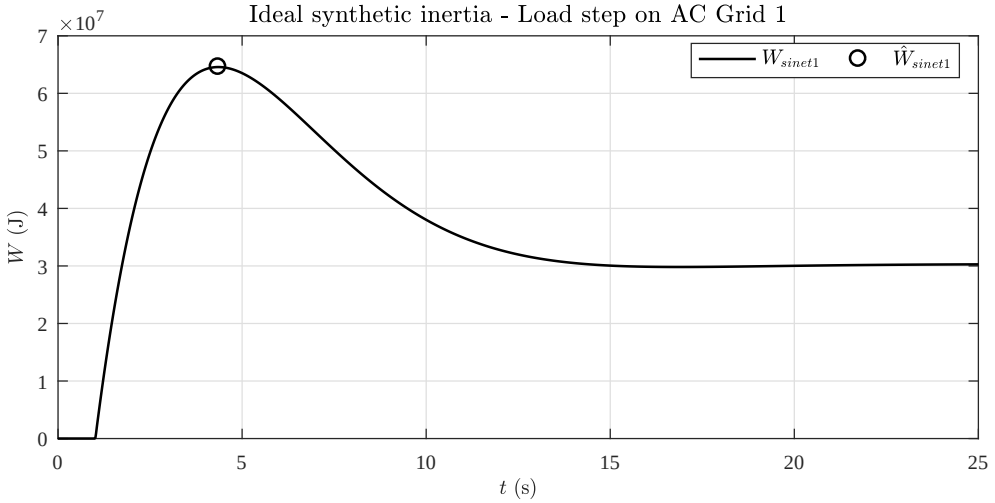

Figure 2.29: Simulation 2 results: net energy (W_{sinet1}) needed to perform synthetic inertia function according to (2.43).

This is given by P_{si1pu} inversion in Fig. 2.25; in fact, fast dynamics of inertial control also compensates primary control overshoot.

Due to this, inertial energy must be estimated on peak value ($\hat{W}_{sinet1}$) and not on final (steady state) value:

$$\hat{W}_{sinet1} = \max\left(W_{sinet1}\right) = 65.3 \text{ MJ} \tag{2.44}$$

Such energy is net because it does not include losses for its generation and transmission on AC grid 1; usign VSC converters to provide it, gross energy must be foreseen in advance.

Next section will present the concept of HVDC-based synthetic inertia, including a calculation of gross energy by means of simulation 1 and 2 data.

2.9 HVDC-VSC synthetic inertia approach

HVDC-VSC based synthetic inertia concept is generally known in literature [74, 91]: converters are used to provide fast transient power according to control algorithms response.

In practice, output from synthetic inertia regulator R_{si} is transferred to VSC converter control, in (algebraic) sum with actual power station setpoint. The concept is shown in Fig. 2.30.

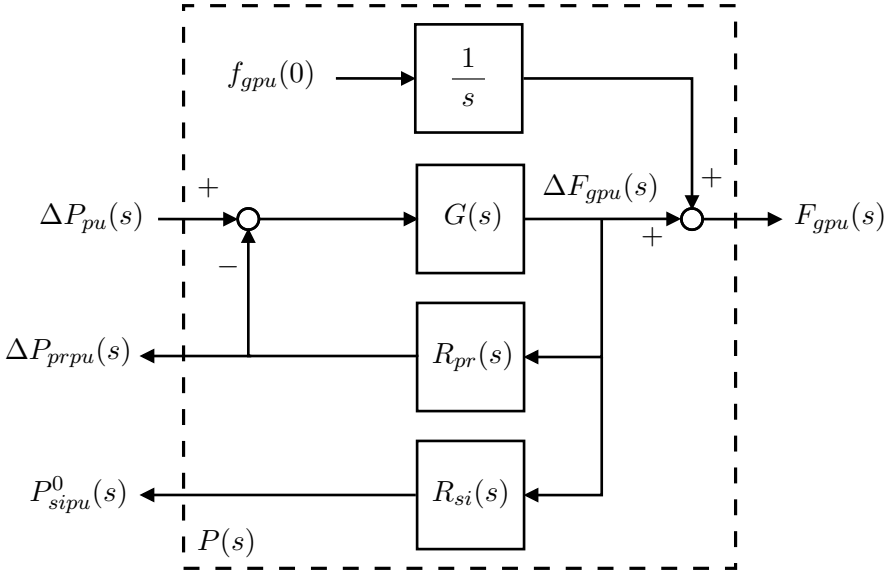

Figure 2.30: HVDC-based synthetic inertia regulator $R_{si}(s)$ and primary frequency regulator $R_{pr}(s)$ in Laplace domain. $P^0_{sipu}(s)$ is transferred to HVDC station controller and summed at power setpoint.

Besides control implementation, one of main topic about such technique is where to access energy needed to realize inertial power flow.

Most of recent works focus on wind farms spinning reserve [92], also with the help of storage capacitors or lithium batteries [93, 94]; such approach is definitely promising and interesting, but has two main disadvantages:

- despite growing size, wind turbines inertia is globally low compared to a traditional generator;

- wind farms are not available everywhere in order to realize such functionality.

A possible solution is using the HVDC link to keep power from another AC grid (AC grid 2 in the specific case); the result is a frequency drift also in the second network, due to transitory power imbalance: the "disturbance" is propagated from one synchronous zone to another one.

To avoid such effect, a further option is going to be investigated: keeping the whole energy from a storage system. Every AC/DC station is equipped with DC-side capacitive filters, to limit voltage ripple; because a HVDC link still provides a couple of high power converters, there is no gain in adding a further converter for

storage interface: DC capacitors can be oversized to store enough energy and perform synthetic inertia.

This way, DC link itself becomes the storage device.

As shown before, simulation model uses three level NPC converters to create a bipolar grid, with neutral point grounded at both sides (Fig. 2.7).

Fig. 2.31 focuses on DC link capacitors setup.

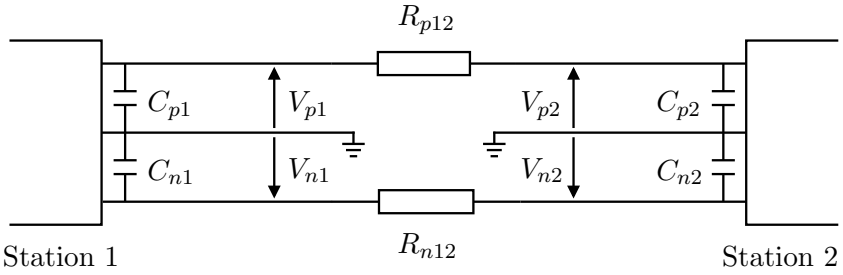

Figure 2.31: HVDC link used in simulation models (Fig. 2.20 and followings): bipolar structure is given by three-phase NPC converters. DC pole capacitors must be oversized to provide energy storage features.

Spilling or injecting energy from/to DC link implies a voltage variation; once maximum and minimum thresholds are given, energy depends on capacitance only.

Observing Fig. 2.31, cable per-length capacitance is neglected. Resistors (R_{p12} and R_{n12}) model DC losses and voltage drops. Each station capacitor is called pole capacitor, being subjected to a so-called pole voltage, positive (V_{p1}, V_{p2}) or negative (V_{n1}, V_{n2}).

Neglecting in this phase line resistance, total DC link capacitance C_{dc12} is:

$$C_{p1} = C_{p2} = C_{n1} = C_{n2} = C_{dc12} \tag{2.45}$$

Due to DC link structure and symmetry, any pole capacitor is set equal to C_{dc12}.

As explained above, power converters have a certain level of efficiency, so energy needed to provide expected inertial responses, then capacitor sizing, must be a little higher than theoretical one.

In this work, HVDC stations initially work in steady state, according to power flows of Fig. 2.20 and Tab. 2.3.

For $t \leq T_{l1}$, DC link losses $P_{jdc12pu}$ are constant and equal to:

$$P_{jdc12pu} = P_{ac1pu} - P_{ac2pu} = -0.006 \tag{2.46}$$

P_{ac1pu} and P_{ac2pu} values are available from both simulation 1 and simulation 2 in steady state condition ($t \leq T_{l1}$); as shown in Fig. 2.25, power flow through HVDC link does not change during inertial phase, so DC link efficiency η_{dc12} results:

$$\eta_{dc12} = 1 - \frac{P_{jdc12pu}}{P_{ac1pu}} = \frac{P_{ac2pu}}{P_{ac1pu}} = 0.93 \tag{2.47}$$

Using such efficiency value, gross inertial energy to be preventively stored in DC link results from $\hat{W}_{is1net}$ of simulation 2:

$$W_{sigross1} = \frac{\hat{W}_{sinet1}}{\eta_{dc12}} = 70.2 \text{ MJ} \tag{2.48}$$

Result of (2.48) is a simplification because during inertial transient VSC converter working point will be change, thus the efficiency: anyway, a reasonable precautionary margin is given by choosing $\hat{W}_{is1net}$ to compute gross energy; as shown in Fig. 2.29, energy at the end of transient is about one half of $\hat{W}_{is1net}$.

DC link voltage fluctuation is also simplified, according to (2.45): neglecting line resistance, voltage is considered constant along the whole line, in order to compute total DC link capacitance in a easy way.

Assuming rated pole voltage $V_{pn} = V_{nn} = 100$ kV as base value, initial and minimum voltage thresholds during inertial phase are set:

$$V_{pn} = 100 \text{ kV} \quad , \quad V_{dcpu} = 1 \quad , \quad V_{dcminpu} = 0.9 \tag{2.49}$$

Due to all above calculations and assumptions, DC link capacitance sizing is the following:

$$C_{dc12} = \frac{W_{sigross1}}{2(V_{dcpu}^2 - V_{dcminpu}^2)V_{pn}^2} = 18.48 \text{ mF} \tag{2.50}$$

In practice, during inertial transient, it is expected DC link voltage will be lowered at about 0.9 p.u. (a little bit less, considering precautionary sizing used for capacitors). After $t = 5$ s, DC link voltage should rise again, according to energy profile in Fig. 2.29.

Such behavior depends not only by correct capacitor sizing but also by VSC converter ability in following synthetic inertia power setpoint P_{si1pu}^0.

Next simulation implements DC link capacitance oversizing and HVDC-based inertial control.

2.9.1 Simulation 3: HVDC-based synthetic inertia algorithm

Simulation 2 is repeated using controller shown in Fig. 2.30 in replacement of the one in Fig. 2.21. Synthetic inertia power (P_{si1pu}) comes from station 1 VSC converter by means of signal P^0_{si1pu}. DC link capacitance (C_{dc12}) is empowered according to (2.50).

Simulation grid setup is shown in Fig. 2.32.

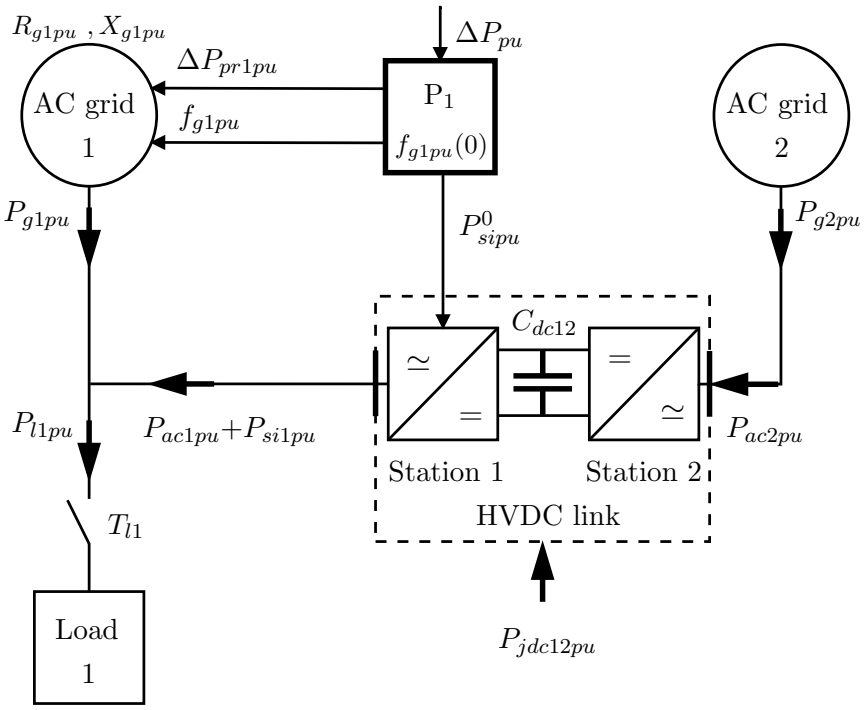

Figure 2.32: Network used in HVDC-based synthetic inertia simulation. AC grid 1 frequency system (bold square) is shown in Fig. 2.30. DC link (C_{dc12}) is sized according to calculations in Par. 2.9.

Steady state conditions before load step are the same as simulation 1 and 2, as shown in Tab. 2.3.

As previously, HVDC stations are both controlled as *Slaves*; station 2 keeps constant power flow at AC grid 2 side, while station 1 manages inertial power in addition to original setpoint. DC link power flow in steady state is set as previously.

Synthetic inertia coefficient is set as one half of AC grid 1 starting time:

Targets of simulation 3 are:

- testing HVDC power response in comparison to ideal synthetic inertia algorithm;
- verify proper sizing of DC link capacitance in order to "protect" AC grid 2 by frequency disturbance.

Simulation 3 power profiles are shown in Fig. 2.33.

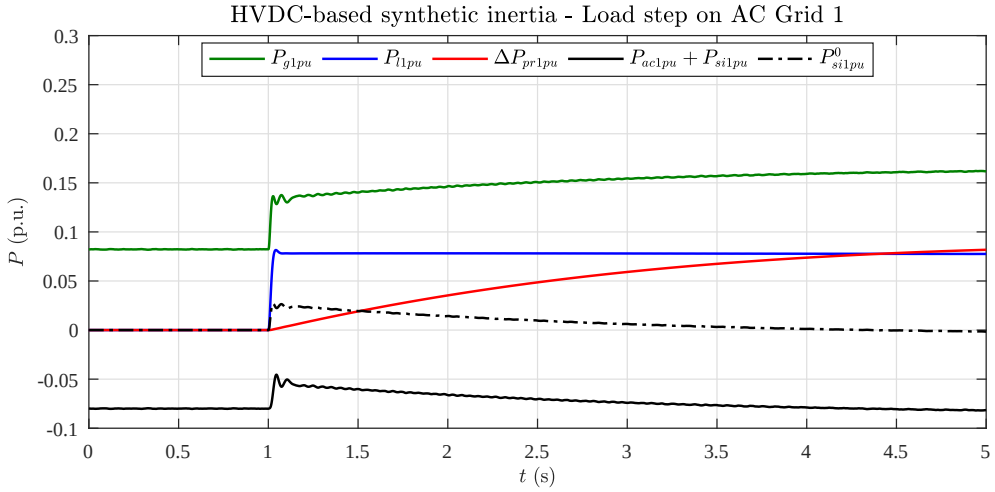

Figure 2.33: Simulation 3 results: power profiles on AC grid 1 with HVDC-based synthetic inertia.

Base power: 2000 MVA.

Primary frequency control still balances power in about 15 s after loading, at lower slope; simulation time was then limited at 5 s to highlight transient results. Primary power P_{pr1pu} is still provided by AC grid 1 itself.

Fig. 2.34 shows station power profiles (AC side) and their setpoint, respectively.

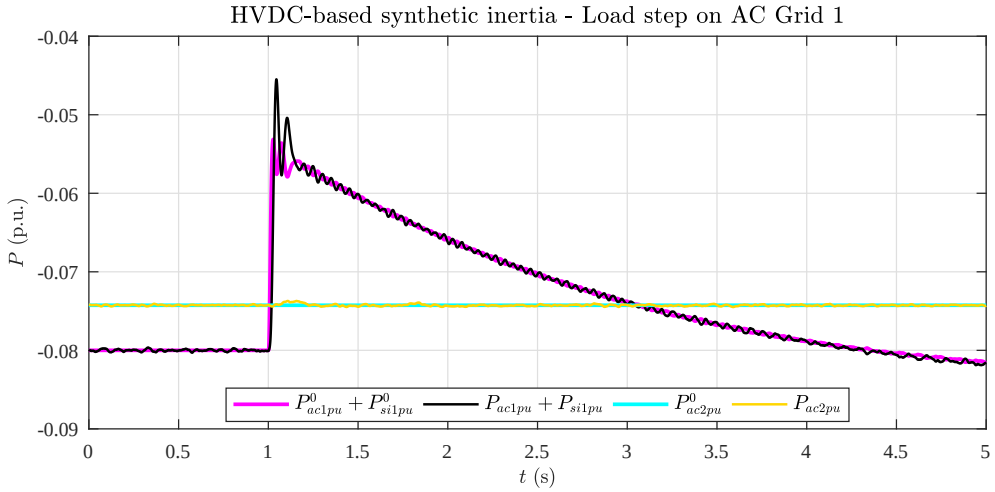

Figure 2.34: Simulation 3 results: HVDC stations power profiles (and setpoint) with HVDC-based synthetic inertia.

Base power: 2000 MVA.

Apart minor oscillations due to VSC converter response, stations perfectly follow setpoints given by respective controllers; inertial power P_{si1pu} has the same profile as simulation 2.

The result is that load step effect is not propagated to AC grid 2, while DC link provides necessary energy to realize the inertial function.

Fig. 2.35 shows voltage profiles of HVDC stations (DC link voltage at both sides).

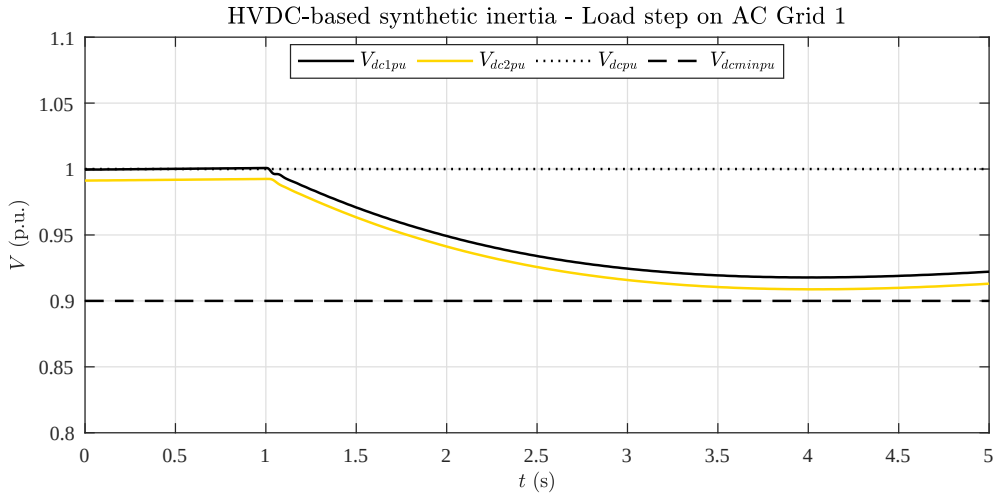

Figure 2.35: Simulation 3 results: HVDC stations voltage profiles with HVDC-based synthetic inertia.

Base voltage: 200 kV.

As expected, voltage is reduced by inertial power spill, it reaches the minimum within given tolerance of 0.9 p.u.. Also V_{dc2pu}, initially lower (0.99 p.u.), does not falls below $V_{dcminpu}$.

HVDC section is sized properly to provide to AC grid 1 needed inertial power.

It must be noted that DC voltages in Fig. 2.27 have a higher ripple respect to ones in Fig. 2.34: it is another effect of C_{dc12} empowering.

About AC grid 1, frequency profile (in Hz) and MFD are shown in in Fig. 2.36. Results of simulation 2 (ideal synthetic inertia) are plot in black for direct comparison.

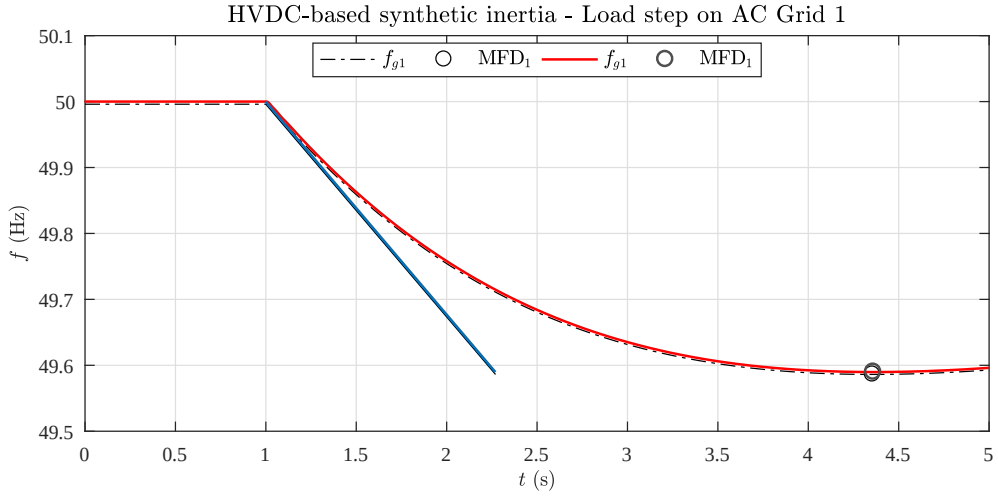

Figure 2.36: Simulation 3 results: frequency profile and MFD (Maximum Frequency Deviation) on AC grid 1 with HVDC-based synthetic inertia. The slope of blue straight line shows graphically ROCOF$_1$ trend at the beginning of transient.

Results of simulation 2 (ideal synthetic inertia) in black for direct comparison.

Simulation 3 numerical results are summarized in Tab. 2.7 and compared to simulation 2 (ideal synthetic inertia) and simulation 1 (no synthetic inertia):

Table 2.7: Simulation 3 results: HVDC-based synthetic inertia.

Simulation	T_{avvg1} (s)	k_{si1} (s)	ROCOF_1 (Hz/s)	MFD_1 (Hz)
1) No synthetic inertia	8	0	-0.50	-440
2) Ideal synthetic inertia	8	4	-0.33 (-34%)	-410 (-7%)
3) HVDC-based synthetic inertia	8	4	-0.33 (-34%)	-410 (-7%)

HVDC-based synthetic inertia has exactly the same effect of ideal synthetic inertia, (ROCOF_1 -33%, MFD -7%).

In can be concluded VSC converter and related capacitors can fulfill inertial requirements in a satisfactory way.

2.9.2 Simulation 4,5 and 6: Unload step test

Simulation 3 results were encouraging by the functional point of view; inertial function was successfully implemented and DC link voltage was kept within expected tolerance band; load steps are probably the worst cases regarding frequency disturbances generation, because extra energy must be provided to compensate them.

In case of load rejection, instead, synthetic inertial contribution should operate in the opposite way, to smooth frequency raise; HVDC equipment is requested to store energy, so DC link voltage will increase accordingly; capacitor sizing is critical due to insulation operative limits.

To test such condition, simulations from 1 to 3 have been repeated changing AC grid 1 initial conditions according to Tab. 2.8.

Table 2.8: Initial load flow results in p.u. for unload step tests (base power A_{g1n}=2000 MVA).

Input	Symbol	Value	Comment
Load 1 active power	P_{l1pu}	-0.08	
Station 1 active power	P_{ac1pu}	0.08	
Station 1 DC voltage	V_{dc1pu}	1	Base voltage V_{dc1n}=200 kV
Output	**Symbol**	**Value**	**Unit**
Station 2 active power	P_{ac2pu}	-0.074	
Station 2 DC voltage	V_{dc2pu}	0.99	Base voltage V_{dc2n}=200 kV

At t=T_{l1}, Load 1 is disconnected from AC grid 1 (unload step).

Simulation 4 models therefore the unload step case with no synthetic inertia, simulation 5 and 6 evaluate ideal and HVDC-based synthetic inertia response in the same condition.

Simulation grid setups are the same as Fig. 2.20, Fig. 2.24 and Fig. 2.32, with the difference that load 1 breaker is initially closed.

HVDC power flow in steady state is set as previously, and also synthetic inertia coefficient.

Inertial controllers are still the ones in Fig. 2.21 and Fig. 2.30, respectively.

According to Tab. 2.8, HVDC initial power flows are still the same, so efficiency η_{dc12} does not change in value:

$$\eta_{dc12} = 1 - \frac{P_{jdc12pu}}{P_{ac1pu}} = \frac{P_{ac2pu}}{P_{ac1pu}} = 0.93 \tag{2.51}$$

In this case, inertial power flow will be reversed, so energy will too: integral of P_{si1pu} becomes the gross energy (it was the net before), because of DC link efficiency:

$$W_{sigross1}(t) = \int P_{si1pu}(t)dt \tag{2.52}$$

As previously, ideal synthetic inertia simulation provides sizing data about energy (Fig. 2.37). As expected, because of model linearity, gross energy in simulation 5 equals (apart the sign) the value of net energy in simulation 2:

$$\hat{W}_{sigross1} = \min\left(W_{sigross1}\right) = -65.3 \text{ MJ} \tag{2.53}$$

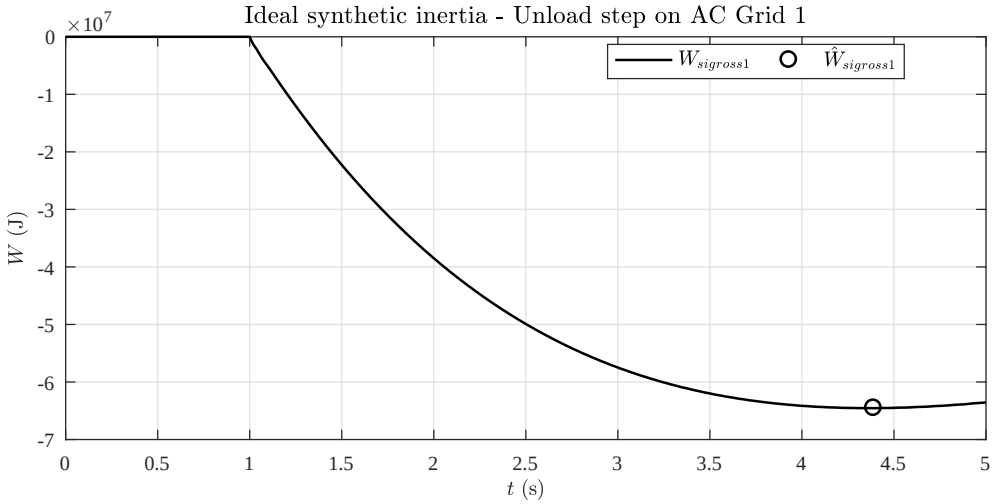

Figure 2.37: Simulation 4 results: gross energy ($W_{sigross1}$) needed to perform synthetic inertia function according to (2.52).

Net energy results:

$$W_{sinet1} = \hat{W}_{sigross1}\eta_{dc12} = -60.7 \text{ MJ} \tag{2.54}$$

As a consequence, DC link capacitance (C_{dc12}) sizing should change respect to (2.50), also because of different voltage gap:

$$V_{pn} = 100 \text{ kV} \quad , \quad V_{dcpu} = 1 \quad , \quad V_{dcMAXpu} = 1.1 \tag{2.55}$$

In practice, during inertial transient, it is expected DC link voltage will increase up to 1.1 p.u. (a little bit less, considering precautionary sizing used for capacitors).

After $t = 5$ s, DC link voltage should fall again, according to Fig. 2.37 results.

Due to all above calculations and assumptions, DC link capacitance sizing is the following:

$$C_{dc12} = \frac{W_{sinet1}}{2(V_{dcpu}^2 - V_{dcMAXpu}^2)V_{pn}^2} = 14.50 \text{ mF} \tag{2.56}$$

Calculations demonstrated that capacitor sizing to handle the unload step is less demanding respect to an equivalent load step: check was necessary to avoid unexpected overvoltage on DC link; for simplicity, capacitors have been kept equal as previous, so simulation 6 was performed with C_{dc12} =18.48 mF.

For brevity, simulation 4 and 5 power profiles are neglected, simulation 6 ones are shown in Fig. 2.38.

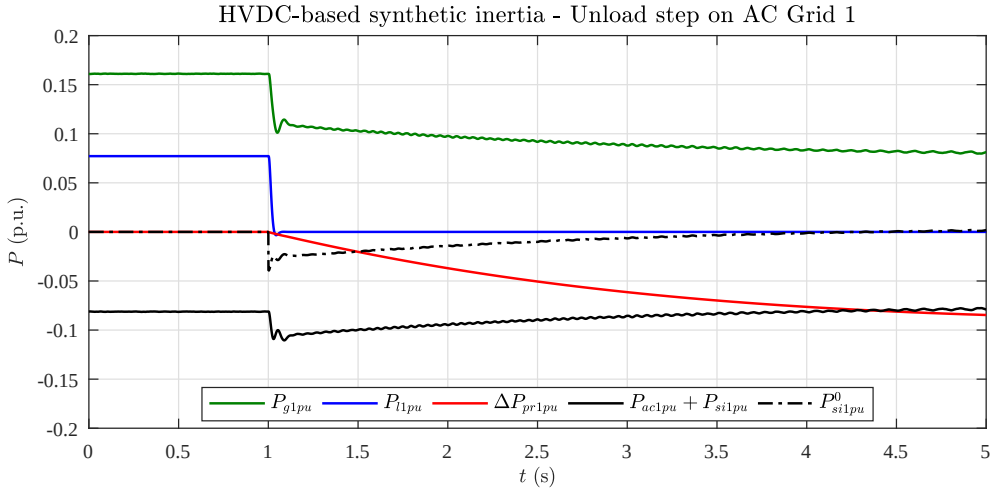

Figure 2.38: Simulation 6 results: power profiles on AC grid 1 with HVDC-based synthetic inertia.

Base power: 2000 MVA.

Primary frequency control still balances power in about 15 s after unloading; simulation time was then limited at 5 s to highlight transient results. Primary power P_{pr1pu} is still managed by AC grid 1 itself.

As previously, HVDC stations are both controlled as *Slaves*; station 2 keeps constant power flow at AC grid 2 side, while station 1 manages inertial power in addition to original setpoint.

Fig. 2.39 shows station power profiles (AC side) and their setpoint, respectively:

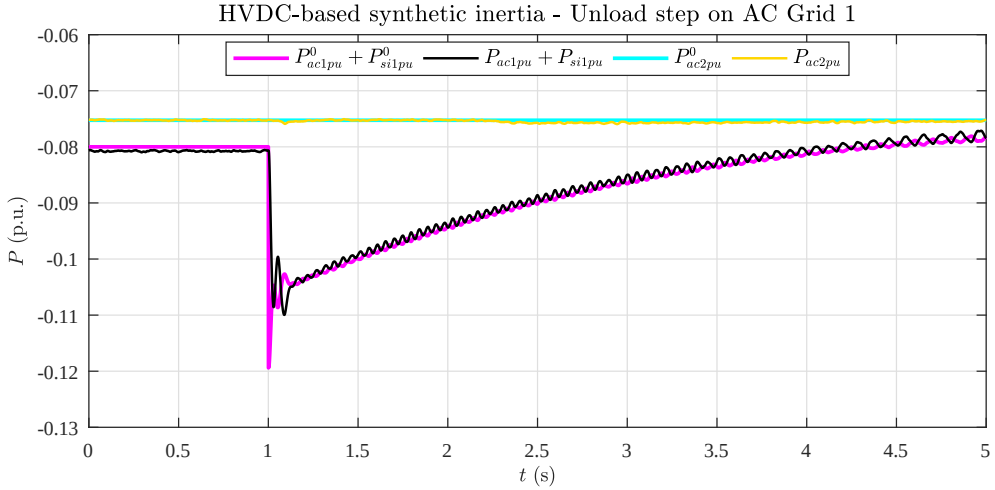

Figure 2.39: Simulation 6 results: HVDC stations power profiles (and setpoint) with HVDC-based synthetic inertia.

Base power: 2000 MVA.

Apart minor oscillations due to VSC converter response, stations perfectly follow setpoint given by respective controllers; inertial power P_{si1pu} has the same profile as simulation 5, here neglected.

The result is that load step effect is not propagated to AC grid 2, while DC link

absorbs energy to realize the inertial function.

Fig. 2.40 shows voltage profiles of HVDC stations (DC link voltage at both sides).

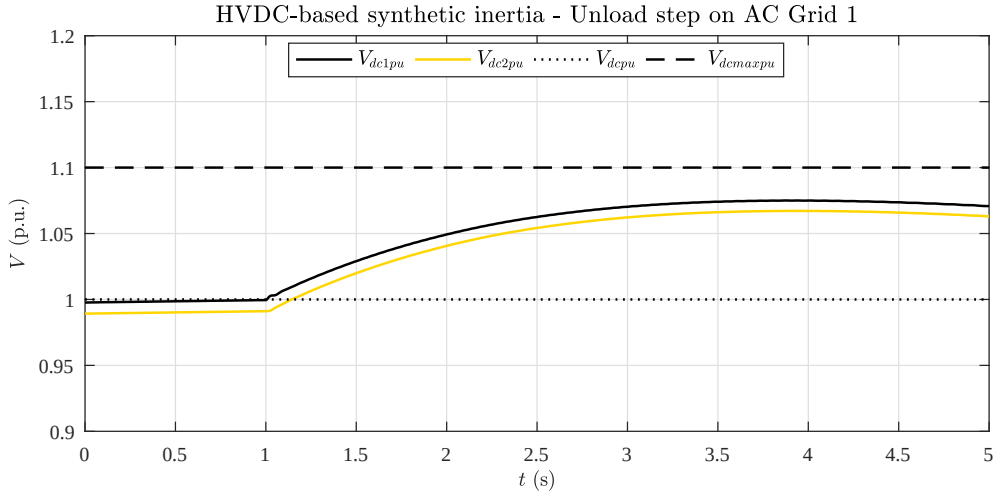

Figure 2.40: Simulation 6 results: HVDC stations voltage profiles with HVDC-based synthetic inertia.

Base voltage: 200 kV.

As expected, voltage is increased by inertial power injection, it reaches the maximum within given tolerance of 1.1 p.u.. In this case, V_{dc2pu} is not an issue, being initially lower (0.99 p.u.).

HVDC section is sized properly to absorb from AC grid 1 the inertial power.

About AC grid 1, simulation 6 frequency profile (in Hz) and MFD are shown in Fig. 2.41. Results of simulation 4 (ideal synthetic inertia) are plot in black for direct comparison.

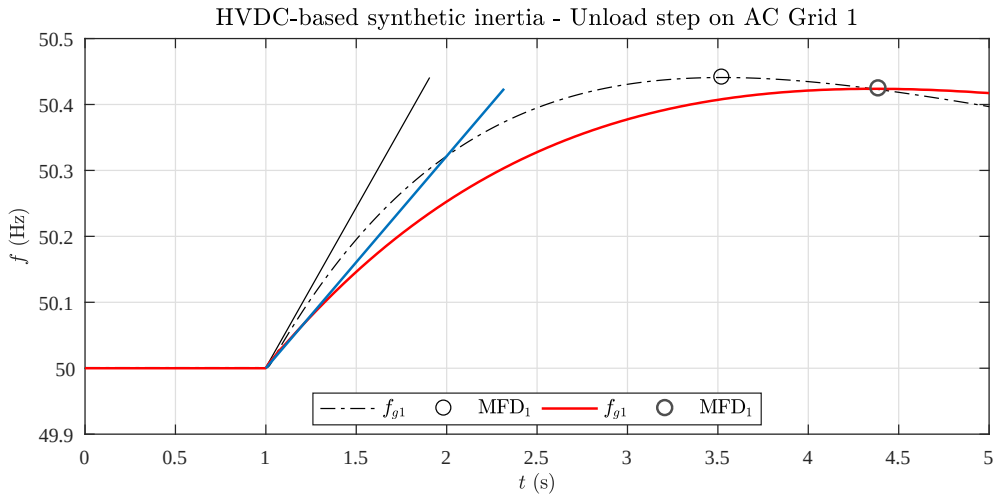

Figure 2.41: Simulation 6 results: frequency profile and MFD (Maximum Frequency Deviation) on AC grid 1 with HVDC-based synthetic inertia. The slope of blue straight line shows graphically ROCOF$_1$ trend at the beginning of transient.

Results of simulation 4 (ideal synthetic inertia) in black for direct comparison.

Simulation 4, 5 and 6 numerical results are summarized in Tab. 2.9.

Table 2.9: Simulation 4, 5 and 6 results: synthetic inertia with unload step.

Simulation	T_{avvg1} (s)	k_{si1} (s)	ROCOF_1 (Hz/s)	MFD_1 (Hz)
4) No synthetic inertia	8	0	0.50	440
5) Ideal synthetic inertia	8	4	0.33 (-34%)	410 (-7%)
6) HVDC-based synthetic inertia	8	4	0.33 (-34%)	410 (-7%)

Results are equal (apart the sign) respect to ones in Tab: 2.7: this is due to system linearity and by proper choice of grid initial conditions.

HVDC-based synthetic inertia, moreover, has the same effect of ideal synthetic inertia, (ROCOF_1 -33%, MFD -7%): once again, VSC converter demonstrated a good dynamic behavior.

2.9.3 HVDC link empowering: sensitivity analysis

Previous simulations showed that energy exchanged by a HVDC link can successfully perform synthetic inertia.

Load step case is the worst for capacitor sizing, because gross energy must be previously stored into DC link. It is therefore interesting assesses how inertial performances are affected by capacitance.

A sensitivity analysis has been done: dependence between the synthetic inertia coefficient (k_{si1}) and pole capacitors sizing (C_{dc12}) has been investigated.

Simulation 2 has been repeated for different values of k_{si1}, with the same starting conditions; case by case, pole capacitors have been sized with (2.50), according to different values of energy given by (2.48).

Results are summarized in Tab. 2.10.

Table 2.10: Simulation 2 results for different values of k_{si1}.

Case	T_{avvg1} (s)	k_{si1} (s)	ROCOF$_1$ (Hz/s)	MFD$_1$ (mHz)	C_{dc12} (mF)
1	8	-	-0.50	-440	(0.07)
2	8	0.05	-0.50 (-)	-437 (-1%)	0.23
3	8	0.10	-0.49 (-1%)	-433 (-2%)	0.45
4	8	0.25	-0.48 (-3%)	-427 (-3%)	1.13
5	8	0.50	-0.47 (-6%)	-423 (-4%)	2.28
6	8	1.00	-0.44 (-11%)	-419 (-5%)	4.58
7	8	2.00	-0.40 (-20%)	-413 (-6%)	9.24
8	8	4.00	-0.33 (-33%)	-410 (-7%)	18.48

Case 1 corresponds to simulation 1, where no synthetic inertia action is given and pole capacitors are sized for DC voltage ripple limitation only; from case 2 to case 8, synthetic inertia coefficient k_{si1} is set from a minimum of 50 ms up to 4 s.

HVDC link capacitor sizing to implement listed values of k_{si1} is shown in Fig. 2.42.

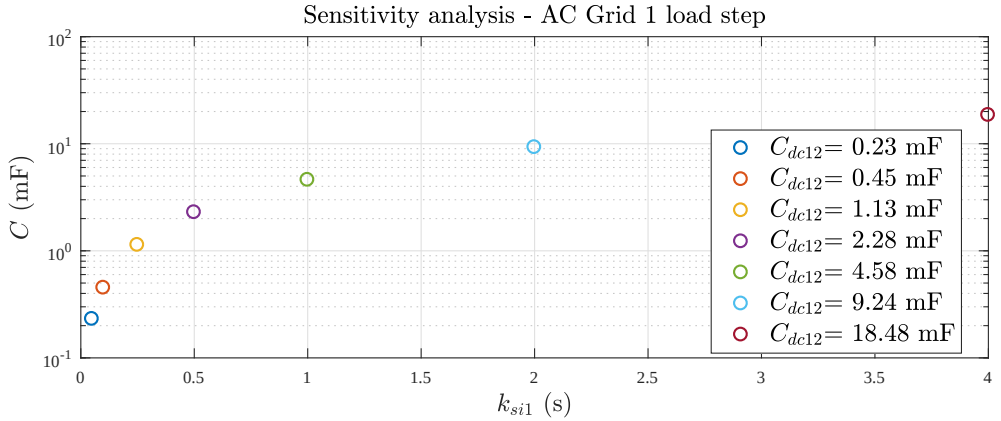

Figure 2.42: Sensitivity analysis: DC link capacitors sizing (C_{dc12}) to implement different values of k_{si1}. Load step on AC grid 1 with HVDC-based synthetic inertia.

The biggest pole capacitor is about 80 times the functional one (70 μF for DC voltage ripple, no synthetic inertia action).

Capacitors sizing could be technically feasible, even not negligible; anyway, tangible effect can be achieved also with half capacitance (9.24 mF).

Simulation 3 has been repeated then, sizing capacitors as in Tab. 2.10; results are listed in Tab. 2.11.

Table 2.11: Simulation 3 synthetic inertia response for different pole capacitors sizing.

Case	T_{avvg1} (s)	C_{dc12} (mF)	k_{si1} (s)	ROCOF$_1$ (Hz/s)	MFD$_1$ (mHz)
1	8	(0.07)	-	-0.50	-440
2	8	0.23	0.05	-0.50 (-)	-437 (-1%)
3	8	0.45	0.10	-0.49 (-1%)	-433 (-2%)
4	8	1.13	0.25	-0.48 (-3%)	-427 (-3%)
5	8	2.28	0.50	-0.47 (-6%)	-423 (-4%)
6	8	4.58	1.00	-0.44 (-11%)	-419 (-5%)
7	8	9.24	2.00	-0.40 (-20%)	-413 (-6%)
8	8	18.48	4.00	-0.33 (-33%)	-410 (-7%)

Comparing Tab. 2.11 with Tab. 2.10, results between simulation 3 and simulation 2 are basically the same (as for Fig. 2.36), confirming the good response of station 1 VSC converter in performing synthetic inertia action.

About performances, capacitance empowering produces only a little effect on MFD$_1$, while improvement on ROCOF$_1$ is remarkable.

Effect of synthetic inertia performances can be graphically appreciated in Fig. 2.43, where AC grid 1 frequency profiles for different values of k_{si1} are shown.

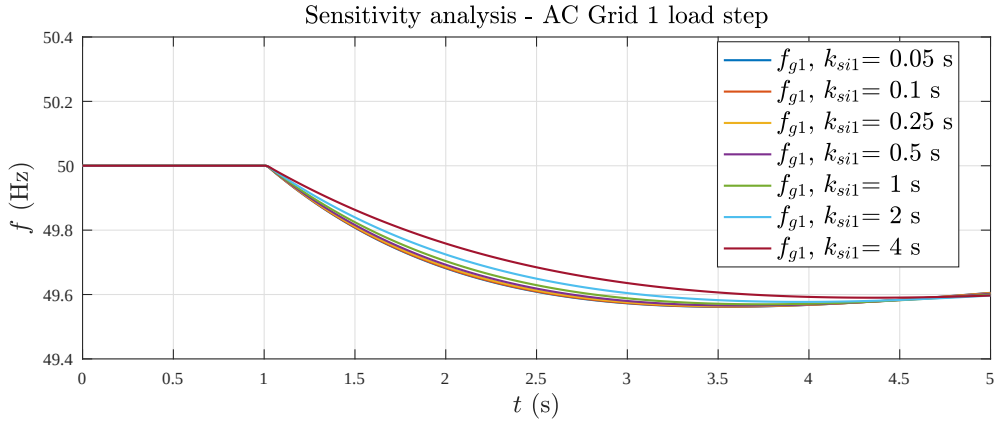

Figure 2.43: Sensitivity analysis: frequency profile on AC grid 1 with different values of k_{si1}. HVDC-based synthetic inertia.

2.9.4 Simulations results

All above simulations show that:

- AC grid frequency variation can be effectively compensated by a synthetic inertia control, provided that the necessary inertial energy and a sufficiently precise and accurate measurement of the frequency derivative is available;

- synthetic inertia can be efficiently implemented into a HVDC power converter, using the energy exchanged with the DC side capacitors; the effect is "transparent" at the downstream AC grid if the capacitors sizing is enough to exchange the total inertial energy needed by the control;

- moderate capacitor oversizing is recommendable because steady state conditions of the grid before synthetic inertia engage are unknown, so the needed power profile could increase losses and waste a strong part of the inertial energy exchanged with the AC grid. The sensitivity analysis shows that, to obtain an effective improvement of the inertia support, the capacitance increase is nor negligible.

About DC-grid control, main issues about "classical" inertial approach are the followings:

- it can be simply implemented on *Slave* nodes only, where direct control of active power is possible;

- during inertial action, *Master* node action must be blocked, let DC link voltage to change according to needed inertial energy.

Second point of above list is definitely demanding, because it puts DC link is out of control; voltage limitation protections are anyway always active in VSC controllers, but it should really preferable achieving synthetic inertial function also on a *Master* node.

Due to this, in next section an innovative synthetic inertial algorithm based on DC link voltage control is presented and then tested.

2.10 Innovative synthetic inertia algorithm: INEC

Consider again electromechanical system in Fig. 2.12, whose status equations in per unit have been developed in Par. 2.7.

$$P_{E_{pu}}(t) - P_{L_{pu}}(t) = \Delta P_{pu}(t) \approx T_{avvG} f_{Gpu}(0) \frac{d\Delta f_{Gpu}(t)}{dt} \tag{2.57}$$

$$T_{avvG} = J_G \frac{(2\pi f_{Gn})^2}{P_{Gn}}. \tag{2.58}$$

T_{avvG} can be expressed by means of an inertial coefficient H_G, defined as the ratio between machine rated energy (W_{Gn}) and rated power (P_{Gn}); in practice, H_G is the time necessary to put the generator at rated speed (starting from zero) applying rated power:

$$H_G = \frac{W_{Gn}}{P_{Gn}} = \frac{1}{2} J_G \frac{(2\pi f_{Gn})^2}{P_{Gn}} = \frac{T_{avvG}}{2} \tag{2.59}$$

Consequently, (2.57) can be written as:

$$\Delta P_{pu}(t) \approx 2 H_G f_{Gpu}(0) \frac{d\Delta f_{Gpu}(t)}{dt}. \tag{2.60}$$

As shown in Fig. 2.13 and Fig. 2.14, model of (2.60) well represents system behavior around rated frequency (f_{G_n}) only; in such case, and neglecting equipment efficiency, it is supposed all power ΔP_{pu} is provided by an equivalent capacitor (C_{dc}), connected to electrical grid by an (ideal) power converter; $V_{C_{dc}}$ is voltage at capacitor terminals, converter power P_{ac} is measured as in Fig. 2.44.

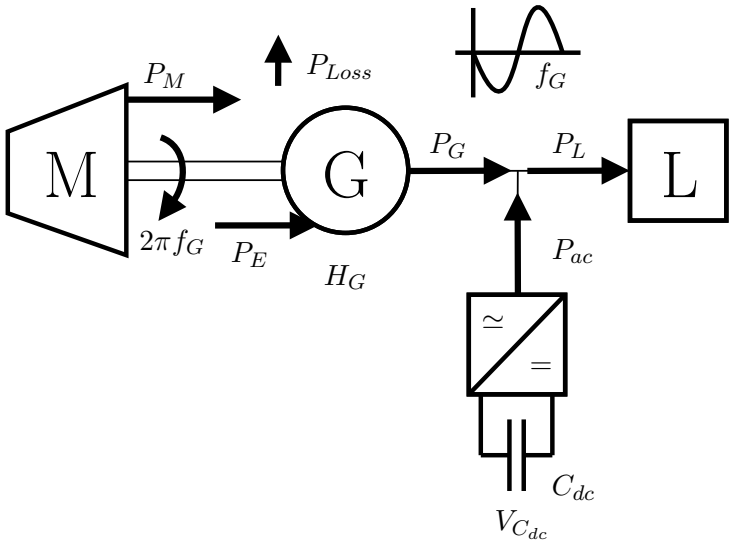

Figure 2.44: Electromechanical system and equivalent capacitor for INEC function.

In per unit, using as base power rated machine electrical power P_{G_n}:

$$P_{acpu}(t) = -\frac{C_{dc} V_{C_{dc}}(t)}{P_{Gn}} \frac{dV_{C_{dc}}(t)}{dt} \tag{2.61}$$

Negative sign of (2.61) means positive power flow with negative capacitor derivative, so positive power flow during discharge, as in all previous simulations.

Due to system power balance:

$$P_{acpu}(t) = -\Delta P_{pu}(t) \tag{2.62}$$

Mechanical and electrical quantities can be equated:

$$2H_G f_{Gpu}(0)\frac{d\Delta f_{Gpu}(t)}{dt} = \frac{C_{dc}V_{C_{dc}}(t)}{P_{Gn}}\frac{dV_{C_{dc}}(t)}{dt} \tag{2.63}$$

Capacitor voltage is shown in per unit, using rated voltage $V_{C_{dcn}}$ as base value:

$$V_{C_{dcpu}}(t) = \frac{V_{C_{dc}}(t)}{V_{C_{dcn}}} \quad , \quad \frac{dV_{C_{dcpu}}(t)}{dt} = \frac{1}{V_{C_{dcn}}}\frac{dV_{C_{dc}}(t)}{dt} \tag{2.64}$$

Equation is then integrated:

$$\int \frac{2H_G f_{Gpu}(0)}{V_{C_{dcn}}^2}\frac{d\Delta f_{Gpu}(t)}{dt}dt = \int \frac{C_{dc}V_{C_{dcpu}}(t)}{P_{Gn}}\frac{dV_{C_{dcpu}}(t)}{dt}dt \tag{2.65}$$

$$\frac{2H_G f_{Gpu}(0)}{V_{C_{dcn}}^2}\Delta f_{Gpu}(t) = \frac{C_{dc}}{P_{Gn}}\frac{V_{C_{dcpu}}^2(t)}{2} + c_0 \tag{2.66}$$

Initial condition are imposed as previously (system in rated conditions, frequency in steady state), capacitor is set charged at voltage $V_{C_{dcpu}}(0)$:

$$f_{Gpu}(0) = 1 \quad , \quad \Delta f_{Gpu}(0) = 0 \tag{2.67}$$

Integration constant c_0 is then computed:

$$c_0 = -\frac{C_{dc}}{P_{Gn}}\frac{V_{C_{dcpu}}^2(0)}{2}. \tag{2.68}$$

Full system model is given by substituting (2.68) and (2.67) into (2.66):

$$\frac{2H_G}{V_{C_{dcn}}^2}\Delta f_{Gpu}(t) = \frac{C_{dc}}{P_{Gn}}\frac{V_{C_{dcpu}}^2(t)}{2} - \frac{C_{dc}}{P_{Gn}}\frac{V_{C_{dcpu}}^2(0)}{2} \tag{2.69}$$

Result is so-called INertia Emulation Control (INEC) algorithm equation, a (non-linear) relation between capacitor voltage and frequency deviation:

$$V_{C_{dcpu}}^2(t) = V_{C_{dcpu}}^2(0) + \frac{4H_G P_{Gn}}{V_{C_{dcn}}^2 C_{dc}}\Delta f_{Gpu}(t) \tag{2.70}$$

$$V_{C_{dcpu}}(t) = \sqrt{V_{C_{dcpu}}^2(0) + \frac{4H_G P_{Gn}}{V_{C_{dcn}}^2 C_{dc}}\Delta f_{Gpu}(t)} \tag{2.71}$$

VSC converter is controlled as *Master* and, as soon as frequency deviation is zero, capacitor is kept at rated voltage; a positive frequency drift (grid acceleration) forces

capacitor charge, to absorb extra mechanical power; a negative frequency drift causes instead a capacitor discharge, providing the grid extra power [2].

Global effect is a formally equal to an inertial rotating mass, by means of parameter H_G and according to available energy stored into C_{dc} (capacitor sizing and its rated voltage).

As previously, concept is extended from a single machine to a complex grid; capacitor becomes a HVDC link, p.u. base values are rated grid apparent power A_{gn} (active powers are computed pretending unitary power factor) and grid rated frequency f_{gn}:

$$V_{dcpu}(t) = \sqrt{V_{dcpu}^2(0) + \frac{4H_g A_{gn}}{V_{dcn}^2 C_{dc}} \Delta f_{gpu}(t)} \tag{2.72}$$

A block diagram of (2.72) is shown in Fig. 2.45.

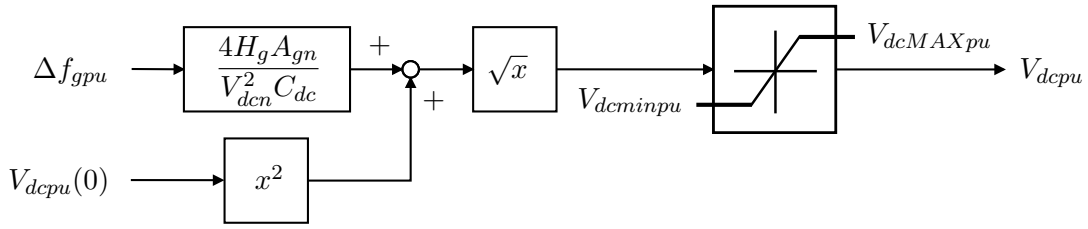

Figure 2.45: INEC synthetic inertia regulator block diagram (R_I).

[2]Epression (2.71) is valid as soon as quantity under square root is positive. With low frequency drops and proper tuning of all other quantities, this is achieved in the most of operative conditions around rated frequency.

The full grid control is shown in Fig. 2.46.

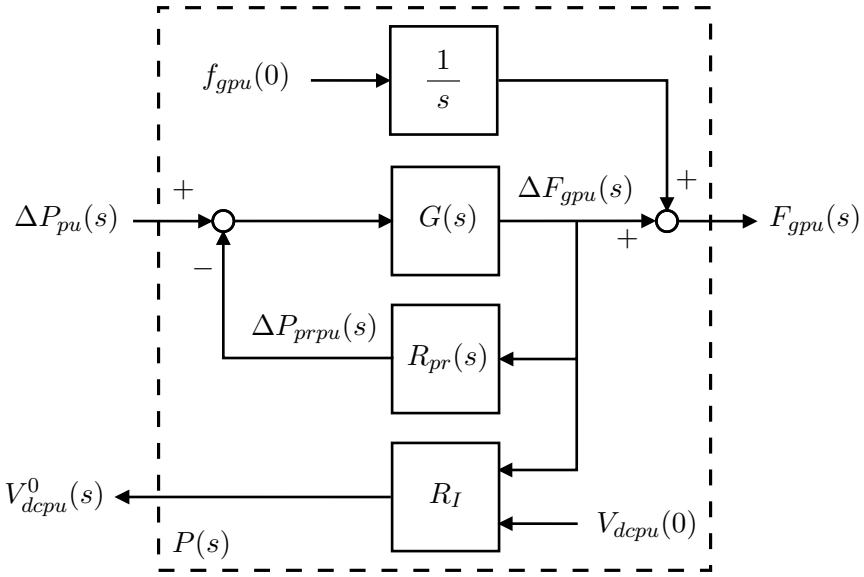

Figure 2.46: INEC synthetic inertia regulator R_I and primary frequency regulator $R_{pr}(s)$ in Laplace domain. $V^0_{dcpu}(s)$ is transferred to HVDC station controller as DC link voltage setpoint.

In practice, output from INEC regulator R_I is transferred to VSC converter control, becoming actual DC link station setpoint; response is mainly depending on converter DC voltage regulator: the fastest it is, the most equipment contributes in increasing system inertia.

Respect to traditional synthetic inertia approach, INEC has theoretically some advantages:

- it can be implemented in the *Master* node of a DC grid;
- it does not require frequency derivative calculation;
- voltage regulation and limits (saturation block in Fig. 2.45) are always active;
- it is self-resetting (DC link voltage goes back at rated value as soon as frequency drift is erased).

On the other side, it has also several drawbacks:

- it is highly non-linear, thus dynamic effect is not so predictable at priori;
- it depends on well-tuning and stability of DC link converter control;
- self-resent must be carefully managed not to generate extra frequency disturbances on the grid.

Next sections will present INEC simulations and a comparison with "classic" inertial algorithm.

2.10.1 Simulation 7: INEC synthetic inertia

Simulation 3 is repeated using controller shown in Fig. 2.46 in replacement of the one in Fig. 2.30. Synthetic inertia power (P_{si1pu}) comes from station 1 VSC converter by means of signal V^0_{dc1pu}. DC link capacitance (C_{dc12}) is empowered according to (2.50).

Simulation grid setup is shown in Fig. 2.47.

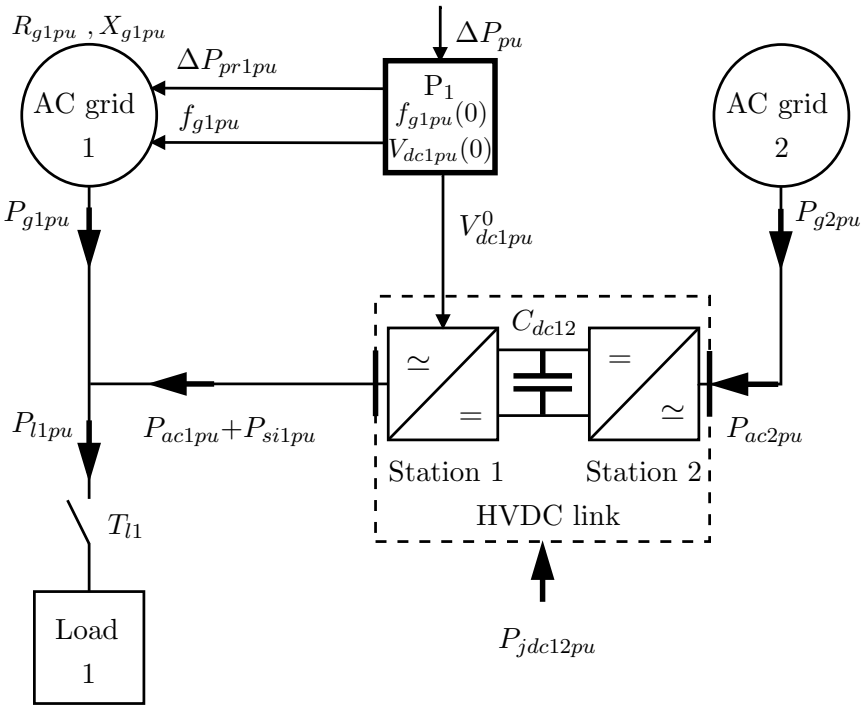

Figure 2.47: Network used in INEC synthetic inertia simulation. AC grid 1 frequency system (bold square) is shown in Fig. 2.46. DC link (C_{dc12}) is sized according to calculations in Par. 2.9.

Station 1 converter is set as *Master*, station 2 as *Slave*; respective voltage and power setpoints are chosen as shown in Tab. 2.3, to achieve same steady state conditions as previously.

According to (2.38) and (2.59), INEC inertial coefficient H_{g1} is set to produce on AC grid 1 the same effect as k_{si}:

$$H_{g1} = \frac{k_{si1}}{2} = 2 \text{ s} \tag{2.73}$$

Targets of simulation 7 are:

- testing INEC power response in comparison to HVDC synthetic inertia algorithm;
- verify proper limiting of DC link voltage in order to "protect" AC grid 2 by frequency disturbance.

Simulation 7 power profiles are shown in Fig. 2.48.

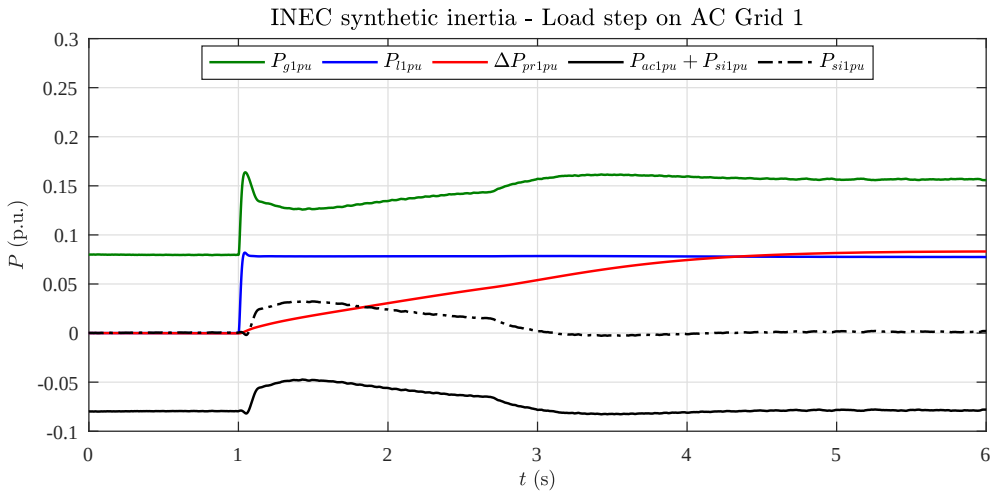

Figure 2.48: Simulation 7 results: power profiles on AC grid 1 with INEC synthetic inertia.
Base power: 2000 MVA.

Respect to Fig. 2.33, P_{si} action is stronger, but it is not as fast as using an algorithm based on frequency drift derivative. This is more evident by comparing Fig. 2.34 with Fig. 2.49.

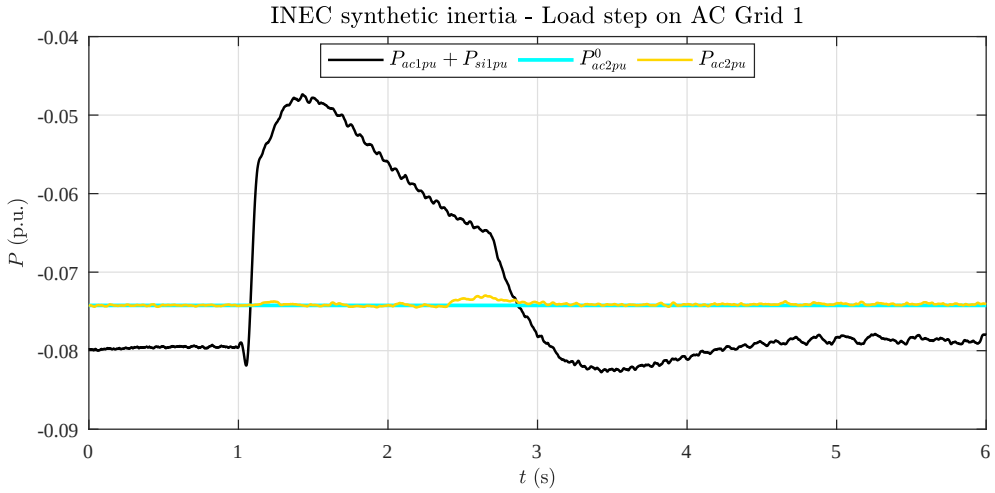

Figure 2.49: Simulation 7 results: HVDC stations power profiles (and setpoint) with INEC synthetic inertia.

Base power: 2000 MVA.

As shown in Fig. 2.50, DC link voltage control well manage power transfer between HVDC and AC grid 1; in particular, all the available inertial energy is transferred, voltage level reaches lower threshold $V_{dcminpu}$.

AC grid 2 is fully protected by frequency disturbance, being station 2 power profile followed by control.

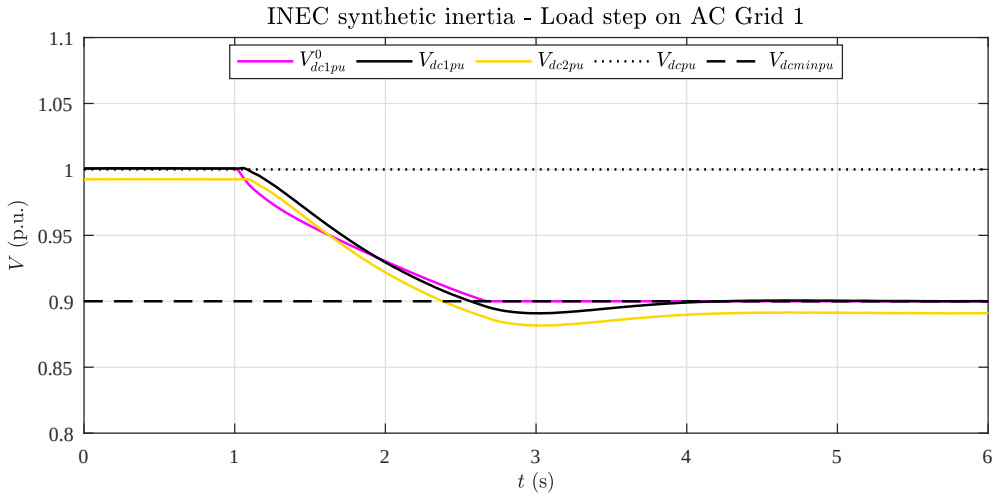

Figure 2.50: Simulation 7 results: HVDC stations voltage profiles with INEC synthetic inertia. Base voltage: 200 kV.

Respect to Simulation 3, small delay in control activation right after load step (t=1 s) causes a degradation in ROCOF performances; more power injection in the first seconds causes instead a stronger frequency deviation. Unfortunately, because available inertial energy has not changed in two cases, as soon as DC link voltage reaches lower threshold, power transfer is stopped by control and frequency profile becomes equal respect to simulation 3. Such aspects can be noted in Fig. 2.51.

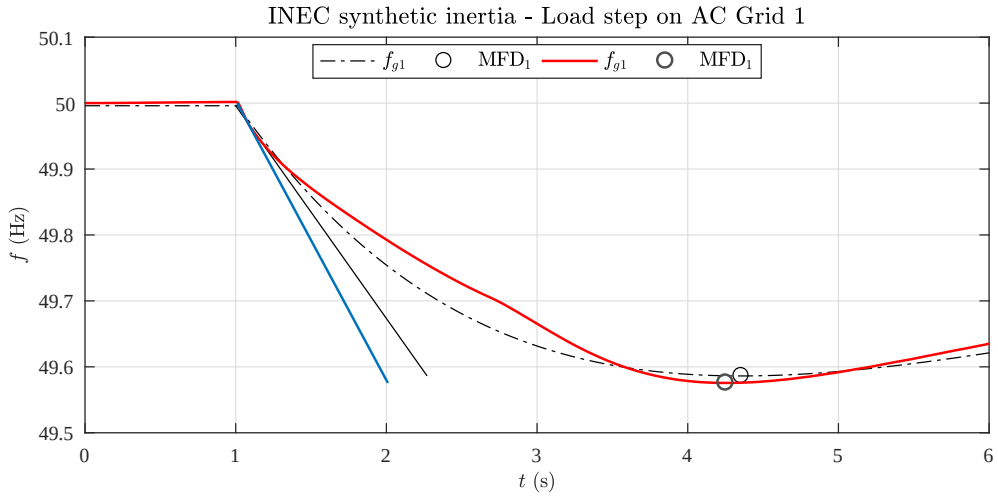

Figure 2.51: Simulation 7 results: frequency profile and MFD (Maximum Frequency Deviation) on AC grid 1 with INEC synthetic inertia. The slope of blue straight line shows graphically ROCOF$_1$ trend at the beginning of transient.
Results of simulation 3 (HVDC-based synthetic inertia) in black for direct comparison.

Simulation 7 numerical results are summarized in Tab. 2.12 and compared to simulation 3 (HVDC-based synthetic inertia):

Table 2.12: Simulation 7 results: INEC synthetic inertia.

Simulation	T_{avvg1} (s)	k_{si1} (s)	H_{g1} (s)	ROCOF$_1$ (Hz/s)	MFD$_1$ (Hz)
3) HVDC-based synthetic inertia	8	4	-	-0.33	-410
7) INEC synthetic inertia	8	-	2	-0.40 (+21%)	-412 (<1%)

Compared to HVDC-based with frequency derivative, INEC control algorithm has a better behavior by DC link voltage point of view, but it cannot achieve acceptable performances in term of ROCOF. Effect on MFD is negligible too. In order to empower and accelerate system response at the very beginning of load transient, some other solutions have been investigated in followings sections.

2.10.2 Simulation 8: INEC-enhanced synthetic inertia

Previous section showed how INEC synthetic inertia algorithm is not sufficiently fast in the very first time of a load step transient: excessive delay in DC link voltage variation causes degradation of performances in terms of ROCOF, with a bad distribution of injected power during the whole transient.

On the other way, direct control of DC link voltage is generally the safest way to operate the system with no risk in exceeding HVDC grid operative limits; it is also the only way to operate a HVDC station in *Master* mode.

Looking for solutions to improve algorithm performances, the easiest measure to speed system response up is by increasing equivalent inertial coefficient H_g: this way, control action should be stronger, forcing a hopefully faster power injection from HVDC to AC grid.

Such action will be effective at the beginning of transient, because inertial energy is still the same (no variations in capacitors sizing and initial voltage): DC link discharge will be probably faster but final threshold $V_{dcminpu}$ will be kept by VSC converter control.

This approach have been named INEC-enhanced synthetic inertia: it is still INEC, HVDC station is still in *Master* mode, only control action entity is higher. Inertial coefficient has been doubled respect to simulation 7:

$$H_{g1} = k_{si1} = 4 \text{ s} \tag{2.74}$$

Targets of simulation 8 are:

- testing INEC-enhanced power response in terms of speed;
- verify proper limiting of DC link voltage in order to "protect" AC grid 2 by frequency disturbance.

Simulation 8 power profiles are shown in Fig. 2.52.

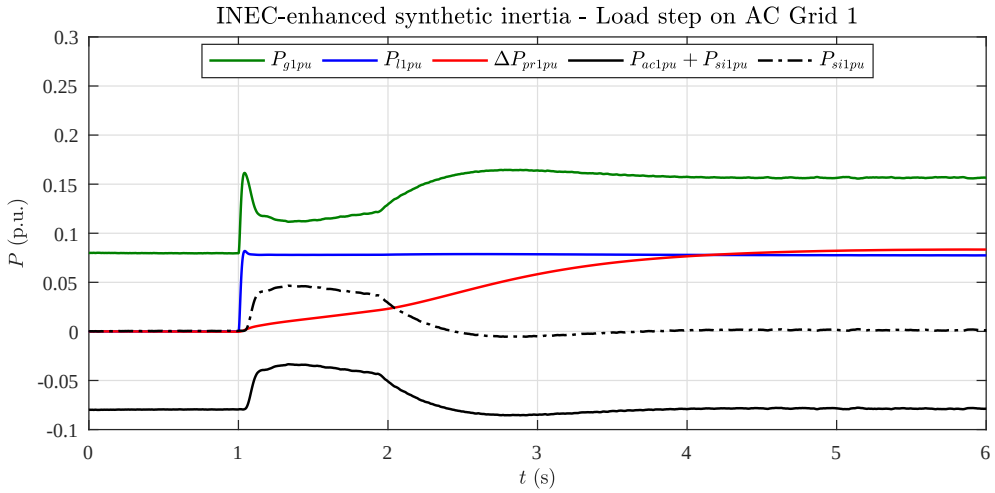

Figure 2.52: Simulation 8 results: power profiles on AC grid 1 with INEC-enhanced synthetic inertia.

Base power: 2000 MVA.

Respect to Fig. 2.48, P_{si} action is stronger as expected, but it is still too slow in the very first time of transient. This is evident by comparing Fig. 2.49 with Fig. 2.53: power peak is higher, but initial delay in injection is basically the same.

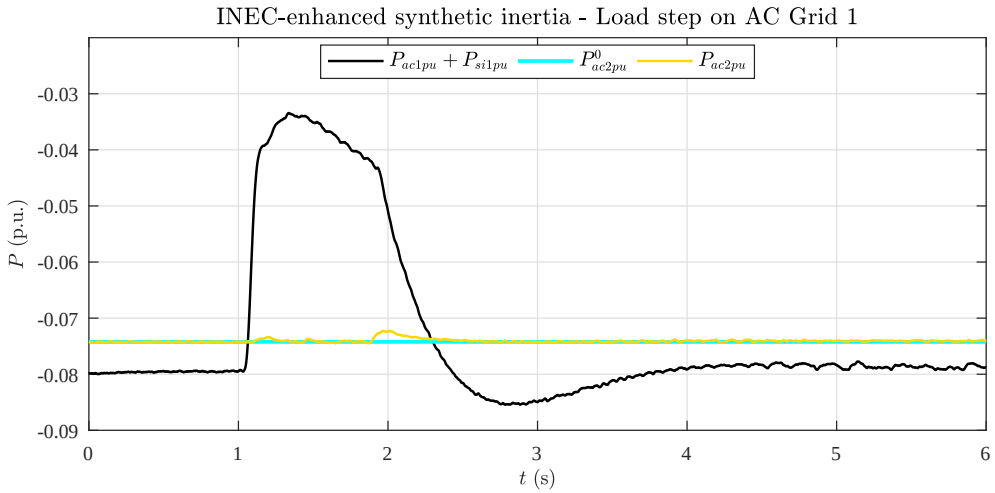

Figure 2.53: Simulation 8 results: HVDC stations power profiles (and setpoint) with INEC-enhanced synthetic inertia.

Base power: 2000 MVA.

As shown in Fig. 2.54, DC link voltage control still well manage power transfer between HVDC and AC grid 1: all the available inertial energy is transferred and voltage level reaches lower threshold $V_{dcminpu}$; anyway, undershoot respect to profile of Fig. 2.50 is a little bit wider. AC grid 2 is also still fully protected by frequency disturbance, being station 2 power profile followed by control.

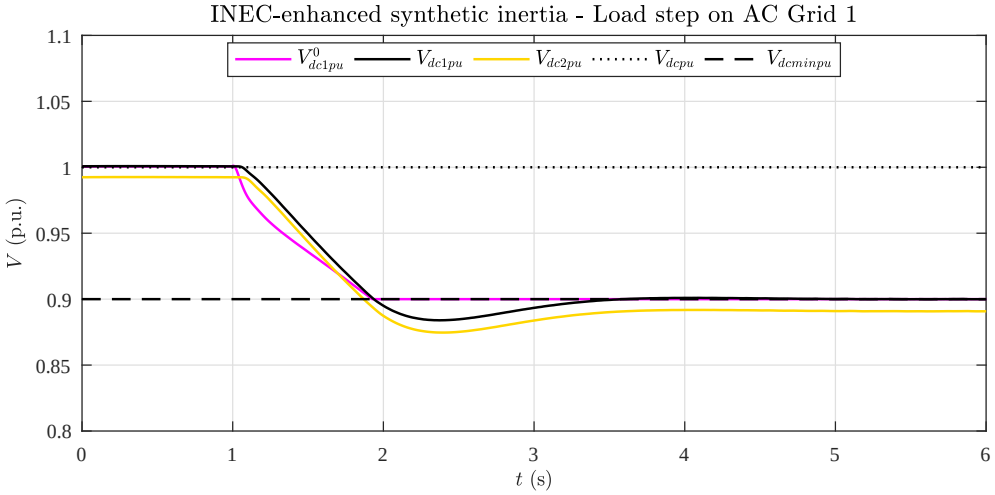

Figure 2.54: Simulation 8 results: HVDC stations voltage profiles with INEC-enhanced synthetic inertia.

Base voltage: 200 kV.

Like Simulation 7, same small delay in control activation right after load step (T_{l1}=1 s) causes exactly the same degradation in ROCOF performances; even more

power injection in the first seconds causes a wider frequency deviation. As expected, despite inertial coefficient change, available inertial energy has not changed in two cases, as soon as DC link voltage reaches lower threshold, power transfer is stopped by control and frequency profile becomes equal respect to simulation 7. Such aspects can be noted in Fig. 2.55.

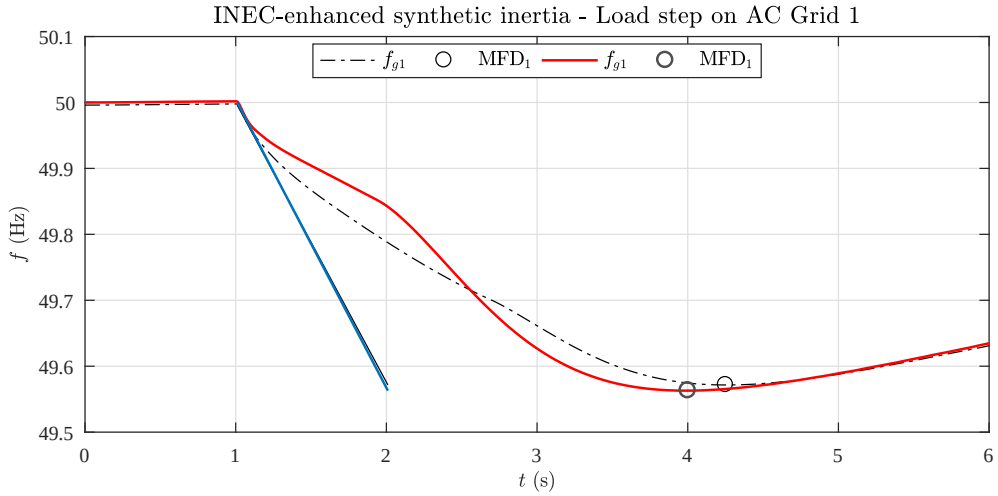

Figure 2.55: Simulation 8 results: frequency profile and MFD (Maximum Frequency Deviation) on AC grid 1 with INEC-enhanced synthetic inertia. The slope of blue straight line shows graphically ROCOF$_1$ trend at the beginning of transient.
Results of simulation 7 (INEC synthetic inertia) in black for direct comparison.

In practice, increasing inertial coefficient value has no positive effects on very first times of transient, ROCOF performances are the same as a "conventional" INEC system.

Simulation 8 numerical results are summarized in Tab. 2.13 and compared to simulation 7 (INEC synthetic inertia).

Table 2.13: Simulation 8 results: INEC-enhanced synthetic inertia.

Simulation	T_{avvg1} (s)	k_{si1} (s)	H_{g1} (s)	ROCOF$_1$ (Hz/s)	MFD$_1$ (Hz)
7) INEC synthetic inertia	8	-	2	-0.40	-412
8) INEC-enhanced synthetic inertia	8	-	4	-0.40	-415 (+1%)

Due to simulation results, INEC-enhanced technique has been abandoned.

It must be observed that performances in simulation 7 and 8 are given also by physical reasons: DC link capacitance is very high compared to conventional one, so control action must be very fast in managing discharge (or charge) phase; the most energy is available, the most control must be faster.

A different tuning of VSC converter is anyway unrecommended, because HVDC link operates most of the time in steady state conditions at rated value: a stronger control action on voltage could generate dangerous oscillations and instability. In order to speed system response up with no impact on control robustness, another faster, transient contribution has been included in the INEC control loop action.

2.11 INEC-derivative synthetic inertia algorithm

Referring to previous INEC theory in Par. 2.10, power balance in (2.62) is completed with an additional contribution; power is injected or extracted from capacitor C_{dc} according to AC grid frequency second derivative[3], by means of a constant K_f (dimensionally, it is s^2):

$$P_{acpu}(t) = -\frac{C_{dc}V_{C_{dc}}(t)}{P_{Gn}}\frac{dV_{C_{dc}}(t)}{dt}\left(1 + K_f\frac{d^2\Delta f_{Gpu}(t)}{dt^2}\right) \tag{2.75}$$

Negative sign of (2.75) means positive power flow with negative capacitor derivative and positive frequency jerk, so positive power flow during capacitor discharge and frequency fall, according to measurement conventions in all previous simulations.

As before, new electrical quantities can be equated to mechanical one:

$$2H_G f_{Gpu}(0)\frac{d\Delta f_{Gpu}(t)}{dt} = \frac{C_{dc}V_{C_{dc}}(t)}{P_{Gn}}\frac{dV_{C_{dc}}(t)}{dt}\left(1 + K_f\frac{d^2\Delta f_{Gpu}(t)}{dt^2}\right) \tag{2.76}$$

Once again, capacitor voltage is shown in per unit, using rated voltage $V_{C_{dcn}}$ as base value; equation is then integrated:

$$\begin{aligned}&\int \frac{2H_G f_{Gpu}(0)}{V_{C_{dcn}}^2}\frac{d\Delta f_{Gpu}(t)}{dt}dt = \\ &= \frac{C_{dc}V_{C_{dcpu}}(t)}{P_{Gn}}\int\left(\frac{dV_{C_{dcpu}}(t)}{dt} + K_f\frac{dV_{C_{dcpu}}(t)}{dt}\frac{d^2\Delta f_{Gpu}(t)}{dt^2}\right)dt\end{aligned} \tag{2.77}$$

At this point, an approximation is performed: observing Fig. 2.50 and Fig. 2.51, it can be noted that, in the very first time of transient (1 s $< t <$ 1.5 s), DC link voltage and grid frequency have very different profiles; voltage changes slowly, and its derivative is more or less constant; this was observed as being main defect about standard INEC approach (it failed in reducing AC grid 1 ROCOF). Frequency, on the other way, has a steeper variation, with also higher jerk.

Because purpose of extra quantity in (2.75) is speed HVDC converter response up, it is reasonable simplify derivative product in (2.77) in the following way:

$$\begin{aligned}&\int_{T_{l1}}^{T_{l1}+\Delta t}\left(\frac{dV_{C_{dcpu}}(t)}{dt} + K_f\frac{dV_{C_{dcpu}}(t)}{dt}\frac{d^2\Delta f_{Gpu}(t)}{dt^2}\right)dt \simeq \\ &\simeq \int_{T_{l1}}^{T_{l1}+\Delta t}\left(\frac{dV_{C_{dcpu}}(t)}{dt} + K_f K_V\frac{d^2\Delta f_{Gpu}(t)}{dt^2}\right)dt\end{aligned} \tag{2.78}$$

Quantities K_V (dimensionally, it is $1/s$) and Δt are constant and they depend on system configuration; While Δt is set positive by definition, K_V sign depends on

[3]In classic mechanics, second derivative of angular speed is called *jerk*. Because AC grid frequency is basically a scaling of synchronous machine mechanical speed (through pole pairs and 2π constants), it can be concluded the additional contribution represents a forcing, a power impulse that must be provided when frequency acceleration changes. Acconrding to (2.35) and Tab. 2.4 settings, frequency profile during a load step has basically an exponential profile (see simulation 1), thus jerk has a peak at the very beginning of transient, exactly when contribution by capacitor is needed to be maximum.

frequency: observing that a negative derivative (frequency fall) requires a capacitor discharge, K_V (capacitor derivative approximation) will be negative too; K_V will be positive in case of frequency raise.

After Δt, voltage profile has changed so much that approximation of (2.78) is no longer valid; anyway, because the effect must be obtained in the very first time of transient, this should not affect significantly the performances. Moreover, as soon as DC link voltage reaches $V_{dcminpu}$, power flow from capacitor must be stopped so any contribution by (2.78) goes to zero.

Such approach is not completely rigorous, but it is a good way to model a power contribution that is maximum at the beginning of transient, in order to achieve expected dynamic performances by INEC control loop action. This is also possible due to DC link capacitors oversizing, otherwise voltage response is definitely faster than grid frequency response.

After above mentioned simplification, (2.77) integration results (boundaries are neglected for simplicity):

$$\frac{2H_G f_{Gpu}(0)}{V_{C_{dcn}}^2}\Delta f_{Gpu}(t) \simeq \frac{C_{dc}}{P_{Gn}}\frac{V_{C_{dcpu}}^2(t)}{2} - K_f K_V \frac{d\Delta f_{Gpu}(t)}{dt} + c_0 \tag{2.79}$$

For simplicity, K_V is set positive, minus prior to K_f and frequency derivative sign fix the calculations.

Initial conditions are imposed as previously:frequency in steady state, capacitor charged at voltage $V_{C_{dcpu}}(0)$;

$$f_{Gpu}(0) = 1 \quad , \quad \Delta f_{Gpu}(0) = 0 \tag{2.80}$$

In addition, also frequency derivative is set to zero:

$$\frac{d\Delta f_{Gpu}(0)}{dt} = 0 \tag{2.81}$$

This is not theoretically correct, no mechanical device can fulfill such condition when a frequency change occurs, anyway it must be remembered that this is an algorithm, it tries to mimic a physical behavior, but no full correspondence to reality is needed as soon as power can be transferred from capacitor to AC grid and vice versa[4].

After such clarification, integration constant c_0 results to be equal to "conventional" INEC theory:

$$c_0 = -\frac{C_{dc}}{P_{Gn}}\frac{V_{C_{dcpu}}^2(0)}{2} \tag{2.82}$$

Full system model is given by substituting (2.82) and (2.80) into (2.79):

$$\frac{2H_G}{V_{C_{dcn}}^2}\Delta f_{Gpu}(t) \simeq \frac{C_{dc}}{P_{Gn}}\frac{V_{C_{dcpu}}^2(t)}{2} - \frac{C_{dc}}{P_{Gn}}\frac{V_{C_{dcpu}}^2(0)}{2} - K_f K_V \frac{d\Delta f_{Gpu}(t)}{dt} \tag{2.83}$$

Result is so-called INEC-derivative algorithm equation:

$$V_{C_{dcpu}}^2(t) = V_{C_{dcpu}}^2(0) + \frac{4H_G P_{Gn}}{V_{C_{dcn}}^2 C_{dc}}\Delta f_{Gpu}(t) + K_f K_V \frac{d\Delta f_{Gpu}(t)}{dt} \tag{2.84}$$

[4]Doing numerical simulations, the approach is formally correct, because first derivative of a signal at a time becomes available only since next computational step.

$$V_{C_{dcpu}}(t) = \sqrt{V^2_{C_{dcpu}}(0) + \frac{4H_G P_{Gn}}{V^2_{C_{dcn}} C_{dc}} \Delta f_{Gpu}(t) + K_f K_V \frac{d\Delta f_{Gpu}(t)}{dt}} \tag{2.85}$$

As previously, concept is extended from a single machine to a complex grid; capacitor becomes a HVDC link, p.u. base values are rated grid apparent power A_{gn} (active powers are computed pretending unitary power factor) and grid rated frequency f_{gn};

$$V_{C_{dcpu}}(t) = \sqrt{V^2_{C_{dcpu}}(0) + \frac{4H_g P_{gn}}{V^2_{C_{dcn}} C_{dc}} \Delta f_{gpu}(t) + R_{Id}(t)} \tag{2.86}$$

$$R_{Id}(t) = k_{Id} \frac{d}{dt} \Delta f_{gpu}(t) \quad , \quad k_{Id} = K_f K_V \tag{2.87}$$

A block diagram of INEC-derivative concept is shown in Fig. 2.56.

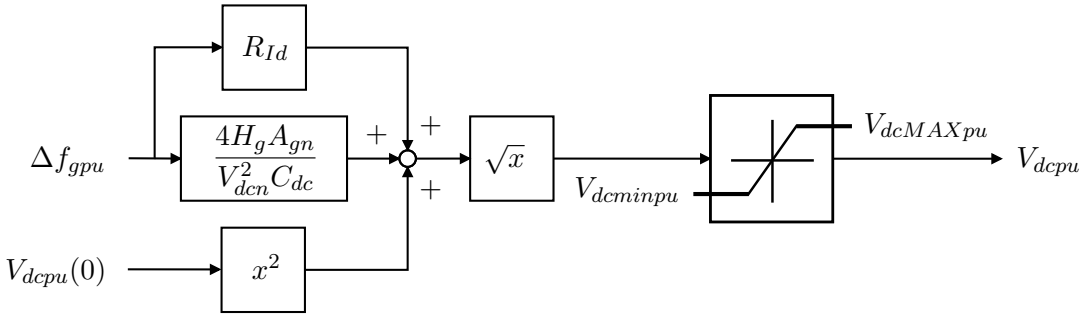

Figure 2.56: INEC-derivative synthetic inertia regulator block diagram (R_{Id}).

INEC-derivative has same advantages of INEC algorithm, but it is much more responsive in very first time of transient; about drawbacks, it needs to perform frequency derivative: same considerations about practical implementation of numerical derivative of Par. 2.8 are valid.

2.11.1 Simulation 9: INEC-derivative synthetic inertia

Simulation 7 is repeated using controller shown in Fig. 2.56 in replacement of the one in Fig. 2.46. Synthetic inertia power (P_{si1pu}) comes from station 1 VSC converter by means of signal V^0_{dc1pu}. DC link capacitance (C_{dc12}) is empowered according to (2.50). Grid setup the same as shown in Fig. 2.47.

Station 1 converter is set as *Master*, station 2 as *Slave*; respective voltage and power setpoints are chosen as shown in Tab. 2.3, to achieve same steady state conditions as previously.

According to (2.38) and (2.59), INEC inertial coefficient H_{g1} is set to produce on AC grid 1 the same effect as k_{si}; INEC-derivative coefficient k_{Id} is set the same way:

$$H_{g1} = \frac{k_{si1}}{2} = 2 \text{ s} \quad , \quad k_{Id} = 4 \text{ s} \tag{2.88}$$

Targets of simulation 9 are:

- testing INEC-derivative frequency response in comparison to INEC algorithm;
- verify proper limiting of DC link voltage in order to "protect" AC grid 2 by frequency disturbance.

Simulation 9 power profiles are shown in Fig. 2.57.

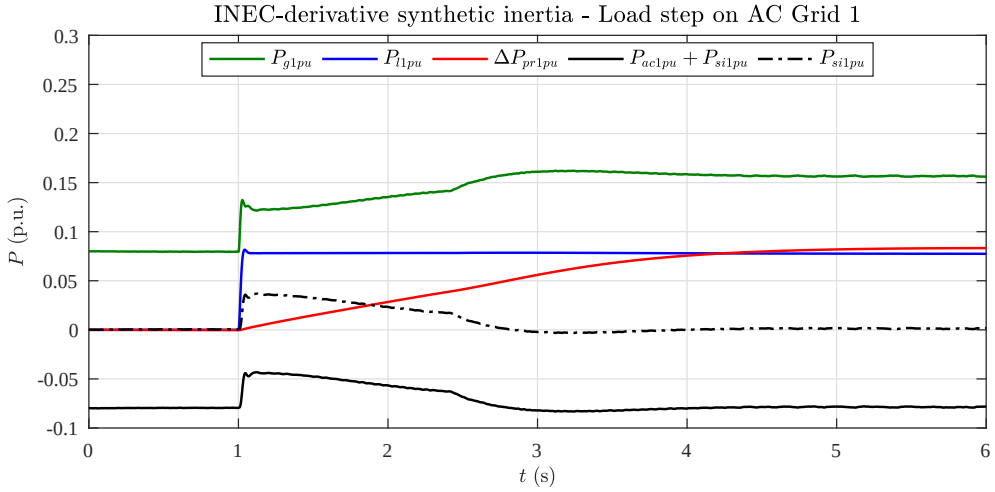

Figure 2.57: Simulation 9 results: power profiles on AC grid 1 with INEC-derivative synthetic inertia.

Base power: 2000 MVA.

From load step ($T_{l1} = 1$ s), stronger regulating power flow discharges DC capacitors (Fig. 2.58).

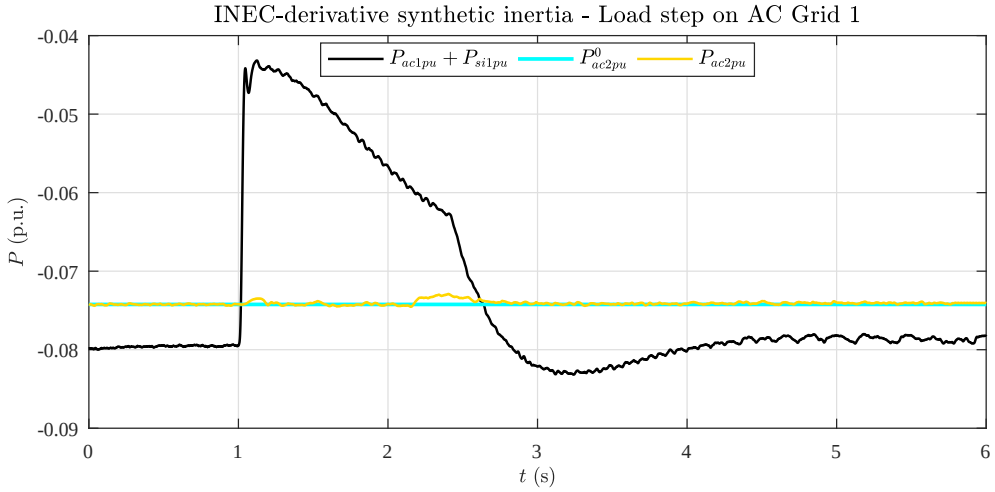

Figure 2.58: Simulation 9 results: HVDC stations power profiles (and setpoint) with INEC-derivative synthetic inertia.

Base power: 2000 MVA.

Faster system response can be noted comparing DC link voltage between INEC (Fig. 2.50) and INEC-derivative case (Fig. 2.59).

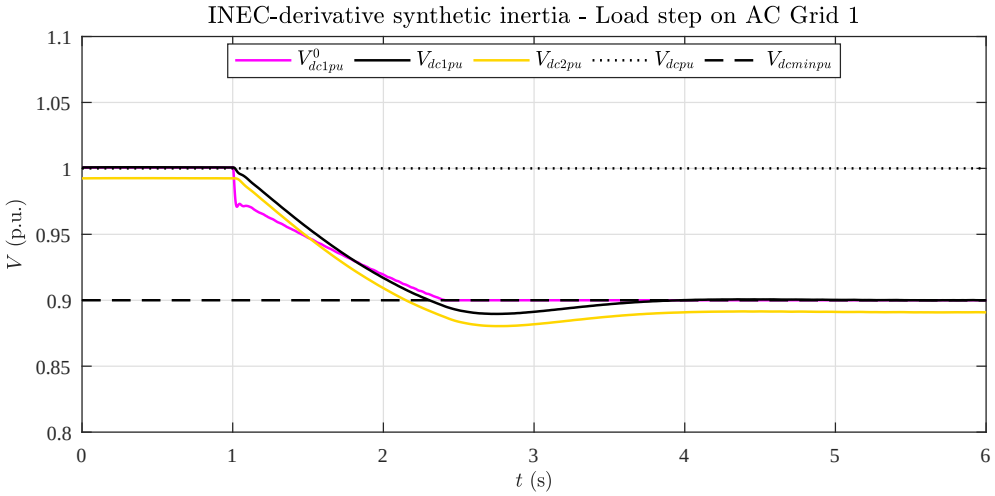

Figure 2.59: Simulation 9 results: HVDC stations voltage profiles with INEC-derivative synthetic inertia.

Base voltage: 200 kV.

Result is an improvement of ROCOF and in general a better profile of frequency, whose deviation is much more limited in the first part of transient (Fig. 2.60).

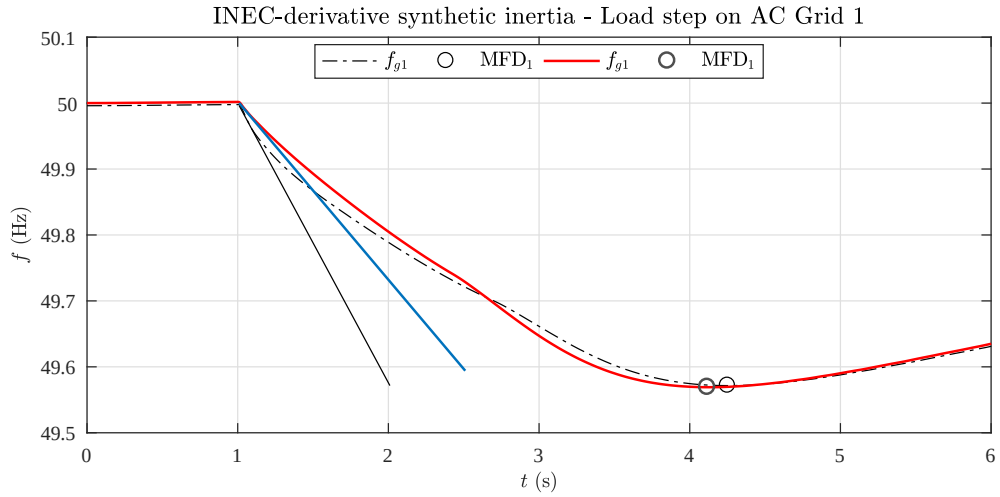

Figure 2.60: Simulation 9 results: frequency profile and MFD (Maximum Frequency Deviation) on AC grid 1 with INEC-derivative synthetic inertia. The slope of blue straight line shows graphically ROCOF$_1$ trend at the beginning of transient.
Results of simulation 7 (INEC synthetic inertia) in black for direct comparison.

Simulation 9 numerical results are summarized in Tab. 2.14 and compared to simulation 7 (INEC synthetic inertia).

Table 2.14: Simulation 9 results. INEC-derivative synthetic inertia.

Simulation	T_{avvg1} (s)	k_{Id} (s)	H_{g1} (s)	ROCOF$_1$ (Hz/s)	MFD$_1$ (Hz)
7) INEC synthetic inertia	8	-	2	-0.40	-412
9) INEC-derivative synthetic inertia	8	4	2	-0.27 (-32%)	-412

All results are then summarized in Tab. 2.15 for direct comparison respect to original case (no synthetic inertia, simulation 1).

Table 2.15: All simulations results.

Simulation	ROCOF$_1$ (Hz/s)	MFD$_1$ (Hz)
1) No synthetic inertia	-0.50	-440
2) Ideal synthetic inertia	-0.33 (-34%)	-410 (-7%)
3) HVDC-based synthetic inertia	-0.33 (-34%)	-410 (-7%)
7) INEC synthetic inertia	-0.40 (-20%)	-412 (-6%)
8) INEC-enhanced synthetic inertia	-0.40 (-20%)	-415 (-6%)
9) INEC-derivative synthetic inertia	-0.27 (-46%)	-412 (-6%)

From given results, it is clear INEC-derivative guarantees better performances, not only respect to INEC (as expected), but also against a "classical" synthetic inertia control, based on power flows weighed according to grid frequency derivative.

About MFD, synthetic inertia contribution is very modest, and differences respect to different simulations are negligible.

As general consideration, there are two main focus:

- About INEC, speed response, then ROCOF reduction, is not only a function of the inertial regulator calibration; it strongly depends on DC voltage controller tuning. This aspect is crucial, as a "slow" voltage control, perfectly reasonable to avoid sudden oscillations on grid voltage, is not suitable for inertial functions. In this sense, "classic" algorithm may guarantees better dynamic performance, being (usually) the active power controller faster than DC voltage one; moreover, DC voltage control tuning must consider significant DC capacitor oversizing. Fast variations in a strongly impressed voltage generates indeed strong power peaks. Such peaks are desired and necessary for the inertial algorithm, but are nevertheless an issue during normal operation of DC connection;

- INEC-derivative approach is absolutely effective, but it "distorts" the original control philosophy; INEC was developed as a way to realize the inertial action with no calculation of frequency derivative (that is not always easy). During simulations, both with classical method and with INEC-derivative, frequency signal was derived in ideal way, without considering actual technological and computational limits (delays, death bands, sampling issues, PLL tuning etc.) ; the result is a critical analysis of both solutions without introducing performance degradation due to external causes.

In the followings, INEC-derivative algorithm has been successfully applied to *Master* node of a tri-terminal HVDC network; simulations about propagation of frequency "disturbance" on different synchronous areas have been performed.

2.12 Multi-terminal HVDC grid

Starting from a two-terminals model (HVDC link, Fig. 2.20), the analysis has been completed with a multi-terminal (3 terminals) model implementation (Fig. 2.61).

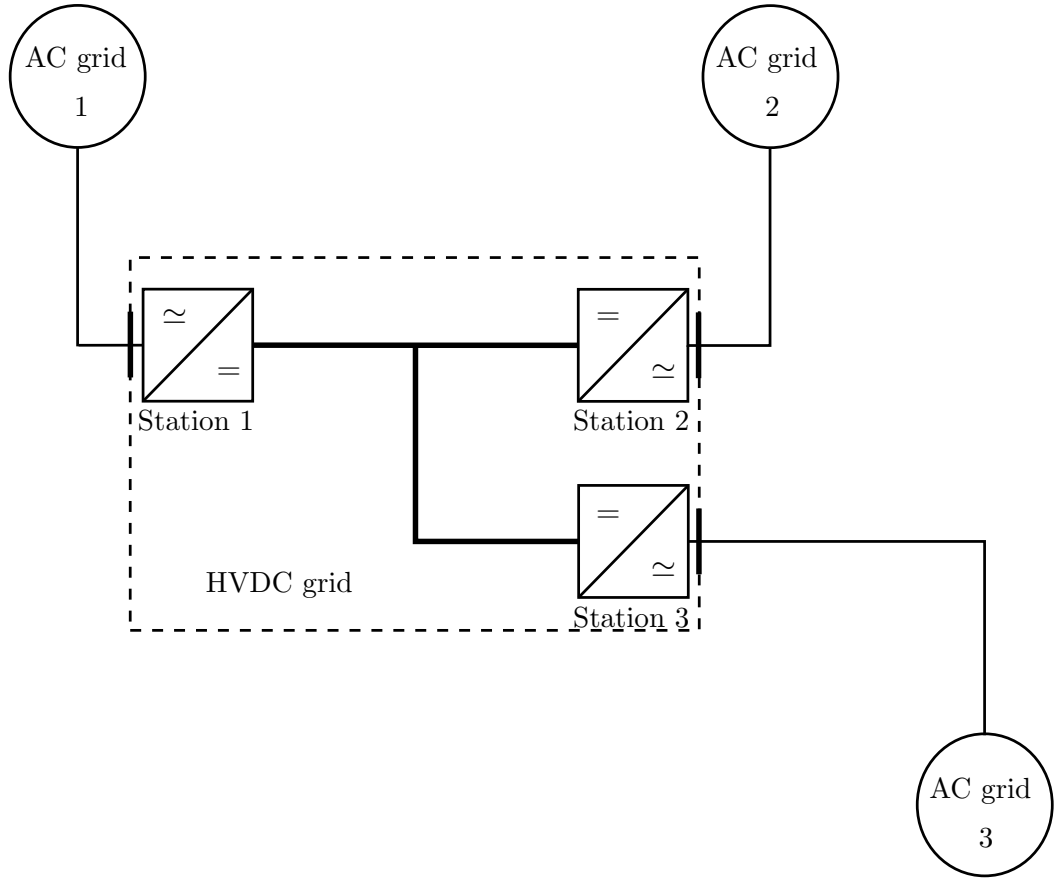

Figure 2.61: Multi-terminal HVDC grid.

HVDC link of previous model is then turned in a HVDC grid; three different AC synchronous areas are connected to AC/DC VSC converters inside power stations.

Working with a HVDC grid, *Master* node and INEC-derivative inertia algorithm is implemented (Station 1); other nodes (Station 2 and 3) must be *Slaves*: power flow is set, DC voltage is given by *Master* (and line losses); for such reason, the easiest way to modify power flow on a *Slave* converter is by a voltage-power *droop* action.

In practice, a DC voltage variation means the *Master* node is exchanging power with its own AC grid to balance a frequency drift.

The idea is splitting (in a controlled way) the frequency drift into two AC grids (1 and 3), while third one (AC grid 2) must be transparent to such "disturbance"; AC grid protection action has been already widely investigated in all previous simulations: anytime, AC grid 2 was protected by proper VSC converter setting.

A *Slave* converter can participate to inertial action by modifying its own power setpoint depending on DC voltage variation: action intensity is controlled by a so-called *droop factor*.

A block diagram of droop control concept is shown in Fig. 2.62.

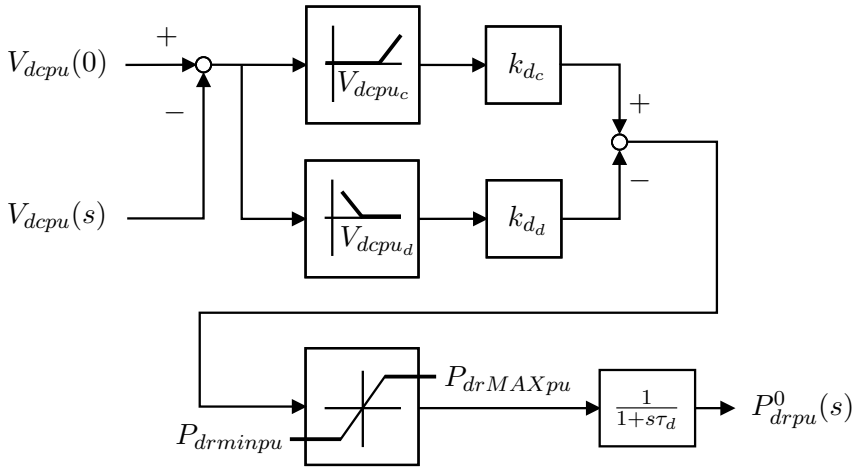

Figure 2.62: Droop algorithm block diagram $R_{dr}(s)$ in Laplace domain.

Droop factor value is split is two factors, one for overvoltage (k_{d_c}) and one for undervoltage (k_{d_c}); usually, global action is symmetrical, so two values are equal.

Droop action static characteristic is shown in Fig. 2.63.

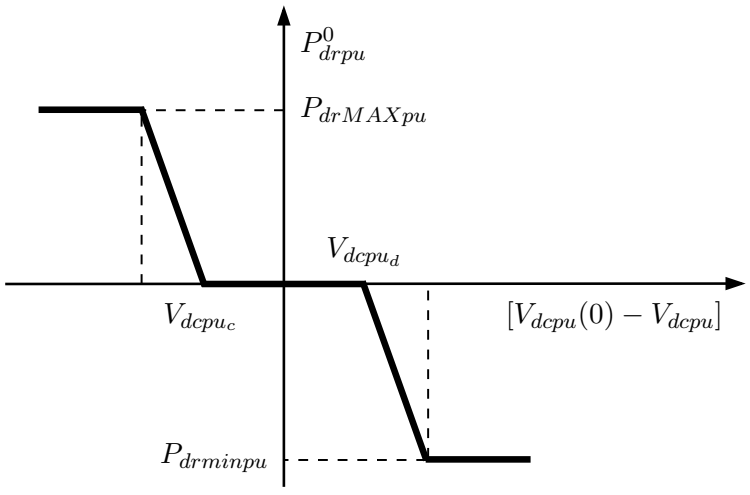

Figure 2.63: Droop action static characteristic. Profile is symmetric due to proper parameters setting (see Tab. 2.17).

An AC grid controller equipped with droop is shown in Fig. 2.64.

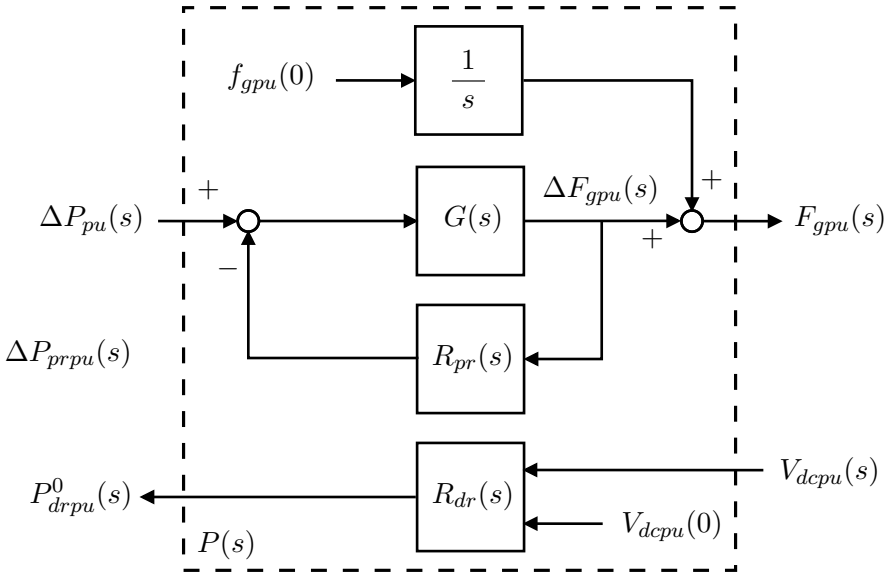

Figure 2.64: Droop regulator $R_{dr}(s)$ and primary frequency regulator $R_{pr}(s)$ in Laplace domain. $P^0_{drpu}(s)$ is transferred to HVDC station controller and summed at power setpoint.

Besides the usual primary frequency control, a power setpoint variation is sent to HVDC-VSC controller. P^0_{drpu} is summed (algebraically) to converter power setpoint: resulting load unbalance causes a frequency drift.

2.12.1 Simulation 10: INEC-derivative synthetic inertia and droop (multi-terminal HVDC)

Simulation 10 uses AC grid 1 controller shown in Fig. 2.46, replacing R_{INEC} block of Fig. 2.45 with INEC-derivative (R_{INECd}) block of Fig. 2.56.

AC grid 3 controller uses a droop correction of HVDC power setpoint, as in Fig. 2.64.

Simulation grid setup is shown in Fig. 2.65.

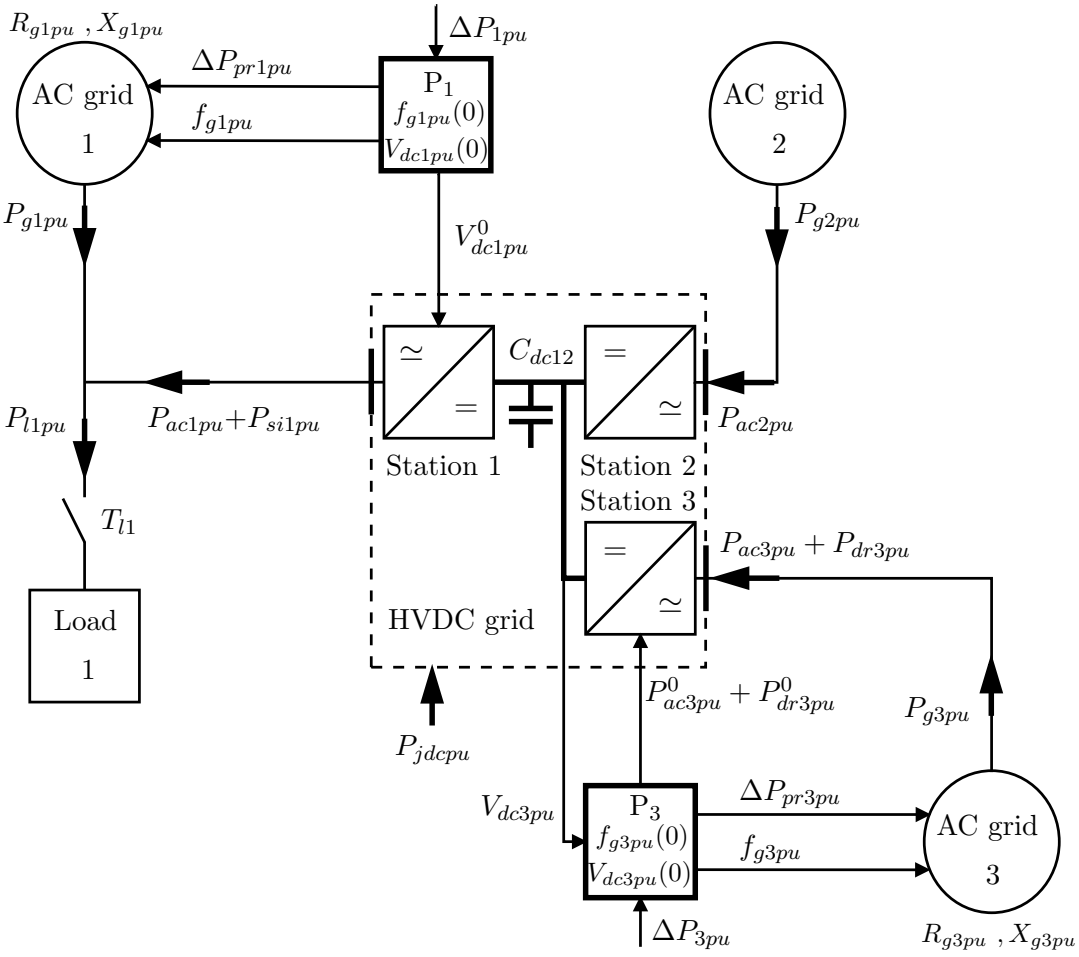

Figure 2.65: Network used in INEC-derivative synthetic inertia simulation with multi-terminal HVDC (HVDC grid). AC grid 1 frequency system (P_1, bold square) is shown in Fig. 2.46. AC grid 3 frequency system (P_3, bold square) is shown in Fig. 2.46 DC link of station 1 and 2 (C_{dc12}) is sized according to calculations in Par. 2.9. DC link of station 3 is not oversized.

A load flow on grid in Fig. 2.65 has been performed, in order to set network in steady state. AC grid 1, AC grid 2 and AC grid 3 rated frequencies are 50 Hz.

Station 1 is set as *Master*, as in simulation 9, station 2 and station 3 are set as *Slaves*: power flows have been derived by initial conditions of simulation 1 (Tab. 2.3) simply by splitting equally previous loading;

Results in p.u. are listed in Tab. 2.16 (base power A_{g1n}=2000 MVA).

INEC-derivative control settings are the same as simulation 9.

Table 2.16: Initial load flow results in p.u. for multi-terminal HVDC grid test (base power A_{g1n}=2000 MVA).

Input	Symbol	Value	Comment
Station 1 active power	P_{ac1pu}	-0.080	
Station 1 DC voltage	V_{dc1pu}	1	Base voltage V_{dc1n}=200 kV
Station 2 active power	P_{ac2pu}	-0.037	
Station 3 active power	P_{ac3pu}	-0.037	
Output	**Symbol**	**Value**	**Comment**
Station 2 DC voltage	V_{dc2pu}	0.995	Base voltage V_{dc2n}=200 kV
Station 3 DC voltage	V_{dc3pu}	0.995	Base voltage V_{dc2n}=200 kV
DC-grid total losses	P_{jdcpu}	-0.006	

AC grid 3 primary frequency control settings are the same as AC grid 1 (Tab. 2.4). Droop action settings are shown in Tab. 2.17.

Table 2.17: Droop action parameter settings
(base power: 2000 MVA, base voltage: 200 kV).

V_{dcpu_c} (p.u.)	V_{dcpu_d} (p.u.)	k_{δ_c} (-)	k_{δ_d} (-)	$P_{drMAXpu}$ (p.u.)	$P_{drminpu}$ (p.u.)	τ_d (ms)
0.05	-0.05	2	2	0.01	-0.01	5

Simulation 10 power profiles are shown in Fig. 2.66.

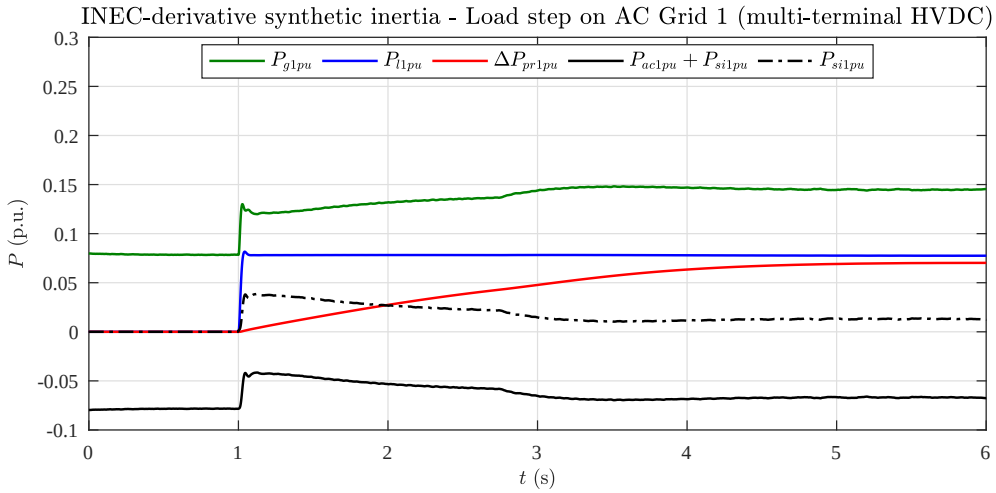

Figure 2.66: Simulation 10 results: power profiles on AC grid 1 with INEC-derivative synthetic inertia (multi-terminal HVDC).
Base power: 2000 MVA.

From load step ($T_{l1} = 1$ s), INEC-derivative regulating power flow appears (Fig. 2.67).

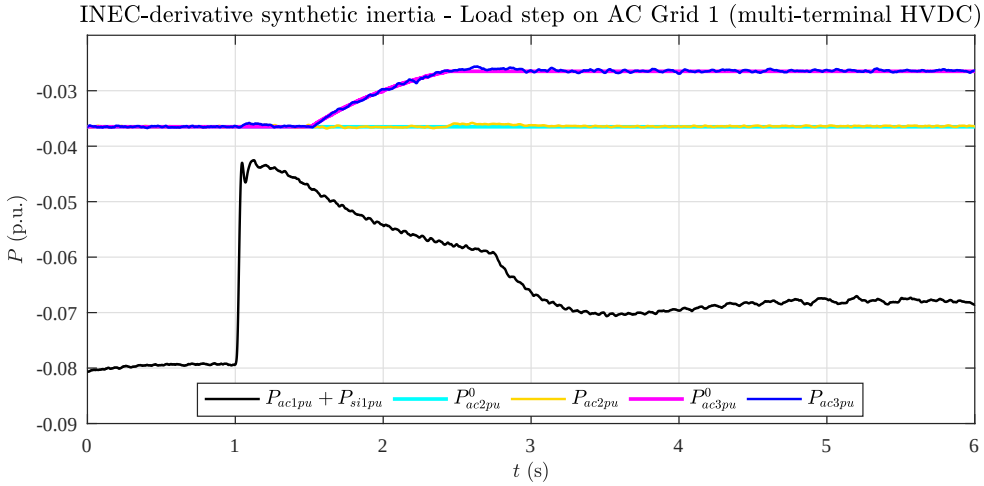

Figure 2.67: Simulation 10 results: HVDC stations power profiles (and setpoint) with INEC-derivative synthetic inertia (multi-terminal HVDC).
Base power: 2000 MVA.

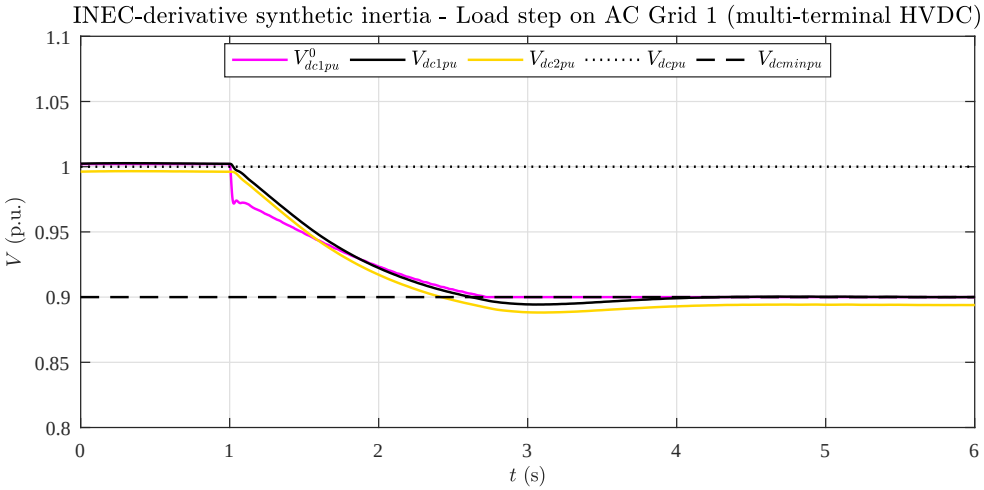

Figure 2.68: Simulation 10 results: HVDC stations voltage profiles with INEC-derivative synthetic inertia (multi-terminal HVDC).
Base voltage: 200 kV.

INEC-derivative action causes discharge of DC grid capacitors; voltage starts falling (Fig. 2.68). As soon as DC grid voltage reaches V_{dcpu_d} ($t \simeq 1.5$ s), droop action modifies power setpoint of station 3 (Fig. 2.67).

Power variation is progressive up to P_{drpu_d}, then it is properly stopped. VSC converter action is adequate both to perform INEC-derivative, both to handle droop power flow.

As result of droop action power is injected from AC grid 3 into DC grid: this causes two effects:

- more energy is available to perform INEC-derivative action on AC grid 1;
- power mismatch on AC grid 3 is generated.

Results are visible in Fig. 2.69 (Simulation 7 results are plot in black for direct comparison).

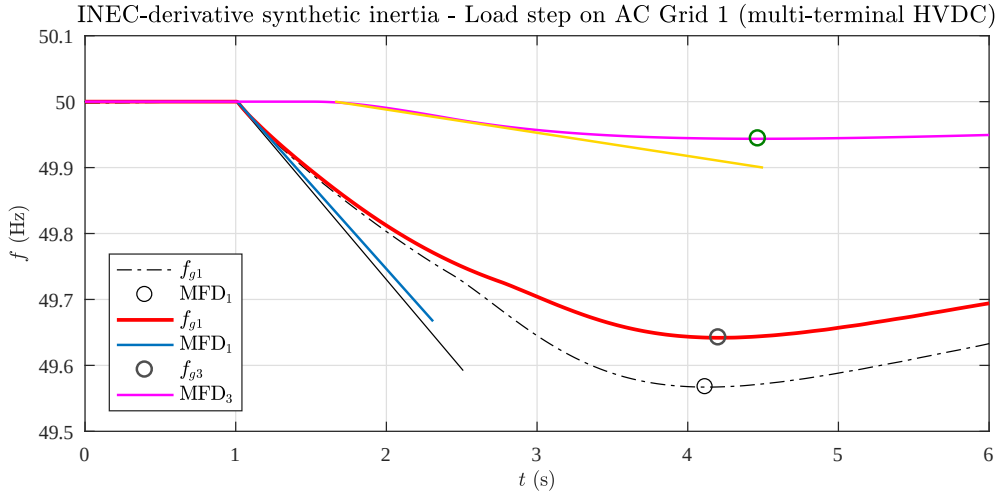

Figure 2.69: Simulation 10 results: frequency profile and MFD (Maximum Frequency Deviation) on AC grid 1 and AC grid 2 with INEC-derivative synthetic inertia and droop control. The slope of blue straight line shows graphically ROCOF_1 trend at the beginning of transient. The slope of yellow straight line shows graphically ROCOF_3 trend at the beginning of transient. Results of simulation 9 (INEC-derivative synthetic inertia in dual-terminal HVDC) in black for direct comparison.

Respect to simpler DC link simulation, AC grid 1 ROCOF is reduced, because INEC action can be longer due to extra energy coming from AC grid 3; as expected, AC grid 3 frequency has itself a drift; due to droop settings, it is a small drift compared to AC grid 1, it can be stopped by primary frequency regulation in a few seconds.

In practice, ROCOF improvement on AC grid 1 is obtained by generating a further ROCOF on AC grid 3 due to power exchange through HVDC.

In this case, MFD improvement in AC grid 1 is remarkable, but a further MFD is generated on AC grid 3.

AC grid 2 is, as previously, not perturbed by load step; power flow, thus frequency, has not changed.

Simulation 10 numerical results are listed in Tab. 2.18.

Table 2.18: Multi-terminal HVDC simulation results.

Simulation	$ROCOF_1$ (Hz/s)	MFD_1 (mHz)	$ROCOF_3$ (Hz/s)	MFD_3 (Hz)
9) INEC-derivative (2 terminals)	-0.27	-412	-	-
10) INEC-derivative and droop	-0.26 (-2%)	-365(-11%)	-0.04	-65

This last simulation shows that, due to HVDC, a frequency disturbance can be "shared" among different synchronous areas. Nevertheless a lack of power/energy always causes a frequency drift (even small), TSO can decide how to manage such event: as example, a weak AC area can be "protected" by frequency disturbance by transferring energy from stronger grids; such action can be total of partial, by proper droop and synthetic inertia tuning.

2.13 Chapter conclusions

This second chapter studied HVDC converters set to provide synthetic inertia into an AC grid.

Activity has been financed by the Research Fund for the Italian Electrical System under the Contract Agreement between RSE S.p.A. and the Ministry of Economic Development. Ideal and HVDC inertial controllers have been implemented and successfully compared.

Loading tests on a grid model showed that:

- AC grid frequency variation can be effectively limited by a synthetic inertia control;
- synthetic inertia lowers primary regulation slope, preserving mechanical equipment from stress;
- necessary inertial energy can be provided by oversized DC link capacitors;
- inertial effect is transparent to other AC grids if capacitors sizing is sufficient to exchange the total inertial energy needed by the control.

HVDC stations must be properly controlled to avoid undesired power flows between AC grids; moreover, a moderate margin on capacitors sizing is recommendable because grid conditions before synthetic inertia engage are unknown: inertial power could increase losses and waste a part of the inertial energy exchanged with the AC grid.

A sensitivity analysis showed that, to obtain a strong inertial support, required capacitance is relevant.

Sizing must be evaluated case by case, according to expected effects; simulations have been performed with load steps and also with unload steps (load rejection).

In this last case, excess of power must be stored within HVDC link, preventing overvoltage; simulations showed that, due to VSC converter efficiency and power flows, capacitor oversizing for discharge case (load step) full covers also charge case (load rejection).

Inertial results were definitely remarkable, unfortunately the "classical" approach has some drawbacks:

- It can be simply implemented on *Slave* nodes only (active power control);
- During inertial action, *Master* node (DC voltage) action must be blocked, let DC link voltage to change according to needed inertial energy.

Trying to overcome such defects, innovative algorithms have been implemented, tested and compared each other: the so-called INEC (INertia Emulation Control) approach showed to be less effective than the classic synthetic inertia approach, based on grid frequency derivative; speed response during very first time of transients is definitely poor.

Several solutions have been studied to empower speed response (trial-error approach): most promising one resulted the so-called INEC-derivative, in which a further component, proportional to frequency acceleration (jerk) was added to control loop.

The result is an algorithm in which frequency derivative signal is still necessary, but it has the great advantage to be applicable in DC grid *Master* nodes: DC voltage control

is always active during inertial action; traditional algorithms work on AC power loop (*Slave* nodes), and voltage controllability is definitely an issue, maximum and minimum limits must be foreseen in advance, also depending on system power flows.

Besides inertial algorithm peculiarities, the study demonstrated how HVDC can be used to connect each other different synchronous areas and exchange power in a controlled way.

The evolution of such concept is the multi-terminal HVDC grid; simulation showed ability of VSC systems to perform synthetic inertia function and, at the same time, "share" a frequency drift on another AC grid; a third AC grid, due to HVDC decoupling, was instead protected from the disturbance.

HVDC links are traditionally built and used to transfer high power over long distances with low losses; in a future prospective, HVDC grids are a valid support for existing AC grids, both for regulation services (like synthetic inertia), both to control and manage active power flows through different synchronous areas.

Thesis work will be concluded in next chapter, in which all conclusions are presented.

CONCLUSIONS

This thesis assessed some evolved features into traditional field of electrical engineering where DC has been introduced since long time; after conclusion of the War of Currents, AC became the standard for most of electrical power systems all over the world; railways and long transmission networks were, for different reasons, a remarkable exception.

Besides such specific applications, and few others like excitation systems or drives, DC technology development was anyway marginal in the global electrification scenario, up to relevant improvement of power electronics technology in the las decades of Twentieth Century: new kind of devices (thyristors at first, then IGBTs), and constant upgrade in rates, robustness and reliability, made static power conversion even more convenient and desirable.

Presently, huge penetration of renewable energy on AC grids is driven by static power conversion, and native DC systems are much more common than in the past.

Progress in microelectronics and controls are also a big part of such process: converters can reach performances in term of speed response and precision that are comparable or even better than any traditional electromechanical equipment.

Due to above mentioned conditions, today DC technology is growing fast, especially in innovative applications like microgrids and the so-called "Industry 4.0".

Nevertheless, DC conversion can express important innovations also in fields that are traditionally much more conservative, like railways, power transmission and distribution [95].

This work tried to analyze in the most realistic way state of the art of such fields; then future improvements and application of most recent technologies were investigated. Innovative power electronic converters (PEC) and energy storage systems (ESS) have been the main topics.

About ESS, focus was on sizing: for railways, target was essentially defining charge cycles, power rates and global efficiency to perform expected functionalities; in HVDC grid, storage by means of capacitor oversizing was the way not to propagate a frequency disturbance among different synchronous areas.

About PECs, focus was on innovative solutions in terms of layouts and controls; in railway field, that means different topologies than old diode rectifiers, and algorithms to handle bi-directional power flows from and to catenary; in HVDC, where VSC converters are still developed and used since today, innovation is the study of ancillary functionalities, whose control loops can be integrated into existing plants.

In railways, also some brief economical scenarios have been evaluated, in order to compare each other different ESS solutions and have an overview of the payback; about HVDC, Cost-Benefit Analysis (CBA) was not possible, because quantifying the economical impact of synthetic inertia on a grid is not as easy as calculating revenues

from energy savings; in addition, talking about HVDC transmission, not only pure economical trade-off is important: strategic plans, international politics and long-term goals are part of the scenario.

Besides economical considerations, DC innovative applications are actually really promising both in terms of hardware and software, as shown by many computer simulations performed during the study:

- braking energy recovery and catenary voltage stabilization increase railway energy savings; stand alone ESS empower the existing network with minimum impact on the infrastructure and also perform extra functionalities diode rectifiers cannot fulfill;

- HVDC stations realize synthetic inertia as ancillary service for AC grids; several synchronous areas can be connected each other exchanging power with full control of frequency drifts, including modulation of disturbances.

The study includes several elements of originality: control algorithms have been carefully studied and tuned, implementing different solutions, testing several alternatives and finding innovative approaches to achieve advantages by different philosophies.

Activity has been characterized by multidisciplinary approach: power electronics, plant building, automation and controls are the most important.

Several topics threated in the text resulted in papers for conferences and publications on international technical journals, as shown in bibliography.

APPENDIX A

ESS CONTROL TUNING FOR TRACTION SIMULATIONS

As said in Par. 1.7.4, DC power network implemented in simulations is complex and time-variant (see Fig. 1.14); procedure for ESS regulation tuning is therefore not unique neither rigorous; a series of assumptions have been introduced, taking into account a reasonable margin in order to compensate non-linearities and approximations.

A.1 Liner model

First step to synthesize a regulator with classical methods is a linear model; looking for a simplification of both Fig. 1.14 and Fig. 1.34, only one ESS is considered and train is modeled as a current generator, assuming braking rheostats are not engaged (that is one of main targets to achieve, so it is reasonable). In addition, catenary topology is frozen as shown in Fig. A.1.

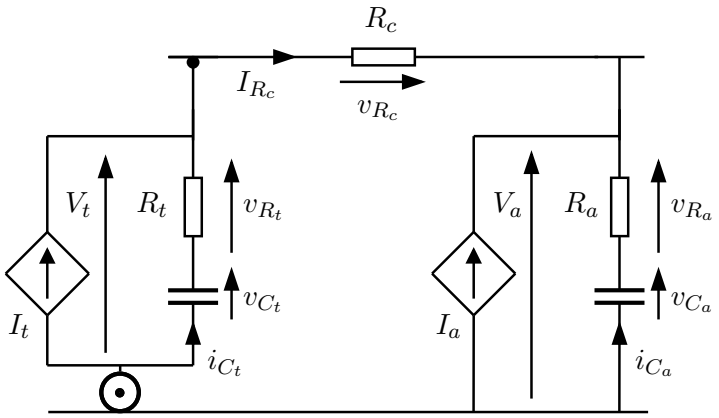

Figure A.1: DC railway time-invariant linear model used for control synthesis.

Following assumptions have been done:

- TSS are disconnected because of diodes reverse polarization;
- TSS filters are neglected, being ESS equipped with its own filters and because storage equipment must be designed to work properly also far from substations (Fig. 1.34);

- R_c value is kept constant, its variance influence will be later on discussed.

Using compact nomenclature $\dot{x} = \frac{dx(t)}{dt}$, components have following constitutive relationships:

$$i_{C_t} = -C_t \dot{v}_{C_t} \tag{A.1}$$
$$i_{C_a} = -C_a \dot{v}_{C_a} \tag{A.2}$$
$$v_{R_t} = -R_t i_{C_t} = R_t C_t \dot{v}_{C_t} \tag{A.3}$$
$$v_{R_a} = -R_a i_{C_a} = R_a C_a \dot{v}_{C_a} \tag{A.4}$$
$$v_{R_c} = -R_c I_{R_c} \tag{A.5}$$

System KVL and KCL con be written:

$$-V_t + R_t C_t \dot{v}_{C_t} + v_{C_t} = 0 \tag{A.6}$$
$$-V_a + R_a C_a \dot{v}_{C_a} + v_{C_a} = 0 \tag{A.7}$$
$$-v_{c_t} + R_t i_{C_t} + R_c i_{R_c} - R_a i_{C_a} + v_{c_a} = 0 \tag{A.8}$$

$$I_t - C_t \dot{v}_{C_t} - I_{R_c} = 0 \tag{A.9}$$
$$I_{R_c} + I_a - C_a \dot{v}_{C_a} = 0 \tag{A.10}$$

Merging (A.8) with (A.9):

$$-v_{c_t} + R_t i_{C_t} + R_c i_{C_t} + R_c I_t + R_a i_{C_t} + R_a I_t + R_a I_a + v_{c_a} = 0 \tag{A.11}$$

and then with (A.1):

$$-v_{c_t} - (R_t + R_c + R_a) C_t \dot{v}_{C_t} + (R_c + R_a) I_t + R_a I_a + v_{c_a} = 0 \tag{A.12}$$
$$\tag{A.13}$$

the first status equation is given:

$$\dot{v}_{C_t} = \frac{1}{(R_t + R_c + R_a) C_t} \Big[- v_{c_t} + v_{C_a} + (R_c + R_a) I_t + R_a I_a \Big] \tag{A.14}$$

Second status equation comes from I_{R_c} equivalence in (A.9) and (A.10):

$$I_t - C_t \dot{v}_{C_t} = -I_a + C_a \dot{v}_{C_a} \tag{A.15}$$
$$-C_t \dot{v}_{C_t} = -I_t - I_a + C_a \dot{v}_{C_a} \tag{A.16}$$

applied in (A.12):

$$-v_{c_t} + (R_t + R_c + R_a)(-I_t - I_a + C_a \dot{v}_{C_a}) + (R_c + R_a) I_t + R_a I_a + v_{c_a} = 0 \tag{A.17}$$
$$-v_{c_t} + (R_t + R_c + R_a) C_a \dot{v}_{C_a} - (R_t + R_c) I_a - R_t I_t + v_{c_a} = 0 \tag{A.18}$$
$$\tag{A.19}$$

Finally:

$$\dot{v}_{C_a} = \frac{1}{(R_t + R_c + R_a) C_a} \Big[v_{c_t} - v_{C_a} + R_t I_t + (R_t + R_c) I_a \Big] \tag{A.20}$$

System can be written in the well-known state-matrix form:

$$\dot{x} = \mathbf{A}x + \mathbf{B}u \tag{A.21}$$

with:

$$x = \begin{bmatrix} v_{C_t} \\ \\ v_{C_a} \end{bmatrix} \qquad u = \begin{bmatrix} I_t \\ \\ I_a \end{bmatrix} \tag{A.22}$$

$$\mathbf{A} = \frac{1}{R_c + R_t + R_a} \begin{bmatrix} -\dfrac{1}{C_t} & \dfrac{1}{C_t} \\ \\ \dfrac{1}{C_a} & -\dfrac{1}{C_a} \end{bmatrix} \tag{A.23}$$

$$\mathbf{B} = \frac{1}{R_c + R_t + R_a} \begin{bmatrix} \dfrac{R_c + R_a}{C_t} & \dfrac{R_a}{C_t} \\ \\ \dfrac{R_t}{C_a} & \dfrac{R_c + R_t}{C_a} \end{bmatrix} \tag{A.24}$$

Stability is given by eigenvalues of state matrix $\mathbf{A}$, those are equal to characteristic polynomial roots in Laplace domain:

$$\psi(s) = \det(s\mathbf{I} - \mathbf{A}) = 0 \tag{A.25}$$

In this case, characteristic polynomial $\psi(s)$ is a second degree one:

$$\psi(s) = s^2 + \frac{(C_a + C_t)s}{C_a C_t (R_a + R_c + R_t)} \tag{A.26}$$

Roots are given by a close-form solution:

$$s_1 = 0; \tag{A.27}$$

$$s_2 = -\frac{C_a + C_t}{C_a C_t (R_c + R_t + R_a)} \tag{A.28}$$

Some important considerations by (A.27) and (A.28) arise:

A) with no control, system is not unstable but it is "only" simply stable; asymptotic stability must be provided by the feedback action and by proper regulator synthesis;

B) R_c value does not compromise stability, being s_2 sign always negative no matter what catenary resistance value.

Regulator synthesis is based on transfer functions analysis; reminding to [96] for a detailed explanation, in the general case of a MIMO (Multiple Input Multiple Output)

linear system, $\mathbf{G}(s)$ represents a matrix of transfer functions from all system inputs $U(s)$ to outputs $Y(s)$ in Laplace domain:

$$sX(s) = \mathbf{A}X(s) + \mathbf{B}U(s) \tag{A.29}$$

$$Y(s) = \mathbf{C}X(s) + \mathbf{D}U(s) \tag{A.30}$$

$$Y(s) = [\mathbf{C}(s\mathbf{I} - \mathbf{A})^{-1}\mathbf{B} + \mathbf{D}]U(s) \tag{A.31}$$

$$\mathbf{G}(s) = \frac{Y(s)}{U(s)} = \mathbf{C}(s\mathbf{I} - \mathbf{A})^{-1}\mathbf{B} + \mathbf{D} \tag{A.32}$$

A and **B** are (A.23) and (A.24); **C** and **D** result from (A.6) and (A.7) merged with (A.14) and (A.20), respectively:

$$V_t = v_{C_t} + R_t C_t \dot{v}_{C_t} = \tag{A.33}$$

$$= v_{C_t} + \frac{R_t}{R_t + R_c + R_a}\Big[- v_{c_t} + v_{C_a} + (R_c + R_a)I_t + R_a I_a\Big] \tag{A.34}$$

$$V_a = v_{C_a} + R_a C_a \dot{v}_{C_a} = \tag{A.35}$$

$$= v_{C_a} + \frac{R_a}{R_t + R_c + R_a}\Big[v_{c_t} - v_{C_a} + R_t I_t + (R_t + R_c)I_a\Big] \tag{A.36}$$

$$\mathbf{C} = \begin{bmatrix} 1 - \dfrac{R_t}{R_t + R_c + R_a} & \dfrac{R_t}{R_t + R_c + R_a} \\ \dfrac{R_a}{R_t + R_c + R_a} & 1 - \dfrac{R_a}{R_t + R_c + R_a} \end{bmatrix} \tag{A.37}$$

$$\mathbf{D} = \begin{bmatrix} \dfrac{R_t(R_c + R_a)}{R_t + R_c + R_a} & \dfrac{R_t R_a}{R_t + R_c + R_a} \\ \dfrac{R_t R_a}{R_t + R_c + R_a} & \dfrac{R_a(R_t + R_c)}{R_t + R_c + R_a} \end{bmatrix} \tag{A.38}$$

Applying (A.32) at (A.23), (A.24), (A.37) and (A.38), transfer functions matrix is:

$$\mathbf{G}(s) = \begin{bmatrix} G_{tt}(s) & G_{ta}(s) \\ G_{at}(s) & G_{aa}(s) \end{bmatrix} = \tag{A.39}$$

$$= \frac{1}{C_a + C_t}\begin{bmatrix} \dfrac{(1 + sR_tC_t)(1 + s[R_a + R_c]C_a)}{s\Big(1 + s[R_a + R_c + R_t]\dfrac{C_aC_t}{C_a + C_t}\Big)} & \dfrac{(1 + sR_aC_a)(1 + sR_tC_t)}{s\Big(1 + s[R_a + R_c + R_t]\dfrac{C_aC_t}{C_a + C_t}\Big)} \\ \dfrac{(1 + sR_aC_a)(1 + sR_tC_t)}{s\Big(1 + s[R_a + R_c + R_t]\dfrac{C_aC_t}{C_a + C_t}\Big)} & \dfrac{(1 + sR_aC_a)(1 + s[R_c + R_t]C_t)}{s\Big(1 + s[R_a + R_c + R_t]\dfrac{C_aC_t}{C_a + C_t}\Big)} \end{bmatrix} \tag{A.40}$$

(A.40) has been written highlighting zeros and poles time constants; as expected, all denominators of $\mathbf{G}(s)$ elements are equal and they correspond to $\varphi(s)$; due to this, same considerations of points A) and B) are valid.

A.2 Block diagram of controlled system

Once complete system is modeled, it must be observed only I_a can be piloted and only V_a can be controlled, despite also I_t and V_t are relevant.

The result is block diagram in Fig. A.2.

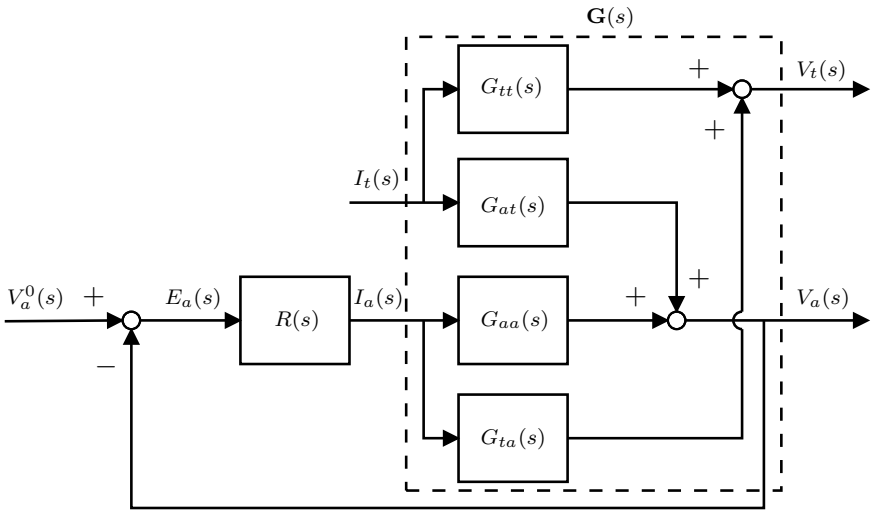

Figure A.2: Block diagram of whole system $\mathbf{G}(s)$ and PID regulator $R(s)$.

PID regulator $R(s)$ receives ESS voltage error $E_a(s)$ and it directly pilots ESS current $I_a(s)$; train current $I_t(s)$ is basically a disturb, that must be compensated in order to achieve the desired ESS voltage setpoint $V_a^0(s)$. Train voltage $V_t(s)$ is not directly controlled but ESS action must be designed to keep it below the rheostat braking threshold.

As shown, system is studied in linear zone, neglecting saturations and activation thresholds presented in Chapter 1; this is not an approximation because PID anti-windup configuration prevents delays or malfunctioning in the controller when saturations or blocking thresholds occur.

A.2.1 Control stability

As said previously, system $\mathbf{G}(s)$ is only simply stable; feedback action and regulator synthesis is expected to make it asymptotically stable; under certain conditions, stability can be proved by analyzing the Bode diagram of the system loop transfer function $L(s)$ (Bode criterion).

$L(s)$ for SISO (Single Input Single Output) systems is given by:

$$L(s) = R(s)G(s) \tag{A.41}$$

In the specific case, $L(s)$ from $V_a^0(s)$ to $V_a(s)$ results:

$$L_{aa}(s) = R(s)G_{aa}(s) \tag{A.42}$$

$R(s)$ is modeled as a PID (Proportional Integral Derivative) regulator, whose ideal transfer function is:

$$R(s) = k_p + \frac{k_i}{s} + sk_d = k_p \frac{T_i T_d s^2 + T_i s + 1}{T_i s} \quad , \quad T_i = \frac{k_p}{k_i} \quad , \quad T_d = \frac{k_d}{k_p} \tag{A.43}$$

$L_{aa}(s)$ has the following structure:

$$L_{aa}(s) = \frac{k_p}{C_a + C_t} \frac{T_i T_d s^2 + T_i s + 1}{T_i s} \frac{(1 + sR_aC_a)(1 + s[R_c + R_t]C_t)}{s\Big(1 + s[R_a + R_c + R_t]\dfrac{C_aC_t}{C_a + C_t}\Big)} \tag{A.44}$$

Bode criterion

To apply Bode criterion, $L_{aa}(s)$ must satisfy some pre-conditions:

a) No poles with real part greater than zero (P=0);

b) Bode diagram of $|L_{aa}(j\omega)|$ cuts zero-db axis once only.

Observing (A.44), condition a) is always guaranteed, no matter what circuit parameters are set; because the numbers of zeros (4) is greater than the number of poles (3), it results that, in some cases, for certain combinations of circuit parameters, condition b) could not be satisfied.

In order to prevent such possibility[1], PID regulator is set as a PI (Proportional Integral), imposing:

$$k_d = 0 \rightarrow T_d = 0 \tag{A.45}$$

$R(s)$ becomes therefore:

$$R(s) = k_p + \frac{k_i}{s} = k_p \frac{1 + T_i s}{T_i s} \quad , \quad T_i = \frac{k_p}{k_i} \tag{A.46}$$

$L_{aa}(s)$ is then:

$$L_{aa}(s) = \frac{k_p}{C_a + C_t} \frac{1 + T_i s}{T_i s} \frac{(1 + sR_aC_a)(1 + s[R_c + R_t]C_t)}{s\Big(1 + s[R_a + R_c + R_t]\dfrac{C_aC_t}{C_a + C_t}\Big)} \tag{A.47}$$

[1]System physical feasibility is an issue too, being number of zeros greater than number of poles; this is a direct consequence of ideal PID structure. When using derivative component, real PID implementation needs a high frequency extra pole; cutting away the derivative part also avoids such necessity.

To make $L_{aa}(s)$ asymptotically stable, $R(s)$ must be tuned to obtain at least a system with:

I) static gain μ_L positive;

II) phase margin φ_m positive.

Static gain is very immediate to determine, phase margin is instead calculated as follows in the Fourier frequency domain (projection of Laplace transfer functions on imaginary axis $j\omega$):

$$\varphi_m = 180^\circ - \frac{180^\circ}{\pi}\left|\varphi_c\right| = \tag{A.48}$$

$$= 180^\circ - \frac{180^\circ}{\pi}\left|\angle L_{aa}(j\omega_c)\right| \tag{A.49}$$

being ω_c system critical pulsation (pulsation at which Bode diagram of module cuts zero-dB axis) and φ_c critical phase (phase value at ω_c, in degrees).

When no zeros or poles are close to critical pulsations (conventionally, they are at least half a decade far away from ω_c), phase margin can be calculated by asymptotic diagrams, computing effect of each pole/zero on the phase:

$$\varphi_m \simeq 180^\circ - \frac{180^\circ}{\pi}\left|S_{dB_0}\frac{\pi}{2} + \sum_{n=1}^{N} + S_{dB_n} \cdot \operatorname{atan}\left(\frac{\omega_c}{\omega_{z_n,p_n}}\right)\right| \tag{A.50}$$

with:

- S_{dB_0}: Bode diagram slope in dB scale[2] at ω=0 (in practice, number of poles in the origin);
- S_{dB_n}: Bode diagram slope in dB scale before the n^{th} pole or zero (not in the origin);
- ω_{z_n,p_n}: pulsation of the the n^{th} pole or zero (not in the origin).

Minimum-phase systems

If system has positive static gain and all poles and zeros are negative or null, it is called minimum-phase type.

In a minimum-phase system, every pole causes a unity slope decrease (in dB scale) on Bode diagram of the module; opposite happens for zeros. As a consequence, if no poles or zeros are close to critical pulsation and the diagram cuts zero-dB axis with S_{dB}=-1, phase margin is close to 90° and system is asymptotically stable.

System bandwidth

In a minimum-phase system, if no poles or zeros are close to critical pulsation and phase margin is greater than 41°, critical pulsation itself is a good approximation of control system bandwidth[3]; if phase margin is greater than 60°, system response is approximately a first order type whose time constant is $1/\omega_c$ [98].

[2] In dB scale, -20 dB/dec equals to -1 slope, -40 dB/dec equals to -2 slope and so on.

[3] Such condition is only necessary and not sufficient; another necessary condition is that gain margin μ_m is greater than 1.7 [97]; anyway, in the most of common systems such conditions are practically enough to define the bandwidth.

A.2.2 PI regulator synthesis

To perform $R(s)$ synthesis, $G_{aa}(s)$ quantities must be first converted in numeric values; according to assumptions made in Par. 1.8.5 about ESS receptivity distance d_a of 8 km and per-length catenary resistance $r_c = 0.075\ \Omega/\text{km}$, R_c value can vary dynamically from zero to 0.6 Ω.

In Fig A.3, two asymptotic Bode diagrams of $G_{aa}(j\omega)$ are shown;

$G_{aa}^{(0)}(j\omega)$ represents $G_{aa}(j\omega)$ with $R_c = 0\ \Omega$, $G_{aa}^{(1)}(j\omega)$ is $G(j\omega)$ with $R_c = 0.6\ \Omega$; both numerical transfer functions are written below:

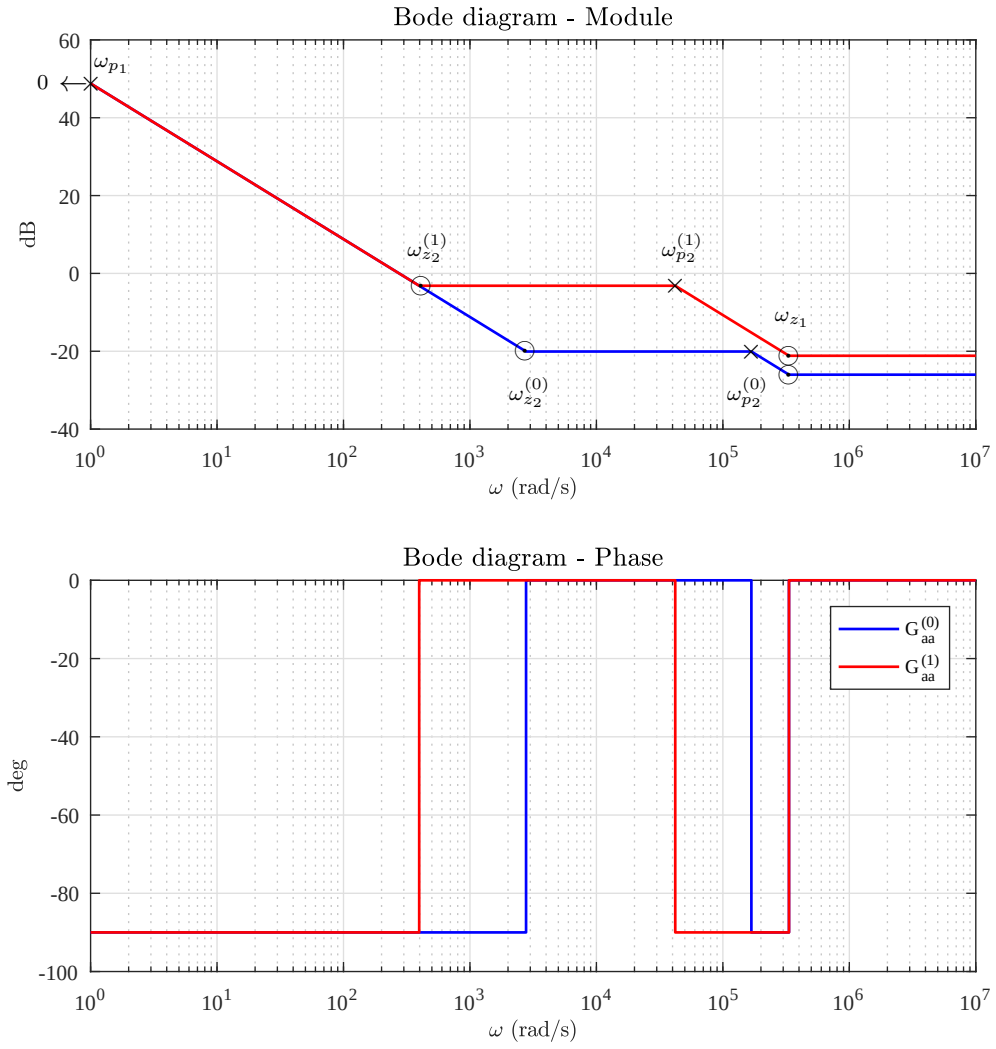

Figure A.3: Asymptotic Bode diagrams of $G_{aa}^{(0)}(j\omega)$ (blue) and $G_{aa}^{(1)}(j\omega)$ (red). Poles are marked with a ×, zeros are marked with a ⊙.

$$k_{aa} = \frac{1}{C_a + C_t} \quad , \quad T_{z_1} = R_a C_a \tag{A.51}$$

$$T_{z_2}^{(0)} = R_t C_t \quad , \quad T_{p_2}^{(0)} = (R_a + R_t)\frac{C_a C_t}{C_a + C_t} \tag{A.52}$$

$$T_{z_2}^{(1)} = (R_c + R_t) C_t \quad , \quad T_{p_2}^{(1)} = (R_a + R_c + R_t)\frac{C_a C_t}{C_a + C_t} \tag{A.53}$$

$$G_{aa}^{(0)}(j\omega) = k_{aa}\frac{(1 + j\omega T_{z_1})(1 + j\omega T_{z_2}^{(0)})}{j\omega(1 + j\omega T_{p_2}^{(0)})} \tag{A.54}$$

$$G_{aa}^{(1)}(j\omega) = k_{aa}\frac{(1 + j\omega T_{z_1})(1 + j\omega T_{z_2}^{(1)})}{j\omega(1 + j\omega T_{p_2}^{(1)})} \tag{A.55}$$

$$G_{aa}^{(0)}(j\omega) = 275.48\frac{(1 + j\omega\ 3 \cdot 10^{-6})(1 + j\omega\ 3.6 \cdot 10^{-4})}{j\omega(1 + j\omega\ 5.95 \cdot 10^{-6})} \tag{A.56}$$

$$G_{aa}^{(1)}(j\omega) = \ 275.48\frac{(1 + j\omega\ 3 \cdot 10^{-6})(1 + j\omega\ 2.5 \cdot 10^{-3})}{j\omega(1 + j\omega\ 2.38 \cdot 10^{-5})} \tag{A.57}$$

$$\omega_{z_1} = \frac{1}{T_{z_1}} = 3.33 \cdot 10^5 \text{ rad/s} \tag{A.58}$$

$$\omega_{z_2}^{(0)} = \frac{1}{T_{z_2}^{(0)}} = 2.78 \cdot 10^3 \text{ rad/s} \tag{A.59}$$

$$\omega_{z_2}^{(1)} = \frac{1}{T_{z_2}^{(1)}} = 3.96 \cdot 10^2 \text{ rad/s} \tag{A.60}$$

$$\omega_{p_1} = 0 \text{ rad/s (pure integrator)} \tag{A.61}$$

$$\omega_{p_2}^{(0)} = \frac{1}{T_{p_2}^{(0)}} = 1.68 \cdot 10^5 \text{ rad/s} \tag{A.62}$$

$$\omega_{p_2}^{(1)} = \frac{1}{T_{p_2}^{(1)}} = 4.20 \cdot 10^4 \text{ rad/s} \tag{A.63}$$

Basically, $G_{aa}^{(0)}(s)$ and $G_{aa}^{(1)}(s)$ represent $L_{aa}(s)$ when regulator $R(s) = 1$ (k_p=1, k_i=0).

According to Bode conditions I) and II) in Par. A.2, both $G_{aa}^{(0)}(s)$ and $G_{aa}^{(1)}(s)$ are asymptotically stable, being:

1. $\mu_L = k_{aa} > 0$;
2. phase margins $\varphi_m^{(0)}$ and $\varphi_m^{(1)}$ positive.

$$\begin{aligned}\varphi_m^{(0)} &\simeq 180^\circ - \frac{180^\circ}{\pi}\left|\varphi_c\right|_{\omega_c^{(0)}=400\ \text{rad/s}} \simeq \\ &\simeq 180^\circ - \frac{180^\circ}{\pi}\left| -1\cdot\frac{\pi}{2} + 1\cdot\text{atan}\left(\frac{\omega_c^{(0)}}{\omega_{z_2}^{(0)}}\right) - 1\cdot\text{atan}\left(\frac{\omega_c^{(0)}}{\omega_{p_2}^{(0)}}\right) + 1\cdot\text{atan}\left(\frac{\omega_c^{(0)}}{\omega_{z_1}}\right)\right| \simeq \\ &\simeq 180^\circ - |-90^\circ + 8.19^\circ - 0.13^\circ + 0.06^\circ| \simeq 98.12^\circ \end{aligned} \tag{A.64}$$

$$\begin{aligned}\varphi_m^{(1)} &\simeq 180^\circ - \frac{180^\circ}{\pi}\left|\varphi_c\right|_{\omega_c^{(1)}=400\ \text{rad/s}} \simeq \\ &\simeq 180^\circ - \frac{180^\circ}{\pi}\left| -1\cdot\frac{\pi}{2} + 1\cdot\text{atan}\left(\frac{\omega_c^{(1)}}{\omega_{z_2}^{(1)}}\right) - 1\cdot\text{atan}\left(\frac{\omega_c^{(1)}}{\omega_{p_2}^{(1)}}\right) + 1\cdot\text{atan}\left(\frac{\omega_c^{(1)}}{\omega_{z_1}}\right)\right| \simeq \\ &\simeq 180^\circ - |-90^\circ + 45.23^\circ - 0.54^\circ + 0.06^\circ| \simeq 134.75^\circ \end{aligned} \tag{A.65}$$

Asymptotic Bode diagrams of $G_{aa}(s)$ could be not fully precise, being $\omega_{z_2}^{(1)}$ too close to critical pulsation ω_c. A deeper analysis on real Bode diagrams of Fig. A.4 goes to little different results:

$$\begin{aligned}\varphi_m^{(0)} &= 180^\circ - \frac{180^\circ}{\pi}\left|\varphi_c^{(0)}\right|_{\omega_c^{(0)}=277\ \text{rad/s}} = \\ &= 180^\circ - \frac{180^\circ}{\pi}\left|\angle G_{aa}^{(0)}(j\omega_c^{(0)})\right| = 180^\circ - |-85^\circ| = 95^\circ \end{aligned} \tag{A.66}$$

$$\begin{aligned}\varphi_m^{(1)} &= 180^\circ - \frac{180^\circ}{\pi}\left|\varphi_c^{(1)}\right|_{\omega_c^{(1)}=383\ \text{rad/s}} = \\ &= 180^\circ - \frac{180^\circ}{\pi}\left|\angle G_{aa}^{(1)}(j\omega_c^{(1)})\right| = 180^\circ - |-46^\circ| = 134^\circ \end{aligned} \tag{A.67}$$

Real critical frequencies are quite different, despite (A.64) and (A.66) results are almost equal; also (A.65) and (A.67) are basically the same. All phase margins are anyway positive, so asymptotic stability is not an issue.

Despite a "simple" unity regulator [$R(s)$ =1] is enough to guarantee $G_{aa}^{(0)}(s)$ and $G_{aa}^{(1)}(s)$ stability, observing Fig. A.4 some considerations about performances arise:

i. $G_{aa}(s)$ degree g is 1 (number of poles in the origin), so steady state error ε_∞ is not zero in case of ramp inputs and disturbances [96];

ii. despite they are a little different, critical pulsations (about 300-400 rad/sec), are satisfactory respect to expected equipment dynamic.

Due to above considerations, the following PI regulator is proposed.

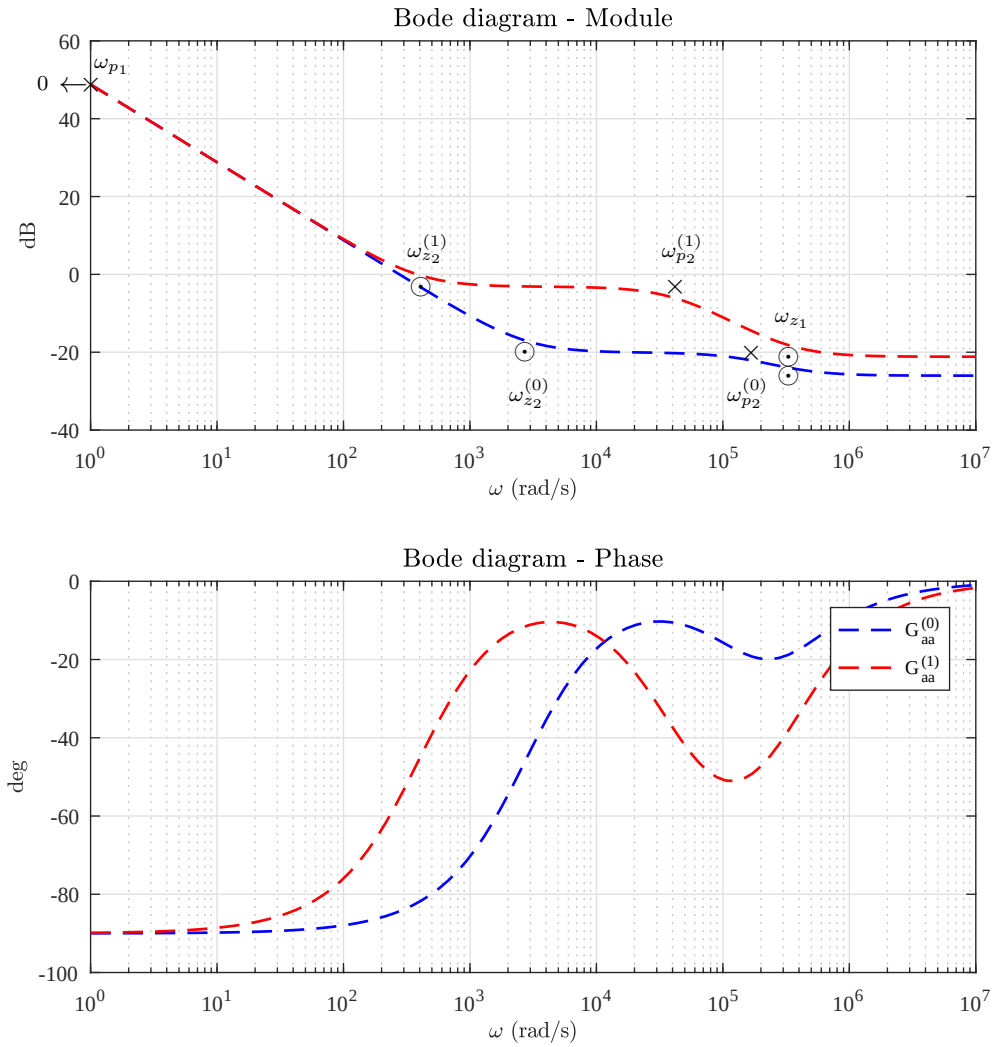

Figure A.4: Real Bode diagrams of $G_{aa}^{(0)}(j\omega)$ (blue) and $G_{aa}^{(1)}(j\omega)$ (red).
Poles are marked with a $\times$, zeros are marked with a $\odot$.

A.2.3 Static project

According to point i. of Par. A.2.2, because train current could be a ramp, $L_{aa}(s)$ transfer function degree g must be increased; a second degree is enough to erase totally the steady state error ε_∞ by a ramp input, but observing Fig. A.2 and (A.40), train current input $I_t(s)$ is multiplied by $G_{at}(s)$, that has a pole in the origin; it means that, in steady state, current ramp input has the effect of a parabola.

As a consequence, it results:

$$g = 2 \quad , \quad U(s) = \frac{A}{s^3} \quad , \quad \varepsilon_\infty = \frac{A}{\mu_L} \tag{A.68}$$

being A input amplitude slope.

Due to above statements, not only PI regulator pole is necessary, but also static gain μ_L must be tuned in order to reduce ε_∞ at a given value.

By data of Fig. 1.22, maximum train current slope is about 150 A/s, so $A = 150$. Looking for an error around 0.5 %, k_p/T_i is chosen accordingly:

$$\mu_L = k_{aa}\frac{k_p}{T_i} \quad , \quad \varepsilon_\infty = \frac{A}{\mu_L} = \frac{AT_i}{k_{aa}k_p} \tag{A.69}$$

$$k_{aa} = 275.48 \quad , \quad \frac{k_p}{T_i} = 10 \quad , \quad \varepsilon_\infty = \frac{150}{2755} \simeq 0.05 \tag{A.70}$$

Static PI regulator $R_0(s)$ is:

$$R_0(s) = \frac{k_p}{T_i s} = \frac{10}{s} \tag{A.71}$$

Fig. A.5 shows asymptotic Bode diagram of $R_0(j\omega)G_{aa}^{(0)}(j\omega)$ and $R_0(j\omega)G_{aa}^{(1)}(j\omega)$.

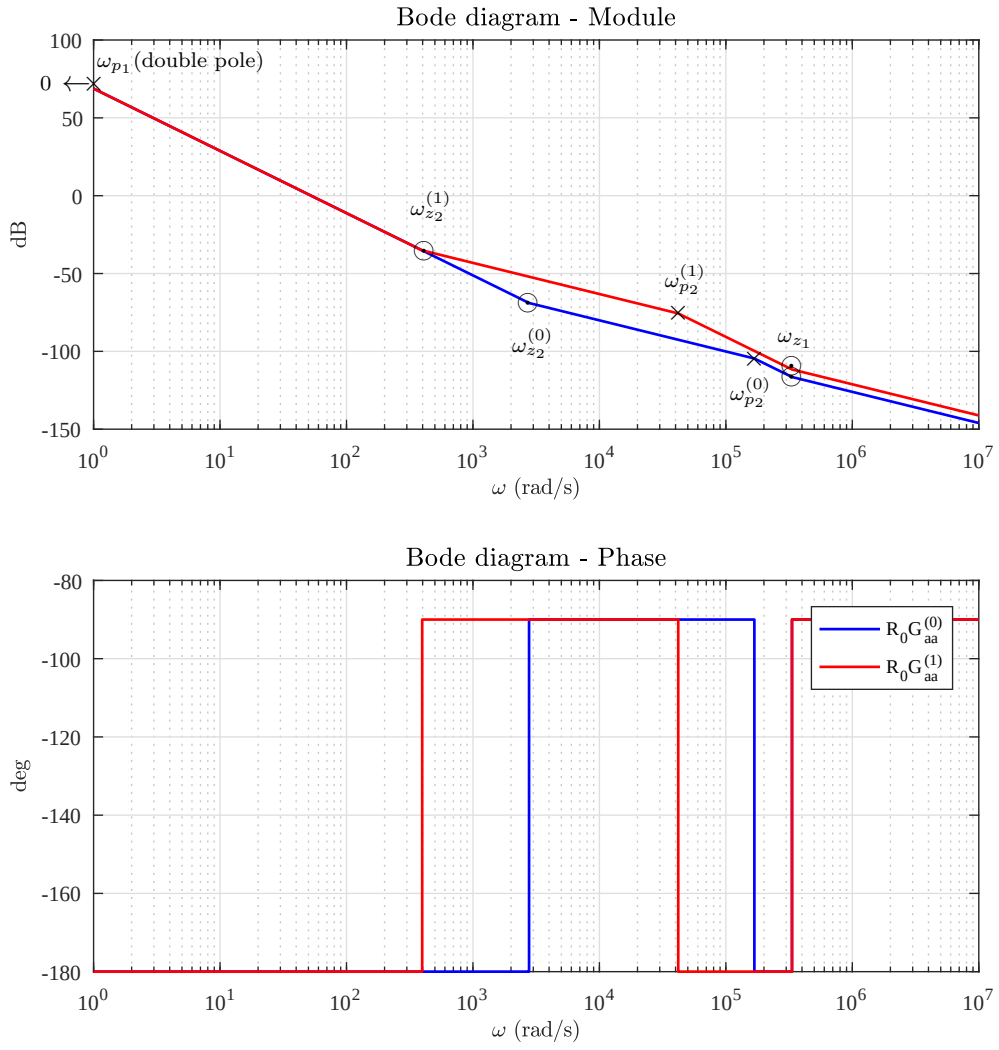

Figure A.5: Asymptotic Bode diagrams of $R_0(j\omega)G_{aa}^{(0)}(j\omega)$ (blue) and $R_0(j\omega)G_{aa}^{(1)}(j\omega)$ (red). Poles are marked with a $\times$, zeros are marked with a $\odot$.

Steady state issues are solved but, respect to Fig. A.3, dynamic performances and stability conditions are definitely poor because:

a) critical pulsations are both reduced at about 50 rad/sec;

b) module diagrams cuts zero-db axis with a slope of -40 dB/dec (slope -2 in dB scale); because no zeros or poles are close to critical pulsations, and being systems minimum-phase ones (see Par. A.2.1), asymptotic phase diagrams well approximate real diagrams around critical pulsation; in particular, critical phases are roughly given by multiplying module diagrams slope by 90°; it results that, for both systems, $\varphi_c^{(0)}$ and $\varphi_c^{(1)}$ are very close to $-2 \cdot 90° = -180°$, so phase margins φ_m are positive but probably very close to zero.

$$\begin{aligned}\varphi_m^{(0)} &\simeq 180° - \frac{180°}{\pi}\left|\varphi_c\right|_{\omega_c^{(0)}=50 \text{ rad/s}} \simeq \\ &\simeq 180° - \frac{180°}{\pi}\left| -2 \cdot \frac{\pi}{2} + 1 \cdot \operatorname{atan}\left(\frac{\omega_c^{(0)}}{\omega_{z_2}^{(0)}}\right) - 1 \cdot \operatorname{atan}\left(\frac{\omega_c^{(0)}}{\omega_{p_2}^{(0)}}\right) + 1 \cdot \operatorname{atan}\left(\frac{\omega_c^{(0)}}{\omega_{z_1}}\right)\right| \simeq \\ &\simeq 180° - |-180° + 1.03° - 0.02° + 0.01°| \simeq 1.02° \end{aligned} \tag{A.72}$$

$$\begin{aligned}\varphi_m^{(0)} &\simeq 180° - \frac{180°}{\pi}\left|\varphi_c\right|_{\omega_c^{(1)}=50 \text{ rad/s}} \simeq \\ &\simeq 180° - \frac{180°}{\pi}\left| -2 \cdot \frac{\pi}{2} + 1 \cdot \operatorname{atan}\left(\frac{\omega_c^{(1)}}{\omega_{z_2}^{(1)}}\right) - 1 \cdot \operatorname{atan}\left(\frac{\omega_c^{(1)}}{\omega_{p_2}^{(1)}}\right) + 1 \cdot \operatorname{atan}\left(\frac{\omega_c^{(1)}}{\omega_{z_1}}\right)\right| \simeq \\ &\simeq 180° - |-180° + 7.18° - 0.07° + 0.01°| \simeq 7.12° \end{aligned} \tag{A.73}$$

Condition b) and (A.72), (A.73) are verified by calculating actual phase margins through real Bode diagrams of Fig. A.6:

$$\begin{aligned}\varphi_m^{(0)} &= 180° - \frac{180°}{\pi}\left|\varphi_c^{(0)}\right|_{\omega_c^{(0)}=52 \text{ rad/s}} = \\ &= 180° - \frac{180°}{\pi}\left|\angle[R_0(j\omega_c^{(0)})G_{aa}^{(0)}(j\omega_c^{(0)})]\right|_{\omega_c^{(0)}=52 \text{ rad/s}} = \\ &= 180° - |-179°| = 1° \end{aligned} \tag{A.74}$$

$$\begin{aligned}\varphi_m^{(1)} &= 180° - \frac{180°}{\pi}\left|\varphi_c^{(1)}\right|_{\omega_c^{(1)}=52 \text{ rad/s}} = \\ &= 180° - \frac{180°}{\pi}\left|\angle[R_0(j\omega_c^{(1)})G_{aa}^{(1)}(j\omega_c^{(1)})]\right|_{\omega_c^{(1)}=52 \text{ rad/s}} = \\ &= 180° - |-172.5°| = 7.5° \end{aligned} \tag{A.75}$$

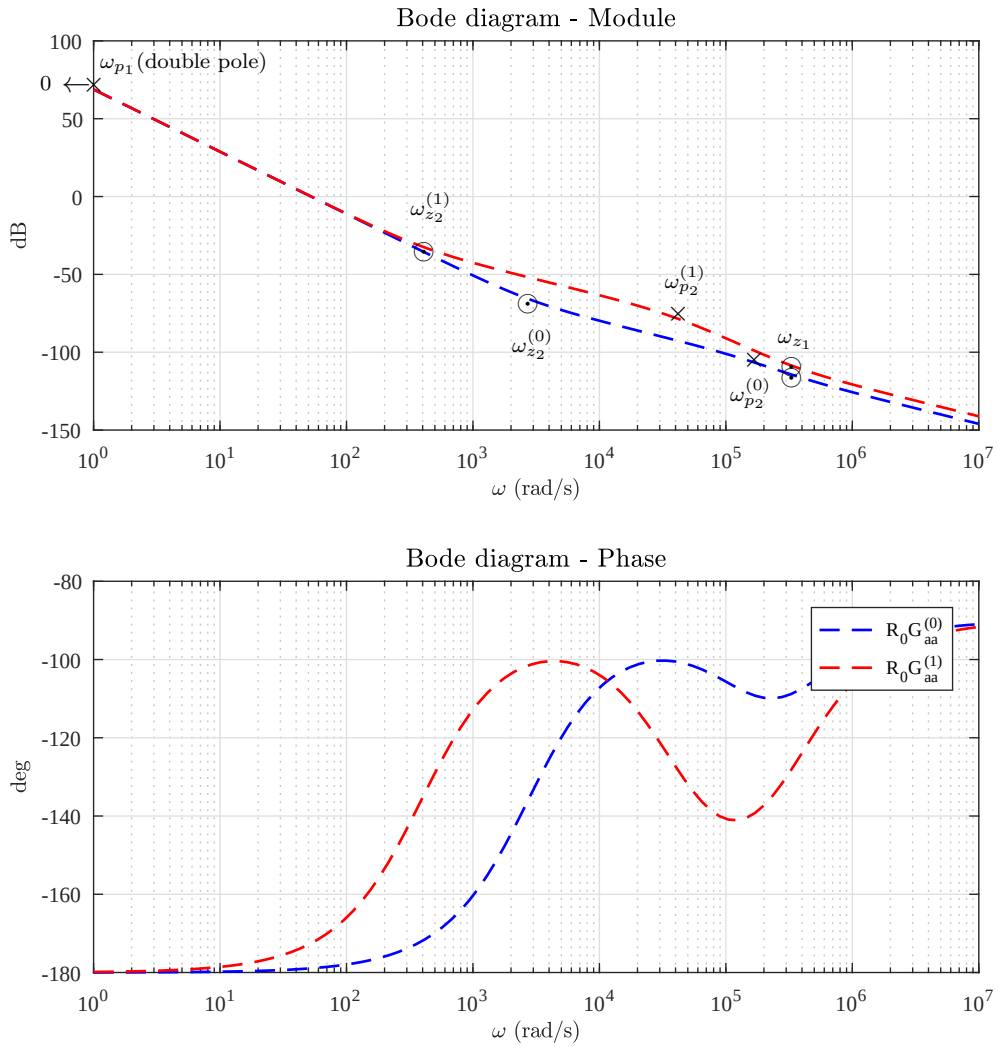

Figure A.6: Real Bode diagrams of $R_0(j\omega)G_{aa}^{(0)}(j\omega)$ (blue) and $R_0(j\omega)G_{aa}^{(1)}(j\omega)$ (red).
Poles are marked with a $\times$, zeros are marked with a $\odot$.

Results are as equal as asymptotic.

Practical system stability robustness wishes a phase margin greater than 60°, in order to avoid oscillations (first order system); dynamic project is then necessary to place properly the remaining PI zero and obtain such effect.

A.2.4 Dynamic project

Dynamic project for PI regulator essentially means placing properly the available zero to get the needed performances in terms of phase margin; acceptable solutions are not unique, they depend by designer experience. Process described in the followings is the result of several attempts, here not reported for brevity.

Observing module diagrams in Fig. A.5 and Fig. A.6, it can be noted that -2 slope region goes from 1 rad/sec to about 1000 rad/sec (with only a minimum deviation in $L_{aa}^{(1)}$ due to $\omega_{z_2}^{(1)}$); according to considerations at Par. A.2.1, for phase-minimum system is recommendable the module diagram cuts zero-db axis with -1 slope and no zeros or poles are close to ω_c: in this way a phase margin of about 90° is achieved.

Conventionally, no close poles or zeros means a distance of about half a decade at both sides of to ω_c.

All above considerations goes to place PI zero (ω_{z_R}) at 10 rad/s, as shown in asymptotic diagram of Fig. A.7.

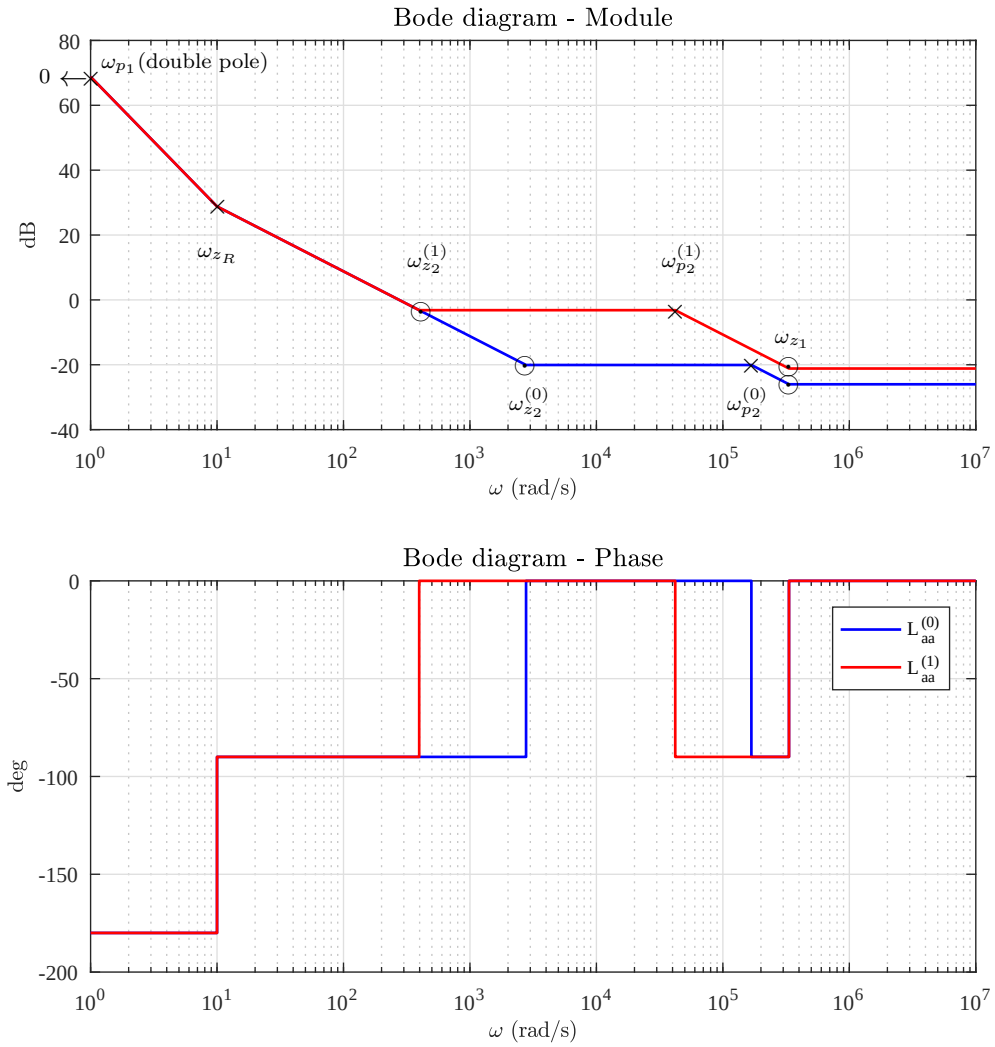

Figure A.7: Asymptotic Bode diagrams of $L_{aa}^{(0)}(j\omega)$ (blue) and $L_{aa}^{(1)}(j\omega)$ (red).
Poles are marked with a ×, zeros are marked with a ⊙.

Considering (A.70), PI setting results:

$$\omega_{z_R} = 10 \text{ rad/s} \quad , \quad \frac{k_p}{T_i} = 10 \quad , \quad T_i = 0.1 \text{ s} \tag{A.76}$$

$$k_p = 1 \quad , \quad k_i = 10 \tag{A.77}$$

$L_{aa}^{(0)}$ matches conditions on -1 slope and pole-zero distance, so asymptotic calculations on phase margin should be close to real ones; about $L_{aa}^{(1)}$, due to $\omega_{z_2}^{(1)}$, comparison with real results of Fig. A.8 are necessary.

$$\begin{aligned}
\varphi_m^{(0)} &\simeq 180^\circ - \frac{180^\circ}{\pi}\left|\varphi_c\right|_{\omega_c^{(0)}=300 \text{ rad/s}} \simeq \\
&\simeq 180^\circ - \frac{180^\circ}{\pi}\left| - 2 \cdot \frac{\pi}{2} + 1 \cdot \operatorname{atan}\left(\frac{\omega_c^{(0)}}{\omega_{z_R}}\right) + 1 \cdot \operatorname{atan}\left(\frac{\omega_c^{(0)}}{\omega_{z_2}^{(0)}}\right) - 1 \cdot \operatorname{atan}\left(\frac{\omega_c^{(0)}}{\omega_{p_2}^{(0)}}\right) + \right. \\
&\left. + 1 \cdot \operatorname{atan}\left(\frac{\omega_c^{(0)}}{\omega_{z_1}}\right)\right| \simeq \\
&\simeq 180^\circ - |-180^\circ + 88.09^\circ + 6.16^\circ - 0.10^\circ + 0.04^\circ| \simeq 94.20^\circ
\end{aligned} \tag{A.78}$$

$$\begin{aligned}
\varphi_m^{(0)} &\simeq 180^\circ - \left|\varphi_c\right|_{\omega_c^{(1)}=300 \text{ rad/s}} \simeq \\
&\simeq 180^\circ - \frac{180^\circ}{\pi}\left| - 2 \cdot \frac{\pi}{2} + 1 \cdot \operatorname{atan}\left(\frac{\omega_c^{(0)}}{\omega_{z_R}}\right) + 1 \cdot \operatorname{atan}\left(\frac{\omega_c^{(1)}}{\omega_{z_2}^{(1)}}\right) - 1 \cdot \operatorname{atan}\left(\frac{\omega_c^{(1)}}{\omega_{p_2}^{(1)}}\right) + \right. \\
&\left. + 1 \cdot \operatorname{atan}\left(\frac{\omega_c^{(1)}}{\omega_{z_1}}\right)\right| \simeq \\
&\simeq 180^\circ - |-180^\circ + 88.09^\circ + 37.09^\circ - 0.41^\circ + 0.05^\circ| \simeq 124.82^\circ
\end{aligned} \tag{A.79}$$

$$\begin{aligned}
\varphi_m^{(0)} &= 180^\circ - \frac{180^\circ}{\pi}\left|\varphi_c^{(0)}\right|_{\omega_c^{(0)}=277 \text{ rad/s}} = \\
&= 180^\circ - \frac{180^\circ}{\pi}\left|\angle[L_{aa}^{(0)}(j\omega_c^{(0)})]\right|_{\omega_c^{(0)}=277 \text{ rad/s}} = \\
&= 180^\circ - |-86^\circ| = 94^\circ
\end{aligned} \tag{A.80}$$

$$\begin{aligned}
\varphi_m^{(1)} &= 180^\circ - \frac{180^\circ}{\pi}\left|\varphi_c^{(1)}\right|_{\omega_c^{(1)}=383 \text{ rad/s}} = \\
&= 180^\circ - \frac{180^\circ}{\pi}\left|\angle[L_{aa}^{(1)}(j\omega_c^{(1)})]\right|_{\omega_c^{(1)}=383 \text{ rad/s}} = \\
&= 180^\circ - |-48^\circ| = 132^\circ
\end{aligned} \tag{A.81}$$

Comparing (A.78) with (A.80) and (A.79) with (A.81), real stability performances are a little better than expectations by asymptotic analysis; asymptotic data will be used, being the most precautionary ones.

The result is that PI controlled system is fully stable and stability is robust during catenary resistance variations and no matter what other parameters slight deviations.

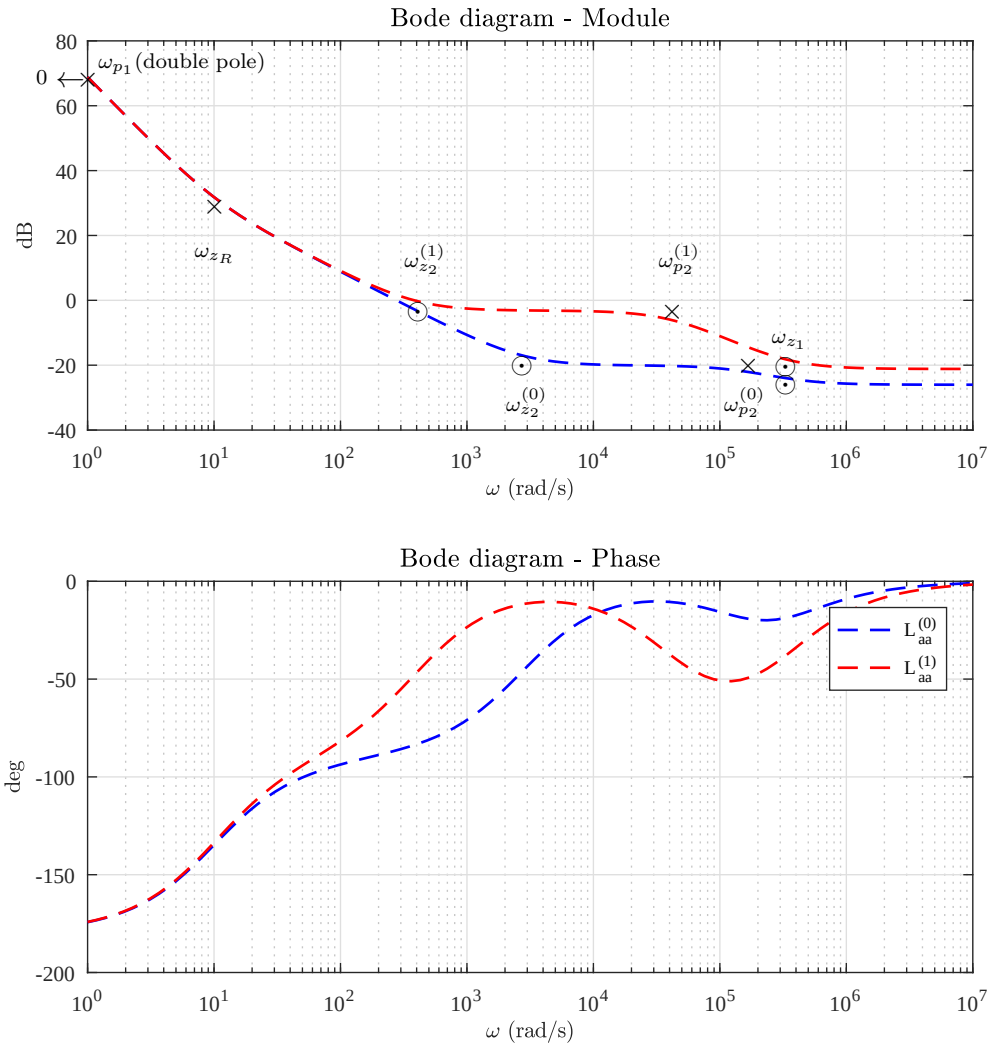

Figure A.8: Real Bode diagrams of $L_{aa}^{(0)}(j\omega)$ (blue) and $L_{aa}^{(1)}(j\omega)$ (red).
Poles are marked with a $\times$, zeros are marked with a $\odot$.

A.2.5 Time delays effect

Looking at block diagrams in Fig. 1.45, Fig. 1.47 and Fig. 1.50, some time constants (τ) have been included to smooth oscillations in the control variable and simulate the ESS converter response.

Real converter modulates voltage to generate needed current: PWM generation implies a small delay, but considering the high switching frequency, it can be considered negligible. What really affects system dynamic is converter smoothing series inductance, that limits maximum current slope; a first time constant with unitary static gain is a good approximation of such effect.

Delays cause a phase margin decay; the maximum time delay the control system can tolerate depends on minimum acceptable phase margin φ_m^* (greater than 60° is desirable for first time response, greater than 41° is needed for bandwidth definition).

Using first order delay approximation and asymptotic diagrams:

$$\tau \leq \tan\left|(\varphi_m^* - \varphi_m)\frac{\pi}{180^\circ}\right|\frac{1}{\omega_c} \tag{A.82}$$

(A.82) has been computed with data coming from (A.78) and (A.79); target phase margin φ_m^* has been chosen equal to 41° and also equal 60°.

Results are summarized in Tab. A.1.

Table A.1: Maximum admissible time delays (τ) in regulation loop.

System	φ_m^* (deg)	φ_m (deg)	ω_c (rad/s)	τ (ms)
$L_{aa}^{(0)}(s)$	41	88.09	300	4.5
	60	88.09	300	2.3
$L_{aa}^{(1)}(s)$	41	124.82	300	30.8
	60	124.82	300	7.1

Time delays are strictly dependent by converter ability to force needed current from and to catenary in a short time by varying dynamically its own voltage: the greater voltage margins are, the faster converter response is.

To perform some basic calculations about converter operative margins, following hypothesis have been done:

- by RFI standard [99], TSS DC smoothing reactors have a nominal inductance of 6 mH (rated current 1800 A); the same component is used also for ESS installation (L_a=6mH).
- train is modeled like a power generator (an ideal current generator I_t with an ideal voltage generator V_t in parallel: active power setpoint is given by $P_t = V_t \cdot I_t$;
- train is very far from ESS, at the limit of receptivity distance d_a: total loop resistance is R_c=0.6 Ω;
- train absorbed power P_t is assumed to be maximum ($\hat{p}_t$=-5 MW, heaviest loading condition);
- train voltage V_t is assumed to be the minimum absolute catenary voltage in abnormal condition ($V_{t_{min}}$=2300 V, Tab. 1.3, heaviest condition by the current point of view);
- parallel filters (capacitors etc.) are neglected, voltages are supposed constant, being current dynamics necessarily faster than voltage variations (current flows control the voltage at the equipment).

According to above statements, equivalent circuit in steady state is given in Fig. A.9.

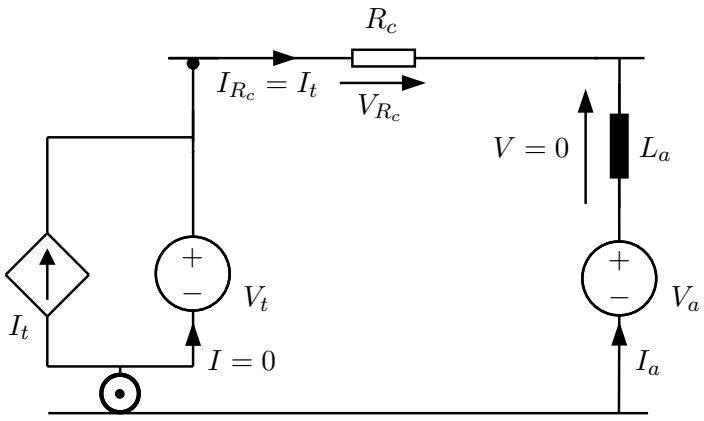

Figure A.9: Equivalent circuit (in steady state) for power converter margins evaluation.

Voltage drop accross L_a is zero, ESS current I_a must be constant and equal to train current I_t in module, in a way that current through ideal voltage generator $V_{t_{min}}$ is zero; to achieve this, V_a must be raised accordingly:

$$I_{R_c} = I_t = \frac{\hat{p}_t}{V_t} \tag{A.83}$$

$$I_a = -I_t = -\frac{\hat{p}_t}{V_t} \tag{A.84}$$

$$V_a = V_{R_c} + V_t \tag{A.85}$$

$$V_a = R_c I_a + V_t = \tag{A.86}$$

$$= R_c \frac{-\hat{p}_t}{V_{t_{min}}} + V_{t_{min}} = 0.6 \cdot \frac{5 \cdot 10^6}{2300} + 2300 = 3604 \ V$$

As a consequence, in the heaviest loading condition, ESS has a ΔV_a margin of about 400 V (4 kV is the catenary voltage limit) to force current at the needed dynamic.

A rude calculation based on a linear first order system gives:

$$\frac{\Delta V_a}{L_a} \simeq \frac{\Delta I_a}{\Delta t} = \frac{400}{6 \cdot 10^{-3}} = 6.67 \cdot 10^4 \text{A/s} \tag{A.87}$$

This is the current slope that can be achieved in the very first time of the transient, when τ is a good approximation of current slope.

Such performance is redundant respect to system needs. As stated above, maximum train current slope is about 150 A/s; ESS converter must be able to easily compensate such disturbance, so a slope of 1500 A/s (ten times higher) is set as target:

$$\Delta V_a \simeq L_a \frac{\Delta I_a}{\Delta t} = 6 \cdot 10^{-3} \frac{1500}{1} = 9\text{V} \tag{A.88}$$

Same check is performed during train brake, with following assumptions:

- by RFI standard [99], TSS DC smoothing reactors have a nominal inductance of 6 mH (rated current 1800 A); the same component is used also for ESS installation (L_a=6mH).

- train is modeled like a power generator (an ideal current generator I_t with an ideal voltage generator V_t in parallel: active power setpoint is given by $P_t = V_t \cdot I_t$);
- train is very far from ESS, at the limit of receptivity distance d_a: total loop resistance is R_c=0.6 Ω;
- train generated power P_t is assumed to be maximum ($\hat{p}_t$=5 MW, heaviest loading condition);
- train voltage V_t is assumed to be the braking voltage threshold (V_b=4 kV), that is maximum absolute catenary voltage, heaviest condition by the voltage point of view;
- parallel filters (capacitors etc.) are neglected, voltages are supposed constant, being current dynamics necessarily faster than voltage variations (current flows control the voltage at the equipment).

Circuit of Fig. A.9 is still valid, so (A.85) and (A.86) are computed again, to lower V_a accordingly:

$$V_a = V_{R_c} + V_t \tag{A.89}$$

$$V_a = R_c I_a + V_t = \tag{A.90}$$

$$= R_c \frac{-\hat{p}_t}{V_b} + V_b = 0.6 \cdot \frac{-5 \cdot 10^6}{4000} + 4000 = 3250 \ V$$

V_a is within minimum catenary voltage tolerance in normal condition, with high margin of regulation.

Because circuit topology is the same, considerations and calculations of (A.87) and (A.88) are still valid.

Next section shows system expected responses at canonical inputs.

A.2.6 Canonical inputs simulations

System response is tested by a unit step of setpoint signal ${V_a}^0(s)$ and by a ramp of train current $I_t(s)$ (slope 300 A/s, satured at $t = 2$ s), considering block diagram of Fig. A.2; regulator is set as shown in (A.77); a delay τ of 2 ms is considered, according to considerations of previous section.

Fig. A.10 shows PI controlled system response to ESS setpoint step.

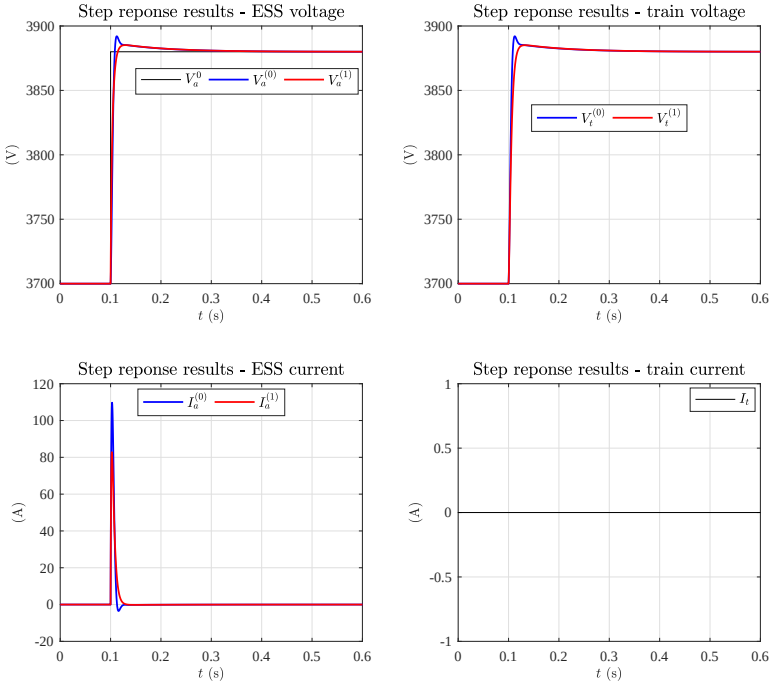

Figure A.10: PI controlled system response to ESS setpoint step.

Significant performances parameters at step response are summarized in Tab A.2.

Table A.2: Step response performance parameters.

Parameter	Unit	$R_c = 0\ \Omega$	$R_c = 0.6\ \Omega$
Rise time	ms	5.7	7.6
Settling time	ms	66.3	68.8
Overshoot	%	7	3
Peak	p.u.	1.07	1.03
Peak time	ms	12.3	29.1

Fig. A.11 shows PI controlled system response to a train current ramp.

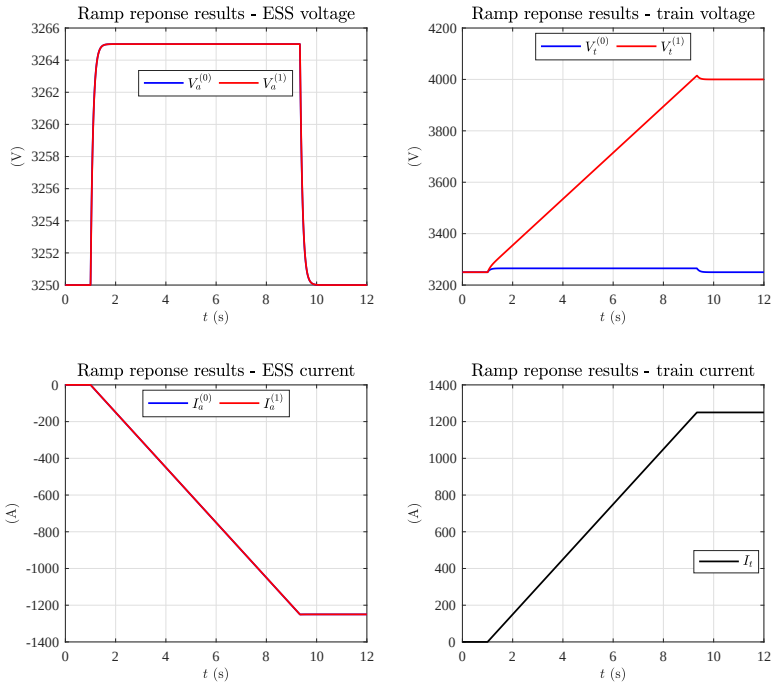

Figure A.11: PI controlled system response to a train current ramp.

PI ramp response shows very good capability of the system in compensating effect of train current, that is basically a disturbance for catenary voltage control. Follow-up is fast and steady state error is within 0.5 % of tolerance, as expected by controller tuning.

A.3 Droop control

Droop control is basically a kind of proportional control.

Droop coefficient k_δ can be obtained by PI regulator parameters to have the same static gain:

$$k_p = 1 \quad , \quad k_i = 10 \tag{A.91}$$

$$k_\delta = \frac{k_i}{k_p} = 10 \tag{A.92}$$

Loop transfer function of droop action is then $k_\delta G_{aa}(s)$. As already mentioned in Par. A.2.2, G_{aa} is asymptotically stable for any value of R_c; in fact, $k_\delta G_{aa}$ Bode diagram is the same as Fig. A.4, shifted above of 20 dB in module, as shown in Fig. A.12.

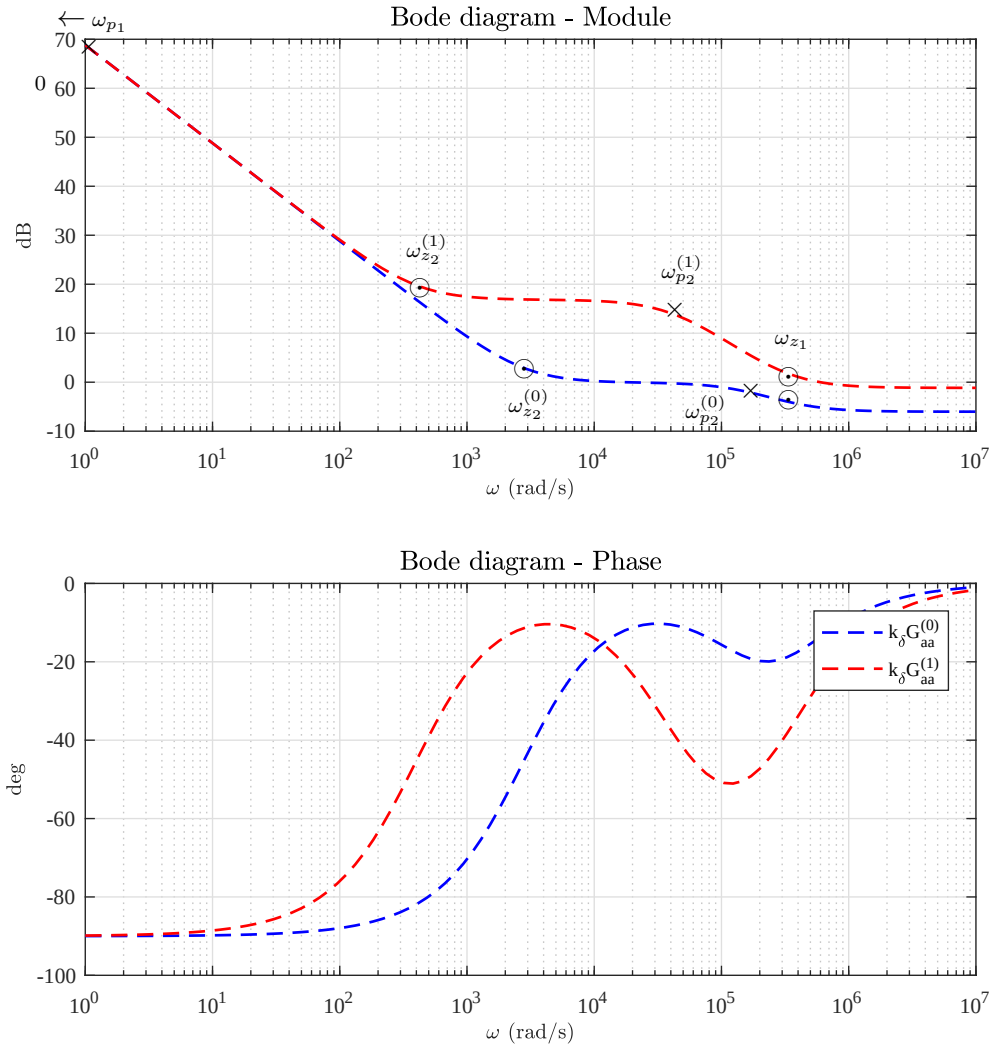

Figure A.12: Bode diagrams of $k_\delta G_{aa}^{(0)}(j\omega)$ (blue) and $k_\delta G_{aa}^{(1)}(j\omega)$ (red).
Poles are marked with a $\times$, zeros are marked with a $\odot$.

Dynamic response is guaranteed due to very high gain; unfortunately, because of insufficient system degree g, steady state conditions could be not optimal.

Fig. A.13 shows droop controlled system response to ESS setpoint step.

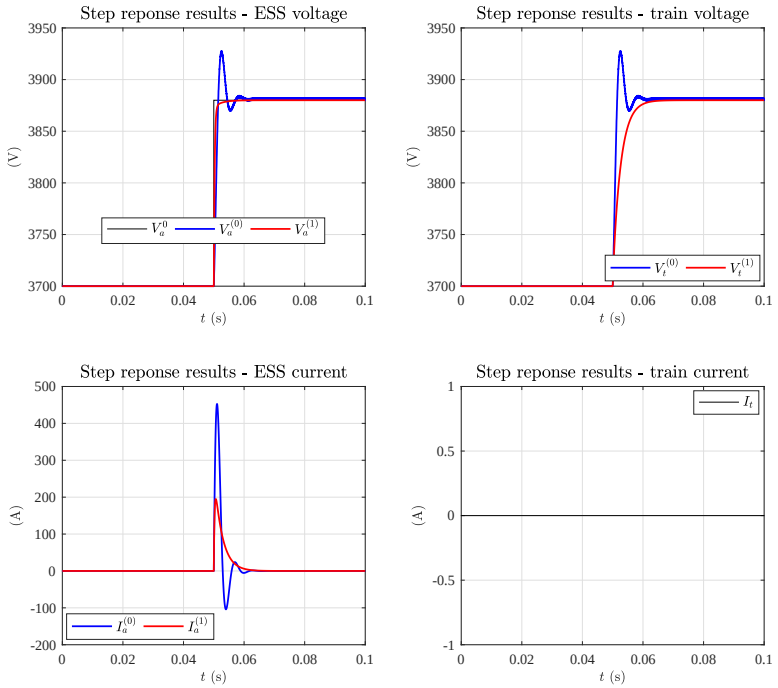

Figure A.13: Droop controlled system response to ESS setpoint step.

Fig. A.14 shows droop controlled system response to a train current ramp.

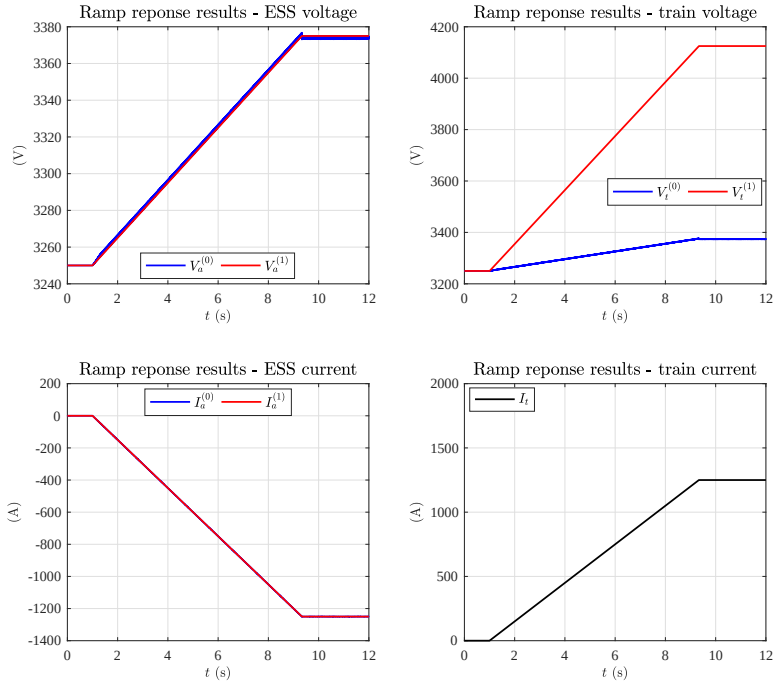

Figure A.14: Droop controlled system response to a train current ramp.

In simulations, still a delay τ of 2 ms has been considered, according to considerations of previous section.

Comparing Fig. A.10 with Fig. A.13 and Fig. A.11 with Fig. A.14, it is evident the droop control is really fast and as robust as PI as well, but it has limited capability in keeping train and ESS voltage within the given tolerance.

This is the main reason PI regulator was successfully implemented in mixed control for ESS charge phase (voltage peak limitation), when catenary voltage could reach easily the braking limit of V_b; droop control was optimal instead in ESS discharge phase (voltage boosting), when absolute precision is not an issue (see data analysis in Par. 1.8.11).

A.4 Appendix conclusions

This appendix deeply explained regulator synthesis and tuning for the system used in most of chapter 1 simulations.

Dynamic system was built starting from components constitutive relationships, MIMO linear model was synthesized both in terms of space-state matrix, both in terms of transfer functions.

Stability conditions were investigated using Bode criterion, considering effects of parameters changing (catenary resistance in particular) and non-ideal behavior of power converter (time delays and forcing capability).

PI regulator was tuned in order to guarantee system performances and asymptotic stability in the worst operative conditions. Droop control tuning and performances were investigated too, comparing static and dynamic behavior respect to PI regulator: PI control was preferred in ESS charge phase while droop was chosen in ESS discharge phase (mixed control of Fig. 1.50).

Theoretical results have been fully proved by canonical input responses and by complete equipment simulations in Chapter 1.

APPENDIX B

Dual Active Bridge (DAB) Converters in ESS

This appendix deepens Dual Active Bridge (DAB) concept for storage systems, including ESS duty, power transfer behavior and an essential comparison with other kind of power electronic converters.

Equipment brief topology to achieve functionalities described in Chapter 1 is presented too.

B.1 Charge and discharge profiles

The ESS can be considered a "cyclic duty energy interface" to a network, in sense that:

- energy interface: it doesn't produce or consume energy (efficiency apart), it only manages energy coming from another source;
- cyclic duty: the possibility to exchange power with the network depends on the energy level of the storage device, that is intrinsically cyclic.

B.1.1 ESS model

When a device is connected to a grid, it's important defining its own model representation; basically, every grid component is intended as an equivalent load or generator, with proper nominal power (generated and/or absorbed) and an efficiency level; this is the standard approach to perform power flow analysis and also to define requirements/prescriptions.

In Chapter 1, specific ESS working cycle has been analyzed; in following section, a general ESS cycle is given; for generality, the nature of the storage and the converter technology are not specified.

B.2 General ESS Working cycle

Usually, a power electronics converter has a well-known capability; since the global system duty is function of energy level and overload possibilities, can be useful define two basic working conditions:

- NOC, Normal Operation Condition;
  it means the system can work continuously, with optimal performance, efficiency and life time;

- EOC, Exceptional Operation Condition;
  it means the system can work for a short time and occasionally to reach further performances.

EOC could reduce the ESS efficiency and life time, so the number and the frequency of exceptional periods should be agreed between customer and manufacturer. Here below only NOC condition is considered, according to following definitions.

B.2.1 Definitions

Without intentional oversizing, the converter is usually designed to be poorly overloadablel.

Energy level becomes therefore a relevant parameter in defining system performances.

To describe ESS NOC and EOC, some definitions about energy are introduced:

- $W_{a_{max}}$: Maximum energy;
  the storage device does not allow further energy (eg. physical, technological or economic limit);

- $W_{a_{mal}}$: Maximal energy;
  the storage device allows further energy charge (till $W_{a_{max}}$) but it is not convenient to perform (eg. efficiency fall, excessive charge time, lifetime reduction, thick margin between $W_{a_{mal}}$ and $W_{a_{max}}$);

- $W_{a_{min}}$: Minimum energy;
  the storage device does not allows further discharge (eg. physical, technological or economic limit);

- $W_{a_{mil}}$: Minimal energy;
  the storage device allows further energy discharge (till $W_{a_{min}}$) but it is not convenient to perform (eg. efficiency fall, low power level, lifetime reduction, thick margin between $W_{a_{mil}}$ and $W_{a_{min}}$).

All these quantities can be related to ESS cycle.

In a $W - t$ plan, three operative areas are created, as shown in Fig. B.1:

a) $W_{a_{max}} \leftrightarrow W_{a_{mal}}$: EOC;

b) $W_{a_{mal}} \leftrightarrow W_{a_{mil}}$: NOC;

c) $W_{a_{mil}} \leftrightarrow W_{a_{min}}$: EOC.

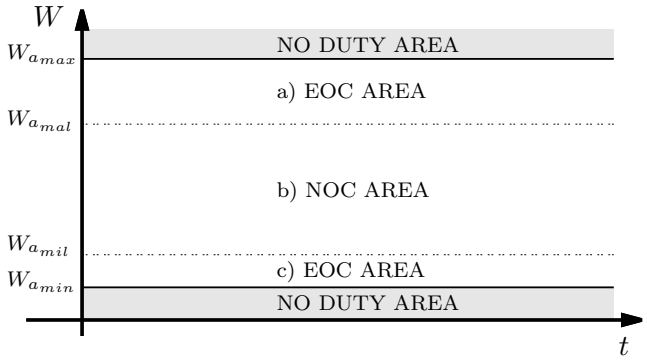

Figure B.1: ESS operative areas.

Considering that:

- above $W_{a_{max}}$ and below $W_{a_{min}}$ the ESS cannot work (NO DUTY AREA);
- in area a) the system has very limited operation in charge;
- in area c) the system has very limited operation in discharge.

As said, area (b) is the only one in which the ESS has full operation margin; ESS working duties are therefore designed to stay within area (b), with exceptional possibility to provide extra charge in area (a) and extra discharge in area (c).

B.2.2 General ESS working cycle

Consider a general multiport ESS device: for every single port, the net energy exchanged at any time is easy to measure with a meter; the gross energy stored in the device depends on the storage technology, converter topology, power losses and many other factors (eg. auxiliary circuit consumption).

To determine in a quite simple way system performances, an appropriate combination of charge/discharge sessions can be done, in a way that at the end of the cycle the energy into the storage is the same as it was at the beginning.

Consider for simplicity a single port and a single storage device: testing the NOC duty, test cycle starts from $W_{a_{mal}}$, goes to $W_{a_{mil}}$ and goes back to $W_{a_{mal}}$.

System can be controlled to maintain the power profile as much as possible constant, but of course some deviations are expected, because of storage device peculiarities.

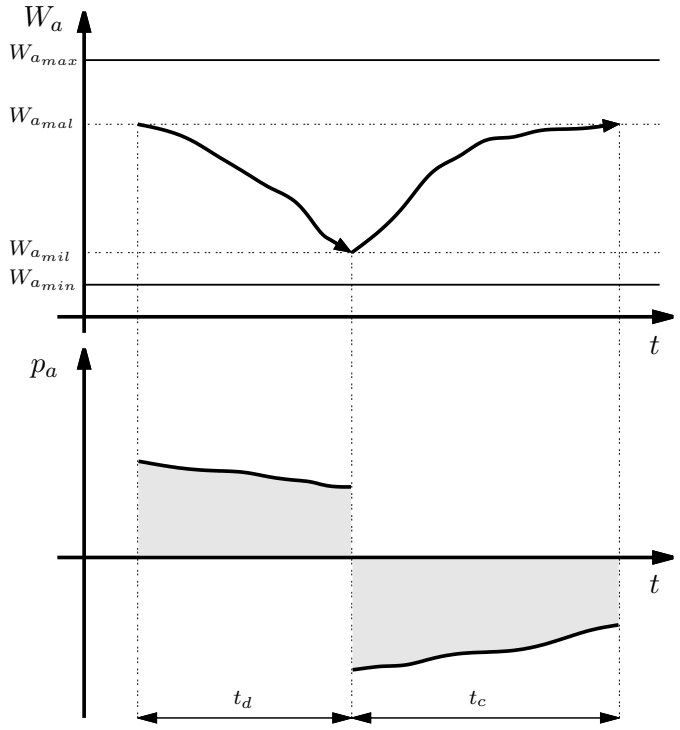

Figure B.2: Generic ESS cycle representation
Profiles are general and indicative.

Fig. B.2 shows an indicative profile of the cycle; discharge time t_d and charge time t_c are also tunable, to fulfill dynamic requirements and considering the specific storage size and technology.

ESS efficiency in charge and discharge for a specific case has been already presented in Par. 1.8.5: considering again previous formulas, global efficiency η for a general case is given accordingly:

$$W_{a_{mal}} - W_{a_d} + W_{j_{a_d}} = W_{a_{mil}} \tag{B.1}$$

$$W_{j_{a_d}} = W_{a_{mil}} - W_{a_{mal}} + W_{a_d} \tag{B.2}$$

$$W_{a_{mil}} - W_{a_c} + W_{j_{a_c}} = W_{a_{mal}} \tag{B.3}$$

$$W_{j_{a_c}} = W_{a_{mal}} - W_{a_{mil}} + W_{a_c} \tag{B.4}$$

$$\eta = \oint_W p_a(t)\, dt = 1 - \frac{W_{j_{a_d}} + W_{j_{a_c}}}{W_{a_c}} = \frac{W_{a_d}}{-W_{a_c}} \tag{B.5}$$

Result of (B.5) is the most general, it can be achieved by simple energy measurements at ESS terminals and by knowing ESS energy state.

It is important specify that process must be cyclic (initial and final levels must be the same) and any energy loop can be theoretically used; anyway, in case system is not linear, same loops at different energy levels could result in different efficiency values.

Using the whole ESS capacity ($W_{a_{mal}} - W_{a_{mil}}$), efficiency is the average defined in the full energy capability.

In case ESS efficiency is considered constant (even if different in charge and discharge) the well-known result of global efficiency value is achieved:

$$W_{a_{mal}} - W_{a_d} + \Big(1 - \frac{1}{\eta_{a_d}}\Big) W_{a_d} = W_{a_{mil}} \tag{B.6}$$

$$W_{a_{mal}} - W_{a_{mil}} = W_{a_d} - \Big(1 - \frac{1}{\eta_{a_d}}\Big) W_{a_d} \tag{B.7}$$

$$W_{a_{mil}} - W_{a_c} + (1 - \eta_{a_c}) W_{a_c} = W_{a_{mal}} \tag{B.8}$$

$$W_{a_{mal}} - W_{a_{mil}} = -W_{a_c} + (1 - \eta_{a_c}) W_{a_c} \tag{B.9}$$

$$W_{a_d} - \Big(1 - \frac{1}{\eta_{a_d}}\Big) W_{a_d} = -W_{a_c} + (1 - \eta_{a_c}) W_{a_c} \tag{B.10}$$

$$\frac{W_{a_d}}{\eta_{a_d}} = -\eta_{a_c} W_{a_c} \tag{B.11}$$

$$\eta = \frac{W_{a_d}}{-W_{a_c}} = \eta_{a_c} \eta_{a_d} \tag{B.12}$$

Besides ESS efficiency, also power converter structure is crucial for performance and costs evaluation; in the followings, several kinds of converters for DC networks are briefly analyzed and compared.

B.3 Converters for DC networks: state of the art

Normally, DC-DC conversion does not require AC stages; anyway, thinking about high power/voltage networks, some problems arise:

- SAFETY: galvanic insulation from HV side of the converter becomes mandatory if the equipment has low voltage ports;
- EFFICIENCY: DC-DC direct conversion at very different voltage levels reduces the global converter efficiency;
- MANUFACTURING: without galvanic insulation, also the low voltage ports must be designed and protected for the HV; this is not practical, nether reasonable, nether economically sustainable.

As a result, choosing a DC-AC-DC approach is practically mandatory; insulation transformers are the only devices able to solve above problems.

Because the system has power converters at every port, AC voltage is internally generated in order to reduce transformers dimensions, losses etc.; the result is a so-called Solid State Transformer (SST) or Power Electronics Transformer (PET), in which high frequency AC voltage is used to transfer power between insulated power sections.

SST structure concept is shown in Fig. B.3.

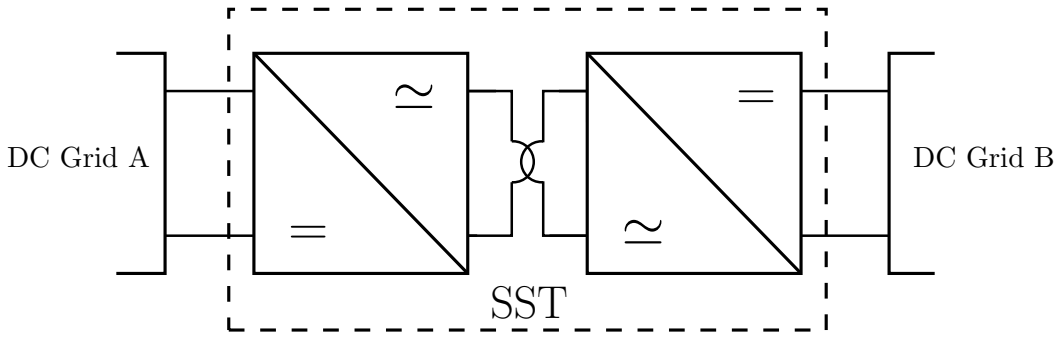

Figure B.3: SST structure concept.

System is composed by a high frequency transformer fed by by a couple of DC-AC converters (precisely, DC-AC and AC-DC), fully reversible and fully controllable.

In following subsections, a brief overview of several DC-AC converter is shown; the description includes a typical circuit layout and a list of main advantages and disadvantages, mostly related to SST structure implementation.

Later on, further considerations will came from direct comparison of the different solutions.

B.3.1 Cascaded H-bridge converter (CHB)

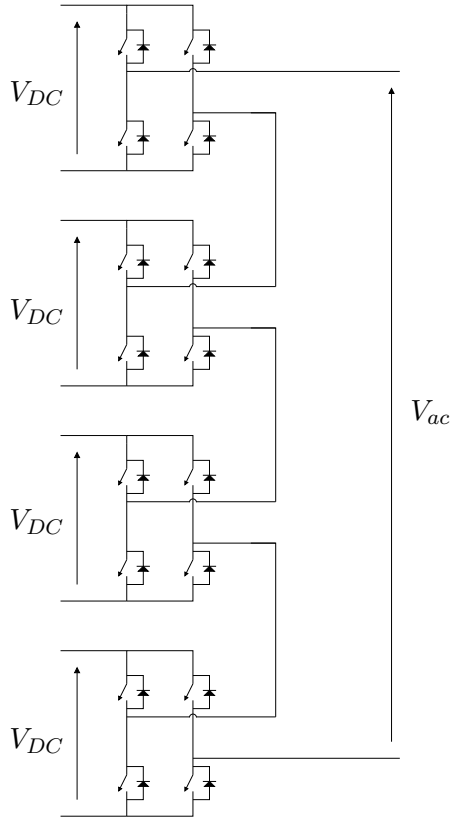

Figure B.4: Cascaded H-bridge converter.

Main advantages:

- every H-bridge module has the same structure, no further elements to connect the several blocks, so the configuration is full mudular;
- soft-switching techniques applicable, to reduce losses;
- choosing properly different values of V_{DC}, significant reduction of DC modules is possible.

Main disadvantages:

- every H-bridge needs an indipendent power supply.

B.3.2 Neutral Point Clamped converter (NPC)

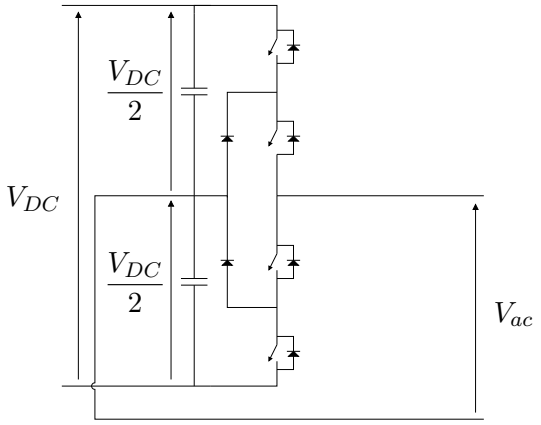

Figure B.5: Neutral Point Clamped converter.

Main advantages:

- with high number of voltage levels, very low voltage harmonic distortion;
- power electronic components voltage sizing is very favorable.

Main disadvantages:

- high number of voltage levels requires many clamping diodes;
- capacitors pre-charge circuits are mandatory;
- control complexity due to capacitors voltage balancing and monitoring.

B.3.3 Flying Capacitor converter (FC)

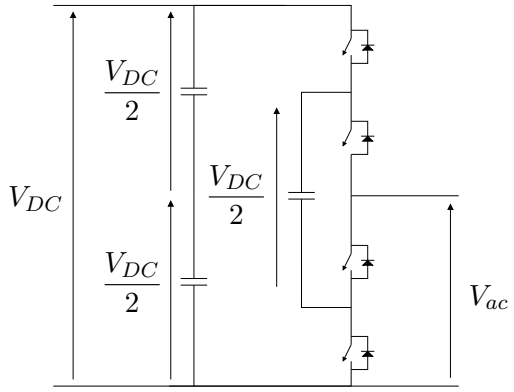

Figure B.6: Flying Capacitor converter.

Main advantages:

- full modular structure;
- with high number of voltage levels, very low voltage harmonic distortion;
- power electronic components voltage dimensioning is very favorable;
- capacitors can face temporary supply loss.

Main disadvantages:

- high number of voltage levels requires many capacitors;
- capatitors pre-charge circuits are mandatory, also discharge circuits;
- control complexity due to capacitors voltage balancing and monitoring.

B.3.4 Dual Active Bridge converter (DAB)

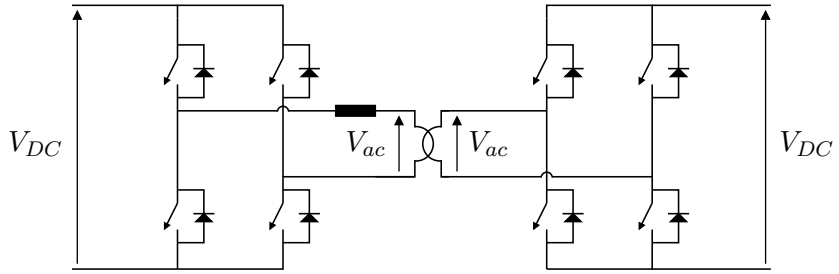

Figure B.7: Dual Active Bridge Converter.

Main advantages:

- full modular structure;
- full symmetric structure;
- low number of passive components;
- soft-switching possible;
- high density power.

Main disadvantages:

- power electronic components voltage sizing is not favorable;
- single level converter;
- series reactors are necessary.

B.4 Converters comparison

Advantages and disadvantages listed in previous sections can be used to compare critically the different technical solutions; to begin, looking at the several circuit layouts, some general considerations arise:

- high voltage converters must be sized considering components capabilities; not all kind of topologies are possible; a trade-off between technology and performance is mandatory;
- low voltage converters are not a big deal by the sizing point of view; any kind of topology is suitable; key factors are performance and efficiency;
- between a single phase or a three phase topology, single phase seems to be much more "modular oriented"; in fact, a three phase (or a multi-phase) behavior can be obtained connecting properly three (or more) single phase stages; convenience of such approach depends on the increasing of power components respect to "native" three phase layout;
- considering high frequency to reduce transformers sizing (some kHz), containment of switching losses become relevant; harmonic distortion is a topic too, although the AC side in the multiport is for internal use only.

CHB topology has the biggest disadvantage to need independent power supplies; considering the multiport to be connected without limitations at every DC grid, this is a heavy constraint; all other topologies are suitable to realize the concept in Fig. B.3, but the only fully symmetrical and fully modular solution is given by the DAB topology; possibilities offered by DAB converter combination are several: many converter modules can be put in series on port 1 (DC catenary side), to withstand the voltage level; high frequency transformers provide galvanic insulation and voltage scaling; regarding outputs, many module outputs can be connected in parallel at port 2 (DC ESS side), to reach the wanted power level. To generate AC voltage necessary for high quality auxiliary power supplied, two different solutions are shown.

In Fig. B.8, some H-bridge converters are not in parallel on DC ESS side but they are used to spill some power from catenary to generate AC at port 3 (industrial frequency); because DAB is essentially a DC-DC converter in such configuration, a further DC-AC inverter is anyway necessary.

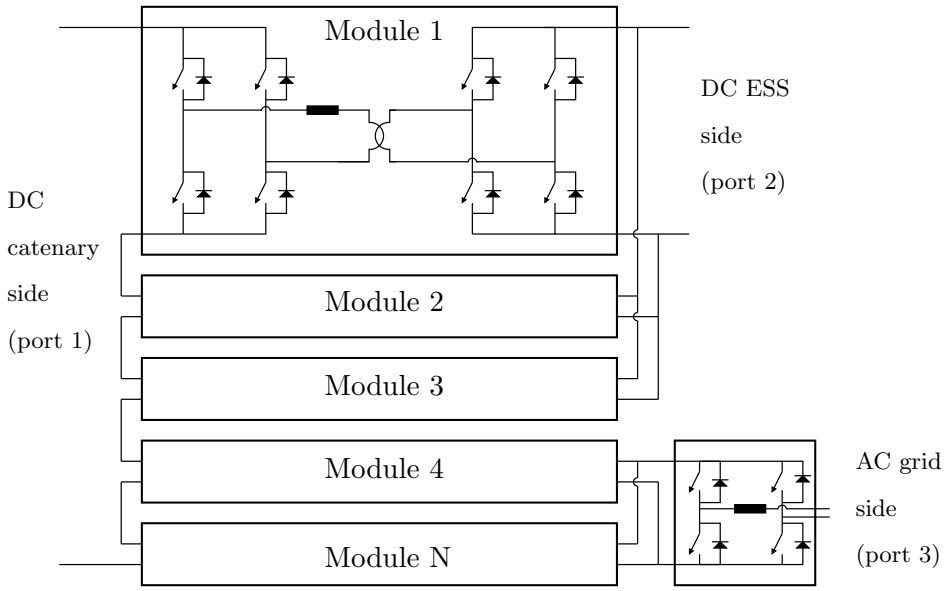

Figure B.8: DAB converters combination (a): many modules are put in series on port 1 (DC), to withstand the voltage level; high frequency transformers provide galvanic insulation and voltage scaling; many module outputs are connected in parallel at port 2 (DC), to reach the wanted power level. Further H-bridge converters can generate AC at port 3 (industrial frequency).

Above solution, nevertheless fascinating and challenging by the control point of view, has several big disadvantages, most of all in components sizing; consider for simplicity a two modules only example, as shown in Fig. B.9.

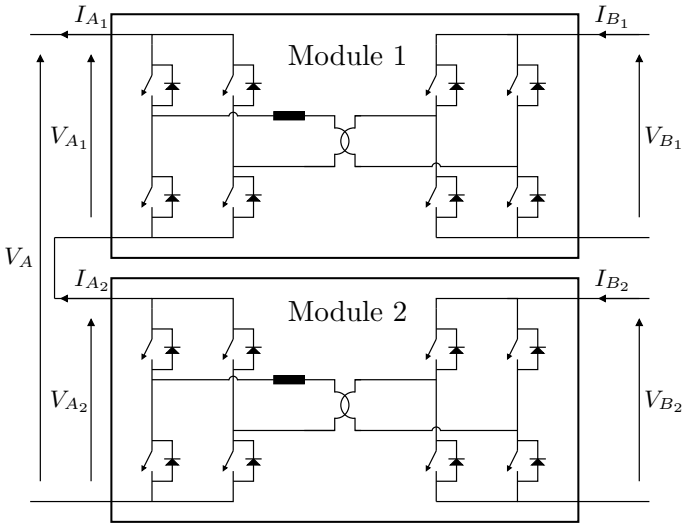

Figure B.9: DAB converter combination (a) with two modules only.

Two converter modules are put in series on A-side (port A), to withstand a higher voltage level; embedded Power Electronics Transformers (PET) provide galvanic insulation and voltage scaling; two module outputs (port B_1 and B_2) are then available on B-side.

Port A constitutive equations are:

$$I_{A_1} = I_{A_2} \tag{B.13}$$

$$V_A = V_{A_1} + V_{A_2} \tag{B.14}$$

Port B_1 and B_2 could appear totally independent, but a power balance shows that some working conditions are not recommended at all; in fact, supposing

$$\begin{cases} V_A I_{A_1} \geq 0 \ , \ I_{A_1} \geq 0 \\ V_{B_1} I_{B_1} \geq 0 \ , \ I_{B_1} \geq 0 \\ V_{B_2} I_{B_2} \leq 0 \ , \ I_{B_2} \leq 0 \end{cases} \tag{B.15}$$

the only way to obtain such condition is imposing also:

$$V_{A_2} \leq 0 \tag{B.16}$$

As shown, opposite power flows on B-side ports, or at least zero power flow at one of two, goes to a voltage inversion or cancellation at A-side.

Two main problems then arise:

- DAB conventional blocking diodes are not enough, fully bi-directional solid state switches (see Fig. B.10) are needed;
- a single converter of A-side has to withstand the rated full voltage of port A or even more.

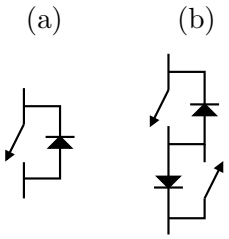

Figure B.10: Fully bi-directional solid state switch (b). Structure is composed by two couples of traditional switch-diode modules (a) in counter-series.

All above considerations result in HW and control complication, losses increase and not so relevant advantages by independent control of B-side ports.

A smarter way to connect the B-side ports is instead shown in Fig. B.11: module outputs are all connected in parallel, creating a common link to feed DC loads (ESS on port B_1); AC grid (port B_2) can be connected at the same link through an interface converter. All ports are fully bi-directional, power flows are independent and the system is completely scalable; series connection on A-side is useful to handle high voltages and the structure provides, if needed, a certain level of redundancy (N-1 or more).

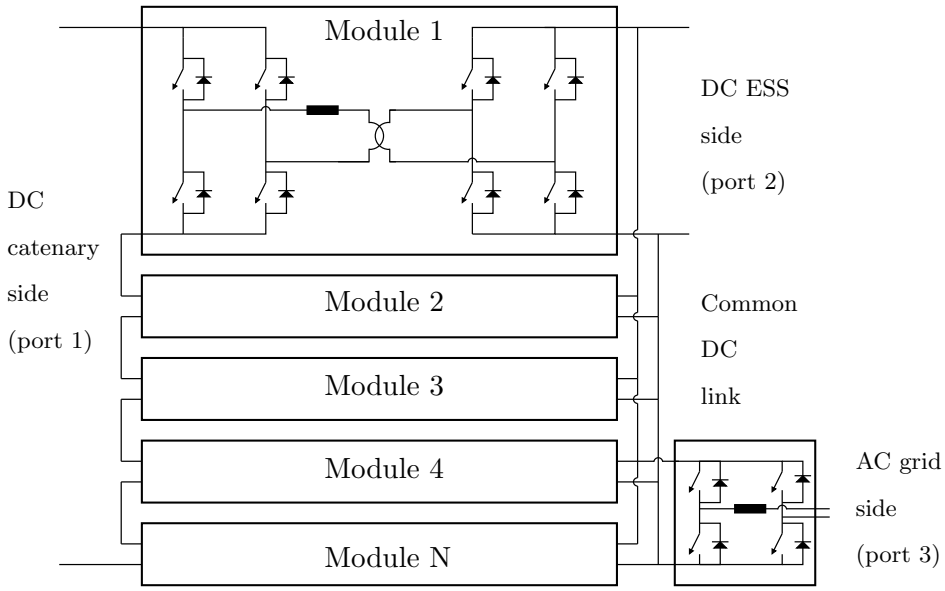

Figure B.11: DAB converters combination (b): mavy modules are put in series on port 1 (DC), to withstand the voltage level; high frequency transformers provide galvanic insulation and voltage scaling; all module outputs are connected in parallel to create a common DC link to supply directly port 2 (DC); further H-bridge converters are connected to DC link to generate AC at port 3 (industrial frequency).

Such approach, has been used in Par. 1.10.5 for multiport simulation (Fig. 1.62).

In the followings, DAB concept will be analyzed, at first considering the basic structure and then the control strategy.

B.5 Dual Active Bridge basic structure

A dual active bridge converter is composed by two independent fully controlled H-bridges with a leakage inductance in between, as shown in Fig. B.12.

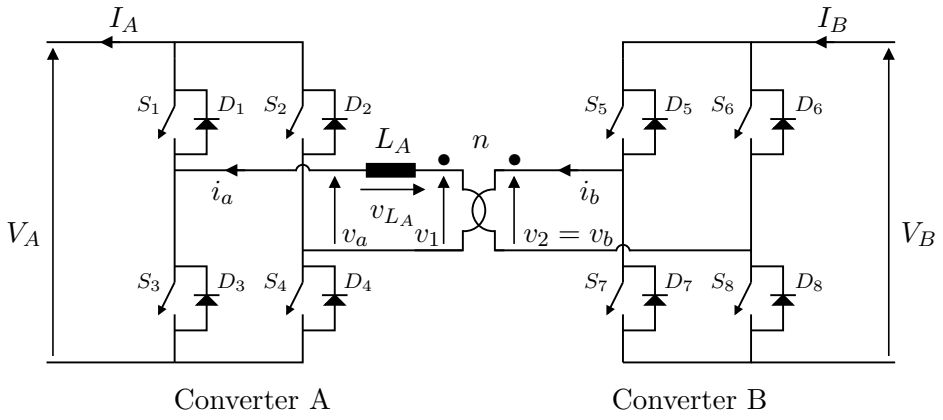

Figure B.12: DAB structure.

The leakage inductance can be obtained using the short circuit inductance of a decoupling transformer, that is designed to work properly at the switching frequency of the two converters; this way, the two converters can operate at very different voltage level, thus being galvanically insulated each other.

H-bridge converters operate at the same switching frequency, and the power flow is controlled by imposing the phase shift (thus the time delay) between the two converters waveforms. Operating at mid-high frequency, usually the converters work in square wave mode: this results in a quite big harmonic content in the current waveform, but very far from the DC component, that is the wanted effect to transfer successfully active power from the two DC sections at the edges; moreover, the square wave control permit to operate, under certain conditions, in soft switching mode.

DC gate voltages that let the H-bridges working are kept by interface capacitors, that provide also a positive filtering effect.

For the following considerations about DAB control, two ideal DC voltage generators placed at the electric ports.

B.6 Dual Active Bridge control strategy

As said in section B.5, the phase shift between the two H-bridge converters is the only way to control the active power flow between the two electric gates; in Fig. B.13, converter A waveforms at a given shift time τ are shown.

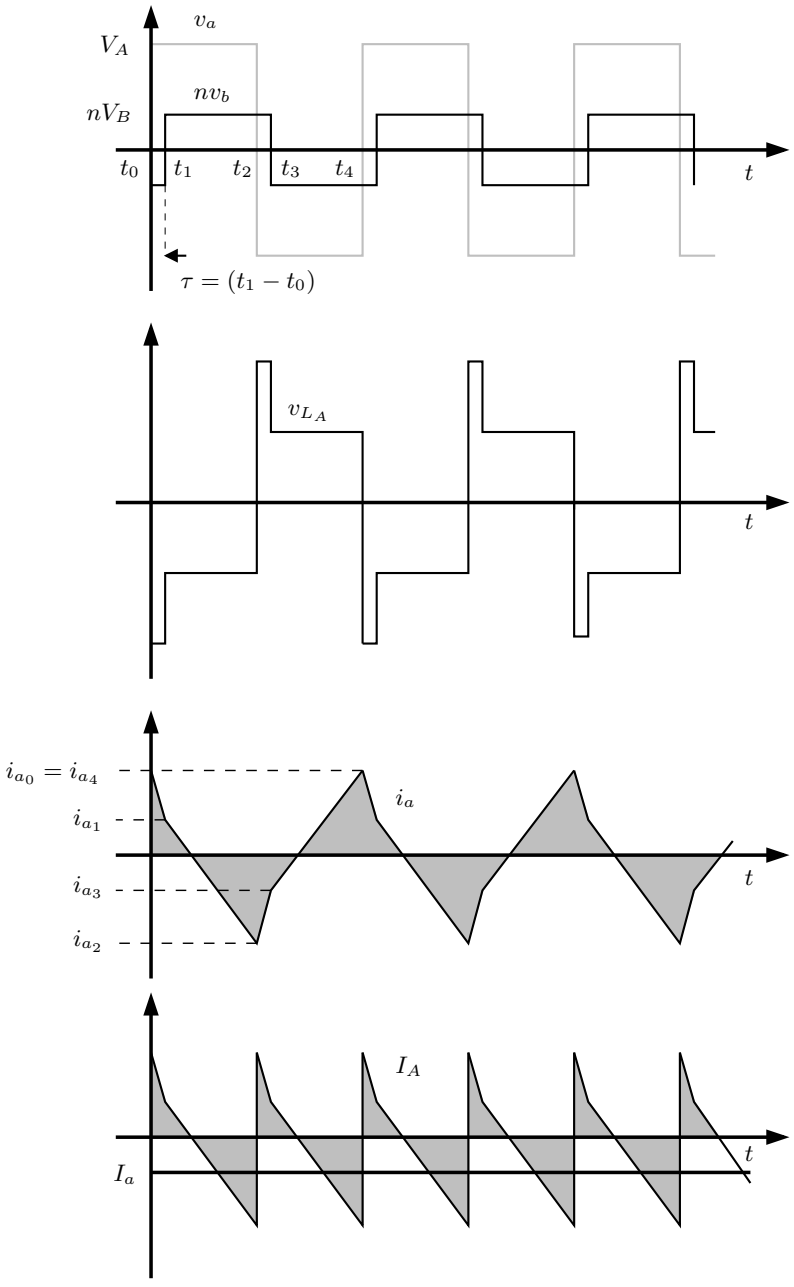

Figure B.13: DAB voltage and current waveforms on converter A.

Fig B.13 is similar to Fig. 1.63, with more details about voltage and current quantities; also measurement conventions are the same.

Consider the following equation:

$$v_{L_A}(t) = v_1(t) - v_a(t) \tag{B.17}$$

with

$$v_1(t) = nv_2(t) = nv_b(t) \tag{B.18}$$

due to the transformer ratio:

$$n = \frac{v_1}{v_2} \tag{B.19}$$

A switching function $\mathrm{swf}(t)$, is applied at the two converters in order two generate two square-wave signals; $v_1(t)$ is shifted by $v_a(t)$ of τ:

$$v_a(t) = V_A \ \mathrm{swf}(t) \tag{B.20}$$

$$v_1(t) = nV_B \ \mathrm{swf}(t - \tau) \tag{B.21}$$

τ can be positive either negative: v_1 is then in lag or in lead respect to v_a.

Fig. B.13 shows v_a and v_1 profiles according to (B.20) and (B.21): $\tau = (t_1 - t_0)$; Assuming the circuit purely inductive (or with a very long time constant respect to switching period), the general solution to find $i_a(t)$ is

$$i_a(t) = \frac{1}{L_A} \int v_{L_A}(t)dt + i_a(0) \tag{B.22}$$

In steady state, current $i_a(t)$ must be periodic and zero-average value; currents in points t_0, t_1, t_2, t_3 and $t_4 \equiv t_0$ can be analytically calculated:

$$i_{a_1} = \frac{1}{L_A} \int_{t_0}^{t_1} v_{L_A}(t)dt + i_{a_0} = \frac{1}{L_A}(-V_A - nV_B)(t_1 - t_0) + i_{a_0} \tag{B.23}$$

$$i_{a_2} = \frac{1}{L_A} \int_{t_1}^{t_2} v_{L_A}(t)dt + i_{a_1} = \frac{1}{L_A}(-V_A + nV_B)(t_2 - t_1) + i_{a_1} \tag{B.24}$$

$$i_{a_3} = \frac{1}{L_A} \int_{t_2}^{t_3} v_{L_A}(t)dt + i_{a_2} = \frac{1}{L_A}(V_A + nV_B)(t_3 - t_2) + i_{a_2} = -i_{a_1} \tag{B.25}$$

$$i_{a_4} = \frac{1}{L_A} \int_{t_3}^{t_4} v_{L_A}(t)dt + i_{a_3} = \frac{1}{L_A}(V_A - nV_B)(t_4 - t_3) + i_{a_3} = i_{a_0} \tag{B.26}$$

Being T_s the switching period,

$$\omega_s = \frac{2\pi}{T_s} \tag{B.27}$$

$$\Delta = \omega_s t \tag{B.28}$$

port voltages can be defined as function of shift angle δ:

$$\delta = \omega_s \tau = \omega_s (t_1 - t_0) \tag{B.29}$$

$$v_a(\Delta) = V_A \text{ swf}(\Delta) \tag{B.30}$$

$$v_1(\Delta) = nV_B \text{ swf}(\Delta - \delta) \tag{B.31}$$

Like τ, since δ is positive in (B.29), v_1 is in lag respect to v_a.
This way, (B.23), (B.24), (B.25) and (B.26) can be re-written as:

$$i_{a_1} = \frac{1}{\omega_s L_A}(-V_A - nV_B)\delta + i_{a_0} \tag{B.32}$$

$$i_{a_2} = \frac{1}{\omega_s L_A}(-V_A + nV_B)(\pi - \delta) + i_{a_1} \tag{B.33}$$

$$i_{a_3} = \frac{1}{\omega_s L_A}(V_A + nV_B)\delta + i_{a_2} = -i_{a_1} \tag{B.34}$$

$$i_{a_4} = \frac{1}{\omega_s L_A}(V_A - nV_B)(\pi - \delta) + i_{a_3} = i_{a_0}. \tag{B.35}$$

Substituting (B.34) into (B.32) it results

$$i_{a_0} = -i_{a_2} \tag{B.36}$$

so, combining (B.33) and (B.32) with (B.36):

$$i_{a_1} = \frac{1}{\omega_s L_A}(-V_A - nV_B)\delta - \frac{1}{\omega_s L_A}(-V_A + nV_B)(\pi - \delta) - i_{a_1} \tag{B.37}$$

$$i_{a_1} = \frac{1}{2\omega_s L_A}\Big[V_A(\pi - 2\delta) - nV_B\pi\Big] \tag{B.38}$$

and (B.38) with (B.32):

$$i_{a_0} = i_{a_1} - \frac{1}{\omega_s L_A}(-V_A - nV_B)\delta \tag{B.39}$$

$$i_{a_0} = \frac{1}{2\omega_s L_A}\Big[V_A\pi - nV_B(\pi - 2\delta)\Big] \tag{B.40}$$

AC converter current $i_a(t)$ is given by (B.40), (B.38), (B.33), (B.34) and (B.35); its rectified component is $I_A(t)$, so the average DC converter current I_a can be calculated as follows:

$$I_a = \frac{2}{T_s}\int_0^{\frac{T_s}{2}} i_a(t)dt = \frac{1}{\pi}\Big[\int_0^{\delta} i_a(\Delta)d\Delta + \int_{\delta}^{\pi} i_a(\Delta)d\Delta\Big] \tag{B.41}$$

with:

$$i_a(\Delta) = \frac{i_{a_1} - i_{a_0}}{\delta}\Delta + i_{a_0}, 0 \le \Delta \le \delta \tag{B.42}$$

$$i_a(\Delta) = \frac{i_{a_2} - i_{a_1}}{\pi - \delta}(\Delta - \delta) + i_{a_1}, \delta \le \Delta \le \pi \tag{B.43}$$

Substituting (B.32) and (B.40) into (B.42),

$$\int_0^{\delta} i_a(\Delta)d\Delta = \int_0^{\delta}\left\{-\frac{1}{\omega_s L_A}(V_A+nV_B)\Delta+\frac{1}{2\omega_s L_A}\Big[V_A\pi-nV_B(\pi-2\delta)\Big]\right\}d\Delta = \tag{B.44}$$

$$= \frac{1}{2\omega_s L_A}\left\{-(V_A+nV_B)\Delta^2+\Big[V_A\pi-nV_B(\pi-2\delta)\Big]\Delta\right\}_0^{\delta} = \tag{B.45}$$

$$= \frac{1}{2\omega_s L_A}\left\{-(V_A+nV_B)\delta^2+\Big[V_A\pi-nV_B(\pi-2\delta)\Big]\delta\right\} = \tag{B.46}$$

$$= \frac{1}{2\omega_s L_A}(-V_A\delta^2 - nV_B\delta^2 + V_A\pi\delta - nV_B\pi\delta + nV_B 2\delta^2) = \tag{B.47}$$

$$= \frac{\delta}{2\omega_s L_A}\Big[V_A(\pi-\delta) - nV_B(\pi-\delta)\Big] = \tag{B.48}$$

$$= \frac{\delta}{2\omega_s L_A}(V_A - nV_B)(\pi-\delta). \tag{B.49}$$

Substituting (B.33) and (B.38) into (B.43),

$$\int_{\delta}^{\pi} i_a(\Delta)d\Delta = \int_{\delta}^{\pi}\left\{\frac{1}{\omega_s L_A}\Big[(-V_A+nV_B)\Delta-(-V_A+nV_B)\delta\Big]+\frac{1}{2\omega_s L_A}\Big[V_A(\pi-2\delta)-nV_B\pi\Big]\right\}d\Delta = \tag{B.50}$$

$$= \frac{1}{2\omega_s L_A}\left\{(-V_A+nV_B)\Delta^2-2(-V_A+nV_B)\delta\Delta+\Big[V_A\pi-2V_A\delta-nV_B\pi\Big]\Delta\right\}_{\delta}^{\pi} = \tag{B.51}$$

$$= \frac{1}{2\omega_s L_A}\Big[(-V_A+nV_B)(\pi^2-\delta^2)-2(-V_A+nV_B)(\delta\pi-\delta^2)+(V_A\pi-2V_A\delta-nV_B\pi)(\pi-\delta)\Big] = \tag{B.52}$$

$$= \frac{1}{2\omega_s L_A}\Big[-V_A\pi^2+V_A\delta^2+nV_B\pi^2-nV_B\delta^2+2V_A\delta\pi-2V_A\delta^2-2nV_B\delta\pi+2nV_B\delta^2+ \\ +V_A\pi^2-V_A\pi\delta-2V_A\delta\pi+2V_A\delta^2-nV_B\pi^2+nV_B\delta\pi\Big] = \tag{B.53}$$

$$= \frac{\delta}{2\omega_s L_A}\Big[-V_A(\pi-\delta)-nV_B(\pi-\delta)\Big] = \tag{B.54}$$

$$= \frac{\delta}{2\omega_s L_A}(-V_A-nV_B)(\pi-\delta) \tag{B.55}$$

Combining (B.49) and (B.55) into (B.41)

$$I_a = \frac{1}{\pi}\Big[\frac{\delta}{2\omega_s L_A}(-V_A-nV_B)(\pi-\delta)+(V_A-nV_B)(\pi-\delta)\Big] = \tag{B.56}$$

$$= \frac{1}{\pi}\Big[\frac{\delta}{2\omega_s L_A}(-2nV_B)(\pi-\delta)\Big] = \tag{B.57}$$

the average DC converter current I_a is:

$$I_a = -\frac{nV_B}{\omega_s L_A}\delta\Big(1-\frac{\delta}{\pi}\Big) \quad , \quad \delta > 0 \tag{B.58}$$

Result of (B.58) is shown in Fig. B.13: when shift angle is positive, thus v_1 is in lag respect to v_a, average converter current at port A is negative.

By transformer constitutive equation, considering measurement conventions of Fig. (B.13), current at port B can be found:

$$n = \frac{i_2}{i_1} \tag{B.59}$$

$$i_b(t) = ni_a(t) = \frac{n}{L_A}\int v_{L_A}dt + i_b(0). \tag{B.60}$$

Calculations are similar to previous ones, they are omitted for brevity; average DC converter current I_b is:

$$I_b = -\frac{nV_A}{\omega_s L_A}\delta\Big(1-\frac{\delta}{\pi}\Big) \quad , \quad \delta > 0 \tag{B.61}$$

Previous equations have been performed with positive shift angle; repeating the same analysis with a negative phase shift, the following solutions are obtained:

$$I_a = -\frac{nV_B}{\omega_s L_A}\delta\left(1+\frac{\delta}{\pi}\right) \quad , \quad \delta < 0 \tag{B.62}$$

$$I_b = -\frac{nV_A}{\omega_s L_A}\delta\left(1+\frac{\delta}{\pi}\right) \quad , \quad \delta < 0 \tag{B.63}$$

Comparing (B.58) with (B.62) and (B.61) with (B.63), a more general formulation, not depending on phase shift sign, is possible:

$$I_a = -\frac{kV_B}{\omega_s L_A}\delta\left(1-\frac{|\delta|}{\pi}\right) \quad , \quad -\frac{\pi}{2} \leq \delta \leq \frac{\pi}{2} \tag{B.64}$$

$$I_b = -\frac{kV_A}{\omega_s L_A}\delta\left(1-\frac{|\delta|}{\pi}\right) \quad , \quad -\frac{\pi}{2} \leq \delta \leq \frac{\pi}{2} \tag{B.65}$$

By (B.64) and (B.65) analysis, peaks of average current are given by δ equal to $\pi/2$ or $-\pi/2$; control target is setting δ within such span, transferring current from port A to port B and vice versa.

About active power flows, they are given by average currents only (direct component of rectified current): neglecting for simplicity power losses, it can be written:

$$P_A = P_B \tag{B.66}$$

$$V_A I_a = V_B I_b \tag{B.67}$$

(B.64) and (B.65) show that, once V_A and V_B are given and constant, the power flow is given by the shift angle δ through the followings:

$$P_A = -V_A\frac{kV_B}{\omega_s L_A}\delta\left(1-\frac{|\delta|}{\pi}\right) \quad , \quad -\frac{\pi}{2} \leq \delta \leq \frac{\pi}{2} \tag{B.68}$$

$$P_B = P_A = -V_B\frac{kV_A}{\omega_s L_A}\delta\left(1-\frac{|\delta|}{\pi}\right) \quad , \quad -\frac{\pi}{2} \leq \delta \leq \frac{\pi}{2} \tag{B.69}$$

In case port voltages are not constant (as in Par. 1.10.5 simulations), the control can compensate such disturbances by adjusting δ value accordingly.

In Fig. B.14 a plot of $P(\delta) = \delta\left(1-\frac{|\delta|}{\pi}\right)$ is given; the function is not linear; it means that the control action is stronger for some angle values and weaker in some others; this could introduce system instability. The first step is multiply the control action by a dynamic gain $G(\delta)$:

$$G(\delta) = \left(1-\frac{|\delta|}{\pi}\right)^{-1} \quad , \quad -\frac{\pi}{2} \leq \delta \leq \frac{\pi}{2} \tag{B.70}$$

Also $G(\delta)$ is plot in Fig. B.14.

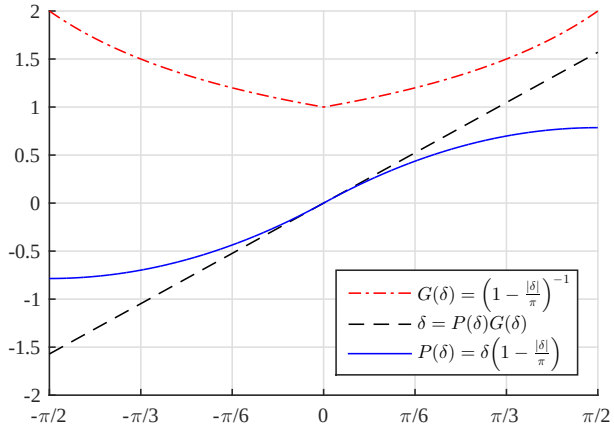

Figure B.14: $P(\delta)$, $G(\delta)$ and δ plots in interval $-\frac{\pi}{2} \leq \delta \leq \frac{\pi}{2}$.

The system controls converter current, value of I_a is calculated every switching period, δ is then properly adjusted.

Control has been successfully implemented and tested in simulations of Par. 1.10.5; mixed regulator of Fig. 1.50 generates current setpoint I_a^0 and then a faster PID controller (PID_δ) operates on the shift angle δ.

Fig. B.15 shows the concept.

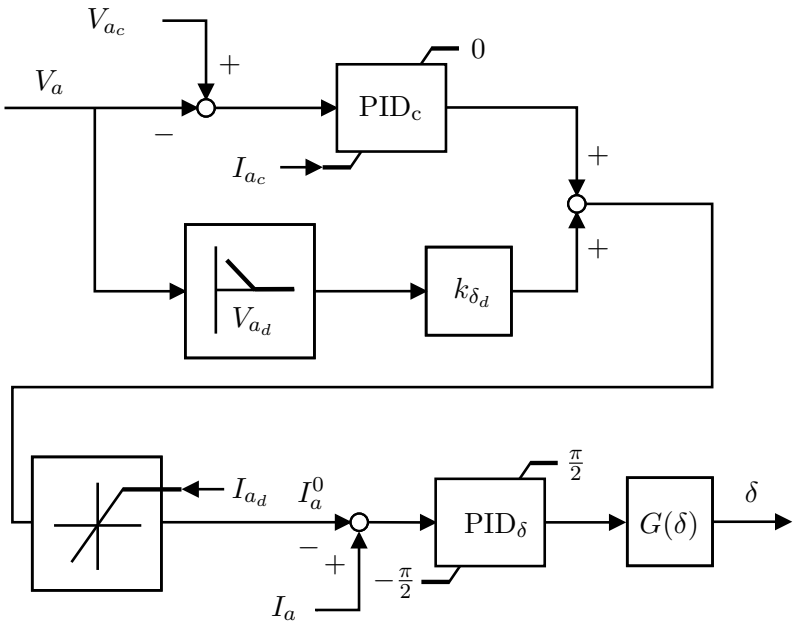

Figure B.15: Block diagram of DAB control: PID in charge, droop in discharge. A faster PID controls shift angle and signal is conditioned by $G(\delta)$ block.

B.7 Appendix conclusions

This appendix described Dual Active Bridge (DAB) converter used to implement ESS system for railway applications.

At the beginning, ESS charge and discharge profiles were analyzed and general approach to evaluate equipment efficiency has been presented.

In the followings, comparison between different power converter let to evaluate main advantages of DAB configuration respect to other ones: as a result, DAB structure was chosen.

Equipment has been presented in detail, focusing on modules arrangement to obtain a modular structure and describing theoretically control strategy based on shift angle between port voltages.

Both converter layout and control logic were successfully implemented and in simulations of Chapter 1, giving positive results in terms of performances.

APPENDIX C

DIRECT CURRENT YESTERDAY

C.1 Origins

Direct Current (DC) was the first, and for many centuries the only, form of electricity known by human beings: evidences of electric effects involving friction of materials (amber) date back to the ancient Greeks.

Anyway, until the end of 17^{th} Century, electricity was considered only a strange, useless curiosity. Things changed in the 1700s with first scientific experiments: rude electrostatic generators, like the Leyden jar, and friction machines, made an empiric knowledge of the electrostatic laws possible.

Other milestones were the experiments on so-called "animal electricity" by Luigi Galvani (1737-1798) and the invention, in 1800, of the first electric generator, the battery; its inventor, Alessandro Volta (1745-1827), demonstrated the electricity was effectively a fundamental property of some materials, and not a "fluid" that is exchanged between objects, like many others supposed before.

Due to batteries, electric power was, for the first time ever, available, storable, and measurable; besides Volta's battery (Fig. C.1), several types of design and chemical combinations were found (e.g. lead-acid cell, still widely use today).

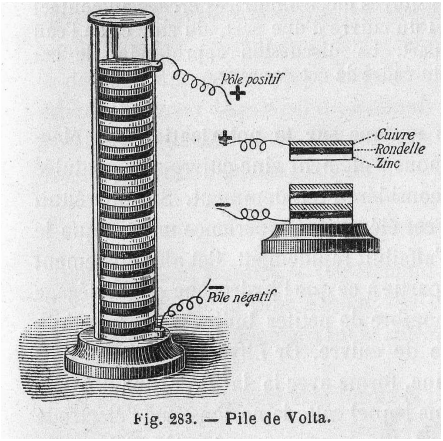

Figure C.1: Volta battery model in old publication (Canada, 1800. Source: museevirtuel.ca).

First electric devices have been electric-arc lamps (Fig. C.2): electricity came out from laboratories to have a concrete, practical utilization. In the first 1800s, utilization of this new energy was limited at telegraph and public lighting; anyway, modest battery

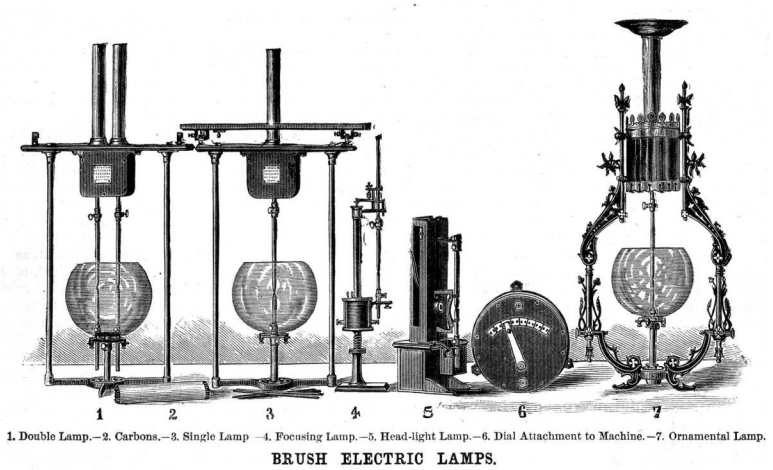

Figure C.2: Carbon arc-lamp models (Ohio, United States of America, 1881. Source: Scientific American).

storage capacity and difficulty in transferring high power through long distances made the "old" gas or oil lamps a better choice.

The greatest difficulty in the diffusion of electricity was the final utilization: apart telegraph, current could provide only light or heat; for horse-power, steam and animal traction were necessary.

The paradigm changed again in the last decades of 19^{th} Century, due to new discovers about electricity and electromagnetism: André-Marie Ampère (1775-1836), Hans Christian Ørsted (1777-1851), Joseph Henry (1797-1878), Michael Faraday (1791-1867), Franz Ernst Neumann (1798-1895), Heinrich Friedrich Emil Lenz (1804-1865), Gustav Robert Georg Kirchhoff (1824-1887), James Clerk Maxwell (1831-1879) and other brilliant scientists, even not at the same time and in the same way, theorized, experimented and expressed fundamental relationships between electricity and magnetism. Pillars of electrical science had been built. The link between electricity and mechanics (and vice-versa) became possible.

Antonio Pacinotti (1841-1912) and Zenobe-Theophile Gramme (1826-1901) found a way to convert mechanical energy into electric energy by a machine (the dynamo, Fig. C.3 and C.4).

Both Pacinotti and Gramme machines produced natively alternating current (AC), thanks to rotation of conducting coils inside a constant magnetic field; because of historical background on DC, AC was considered useless by the practical point of view, so dynamos convert AC into DC by means of a mechanical structure called collector or commutator (Fig. C.5): a rotary electrical switch that periodically reverses the current direction between the rotor and external circuit by means of carbon brushes.

Being composed of multiple metal contact segments and sliding contacts (brushes of soft conductive material like carbon), commutator is effectively the dynamo's weakest part: in general, because of friction losses and electric sparkling, maximum mechanical speed is limited, and also maximum voltage level is limited at some hundred of Volts. Also maintenance costs, due to carbon brushes consumptions, are relevant.

Despite such defects, dynamo had a huge success, also because of reversibility: it can be used like a generator or like a motor.

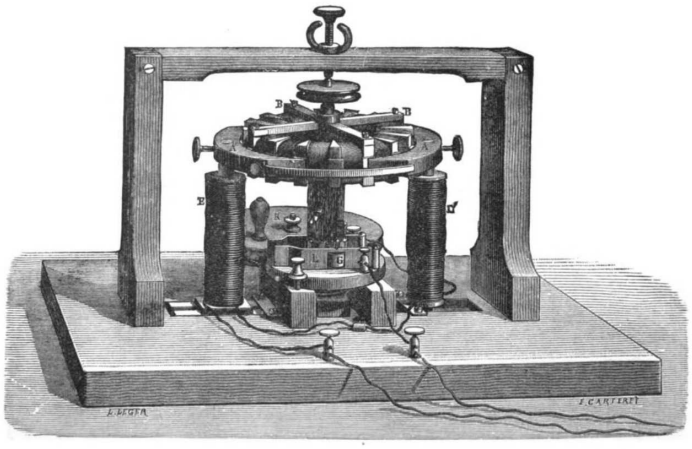

Figure C.3: Drawing of Antonio Pacinotti's dynamo (New York, United States of America, 1884. Source: Heinrich Schellen, "Magneto-electric and Dynamo-electric Machines").

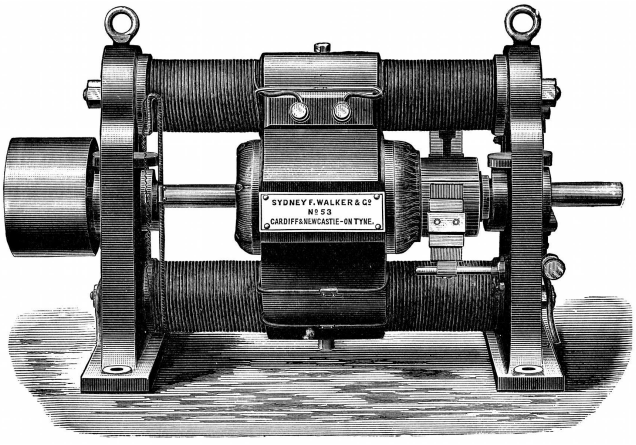

Figure C.4: Drawing of 1884 Gramme's dynamo (London, United Kingdom, 1892. Source: Walker, Sydney F, "Electric Lighting for Ships").

Figure C.5: Commutator and carbon brushes of a DC electrical machine.

In 1870, a dynamo coupled to a water turbine initiated the commercial production of electric energy. At the end of 1800, the most common way to produce, transfer and use electric energy was based on dynamos and DC motors (Fig. C.6).

American inventor and businessman Thomas Alva Edison (1847-1931) invested huge capitals to develop and patent a DC production and distribution system, mainly for competing against gas-based lighting. Having also patented the electric light bulb, the Edison Electric Illuminating Company, founded in 1880, installed and commissioned several DC-based lighting systems during the 1880s.

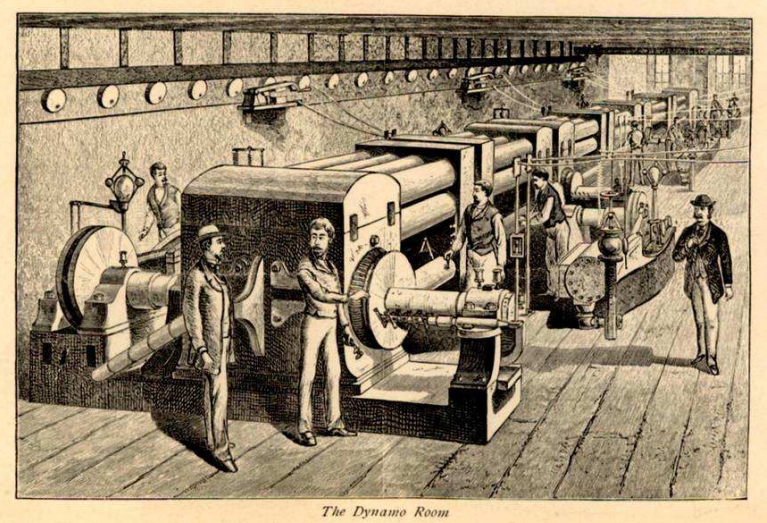

Figure C.6: Dynamo room in Pearl Street Station, first power plant ever, based on Edison DC-system (New York City, United States of America, 1882. Source: Photographic Services of the Consolidated Edison Company of New York).

Edison had good success also out of U.S.A.: since 1883, Milan city center, Piazza del Duomo and some streets abroad (included Teatro alla Scala), were lighted by the first power plant in Continental Europe; such plant was placed in the near Via Santa Radegonda (close to the Dome), and it used steam turbines and Edison dynamos (fig. C.7).

Anyway, Edison system demonstrated several defects since the beginning:

- lack of global efficiency by transmission losses at low voltage levels;
- modest maximum line length because of series voltage drops;
- noisy and smoky steam generators installed very close to people buildings.

Serbian-American scientist, engineer and inventor Nikola Tesla (1856-1943) worked for Edison Company. Looking for DC issues solution, he developed innovative devices for multi-phase alternating current system; between 1885 and 1889, Tesla and Italian scientist Galileo Ferraris (1847-1897) both discovered that a system of alternating currents, if properly injected into coils, can generate a rotating magnetic field able to produce mechanical power (Fig. C.8); DC motors defects, especially voltage limitations and brushes consumption, were completely overcame.

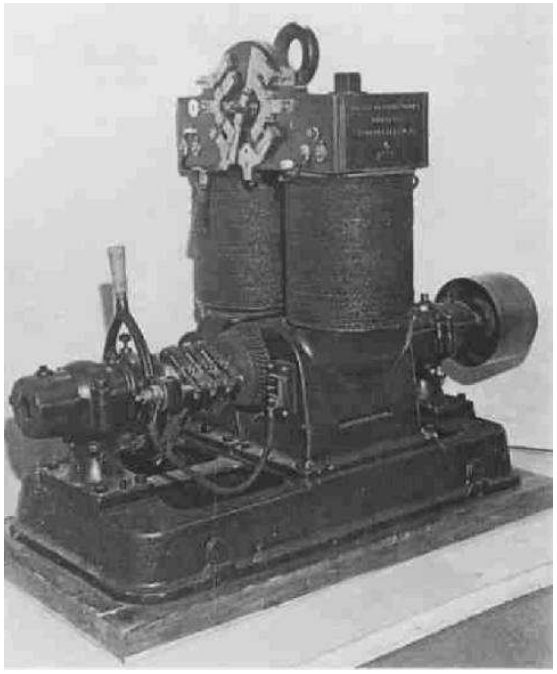

Figure C.7: Edison dynamo installed in via Santa Radegonda power plant. (Milan, Italy, 1883. Source: storiadimilano.it).

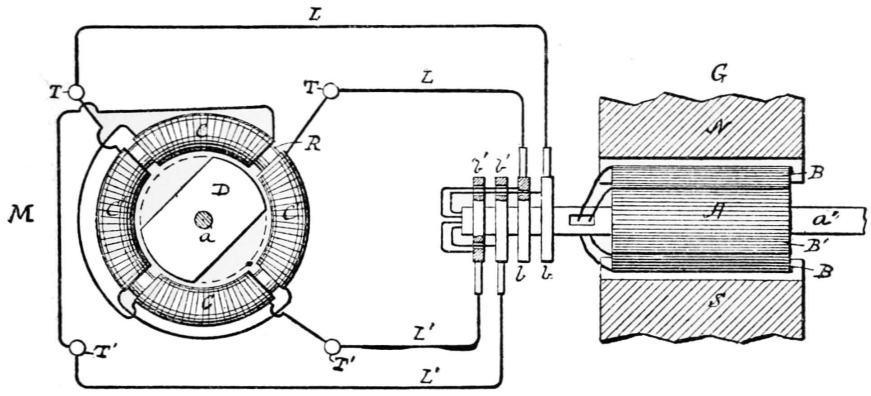

Figure C.8: Tesla first multi-phase AC motor design (United States of America, 1888. Source: U.S. Patent Office Archive).

A feud between Edison and Tesla caused Tesla quitting from Edison company; after several jobs, he was hired by George Westinghouse (1846-1914), American entrepreneur and inventor, who invested in AC to compete against Edison DC system.

Tesla-Edison dualism, AC versus DC, in late 1800s, caused the so-called War of Currents.

C.2 The War of Currents

In 1882, Edison DC power plant in New York City, Pearl Street Station (see fig. C.6), was the benchmark for commercial production and distribution of electricity. Despite the best available technology, only 3.3 square km around the plant have been reached by energy, in Lower Manhattan.

In 1886 George Westinghouse, who had success by inventing and commercializing the first railway pneumatic brakes, bought Nikola Tesla patents on multi-phase alternating current devices, and founded the Westinghouse Electric Corporation. Later on, in 1888, Tesla was hired by Westinghouse, becoming the emblem of AC for Westinghouse Electric.

Edison and Westinghouse companies started competing on the new-born electric market: media of the time described this dispute as a war (the War of Currents), with massive and brutal marketing campaigns. Ignoring the most scandalistic aspects, AC system became popular at World's Fair Colombian Exposition in Chicago, in 1893; illumination was provided by Westinghouse, and a pavilion dedicated to AC was installed.

Later on, in 1896, AC received the definitive consecration with inauguration of Niagara Falls Power Plant (Adam Plant, Fig. C.9) a 75 MW hydroelectric plant that supplied the city of Buffalo, 32 km far away; several smaller AC power plants had been built before in America and Europe, but Adam Plant became the symbol of definitive conclusion of the War of Currents.

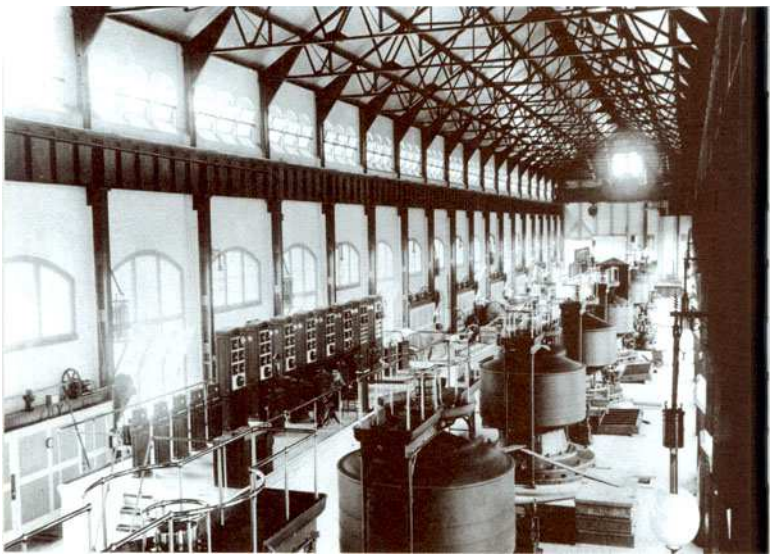

Figure C.9: Niagara Falls Power Plant machine room (United States of America, 1896. Source: teslaresearch.jimdo.com).

In 1892 Edison Electric Illuminating Company had been merged with Westinghouse's chief AC rival, the Thomson-Houston Electric Company, making an even bigger competitor, General Electric; operation was driven by financier and banker John Pierpont Morgan Sr. (1837-1913). After AC "victory", General Electric invested huge capitals in that technology, competing against Westinghouse: commercial, patenting and marketing feud was extremely expensive, both companies almost bankrupted; Westinghouse Electric Corporation had financial troubles in 1890, and several re-capitalizations.

Nikola Tesla left Westinghouse in 1888, to pursuit other scientific interests, mainly about radio waves and wireless transmission of electricity.

AC succeed respect to DC due to Tesla generators and motors, but also by the diffusion of a static electric machine that had been developing in Europe since the beginning of electrification early years: the transformer.

C.3 AC breakthrough: the transformer

In 1931 Michael Farady invented the so-called induction ring, the first rude transformer. He used it for experiments about electro-magnetic induction, without specific practical use.

First transformer to be widely used was the induction coil (Fig, C.10), invented by Clergymen Nicholas Callan (1799-1864), of Manyooth College, Ireland, in 1836.

Figure C.10: Clergymen Callan's Induction Coil at the National Science Museum. (Maynooth, Ireland, 1845. Source: Wikimedia Commons).

Induction coils were developed by trial also from Russian scientists between 1830 and 1870, in order to increase battery voltages: special vibrating contacts interrupted periodically DC currents to produce the needed variable maghetic flux; basic principles of not-continuous current conversion were discovered. In 1878, Ganz Company in Hungary started manufacturing electric lighting equipment based on induction coils; more than 50 systems were successfully commissioned in Austro-Hungarian Empire.

Lucien Gaulard (1850-1888) and John Dixon Gibbs (1834-1912) first proposed a "secondary generator" device with an iron-based magnetic choke and an open-core, in London, in 1882;

In 1884, Károly Zipernowsky (1853-1942), Ottó Bláthy (1860-1939) and Miksa Déri (1854-1938), three engineers associated with the Ganz factory (known as ZBD team, by their surnnames initials), determined that open-core devices were impractical, as they were incapable of reliably regulating voltage. Their 1885 patent for novel transformers described designs with closed magnetic circuits (later called ZBD transformers). ZBD transformers were 3.4 times more efficient than the open-core devices of Gaulard and Gibbs. The Ganz factory in 1884 shipped the world's first high-efficiency AC transformers.

When employed in parallel connected electric distribution systems, closed-core transformers finally made it technically and economically feasible to provide electric power for lighting in homes, business and public spaces. The AC power systems were developed and adopted rapidly in Europe after 1886 due to their ability to distribute electricity efficiently over long distances, overcoming the limitations of the direct current system. In 1886, the ZBD engineers designed the world's first power station that used AC generators to power a parallel-connected common electrical network, the steam-powered Rome-Cerchi power plant. Rome was the first large European metropolis to be AC electrified, in 1886.

George Westinghouse bought Goulard and Gibbs patents in 1885; development of an industrial product was given to engineer William Stanley (1858-1916).

First Stanley patent was a set of induction coils with soft-iron cores and adjustable air-gaps in order to regulate electro-motive force on the secondary windings. Stanley also soon understood open-core was a disadvantage in terms of efficiency, and finally, in 1886, he proposed an industrial design with a continuous magnetic core.

Figure C.11: William Stanley first industrial transformer model (United States of America, 1886. Source: edisontechcenter.org).

Finally, in 1893, Westinghouse Company started erection of Niagara Falls Power Plant; powerful step-up transformers made AC power transmission through long distances technically possible and economically convenient (Fig. C.12).

AIR-BLAST TRANSFORMERS AT NIAGARA FOR THE EARLY TRANSMISSION TO BUFFALO

Figure C.12: Niagara Falls Power Plant step-up transformers (United States of America, 1896. Source: teslaresearch.jimdo.com).

C.4 The end of DC?

At the beginning of 20th Century, AC was the benchmark for electric transmission and distribution systems. Nevertheless, DC did not disappear; in fact, it became essential inside power plants, providing AC alternators the so-called excitation.

Basic principles of AC generator, known also as alternator (Fig. C.13), were proposed since Michael Faraday experiments; in 1832 an instrument maker from Paris, Hippolyte Pixii (1808-1835) built an early form of alternating current electrical generator, based on Faraday's principle of magnetic induction (later on, such device will be converter in dynamo by using a commutator, see Par. C.1).

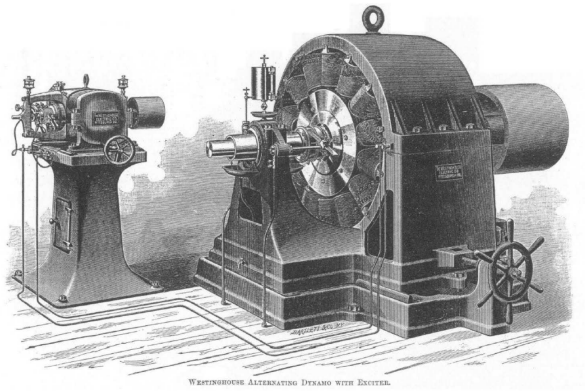

WESTINGHOUSE ALTERNATING DYNAMO WITH EXCITER.

Figure C.13: Alternator coupled to Dynamo-exciter; belt between generator and dynamo shafts is missing (United States of America, first 1900s. Source: Wikimedia Commons).

First alternators used permanent magnets to generate rotor magnetic field; as AC power plants were built, such solution became impracticable: natural magnets are relatively rare, and no field regulation is possible. Iron alternator rotors were then equipped with copper windings (so-called excitation or filed windings), in which a DC flow could produce a controllable magnetic field. Because of rotation, DC source was connected to rotor by means of slip-rings and carbon brushes; power source was given by batteries, series rheostats could modulate the current flow (so magnetic field). Anyway, this solution was not suitable for powerful generators, since batteries had to be replaced or recharged.

Dynamos appeared a good way to overcome the problem: alternator rotor was supplied by a dynamo (so-called dynamo-exciter), both machines were connected at the same mechanic shaft (directly or indirectly through a belt). Dynamo-exciter field was given by permanent magnets (for small machines only) or through another excitation circuit supplied by a smaller permanent magnets DC generator (also know as pilot-exciter), still linked to main shaft. Alternator field control resulted in modulating pilot-exciter current by means of rheostats (Fig. C.14). Through years, many different types of excitation configurations were successfully implemented.

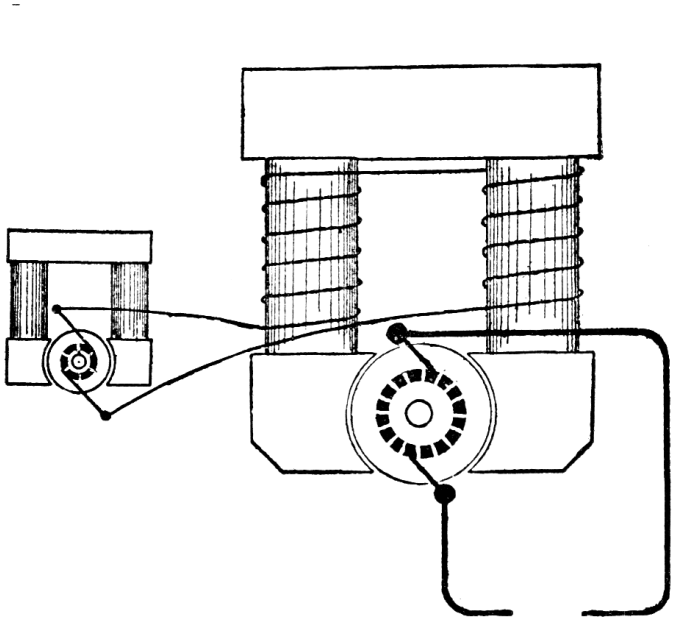

Figure C.14: Schematic diagram of permanent magnets Pilot-exciter feeding a Dynamo-exciter (United Kingdom, late 1800s. Source: Wikimedia Commons).

Another field of application for DC was machinery: some industries had already invested capitals in DC motors, when system changed to AC, a solution was using rectification units composed by multi-phase AC motors mechanically coupled to dynamos; efficiency was lower, but DC motor could be easily controlled in speed.

Previous examples shows how DC, being overcame by AC for transmission and generation networks, was "re-invented" for other purposes; research and implementations preceded in all kind of applications in which AC was not convenient or inadequate.

Anyway, nevertheless extremely important, both excitation systems and industrial machinery were really sectoral and minor applications; at beginning of 20^{th} Century, DC was still confined inside power plants or industries.

Grid-supplied AC motors work at almost constant speed, and low-speed torque is generally poor; extra gears, connecting rods and cams become necessary to obtain the needed performances.

A series-excited DC motor has instead a very useful mechanical characteristic: high torque at low speed (even zero) and self-regulation of magnetic field at high speed; engineers soon realized DC motors were ideal for traction (Fig. C.15).

Figure C.15: Exhibition railway with the first electric locomotive (Germany, 1879. Source: Siemens Archives).

The main application that saved DC from extinction after the War of Currents is railway.

C.5 DC railways

In a few countries all over the world, steam locomotives are still operational; apart environmental considerations about the massive generation of carbon dioxide and other toxic combustion sub-products, at the end of the 19^{th} Century, the main reason most of European and American rail companies switched on electric traction was practical:

- increase travel comfort (fumes and smoke intoxicated passengers, especially under tunnels);
- reduce operating costs (coal and water transportation/stock).

Figure C.16: Sulfurous fumes and smoke on Victorian Tube; at that time, all locomotives were steam (London, late 1800s. Souce: bbc.com).

The new-born electric power appeared immediately a valid alternative to steam. At first, DC systems were successfully commissioned and operated, but, as said in Par. C.1, efficiency was an issue; nevertheless, DC traction was extensively implemented in Europe and America for urban transportation (cable-bus, tramway); the modest power consumptions let the utilization of lower voltage levels (as example, 500-600 V DC), generated by rotating machines (dynamos, see Par. C.1). Multi-phase AC had already become a standard for high power transmission and distribution, so the system was applied to heavy railway.

The result was a proliferation of many kinds of technical solutions, different frequencies and voltage levels; lack of standardization agreements was not only between different Nations, but even among rail companies operating in the same region. In general, using AC three-phase, energy transmission was given by complex uptake systems (Fig. C.16 and C.17), with three or two pantographs (third phase could be a supplementary rail, or the rail itself, very dangerous for people safety!).

Infrastructure was expensive and special precautions (protection screens, insulators etc.) were necessary at interceptions.

On board, traction system implementation was quite intricate too; special asynchronous motors, to be slower compared to industrial machineries, were combined and connected in different ways through rheostats and slip-rings, in order to obtain a sufficient set of torque-speed characteristics.

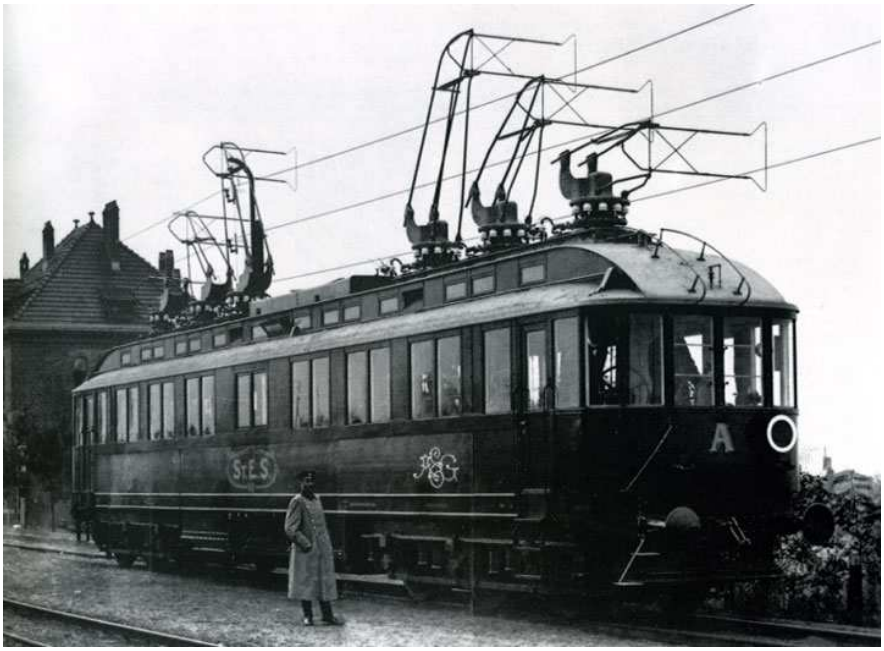

Figure C.17: Three-phase, three-wires locomotive by AEG (Germany, beginning of 1900s). Source: ilmondodeitreni.it.

Nevertheless, the three-phase medium voltage systems (usually 3.6 kV) became a benchmark in Northern Italy up to Twenties of 20^{th} Century (Fig. C.18), being the only possible way to feed heavy trains on high-slope tracks (like Simplon Pass).

Other attempts in AC traction were successful in Central-Northern Europe: single-phase, low frequency (15-16$\frac{2}{3}$-20 Hz) and high voltage (up to 25 kV) systems had been used in Germany, Switzerland and Austria since the 1920s; such systems needed any-

Figure C.18: Three-phase catenary at Vievola (France, 1970, the very last period of three-phase railway. Source: stagniweb.it).

way heavy step-down transformers on locomotives and used single-phase AC collectors motors, with the same maintenance defects of DC.

In all AC solutions, supply frequency was necessarily slower than industrial 50 Hz, both for better induction motors speed control, both for reducing series-inductive voltage drops, and for growing electromagnetic compatibility issues with telegraph lines, usually close to railroads; special generators inside power plants, or rotating conversion groups at substations, became therefore necessary; the traction grid was completely detached by the common AC grid.

The Mercury-arc valve (Fig. C.19), invented by Peter Cooper Hewitt in 1902 and improved during the Twenties and Thirties of 20^{th} Century, changed the paradigm: for the first time in history, a static high-power AC/DC rectifier was available; early rectification substations were bulky and lossy (and mercury is very toxic also, despite at that time such aspect was basically irrelevant!), but their introduction made the construction of powerful single-phase DC lines possible; AC supply could be directly the common 50 Hz industrial grids, and only one catenary cable was necessary. Those features reduced drastically infrastructure costs: DC railway era had finally started.

Figure C.19: Early Mercury-arc valve.

DC voltage of 3000 V (3 kV DC) became soon a general standard, at least in South-Western Europe: it was a good compromise between needed power density, acceptable series losses and train commutators decay.

DC motors, especially in so-called series excitation configuration, have a mechani-

cal characteristic much more suitable than asynchronous for traction; they got also a remarkable improvements of locomotives performances, despite issues on maintenance; anyway, the technical-economic trade-off hung sharply for DC. Ironically, when the rest of civilized world moved definitively to AC, most railways moved to DC.

In late 1940s and then in 1950s, further step-forward was achieved by silicon industry; the diode rectifier is the natural successor of the Mercury-arc valve, but only in the first 1960s those components reached enough power and voltage level to be seriously comparable with previous ones; since then, and up today, most of AD/DC rectifiers in rail substations are based on the same concept (Fig. C.20).

Figure C.20: Solid-state substation diode rectifier, commissioned in 1960s, now dismissed (Novate Milanese, Italy. Source: delta-november.it).

On board side, power electronics industry has created a variety of controlled and semi-controlled valves, which are the base for modern traction drives; now-days, synchronous or asynchronous motors are widely used in locomotives, being efficiently controlled by DC/AC power electronics inverters. DC catenary is feed by 50 Hz AC transmission and distribution lines, AC/DC conversion is operated into substations displaced on the railway track at several intervals.

Chapter 1 will introduce state of the art of modern 3 kV DC systems, mainly focusing on Italian specifications about substations and diode rectifiers.

About transmission lines, instead, 3 kV was definitely insufficient to guarantee an acceptable level of efficiency through long distances (eg. more than 50 km); the only

way to proceed in that direction was increasing any further the voltage, introducing the so-called High Voltage Direct Current systems (HVDC, Fig. C.21).

Figure C.21: HVDC long lines crossing in North Dakota, U.S.A. (United States of America, 2010. Source: Wikimedia Commons).

C.6 HVDC systems

As already mentioned in Par. C.5, AC was the best way to transfer and distribute electric power from plants to cities and industrial centers (Fig. C.22); such technology started showing defects as soon as lines distances increased: capacitive and inductive parasitic effects produce relevant voltage drops and energy losses. Step-up substations become necessary, and the only way to reduce power losses was increasing further the voltage level (220 kV AC systems were established in the 1920s).

Figure C.22: Adam AC power plant at Niagara Falls (United States of America, 1895. Source: Wikimedia Commons).

A High Voltage Direct Current (HVDC) system could theoretically resolve such issues, at least for longest lines: the effects of capacitance and inductance become irrelevant, and the high voltage level can properly contain the power losses.

Anyway, in principle the main problem of DC power generation was exactly the voltage level; the impossibility of obtaining high voltages with rotating machines, and further difficulties in power conversion, decreed AC success that lasts up today; several attempts took place using low-speed DC machines put in series (low speed was essential for preserve commutators), so only slow hydro turbines could provide the necessary power.

So-called Thury systems (Fig. C.23), by the name of its inventor, Swiss electrical pioneer René Thury (1860-1938), were installed in Italy, Switzerland, United Kingdom and France at the beginning of 20^{th} Century; the most powerful was the 20 MW Moutiers-Lyon system, at 150 kV, that remained in service from 1906 to 1937. Anyway, the Thury system needed frequent and expensive maintenance, and proved to be inadequate for higher power ratings.

Once again, the Mercury-arc valve changed the paradigm, but at the beginning of 20^{th} Century, soon after the invention, technology was not ready for the scope. Since 1929 Uno Lamm, a Swedish electrical engineer working for ASEA (ABB after 1988), leaded a team for developing a High Voltage Mercury-arc valve. In 1939, Lamm's

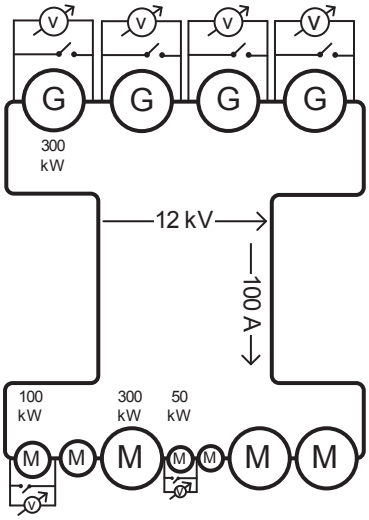

Figure C.23: Principle diagram of a Thury system.

team had perfected a system of grading electrodes into a single-phase Mercury-arc valve construction, which could withstand large inverse voltages. The valve was able to operate as a rectifier.

In the 1930s, then during the Second World War, several experimental HVDC systems were tested in Europe and America. A 60 MW at ±200 kV HVDC link was commissioned in Germany (April 1945), between the Vockerode generating station on the river Elbe to Berlin over a distance of 115 km; system never became operational due to Germany surrender, it was de-assembled and re-assembled in Soviet Union to build an experimental line between Moskow and Kasira in 1950.

After twenty years of research and experiments, the first commercial HVDC link between the island of Gotland and the Swedish mainland was finally commissioned by ASEA in 1954 (Fig. C.24). Thanks lo Lamm's research, it could transfer 20 MW at 100 kV over a 98 km submarine cable.

HVDC development continued in parallel in Western and Eastern Blocks during the Cold War: in America and Soviet Union, due to wide distances between power plants and big cities, major efforts were concentrated on land transmission lines.

In Europe, instead, where distances are more modest, HVDC installations have been used essentially for sea crossings: AC systems encounter operational difficulties with long cable lines, due to heavy currents required to charge and discharge capacitances each cycle; in such conditions, HVDC is the only practical solution, and extra costs by conversion substations (erection and operation) are widely justified.

In December 1966, Sardinia Island (Italy) was connected to Continental Italy through Corsica Island (France) by means of a 413 km long HVDC cable (with 121 km of submarine cable). Connection was called SACOI (SArdinia-COrsica-Italy, Fig. C.25). Initially, two Mercury-arc-based AC/DC substations were placed at line sides, in Codrogianos (Sardinia) and San Dalmazio (Tuscany); later on, in 1987, a third substation has been erected in Lucciana, close to Bastia (Corsica); due to this, SACOI became the first ever multi-terminal HVDC link in the World (and one of the very few existing up today). HVDC technology development was very fast: at every new installation, both

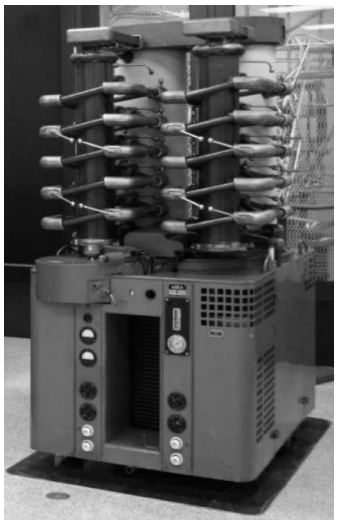

Figure C.24: ASEA-design Mercury-arc rectifer installed in Gotland conversion stations (Sweden, 1954. Source: ABB).

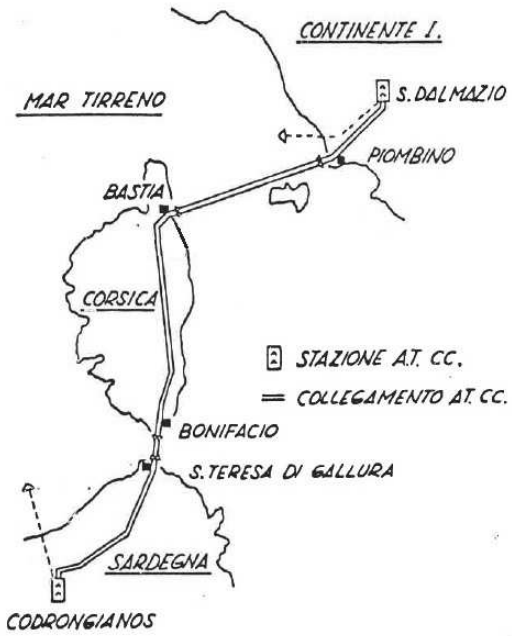

Figure C.25: Original handmade map of SACOI, after introduction of Lucciana substation (Italy, 1987. Source: Terna).

power and voltage levels increased constantly. The Pacific Intertie Project (U.S.A., 1970, Fig. C.26) and the Volgograd-Donbass HVDC System (Soviet Union, 1965) are remarkable examples of such progress.

SACOI third AC/DC substation did not use anymore Mercury-arc valve but a

Figure C.26: ASEA-design Mercury-arc rectifer installed in Pacific Intertie project (United States of America, 1970. Source: ABB).

silicon-based solid state technology, developed and commercialized since the early 1970s: the thyristor.

In 1970, Gotland substations were re-engineered to transmission capacity of 30 MW at 150 kV by using the first thyristor module for HVDC applications. Also Soviet Union and U.S.A. soon adopted thyristor technology for HVDC converters (Fig. C.27).

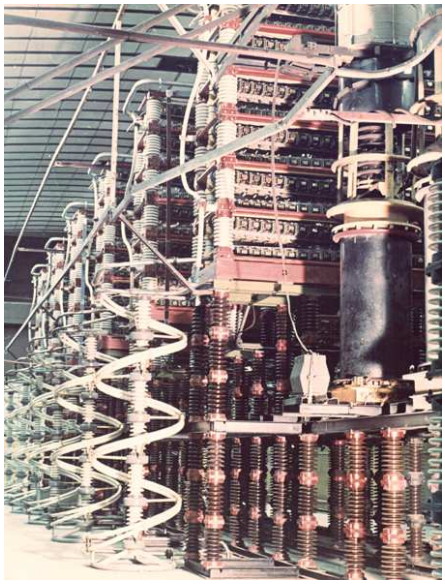

Figure C.27: High-voltage thyristor converter valve group at the Volzhskaya converter station (Soviet Union, 1974. Source: tdworld.com).

Thyristor technology makes impossible component controlled turning-off; due to

this, thyristor-based power electronic converters cannot be used as VSC (Voltage Source Converters) but "only" as CSC (Current Source Converters).

The most common design for a CSC is called LCC (Line Commutated Converter); it needs a "pilot voltage source" to drive valves turning-off and does not allow current-flow inversion; active power flow is well managed by controlling the rectified DC-side voltage, while reactive power cannot be controlled; in general, LCC currents are in lag respect to pilot voltage, so, according to loads measurement convention, it is said the converter absorbs positive reactive power. Moreover, due to low frequency (industrial frequency) commutations, AC has a strong low-harmonic content, that must be filtered.

Anyway, due to undisputed reliability and robustness, thyristor became the benchmark for high power and high voltage energy applications all over the World; new HVDC projects adopted thyristors as switching devices, and most of existing substations were progressively refurbished with thyristor-based power electronic converters.

Since 1980, fully turn-on-off silicon-based device became available: the IGBT (Insulated Gate Bipolar Transistor) structure overcomes thyristor limitations, but, at the beginning, power rates and reliability were insufficient.

Progresses in silicon technology made IGBT more and more attractive for high power ratings, and finally, in 1999, the first commercial IGBT-based HVDC system was commissioned (in Gotland Island, Sweden).

IGBT technolgy for HVDC was (commercially) called HVDC-Light, because maximum power ratings were anyway lower than thyristors; sometimes, it is also called HVDC-Plus, pointing the extended control capability respect to thyristors. Dually, "old" thyristor systems are instead called HVDC-Large or HVDC-Classic.

IGBT converters (Fig. C.28) can be VSC type: they can operate in island mode, with no "pilot voltage" needed. Morevoer, they can manage both active and reactive power flows between AC and DC side, and they let reverse current flow. By using PWM (Pulse Width Modulation) switching technology, harmonics can be shifted at higher frequencies, even if commutation losses are usually higher.

Figure C.28: IGBT-based modules for HVDC converter.

Today, IGBT-based technology is the most advanced and rising solution for HVDC development all over the World.

Chapter 2 will introduce state of the art of modern VSC HVDC systems, mainly focusing on substations setup and power conversion.

C.7 Appendix conclusions

This appendix was a brief historical analysis about DC current system development, from first rude experiments to the "competition" against AC.

Due to undiscussed advantages and benefits, AC made possible the creation of power networks as we know today.

DC was "confined" in some specific fields of application; two of them, maybe the most remarkable in terms of interest and diffusion, have been presented: railway traction and power transmission over long distances or sea crossings. They have been briefly described focusing on some milestones, including diagrams and photos to provide a little overview of technological and technical progress through years.

Since the beginning of electrification, such applications "saved DC from extinction" and later on, due to huge progress in power electronics and science of materials, DC received a new an powerful impulse in the last century.

Now days, DC has been re-discovered and re-invented for many kind of different applications and purposes; control algorithms and power converters give the possibility to perform brand new functionalities and services on the existing, well-tested and mature power DC grids.

NOMENCLATURE

Chapter 1

	Description	Unit
A	Coefficient for train specific friction losses	-
A_s	TSS transformer rated power	VA
AC	Alternating Current	-
a_t	Train acceleration	m/s^2
B	Coefficient for train specific aerodynamic losses	s^2/m^2
CAGR	Compound Annual Growth Rate	-
CC	CortoCircuitatore (Earthing Switch)	-
CO_2	Carbon Dioxide	-
C_a	ESS filter capacitance	F
C_s	Substation filter capacitance	F
C_t	Train filter capacitance	F
C_W	Non-domestic utilities energy cost	€/kWh
c€	Euro-cent	-
DAB	Dual Active Bridge converter	-
D_b	Braking diode, train model	-
D_c	Charge diode, ESS model	-
D_d	Discharge diode, ESS model	-
D_s	Diode, substation rectifier model	-
DC	Direct Current	-
$\Delta\eta\%$	Percentage efficiency gap	%
d_a	ESS receptivity distance	m
d_t	GPS train position	m
E	Generic DC voltage generator	V
EEA	European Environmental Agency	-
ESS	Energy Storage System	-
η	System global energy efficiency	-
η_{a_c}	ESS average efficiency in charge	-
η_{a_d}	ESS average efficiency in discharge	-
η_t	Train global electrical and mechanical efficiency	-
δ	Droop global action	A
δ_c	Droop action, negative current charge	A
δ_d	Droop action, positive current discharge	A
ε_c	Regulator error signal, negative current charge	V
ε_d	Regulator error signal, positive current discharge	V
FC	Flying Capacitance	-
F_t	Train traction force	N
$\mathbf{G}$	Conductance matrix	Ω^{-1}
G	Conductance	Ω^{-1}

continued on next page

continued from previous page

	Description	Unit
GPS	Global Positioning System	-
$g_{n,n}$	Generic element of **G** matrix	Ω^{-1}
g	Gravity acceleration	m/s^2
γ	Mixed control global action	A
HV	High Voltage	-
h_t	Train altitude	m
h_{t_1}	Initial train altitude	m
h_{t_2}	Final train altitude	m
I	Current vector	A
IB	Investment balance	€
IC	Investment costs	€
IG	Investment gainings	€
IR	Interruttore (extra)Rapido (Fast DC Switch)	-
I_{A_1}	Port A_1 rectified current	A
I_a	ESS current	A
i_{a_1}	Port A_1 module 1 alternating current	A
I_{a_c}	ESS charge current threshold	A
I_{a_d}	ESS discharge current threshold	A
$I_{a_{pc}}$	ESS post-charge current	A
I_{amax}	ESS maximum current	A
I_{B_1}	Port B_1 rectified current	A
I_b	Train braking current	A
i_{b_1}	Port A_1 module 1 alternating current	A
i_{b_2}	Port B_2 alternating current	A
I_n	Nominal current	A
I_s	Substation model current	A
I_t	Train current	A
i_n	-$\sum$ of currents converging at node n	A
JRC	Joint Research Committee	-
K	Total number of trains per year	-
k_{δ_c}	Droop coefficient, negative current charge	-
k_{δ_d}	Droop coefficient, positive current discharge	-
k_i	PID controller integral gain	-
k_m	Train equivalent rotating mass coefficient	-
k_p	PID controller proportional gain	-
L-C	Rectification group DC filter	-
LT	Expected equipment lifetime	years
L_{A_1}	Port A_1 module 1 series inductance	H
M	Total network nodes	-
MV	Medium Voltage	-
Mil€	Million of Euro	-
m_t	Train mass	kg
μC	Micro-controller	-
N	Total network nodes	-
NPC	Neutral Point Clamped	-
n	Number of TSS rectification groups	-
n_1	Module 1 transformer ratio	-
P_a	Average ESS power	W
P_b	Average train rheostatic braking power	W
P_n	Nominal power	W
P_t	Average train traction power	W
P_{t_k}	Average train power by kinetic energy	W

continued on next page

continued from previous page

	Description	Unit
P_{t_p}	Average train power by potential energy	W
PET	Power Electronics Transformer	-
PI	Proportional Integral control	-
PID	Proportional Integral Derivative control	-
PID_c	PID control for ESS charge	-
PID_d	PID control for ESS discharge	-
p_a	ESS instantaneous power at catenary terminals	W
$p_{a_{pc}}$	ESS instantaneous post-charge power at catenary terminals	W
p_{amax}	ESS instantaneous maximum power	W
$\lvert\hat{p_a}\rvert$	ESS power, absolute peak value	W
$\lvert\hat{p_b}\rvert$	Train rheostatic braking power, absolute peak value	W
$\lvert\hat{p_t}\rvert$	Train power, absolute peak value	W
p_{aux}	Auxiliaries train power	W
p_b	Train instantaneous rheostatic braking power	W
p_{j_c}	Catenary instantaneous power losses	W
p_{ja_c}	ESS instantaneous power losses in charge	W
p_{ja_d}	ESS instantaneous power losses in discharge	W
p_s	Substation instantaneous power	W
p_t	Train instantaneous traction power	W
R	Generic resistor	Ω
RFI	Rete Ferroviaria Italiana (Italian Railway Network)	-
RZ	Raddrizzatore a diodi (Diode Rectification Group)	-
R_a	ESS filter resistance	Ω
R_c	Catenary resistance	Ω
R_s	Equivalent substation rectifier resistance	Ω
R_{sc}	Substation filter resistance	Ω
R_t	Train filter resistance	Ω
r_c	Per-length catenary resistance	Ω/km
S	Sezionatore (Disconnector)	-
S_t	Average track slope	‰
SC	Scaricatore (Surge Arrester)	-
kWh	Contatore energia (power meter)	-
SOC	State Of Charge	-
s_{t_k}	Braking space, power intensive recovery	m
s_{t_p}	Braking space, energy intensive recovery	m
TA	Trasformatore Amperometrico (Current Transformer)	-
TV	Trasformatore Voltmetrico (Potential Transformer)	-
TG	Trasformatore di Gruppo (Rectifier Transformer)	-
TSR	Treno Servizio Regionale (Regional Service Train)	-
TSS	Traction substation	-
TSA	Trasformatore Servizi Ausiliari (Auxiliary Power Transformer)	-
T_a	ESS working time	s
T_b	Braking time, potential and kinetic energy	s
T_k	Braking time, power intensive recovery	s
T_p	Braking time, energy intensive recovery	s
T_s	Total simulation time	s
t_0	Simulation start time	s
t_c	Charge time	s
t_d	Discharge time	s
t_{pc}	Post-charge time	s
θ	PID control global action	A
θ_c	PID control action, negative current charge	A

continued on next page

continued from previous page

	Description	Unit
θ_d	PID control action, positive current discharge	A
τ_1	DAB voltages shift (Module 1)	s
τ_c	ESS current limiter filtering time constant	s
τ_δ	Droop action delay time constant	s
τ_θ	PID control delay time constant	s
V	Nodal voltage vector	V
VSC	Voltage Source Converter	-
V_a	Catenary voltage at ESS terminals	V
V_{amin}	Average minimum catenary voltage	V
V_{ac}	TSS rectifier phase-to-phase AC input voltage	V
V_{a_c}	Catenary voltage threshold for ESS charge	V
V_{a_d}	Catenary voltage threshold for ESS discharge	V
V_b	Train voltage braking threshold	V
V_s	Ideal voltage generator, TSS model	V
V_t	Train voltage (at pantograph)	V
V_{tmin}	Absolute minimum train voltage	V
V_{t_p}	Average train speed, energy intensive case	m/s
v_{a_1}	Port A_1 module 1 alternating voltage	V
v_{b_1}	Port B_1 module 1 alternating voltage	V
v_n	Nodal voltage between node n and the reference node	V
v_t	Train speed	m/s
v_{t_1}	Initial train speed	m/s
v_{t_2}	Final train speed	m/s
W_{a_1}	ESS maximum cycle limit	J
W_{a_2}	ESS minimum cycle limit	J
W_{a_c}	ESS gross charged energy	J
W_{a_d}	ESS net discharged energy	J
$W_{a_{max}}$	ESS maximum energy limit	J
$W_{a_{min}}$	ESS minimum energy limit	J
$W_{a_{pc}}$	ESS gross post-charge energy	J
W_b	Train rheostatic braking energy	J
$W_{j_{a_c}}$	ESS energy losses in charge	J
$W_{j_{a_d}}$	ESS energy losses in discharge	J
$W_{j_{a_{pc}}}$	ESS post-charge losses	J
W_{j_c}	Catenary energy losses	J
W_s	Substation produced energy	J
$W_{s_{pc}}$	Substation post-charge energy	J
W_t	Train energy	J
W_{t_k}	Train kinetic energy	J
W_{t_p}	Train potential energy	J
Y	Investment span	years
YG	Yearly Gainings	€/year
y	Generic investment year	years

Chapter 2

- Quantities related to different grid/equipment have proper numerical subscript (eg. AC grid 1 frequency is f_{g1});
- Rated quantities are marked with subscript n (eg. AC grid 3 rated apparent power is A_{g3n}).
- Initial state (simulation time t =0) quantities have suffix *(0)* (eg. intial AC grid 2 frequency is $f_{g2}(0)$);
- Maximum value of a limited quantity has subscript MAX (eg. AC grid 2 maximum frequency is f_{g2MAX});
- When used, per unit quantities have same name as physical ones plus subscript pu (eg. AC grid 2 active power in p.u. is P_{g2pu});
- Setpoint quantities have superscript *0* (eg. station 1 AC power setpoint in p.u. is P^0_{ac1pu});
- Laplace-transformed quantities are written in capital and have suffix *(s)* (eg. AC grid 1 frequency in p.u. is $F_{g1pu}(s)$).

	Description	Unit
A_g	AC grid apparent power	VA
AC	Alternating Current	-
c_0	Integration constant	-
C_G	Generator torque	Nm
C_L	Load torque	Nm
C_{dc}	DC equivalent capacitor	V
C_{dc12}	DC link capacitance	F
C_p	HVDC station positive pole capacitance	F
C_n	HVDC station negative pole capacitance	F
DC	Direct Current	-
Δf_G	Generator frequency variation	Hz
Δf_g	AC grid frequency variation	Hz
ΔP	AC grid load (unload) step	W
ΔP_{pr}	AC grid primary frequency power	W
Δt	Time span	s
ENTSO-e	European Network of Transmission System Operators for Electricity	-
η_{dc12}	DC link efficiency	-
f_G	Generator frequency	Hz
f_g	AC grid frequency	Hz
$f_g^{(0)}$	AC grid initial frequency	Hz
$f_g^{(1)}$	AC grid final frequency	Hz
$G(s)$	Grid frequency model (Laplace domain)	-
H_G	Generator inertial coefficient	s
H_g	Grid equivalent inertial coefficient	s
HVDC	High Voltage Direct Current	-
IGBT	Insulated Gate Bipolar Transistor	-
INEC	INertia Emulation Control	-
J_G	Generator inertia momentum	kg/m^2

continued on next page

continued from previous page

	Description	Unit
J_g	AC grid equivalent inertia momentum	kg/m^2
k_{Id}	IEC-derivative coefficient	s
K_f	INEC-derivative frequency coefficient	s^2
k_{sipu}	AC grid synthetic inertia coefficient (p.u.)	s
K_V	INEC-derivative voltage coefficient	1/s
LCC	Line Commutated Converter	-
MFD	Maximum Frequency Deviation	Hz
NPC	Neutral Point Clamped	-
P_{ac}	HVDC station AC side active power	W
P_E	Generator efficient power	W
P_e	AC grid equivalent efficient power	W
$P_e^{(0)}$	AC grid equivalent efficient power starting point	W
$P_e^{(1)}$	AC grid equivalent efficient power final point	W
P_G	Generator active electrical power	W
P_g	AC grid active electrical power	W
P_L	Load electrical power	W
P_{Loss}	Generator mechanical and electrical losses	W
P_l	AC grid equivalent load power	W
P_M	Motor mechanical power	W
PI	Proportional Integral (controller)	-
PPE	Programmations pluriannuelles de l'energie	-
$P(s)$	AC grid complete regulator model (Laplace domain)	-
P_{dr}	Droop action power	W
P_{jdc12}	DC link power losses	W
P_{jdc}	DC grid power losses	W
P_L	Load active power	W
P_l	AC grid equivalent load power	W
P_{pr}	AC grid primary regulation active power	W
P_{si}	AC grid synthetic inertia active power	W
p.u.	Per unit	-
k_{d_c}	Droop coefficient, power charge	-
k_{d_d}	Droop coefficient, power discharge	-
RES	Renewable Energy Sources	-
ROCOF	Rate Of Change Of Frequency	Hz/s
R_g	AC grid resistance	Ω
R_I	IEC regulator model	-
R_{Id}	IEC-derivative regulator model	-
R_{n12}	DC link resistance (negative pole)	Ω
R_{p12}	DC link resistance (positive pole)	Ω
$R_{pr}(s)$	Primary frequency regulator model (Laplace domain)	-
$R_{si}(s)$	Synthetic inertia regulator model (Laplace domain)	-
SACOI	Sardegna Corsica Italia (Sardinia Corsica Italy)	-
σ_G	Generator primary frequency permanent droop	-
σ_g	AC grid equivalent primary frequency permanent droop	-
TSO	Transmission System Operator	-
τ	Washout filter (high-pass) time constant	s
τ_d	Droop action filtering time constant	s
T_1	AC grid primary frequency lead time constant	s
T_2	AC grid primary frequency lag time constant	s
T_{avvG}	Generator starting time	s
T_{avvg}	AC grid equivalent starting time	s
T_l	Loading (unloading) time	s

continued on next page

continued from previous page

	Description	Unit
V_{ac}	AC grid voltage	V
V_{dcpu_c}	Droop DC grid charge threshold in pu	-
V_{dcpu_d}	Droop DC grid discharge threshold in pu	-
$V_{C_{dc}}$	DC capacitor voltage	V
V_{dc}	HVDC station DC voltage	V
VSC	Voltage Source Converter	-
V_n	HVDC station negative pole voltage	V
V_p	HVDC station positive pole voltage	V
X_g	AC grid reactance	Ω
W_G	Generator energy	J
$\hat{W}_{sigross}$	AC grid gross inertial energy (peak value)	J
$W_{sigross}$	AC grid gross inertial energy	J
$\hat{W}_{sinet}$	AC grid net inertial energy (peak value)	J
W_{sinet}	AC grid net inertial energy	J

Appendix A

	Description	Unit
$...^{(0)}$	Any quantity evaluated with $R_c = 0\ \Omega$	-
$...^{(1)}$	Any quantity evaluated with $R_c = 0.6\ \Omega$	-
A	Maximum train current slope	A/s
$\angle L_{aa}(j\omega)$	L_{aa} phase in Fourier frequency domain	rad
$\mathbf{A}$	System state matrix	-
$\mathbf{B}$	System state-input matrix	-
$\mathbf{C}$	System output matrix	-
$\mathbf{C}$	System output-input matrix	-
C_a	ESS filter capacitance	F
C_t	Train filter capacitance	F
DC	Direct Current	-
dB	Decibel	dB
dec	Decade	-
$det(...)$	Matrix determinant	dB
ESS	Energy Storage System	-
$E_a(s)$	ESS voltage setpoint error in Laplace domain	V
d_a	ESS receptivity distance	m
ΔI_a	ESS current slope during forcing (approx.)	V
ΔV_a	ESS voltage forcing margin	V
ε_∞	Steady state regulator error signal	-
φ_m	Phase margin	rad
φ_m^*	Target phase margin for stability	rad
$G(s)$	System transfer function from $U(s)$ to $Y(s)$ (SISO systems)	-
$\mathbf{G}$(s)	Matrix of system transfer functions from $U(s)$ to $Y(s)$ (MIMO systems)	-
$G_{ab}(s)$	Element of $\mathbf{G}$ matrix	
g	System degree (number of poles in the origin)	-
$\mathbf{I}$	Identity matrix	-
I_a	ESS current	A
I_{R_c}	Catenary current	A
I_t	Train current	A
i_{C_a}	ESS filter capacitor current	A
i_{C_t}	Train filter capacitor current	A
$(j\omega)$	Fourier frequency domain operator	-
k_{aa}	G_{aa} static gain	-
k_δ	Droop coefficient	-
k_i	PID controller integral gain	-
k_d	PID controller derivative gain	-
k_p	PID controller proportional gain	-
L_a	ESS smoothing inductance	H
$L(s)$	System loop transfer function	-
$L_{ab}(s)$	$L(s)$ from $V_a^0(s)$ to $V_a(s)$	-
MIMO	Multiple Input Multiple Output system	-
μ_L	System static gain	-
μ_m	System gain margin	-
P_t	Average train traction power	W
PI	Proportional Integral control	-
PID	Proportional Integral Derivative control	-
PWM	Pulse Width Modulation	-
$\hat{p_t}$	Train power, peak value	W
$\psi(s)$	Characteristic polynomial in Laplace domain	-

continued on next page

continued from previous page

	Description	Unit
RFI	Rete Ferroviaria Italiana (Italian Railway Network)	-
$R(s)$	Regulator transfer function	-
$R_0(s)$	Regulator static transfer function	-
R_a	ESS filter resistance	Ω
R_c	Catenary resistance	Ω
R_t	Train filter resistance	Ω
S_{dB_0}	Bode diagram slope in dB scale at ω=0	dB/dec
S_{dB_n}	Bode diagram slope in dB scale before the n^{th} pole or zero	dB/dec
(s)	Laplace domain operator	-
r_c	Per-length catenary resistance	Ω/km
SISO	Single Input Single Output system	-
TSS	Traction substation	-
T_d	PID derivative time constant	s
T_i	PID/PI integral time constant	s
T_p	Pole time constant	s
T_z	Zero time constant	s
t	Time	s
τ	Delay time constant	s
$U(s)$	System input vector in Laplace domain	-
u	System input vector	-
V_a	Catenary voltage at ESS terminals	V
$V_a^0(s)$	ESS setpoint in Laplace domain	V
V_b	Train voltage braking threshold	V
V_t	Train voltage (at pantograph)	V
V_{tmin}	Absolute minimum train voltage	V
v_{C_a}	ESS filter capacitor voltage	V
v_{C_t}	Train filter capacitor voltage	V
v_{R_a}	ESS filter resistor voltage	V
v_{R_c}	Catenary equivalent resistance voltage	V
v_{R_t}	Train filter resistor voltage	V
ω_c	System characteristic pulsation	rad/s
ω_p	Pole pulsation	rad/s
ω_z	Zero pulsation	rad/s
ω_{z_R}	Regulator zero pulsation	rad/s
$\dot{x}$	Compact time-derivative nomenclature	x/s
x	System state vector	-
$Y(s)$	System output vector in Laplace domain	-

Appendix B

	Description	Unit
AC	Alternating Current	-
CHB	Cascaded H-bridge converter	-
DAB	Dual Active Bridge converter	-
$D_{1...8}$	DAB diodes	-
DC	Direct Current	-
Δ	Angle	rad
δ	DAB voltages shift angle	rad
EOC	Exceptional Operation Condition	-
ESS	Energy Storage System	-
η	ESS average efficiency	-
η_{a_c}	ESS average efficiency in charge	-
η_{a_d}	ESS average efficiency in discharge	-
FC	Flying Capacitor converter	-
$G(\delta)$	Linearizing function of $P(\delta)$	-
HV	High Voltage	-
I_A	Port A rectified current	A
I_{A_1}	Port A_1 rectified current	A
I_{A_2}	Port A_2 rectified current	A
I_a	Port A average current	A
I_a^0	Port A average current setpoint	A
i_a	Port A alternating current	A
$i_{a_0...a_4}$	Port A current slope changes	A
I_{a_c}	ESS charge current threshold	A
I_{a_d}	ESS discharge current threshold	A
I_B	Port B rectified current	A
I_{B_1}	Port B_1 rectified current	A
I_{B_2}	Port B_2 rectified current	A
I_b	Port B average current	A
i_b	Port B alternating current	A
k_{δ_d}	Droop coefficient, positive current discharge	-
L_A	Port A leakage inductance	H
N	Total DAB modules	-
NOC	Normal Operation Condition	-
NPC	Neutral Point Clamped converter	-
n	Transformer ratio	-
ω_s	DAB converter switching angular speed	rad/s
P_A	Average power at Port A	W
P_a	Average ESS power	W
P_B	Average power at Port B	W
$P(\delta)$	Power function depending on shift angle	-
PET	Power Electronics Transformer	-
PI	Proportional Integral control	-
PID	Proportional Integral Derivative control	-
PID_c	PID control for ESS charge	-
PID_δ	PID control for DAB shift angle	-
p_a	ESS instantaneous power at catenary terminals	W
$S_{1...8}$	DAB power electronics switches	-
SST	Solid State Transformer	-
swf(t)	Switching function	-
T_s	DAB converter switching period	s

continued on next page

continued from previous page

	Description	Unit
$t_{0...4}$	DAB current slope change times	s
t_c	Charge time	s
t_d	Discharge time	s
θ_c	PID control action, negative current charge	A
τ	DAB voltages shift	s
V_a	Catenary voltage at ESS terminals	V
V_{ac}	Converter phase-to-phase AC voltage	V
V_{DC}	Converter DC voltage	V
V_{a_c}	Catenary voltage threshold for ESS charge	V
V_{a_d}	Catenary voltage threshold for ESS discharge	V
v_1	Transformer primary side alternating voltage	V
v_2	Transformer secondary side alternating voltage	V
V_A	Port A direct voltage	V
V_{A_1}	Port A_1 direct voltage	V
V_{A_2}	Port A_2 direct voltage	V
v_a	Port A alternating voltage	V
V_B	Port B direct voltage	V
V_{B_1}	Port B_1 direct voltage	V
V_{B_2}	Port B_2 direct voltage	V
v_b	Port B alternating voltage	V
v_{L_A}	Voltage drop on port A leakage inductance	V
W_{a_c}	ESS energy	J
W_{a_c}	ESS gross charged energy	J
W_{a_d}	ESS net discharged energy	J
$W_{a_{mal}}$	ESS maximal energy limit	J
$W_{a_{max}}$	ESS maximum energy limit	J
$W_{a_{mil}}$	ESS minimal energy limit	J
$W_{a_{min}}$	ESS minimum energy limit	J
$W_{j_{a_c}}$	ESS energy losses in charge	J
$W_{j_{a_d}}$	ESS energy losses in discharge	J

Appendix C

	Description	Unit
ABB	ASEA Brown Boveri	-
AC	Alternating Current	-
ASEA	Allmänna Svenska Elektriska Aktiebolaget	-
CSC	Current Source Converter	-
DC	Direct Current	-
HVDC	High Voltage Direct Current	-
IGBT	Insulated Gate Bipolar Transistor	-
LCC	Line Commutated Converter	-
PWM	Pulse Width Modulation	-
SACOI	SArdinia-COrsica-Italy	-
U.S.A.	United States of America	-
VSC	Voltage Source Converter	-
ZBD	Zipernowsky-Bláthy-Déri	-

BIBLIOGRAPHY

[1] *TE 193 ed. 1984 - Trasformatori trifasi con la regolazione automatica della tensione sotto carico.* RFI, 1984.

[2] *TC TE SSE 35 ed. 2002 - Trasformatore in M.T. da 5.4 MVA in resina epossidica.* RFI, 2002.

[3] *A China-EU electricity transmission link - Assessment of potential connecting countries and routes.* JRC Science For Policy Report - European Commission, 2017.

[4] *Allegato A15 - Partecipazione alla regolazione di frequenza e frequenza-potenza.* Terna, 2008.

[5] *Merlin Project - Sustainable and intelligent management of energy for smarter railway systems in Europe: an integrated optimization approach - D7.1 Exploitation Plan.* EC Contract No. FP7 - 314125, 2013.

[6] *Merlin Project - Sustainable and intelligent management of energy for smarter railway systems in Europe: an integrated optimization approach - D1.1 Railway network key elements and main sub-systems specification.* EC Contract No. FP7 - 314125, 2013.

[7] *Merlin Project - Sustainable and intelligent management of energy for smarter railway systems in Europe: an integrated optimization approach - D7.5. Guideline for the implementation of network integration (strategic and operational level).* EC Contract No. FP7 - 314125, 2015.

[8] *In2Rail - Innovative Intelligent Rail - Deliverable D11.5 - Integration and Implementation Design - Link to Shift2Rail.* EC Contract No. FP7 - 314125, 2018.

[9] *TE 194 ed. 1980 - Raddrizzatori al silicio.* RFI, 1980.

[10] *Standard di SSE.* RFI, 2003.

[11] *TC TE SSE 50 ed. 2002 - Gruppo raddrizzatore a 1355 Vca / 1800 Vcc da 5.4 MW.* RFI, 2002.

[12] *TE 178 ed. 1984 - Trasformatori trifasi.* RFI, 1984.

[13] Legambiente, "Rapporto pendolaria 2017 - la situazione e gli scenari del trasporto pendolare in italia - trad. Situation and scenarios about commuters transportation in Italy." 2017.

[14] *In2Rail - Innovative Intelligent Rail - Deliverable D10.5 - Final research report "Intelligent AC power supply".* EC Contract No. FP7 - 314125, 2018.

[15] A. Verdicchio, P. Ladoux, H. Caron, and S. Sanchez, "Future DC railway electrification system - go for 9 kV," in *Proc. Ship Propulsion and Road Vehicles Int 2018 IEEE Int. Conf. Electrical Systems for Aircraft, Railway Transportation Electrification Conf. (ESARS-ITEC)*, Nov. 2018, pp. 1–5.

[16] R. Barrero, X. Tackoen, and J. V. Mierlo, "Improving energy efficiency in public transport: Stationary supercapacitor based energy storage systems for a metro network," in *Proc. IEEE Vehicle Power and Propulsion Conf*, Sep. 2008, pp. 1–8.

[17] ——, "Quasi-static simulation method for evaluation of energy consumption in hybrid light rail vehicles," in *Proc. IEEE Vehicle Power and Propulsion Conf*, Sep. 2008, pp. 1–7.

[18] R. Teymourfar, G. Farivar, H. Iman-Eini, and B. Asaei, "Optimal stationary supercapacitor energy storage system in a metro line," in *Proc. 2nd Int. Conf. Electric Power and Energy Conversion Systems (EPECS)*, Nov. 2011, pp. 1–5.

[19] A. Killer, A. Armstorfer, A. E. DÃez, and H. Biechl, "Ultracapacitor assisted regenerative braking in metropolitan railway systems," in *Proc. IEEE Colombian Intelligent Transportation Systems Symp. (CITSS)*, Aug. 2012, pp. 1–6.

[20] Z. Gao, J. Fang, Y. Zhang, D. Sun, L. Jiang, and X. Yang, "Control strategy research of wayside supercapcitor energy storage system for urban rail transit," in *Proc. 26th Chinese Control and Decision Conf. (2014 CCDC)*, May 2014, pp. 4786–4791.

[21] *Prospetto informativo rete 2019.* Ferrovienord, 2017.

[22] *TSR datasheet - italy.hitachirail.com/.* Hytachi Rail (former Ansaldo Breda), 2018.

[23] A. Corti, C. Ongini, M. Tanelli, and S. M. Savaresi, "Quantitative driving style estimation for energy-oriented applications in road vehicles," in *Proc. and Cybernetics 2013 IEEE Int. Conf. Systems, Man*, Oct. 2013, pp. 3710–3715.

[24] M. Shimada, R. Oishi, D. Araki, and Y. Nakamura, "Energy storage system for effective use of regenerative energy in electrified railways," *Hitachi review*, vol. 59, no. 1, pp. 33–38, 2010.

[25] F. Perticaroli, "Sistemi elettrici per i trasporti: trazione elettrica." Masson, 2001.

[26] M. Brenna, F. Foiadelli, and D. Zaninelli, "Electrical railway transportation systems." Wiley-IEEE Press, 2018.

[27] Y. Yoshida, H. P. Figueroa, and R. A. Dougal, "Comparison of energy storage configurations in railway microgrids," in *Proc. IEEE Second Int. Conf. DC Microgrids (ICDCM)*, Jun. 2017, pp. 133–138.

[28] V. Calderaro, V. Galdi, G. Graber, and A. Piccolo, "Optimal siting and sizing of stationary supercapacitors in a metro network using PSO," in *Proc. IEEE Int. Conf. Industrial Technology (ICIT)*, Mar. 2015, pp. 2680–2685.

[29] M. Nick, R. Cherkaoui, and M. Paolone, "Optimal siting and sizing of distributed energy storage systems via alternating direction method of multipliers," in *Proc. Power Systems Computation Conf*, Aug. 2014, pp. 1–7.

[30] A. S. A. Awad, T. H. M. EL-Fouly, and M. M. A. Salama, "Optimal ess allocation for benefit maximization in distribution networks," *IEEE Transactions on Smart Grid*, vol. 8, no. 4, pp. 1668–1678, Jul. 2017.

[31] D. I. Karadimos, A. D. Karafoulidis, D. I. Doukas, P. A. Gkaidatzis, D. P. Labridis, and A. G. Marinopoulos, "Techno-economic analysis for optimal energy storage systems placement considering stacked grid services," in *Proc. 14th Int. Conf. the European Energy Market (EEM)*, Jun. 2017, pp. 1–6.

[32] R. S. Baheti, "Simple anti-windup controllers," in *Proc. American Control Conf*, Jun. 1989, pp. 1684–1686.

[33] K. Sakai and Y. Ishida, "An improved anti-windup control using a pi controller," in *Proc. Modelling and Simulation (AIMS) 2015 3rd Int. Conf. Artificial Intelligence*, Dec. 2015, pp. 197–201.

[34] M. Yang, S. Tang, and D. Xu, "Comments on "antiwindup strategy for pi-type speed controller "," *IEEE Transactions on Industrial Electronics*, vol. 62, no. 2, pp. 1329–1332, Feb. 2015.

[35] A. Clerici, E. Tironi, and F. C. Dezza, "Multiport converters and ess on 3kV DC railway lines: Case study for braking energy savings," in *Proc. IEEE 16th Int. Conf. Environment and Electrical Engineering (EEEIC)*, Jun. 2016, pp. 1–6.

[36] A. Clerici, E. Tironi, and F. Castelli-Dezza, "Multiport converters and ess on 3-kV DC railway lines: Case study for braking energy savings," *IEEE Transactions on Industry Applications*, vol. 54, no. 3, pp. 2740–2750, May 2018.

[37] Y. Jiang, J. Liu, W. Tian, M. Shahidehpour, and M. Krishnamurthy, "Energy harvesting for the electrification of railway stations: Getting a charge from the regenerative braking of trains.a," *IEEE Electrification Magazine*, vol. 2, no. 3, pp. 39–48, Sep. 2014.

[38] A. Gonzalez-Gil, R. Palacin, P. Batty, and J. P. Powell, "Energy-efficient urban rail systems: strategies for an optimal management of regenerative braking energy," in *Transport Research Arena (TRA) 5th Conference: Transport Solutions from Research to DeploymentEuropean CommissionConference of European Directors of Roads (CEDR) European Road Transport Research Advisory Council (ERTRAEuropean Rail Research Advisory Council (ERRAC) Institut Francais des Sciences et Technologies des Transports*, 2014.

[39] F. Ciccarelli, D. Iannuzzi, K. Kondo, and L. Fratelli, "Line-voltage control based on wayside energy storage systems for tramway networks," *IEEE Transactions on Power Electronics*, vol. 31, no. 1, pp. 884–899, Jan. 2016.

[40] *CSN EN 50163 ed. 2 - Railway applications - Supply voltages of traction systems.* European Standard, 2004.

[41] M. Tokudome, K. Tanaka, T. Senjyu, A. Yona, T. Funabashi, and C. H. Kim, "Frequency and voltage control of small power systems by decentralized controllable loads," in *Proc. Int. Conf. Power Electronics and Drive Systems (PEDS)*, Nov. 2009, pp. 666–671.

[42] R. M. Wright, "Understanding modern generator control," *IEEE Transactions on Energy Conversion*, vol. 4, no. 3, pp. 453–458, Sep. 1989.

[43] D. C. Raj and D. N. Gaonkar, "Frequency and voltage droop control of parallel inverters in microgrid," in *Proc. Energy Communication (CIEC) 2016 2nd Int. Conf. Control, Instrumentation*, Jan. 2016, pp. 407–411.

[44] M. Chamana and B. H. Chowdhury, "Droop-based control in a photovoltaic-centric microgrid with battery energy storage," in *Proc. North American Power Symp. (NAPS)*, Sep. 2013, pp. 1–6.

[45] *http://www.trenord.it, Trenord - Official timetable, Panel 167.*

[46] *Relazione annuale sullo stato dei servizi e dell'attivita' svolta (Annual report on the status of services and activities).* Autorita' per l'energia elettrica, il gas e il sistema idrico (Autority for electrical energy, gas and water system), 2017.

[47] L. Cheng, P. Acuna, R. P. Aguilera, J. Jiang, J. Flecther, and C. Baier, "Model predictive control for energy management of a hybrid energy storage system in light rail vehicles," in *Proc. Power Electronics and Power Engineering (CPE-POWERENG) 2017 11th IEEE Int. Conf. Compatibility*, Apr. 2017, pp. 683–688.

[48] J. A. Aguado, A. J. S. Racero, and S. de la Torre, "Optimal operation of electric railways with renewable energy and electric storage systems," *IEEE Transactions on Smart Grid*, vol. 9, no. 2, pp. 993–1001, Mar. 2018.

[49] *Autorita' per l'energia elettrica il gas e il sistema idrico - Relazione annuale sullo stato dei servizi e sull'attivita' svolta - 31 Marzo 2017" (trad. "Autority for electric energy, gas and water system - Annual report on the status of services and activities - March,* 31st *2017).*

[50] W. Zhang and X. Yan, "Fire risk assessment of battery powered ship using entropy cloud method," in *Proc. 4th Int. Conf. Transportation Information and Safety (ICTIS)*, Aug. 2017, pp. 331–336.

[51] G. M. Seok and K. S. Yun, "Performance improvement of fiber supercapacitor by using nico2o4 nano-needles and ag nanowires," in *Proc. IEEE Micro Electro Mechanical Systems (MEMS)*, Jan. 2018, pp. 635–637.

[52] G. Palmieri, F. Vasca, R. Frasca, and P. Marino, "Control of supercapacitor storage system in energy efficient railway vehicles," in *Proc. Automation and Motion 2014 Int. Symp. Power Electronics, Electrical Drives*, Jun. 2014, pp. 801–806.

[53] R. Zhou, Z. Huang, H. Li, Z. Wu, and J. Peng, "An adaptive charging control strategy for ultracapacitor light rail vehicles," in *Proc. IEEE Energy Conversion Congress and Exposition (ECCE)*, Sep. 2016, pp. 1–4.

[54] V. Musolino, A. Pievatolo, and E. Tironi, "A statistical approach to electrical storage sizing with application to the recovery of braking energy," *Energy*, vol. 36, no. 11, pp. 6697 – 6704, 2011.

[55] W. Jiang and B. Fahimi, "Multi-port power electric interface for renewable energy sources," in *Proc. Twenty-Fourth Annual IEEE Applied Power Electronics Conf. and Exposition*, Feb. 2009, pp. 347–352.

[56] A. D. Napoli, F. Crescimbini, S. Rodo, and L. Solero, "Multiple input DC-dc power converter for fuel-cell powered hybrid vehicles," in *Proc. (Cat. No.02CH37289) 2002 IEEE 33rd Annual IEEE Power Electronics Specialists Conf*, vol. 4, 2002, pp. 1685–1690.

[57] H. Tao, J. L. Duarte, and M. A. M. Hendrix, "Multiport converters for hybrid power sources," in *Proc. IEEE Power Electronics Specialists Conf*, 2008, pp. 3412–3418.

[58] D. Dujic, F. Kieferndorf, F. Canales, and U. Drofenik, "Power electronic traction transformer technology," in *Proc. 7th Int. Power Electronics and Motion Control Conf*, vol. 1, Jun. 2012, pp. 636–642.

[59] M. Brenna, F. Foiadelli, E. Tironi, and D. Zaninelli, "Ultracapacitors application for energy saving in subway transportation systems," in *Proc. Int. Conf. Clean Electrical Power*, May 2007, pp. 69–73.

[60] J. Wang, Z. Yang, F. Lin, Y. Zhao, H. Xia, Y. Lu, and X. Zhao, "Thresholds modification strategy of wayside supercapacitor storage considering DC substation characteristics," in *Proc. IECON 2015 - 41st Annual Conf. of the IEEE Industrial Electronics Society*, Nov. 2015, pp. 002 076–002 081.

[61] K. Kwon, K. G. Lee, T. Kim, J. Lee, B. J. Jone, J. Choi, and I. Colak, "Enhanced operating scheme of ess for DC transit system," in *Proc. IEEE Int. Power Electronics and Motion Control Conf. (PEMC)*, Sep. 2016, pp. 1113–1118.

[62] M. Y. Ayad, M. Becherif, A. Henni, A. Aboubou, and M. Wack, "Sliding mode control and unit power factor applied to embarked supercapacitors for electrical train traction," in *Proc. IEEE Int. Symp. Industrial Electronics*, Jul. 2010, pp. 334–339.

[63] A. Bouscayrol, W. Lhomme, C. Demian, A. L. AllÃ¨gre, E. Chattot, and S. E. Fassi, "Experimental set-up to test the power transfer of an innovative subway using supercapacitors," in *Proc. IEEE Vehicle Power and Propulsion Conf*, Sep. 2010, pp. 1–6.

[64] A. L. Allegre, A. Bouscayrol, P. Delarue, P. Barrade, E. Chattot, and S. El-Fassi, "Energy storage system with supercapacitor for an innovative subway," *IEEE Transactions on Industrial Electronics*, vol. 57, no. 12, pp. 4001–4012, Dec. 2010.

[65] M. Khodaparastan and A. Mohamed, "Supercapacitors for electric rail transit systems," in *Proc. IEEE 6th Int. Conf. Renewable Energy Research and Applications (ICRERA)*, Nov. 2017, pp. 896–901.

[66] A. Clerici, E. Tironi, and F. C. Dezza, "Voltage stabilization and efficiency improvements on DC railways by stand alone energy storage systems," in *Proc. IEEE Int. Conf. Environment and Electrical Engineering and 2017 IEEE Industrial and Commercial Power Systems Europe (EEEIC / I CPS Europe)*, Jun. 2017, pp. 1–7.

[67] ENTSO-e, "Project 299 - sacoi3," 2018.

[68] R. Benato, A. Chiarelli, S. D. Sessa, R. D. Zan, M. Rebolini, and M. Pazienza, "HVDC cables along with highway infrastructures: the "piedmont - savoy" Italy - France intertie," in *Proc. AEIT Int. Annual Conf*, Oct. 2018, pp. 1–6.

[69] *Piano di Sviluppo della Rete di Trasmissione Nazionale.* Terna, 2018.

[70] *Annual Work Programme.* ENTSO-e, 2018.

[71] ABB, "Hvdc light - it is time to connect," 2013.

[72] S. D. Boeck, P. Tielens, W. Leterme, and D. V. Hertem, "Configurations and earthing of HVDC grids," in *Proc. IEEE Power Energy Society General Meeting*, Jul. 2013, pp. 1–5.

[73] N. Mohan, T. M. Undeland, and W. P. Robbins, *Power Electronics. Converters, Applications and Design*, Third, Ed. John Wiley and Sons, Inc, 2003.

[74] I. M. Sanz, P. D. Judge, C. E. Spallarossa, B. Chaudhuri, and T. C. Green, "Dynamic overload capability of vsc hvdc interconnections for frequency support," *IEEE Transactions on Energy Conversion*, vol. 32, no. 4, pp. 1544–1553, 2017.

[75] A. K. Sahoo, A. Shahani, K. Basu, and N. Mohan, "Lcl filter design for grid-connected inverters by analytical estimation of pwm ripple voltage," in *Applied Power Electronics Conference and Exposition (APEC), 2014 Twenty-Ninth Annual IEEE.* IEEE, 2014, pp. 1281–1286.

[76] Y. Xiao, J. Zhao, and S. Mao, "Theory for the design of c-type filter," in *Harmonics and Quality of Power, 2004. 11th International Conference on.* IEEE, 2004, pp. 11–15.

[77] Y.-J. Kim and H. Kim, "Optimal inductance ratio of lcl filter for grid connected inverters considering with low order harmonics," in *Industrial Electronics Society, IECON 2016-42nd Annual Conference of the IEEE.* IEEE, 2016, pp. 2355–2360.

[78] P. Tielens and D. Van Hertem, "The relevance of inertia in power systems," *Renewable and Sustainable Energy Reviews*, vol. 55, pp. 999–1009, 2016.

[79] A. Bucurenciu, M. Ndreko, M. Popov, and M. A. van der Meijden, "Frequency response using mtdc grids: A comparative study of common methods," in *PowerTech, 2015 IEEE Eindhoven.* IEEE, 2015, pp. 1–6.

[80] X. Liu and A. Lindemann, "Coordinated control of vsc-HVDC connected offshore windfarms for enhanced ability of providing synthetic inertia," in *Proc. IEEE 6th Int. Symp. Power Electronics for Distributed Generation Systems (PEDG)*, Jun. 2015, pp. 1–6.

[81] L. Orellana, V. Matilla, S. Wang, O. D. Adeuyi, and C. E. Ugalde-Loo, "Fast frequency support control in the gb power system using vsc-hvdc technology," in *Innovative Smart Grid Technologies Conference Europe (ISGT-Europe), 2017 IEEE PES*. IEEE, 2017, pp. 1–6.

[82] O. D. Adeuyi, M. Cheah-Mane, J. Liang, and N. Jenkins, "Fast frequency response from offshore multiterminal vsc –HVDC schemes," *IEEE Transactions on Power Delivery*, vol. 32, no. 6, pp. 2442–2452, Dec. 2017.

[83] V. E. Riquelme and O. H. Chavez, "Towards system-wise synthetic inertia models to study power system frequency response," in *Proc. Information and Communication Technologies (CHILECON) 2017 CHILEAN Conf. Electrical, Electronics Engineering*, Oct. 2017, pp. 1–5.

[84] A. Yazdani and R. Iravani, *Voltage-sourced converters in power systems: modeling, control, and applications*. John Wiley & Sons, 2010.

[85] X. Liu and A. Lindemann, "Control of vsc-HVDC connected offshore windfarms for providing synthetic inertia," *IEEE Journal of Emerging and Selected Topics in Power Electronics*, p. 1, 2017.

[86] M. Maurer, M. Scherer, and D. Whitley, "Optimization strategies for frequency-response coupling between synchronous areas," in *PowerTech, 2017 IEEE Manchester*. IEEE, 2017, pp. 1–6.

[87] H. R. Chamorro, A. C. Sanchez, A. Overjordet, F. Jimenez, F. Gonzalez-Longatt, and V. K. Sood, "Distributed synthetic inertia control in power systems," in *Proc. Int. Conf. ENERGY and ENVIRONMENT (CIEM)*, Oct. 2017, pp. 74–78.

[88] *Codice di trasmissione, dispacciamento, sviluppo e sicurezza della rete*. Terna, 2018.

[89] S. Canevese, A. Iaria, and M. Rapizza, "Impact of fast primary regulation and synthetic inertia on grid frequency control," in *Innovative Smart Grid Technologies Conference Europe (ISGT-Europe), 2017 IEEE PES*. IEEE, 2017, pp. 1–6.

[90] R. Chiumeo, C. Gandolfi, A. Clerici, F. C. Dezza, and R. Zuelli, "Contribution of HVDC systems in increasing the electrical network inertia: A case study," in *Proc. IEEE Int. Conf. Environment and Electrical Engineering and 2018 IEEE Industrial and Commercial Power Systems Europe (EEEIC / I CPS Europe)*, Jun. 2018, pp. 1–6.

[91] H. Liu and Z. Chen, "Contribution of vsc-HVDC to frequency regulation of power systems with offshore wind generation," *IEEE Transactions on Energy Conversion*, vol. 30, no. 3, pp. 918–926, Sep. 2015.

[92] Q. Gao and R. Preece, "Improving frequency stability in low inertia power systems using synthetic inertia from wind turbines," in *Proc. IEEE Manchester PowerTech*, Jun. 2017, pp. 1–6.

[93] Y. Li, Z. Zhang, Y. Yang, Y. Li, H. Chen, and Z. Xu, "Coordinated control of wind farm and vsc–hvdc system using capacitor energy and kinetic energy to improve

inertia level of power systems," *International Journal of Electrical Power & Energy Systems*, vol. 59, pp. 79–92, 2014.

[94] J. Zhu, W. Hung, C. Wang, X. Zhang, S. Bu, Q. Li, H. Urdal, C. D. Booth *et al.*, "Synthetic inertia control strategy for doubly-fed induction generator wind turbine generators using lithium-ion supercapacitors," *IEEE Transactions on Energy Conversion*, 2017.

[95] R. Zuelli, R. G. M. Chiumeo, C. Gandolfi, A. Clerici, S. Pugliese, S. Fratti, and M. Garocchio, "The impact of MVDC links on distribution networks," in *Proc. AEIT Int. Annual Conf*, Oct. 2018, pp. 1–5.

[96] P. Bolzern, R. Scattolini, and N. Schiavoni, "Fondamenti di controlli automatici, 3a edizione," 2008.

[97] G. Guardabassi, "Lezioni di fondamenti di automatica," 2006.

[98] P. Rocco, "Dispense ad uso degli studenti del politecnico di milano per i corsi da cinque crediti didattici - automatica, ingegneria aerospaziale," 2008.

[99] *E-006 ed. 1989 - Reattori elettrici in lastra d'alluminio.* RFI, 1989.